MECHANICAL PROPERTIES OF SHALE GAS RESERVOIR ROCKS AND ITS RELATION TO THE IN-SITU STRESS VARIATION OBSERVED IN SHALE GAS RESERVOIRS

A DISSERTATION

SUBMITTED TO THE DEPARTMENT OF GEOPHYSICS

AND THE COMMITTEE ON GRADUATE STUDIES

OF STANFORD UNIVERSITY

IN PARTIAL FULFILLMENT OF THE REQUIREMENTS

FOR THE DEGREE OF

DOCTOR OF PHILOSOPHY

SRB VOLUME 128

Hiroki Sone

March 2012

I certify that I have read this dissertation and that, in my opinion, it is fully adequate in scope and quality as dissertation for the degree of Doctor of Philosophy.

_____
(Mark D. Zoback) Principal Advisor

I certify that I have read this dissertation and that, in my opinion, it is fully adequate in scope and quality as dissertation for the degree of Doctor of Philosophy.

_____
(Stephen Karner)

I certify that I have read this dissertation and that, in my opinion, it is fully adequate in scope and quality as dissertation for the degree of Doctor of Philosophy.

_____
(Paul Segall)

I certify that I have read this dissertation and that, in my opinion, it is fully adequate in scope and quality as dissertation for the degree of Doctor of Philosophy.

_____
(Norman Sleep)

Approved for the University Committee on Graduate Studies.

ABSTRACT

The main focus of this thesis is to study the basic rock mechanical properties of shale gas reservoir rocks, the in-situ state of stress in shale gas reservoirs, and their inter-relation.

Laboratory studies on the elastic and deformational mechanical properties of gas shales show that these rocks exhibit wide range of mechanical properties and significant anisotropy reflecting their wide range of material composition and fabric anisotropy. The elastic properties of these shale rocks are successfully described by tracking the relative amount soft components (clay and solid organic materials) in the rock and also acknowledging the anisotropic distribution of the soft components. Gas shales were also found to possess relatively stronger degree of anisotropy compared to other organic-rich shales studied in the literature, possibly due to the fact that these rocks come from peak-maturity source rocks. The deformational properties studied by observing the ductile creep behavior and brittle strengths were also found to be influenced by the amount of soft components in the rock and exhibited mechanical anisotropy. A strong correlation between the elastic properties and the deformational properties was also found through comparison of laboratory data. The relation between the elastic modulus and magnitude of ductile creep is investigated through differential effective medium (DEM) modeling of the shale elastic properties. The partitioning of the far-field stress between the stiff and soft components was calculated in the DEM modeling to forward model the ductile creep behavior of the shales.

Results showed that the correlation between the elastic properties and magnitude of ductile creep arises because they are both influenced by the stress partitioning in the rocks.

Examination of a FMI image log from a vertical well in Barnett shale showed that the in-situ state of stress fluctuates rapidly within the reservoir in terms of the orientation and magnitude of the principal stress. The appearance and disappearance of drilling-induced tensile fractures roughly correlated with the variation in the clay and organic content in the formation, suggesting that there is a fluctuation in the magnitude of the horizontal stress difference, on the order of 10 MPa, that may be controlled by the mechanical heterogeneity of the formations. In order to explain the linkage between the observed stress variation and formation heterogeneity, we focused on the variation of ductile creep behavior exhibited by the gas shale rocks observed in the laboratory. The laboratory creep data was analyzed under the framework of viscoelastic theory to quantify its behavior and allow the calculation of the stress carrying capacity of the rocks. The viscoelastic behavior of the gas shales were found to be best approximated by a power-law function of time and the accumulation of differential stress over geological time in these rocks were calculated according to this constitutive description. Stress analysis assuming a simple constant strain rate tectonic loading history over 150 Ma shows that the horizontal stress difference on the order of 10 MPa observed in the Barnett shale can be explained by the variation in viscoelastic properties within the Barnett shale. Our results highlight the importance of acknowledging viscous deformation of shale gas reservoir rocks to understand the current in-situ state of stress in these reservoirs.

A study of frictional properties of a saponite-rich fault gouge from a serpentinite-bearing fault in central Japan is also presented in this thesis. Field characterization of the internal structure of a fault juxtaposing serpentinites and Cretaceous sedimentary rocks show that hydrothermal metasomatic reactions took place at the fault interface which produced peculiar mineral assemblages along the fault plane. The saponite-rich fault gouge resulting from the metasomatic reaction

exhibits extremely low coefficient of friction, ~0.1, at wet conditions and strong velocity-strengthening characteristics. The study highlights the importance of geochemical reactions along fault planes which may ultimately control the overall mechanical behavior of major fault zones.

ACKNOWLEDGMENTS

The years I spent in Stanford were filled with fruitful experiences and I owe many thanks to the people who have helped me grow both academically and personally.

I first would like to thank my advisor, Mark Zoback, for giving me a chance to study in Stanford which has exposed me to countless opportunities that broadened my future. I thank Mark for the great balance of guidance and freedom he has given me, for allowing me time to dig in on complicated ideas while keeping things simple at the end. I greatly admire his enthusiasm towards science and life, which will continue to inspire me in the future. I thank my committee members Paul Segall, Norm Sleep, Gary Mavko, and Stephen Karner for their guidance throughout the course of my study. Through classes, seminars, and discussions, you taught me how to think scientifically and the joy of pursuing geophysics. I also thank the excellent staffs of the Geophysics department for their constant support. Special thanks to Tara Illich and Susan Moskowitz for their friendly and caring help.

I thank the SRB affiliates for their financial support and providing us an excellent research environment. I also thank the companies BP, ConocoPhillips, and UGR for generously providing us the samples and data needed for the research. Special thanks to Ellen Mallman, David Spain, Peter Hennings, and James Packwood

who were always supportive towards my research and facilitated a great collaboration. I also thank Jim Noel from New England Research for the much vital technical assistance he provided over the phone and email.

I will not forget all the fun times I spent with my colleagues in the office: Katie Boyle, Jeremy Brown, Laura Chiaramonte, Indrajit Das, Amy Day-Lewis, Paul Hagin, Rob Heller, Owen Hurd, Madhur Johri, Arjun Kohli, Amie Lucier, Ellen Mallman, Pijush Paul, Hannah Ross, John Vermylen, Rall Walsh, Randy Walters, Ali Yaghoubi, and Alec Yang. Thanks for the great times we had together and I very much look forward to our continued friendship. I could not have survived the lab without the support and fun brought by Ashley Enderlin and Max Praglin. It was a great pleasure to share many memorable moments with you in the lab.

I could not have come this far without the continued support of my family. My parents, Shosuke and Suzuko, has raised me to everything I am today, and I cannot thank enough my wife, Chica, and daughter, Yuri, for the limitless support and happiness they have brought to me. Much credit goes to my wife for the completion of my thesis. Finally, I would like to dedicate this thesis to my grandfather Koichi Aoki, who has guided me in many ways since I gained interest in science in junior high school.

TABLE OF CONTENTS

LIST OF TABLES

Number *Page*

LIST OF FIGURES

Number *Page*

Chapter 1

INTRODUCTION

1.1 Overview and motivation

This thesis is composed of studies related to two topics. Four chapters deal with the rock mechanical and geomechanical characterization of shale gas reservoirs aimed at understanding the fundamental controls on the outcome of hydraulic fracturing operation. The final chapter presents an integrated field and laboratory study of a fault zone material that aims to understand the role of geochemical interactions on the mechanical strength of a fault. Although distinct in focus, these studies demonstrate the importance of the thorough characterization of rock mechanical properties on the understanding of how earth materials deform over various time scales and how it affects the current state of stress in the crust.

Natural gas production from shale gas reservoirs is now proven to be feasible from numerous operations in various shale gas reservoirs in North America, but many challenges still remain in the full exploitation of these unconventional reservoirs. Production from shale gas reservoirs requires stimulation by hydraulic fracturing due to the extremely low permeability of the reservoir rocks. Maximization of reservoir

drainage is further achieved by performing hydraulic fracturing in multiple stages along a horizontal well drilled parallel to the producing formation. While these practices have lead to the economical productions of natural gases in numerous shale gas reservoirs, the problem of optimizing shale gas production has been much involved due to the complicated mechanical response of these reservoirs to fluid and proppant injection, and the variability of reservoir characteristics between reservoirs and within a reservoir.

A common problem encountered in hydraulic fracturing operations in gas shales is the variability and unpredictability of the outcome of hydraulic fracturing. Industry experiences show that injection pressures required to fracture the formation (fracture gradient) oftentimes vary significantly along a well, and there can be intervals where the formation cannot be fractured successfully by fluid injection (Daniels et al., 2007). Shale gas reservoirs also respond to fluid injection in a variety of modes. As observed through microseismic monitoring, distribution of activated seismicity can be confined along a macroscopic fracture plane, but most time they are dispersed throughout a wide region in the reservoir reflecting the development of a complex fracture network. (Waters et al., 2006; Maxwell, 2011). In some cases, there also seems to be a slower mode of deformation involved in the fracturing process as inferred from the tremor-like signals found in the microseismic monitoring data (long period long duration events, Das and Zoback, 2011).

Under this situation, geophysicists and petrophysicists are not only asked to precisely locate the reservoir, but also to understand how the reservoir responds to fluid injection and predict the best location to fracture along the well. The latter is a great challenge since reservoir mechanical properties are oftentimes only characterized through its elastic properties while rock deformation during fracturing takes place beyond the elastic limit and at longer time scales. In some cases, these variations in reservoir responses to fluid injection are found to correlate with the petrophysical properties and seismic attributes in the reservoir (Daniels et al., 2007; Maxwell, 2011; Refunjol et al., 2011). These observations have lead to industry practices of predicting

"sweet-spots", characterized by "brittle" rock properties and suggested low fracture gradients. While these practices are practical, and probably the only feasible approach in daily practice, they are not based on fundamental observations of rock deformational behavior. There is still a severe lack of mechanical understanding on how hydraulic fracturing in shale gas reservoir function and how it ultimately leads to reservoir stimulation.

Regardless of the complexity involved, rock deformation in the subsurface, including hydraulic fracturing upon fluid injection, is controlled by two primary factors; rock deformational property and in-situ state of stress. The first four chapters in this thesis addresses the following questions aimed to enhance our knowledge of rock deformational properties and the in-situ stress state in shale gas reservoirs:

1. What are fundamental controls on the mechanical properties of shale gas reservoir rocks? Material composition? Rock structure?

2. Can we infer anything about the rock deformational properties from their elastic properties? What are the bases for these correlations?

3. What is the in-situ state of stress in shale gas reservoirs and how do they vary?

4. How is the in-situ state of stress related to the formation heterogeneity?

5. How do rock deformational properties and the in-situ stress state relate with one another?

In the final chapter, we study the problem of addressing fault zone mechanical properties from laboratory measured fault gouge properties. Recent studies on frictional properties of fault gouge materials collected from the SAFOD project (Moore and Reymer, 2007; Lockner et al., 2011; Zoback et al., 2010) reported that there are anomalously weak clay minerals along the creeping section of the San Andreas Fault. The finding provides one explanation to the recurring debate of why the fault appears to be weak from field observations, despite the generally high

strength of crustal materials inferred from laboratory experiments. These findings demonstrated the importance of identifying local occurrences of metasomatic products along a fault, which can be responsible for the overall mechanical behavior of a major fault. We report on a study of frictional properties of a saponite-rich fault gouge found in a serpentinite-bearing fault zone along Gokasho-Arashima Tectonic Line in central Japan, which also demonstrates the local presence of anomalously weak materials along faults.

1.2 Thesis outline

This thesis broadly covers three main topics through five chapters: laboratory studies on the mechanical properties of shale gas reservoir rocks (Chapters 2 and 3), observation of stress variations observed in a shale gas reservoir and its relation to rock properties (Chapters 4 and 5), and laboratory study of fault rock properties (Chapter 6).

In Chapter 2, we start by acquiring basic elastic mechanical properties of gas shale sample from several reservoirs in North America through laboratory experiments. The results are compared with the sample material composition and microstructural characteristics to understand the controls on the elastic properties. Specific attention is on what controls the mechanical anisotropy of the gas shale samples. Results are compared with past findings on mechanical anisotropy of organic-lean and organic-rich shales reported in the literature. We find that elastic properties of gas shale exhibit wide range of elastic properties reflecting its wide range of composition and fabric anisotropy. Anisotropy of matured gas shales are also strong compared to other organic-rich shales. A database of elastic properties of gas shales is also provided in this chapter.

Chapter 3 also looks into the deformational mechanical properties of the gas shale samples studied in Chapter 2, also studied through laboratory experiments. Specific attention is on the time-dependent ductile creep properties and the brittle

strength of the rocks. Just as their elastic counterparts, the amount of ductile creep and the brittle strengths of the samples were found to be a function of material composition and exhibit anisotropy. It was found that there is a strong correlation between the elastic and deformational properties although these are fundamentally different mechanical properties operating at different time-scales and different strain-magnitudes. We attempt to provide an explanation to this correlation by modeling the stress partitioning between the soft and stiff components in the rock through anisotropic DEM modeling.

In chapter 4, a thorough examination of a borehole FMI image log from a well in Barnett shale, TX, was conducted to gain information about the in-situ state of stress and its variation in shale gas reservoirs. Observations suggest that the in-situ stress state fluctuates rapidly within the reservoir both in terms of the direction of the principal stresses and magnitude of the horizontal stress differences. Comparison with the lithological variations along the well also indicated that the fluctuation in the stress state is closely related to the mechanical heterogeneity

Following observations from Chapter 4, we address the relation between the mechanical heterogeneity in the reservoir and the observed stress variations in shale gas reservoirs. The laboratory data from Chapters 2 and 3 is analyzed under the framework of viscoelastic theory to quantify the ductile behavior of the gas shale samples studied in this thesis. By applying the linear superposition principal from viscoelastic theory, we calculate the horizontal differential stress accumulation that would occur under a simple constant strain rate tectonic loading history. Results emphasize the importance of rock viscoelastic behavior in understanding the current state of stress in shale gas reservoirs.

In chapter 6, a field and laboratory study of fault rocks found in a serpentinite-bearing fault in central Japan is presented. Microstructural observations and material analyses were conducted to describe the distribution of various types of fault gouge material found between a fault juxtaposing serpentinites and Jurassic sedimentary rocks. Results delineate the hydrothermal metasomatic reactions that took place in the

subsurface between the two distinct lithologies. Friction experiments using the saponite-rich fault gouges collected from the fault zone also showed that the metasomatic product has a coefficient of friction as low as 0.1 and lower, with strongly velocity-strengthening characteristics. The study shows the importance of understanding geochemical reactions that take place specifically at fault contacts between different lithologies which can locally create materials of distinct mechanical behavior that can control the overall mechanical property of a major fault zone.

1.3 References

Das, I, and Zoback, M. D., 2011, Long-period, long-duration seismic events during hydraulic fracture stimulation of a shale gas reservoir: Leading Edge, **30**, 778-786.

Daniels, J., Waters, G., LeCalvez, J., Lassek, J., and Bentley, D., 2007, Contacting more of the Barnett Shale through an integration of real-time microseismic monitoring, petrophysics and hydraulic fracture design: SPE Annual Technical Conference and Exhibition, Anaheim, CA, 110562.

Lockner, D.A., Morrow, C., Moore, D., Hickman, S., 2011, Low strength of deep San Andreas Fault gouge from SAFOD core: Nature, **472**, 82–85, doi:10.1038/nature09927.

Maxwell, S., 2011, Microseismic hydraulic fracture imaging: The path toward optimizing shale gas production: The Leading Edge, **30**, 340-346.

Moore, D.E., Rymer, M.J., 2007. Talc, serpentinite, and the creeping section of the San Andreas fault: Nature, **448**, 795–797.

Waters, G., Heinze, J., Jackson, R., Ketter, A., Daniels, J., and Bentley, D. 2006, Use of horizontal well image tools to optimize Barnett Shale reservoir exploitation: SPE Annual Technical Conference and Exhibition, San Antonio, TX, 103202.

Zoback, M., Hickman, S., Ellsworth, W., 2010. Scientific drilling into the San Andreas Fault zone: EOS, Transactions, American Geophysical Union, **91**, 197–199.

Chapter 2

MECHANICAL PROPERTIES OF SHALE GAS RESERVOIR ROCKS – PART 1: STATIC AND DYNAMIC ELASTIC PROPERTIES AND ANISOTROPY

Abstract

We studied the static and dynamic elastic properties of shale gas reservoir rocks from the Barnett, Haynesville, Eagle Ford, and Fort St. John shale. The elastic properties of these rocks vary significantly between reservoirs and within a reservoir due to the wide variety of material composition and fabric anisotropy exhibited by these organic-rich shales. Elastic properties of gas shales are also strongly anisotropic. The degree of anisotropy was found to correlate with the amount of clay and organic contents in the rock. Because clay and organic contents lower the velocity and elastic modulus of these rocks, degree of anisotropy also strongly correlates with the vertical

velocity and vertical Young's modulus, from which we develop several empirical relations for anisotropy. Comparison of our gas shale anisotropy data with a broader organic-rich shale database (TOC<20%) suggest that gas shales exhibit relatively stronger anisotropy despite their limited organic content (TOC<6%). We suggest that the strong anisotropy of gas shales are attributed to extremely anisotropic fabric of these shales and possibly an anomalously compliant nature of the organic contents. We also studied the difference in static modulus during 1st-loading of pressure on the sample in the lab and during unloading/reloading. We find that the 1st-loading static modulus is on average approximately 20% lower than the unloading/reloading static modulus. This suggest that the static-dynamic relationship used to evaluate reservoir static deformation from seismic/sonic measurements can be different by about 20-30% depending on which static modulus is used. Reservoir stress conditions fluctuate substantially during the development of shale gas reservoirs, thus it is important to consider which static-dynamic relationship is more relevant to the problem of interest.

2.1 Introduction

Hydrocarbon production from unconventional shale gas reservoirs has become more common in the past decade, and there are increasing demands to understand the petrophysical and mechanical properties of these rocks. Characterizing these organic-rich shales can be challenging as these rocks vary quite significantly (Passey et al., 2010). For instance, formations in the Barnett shale are known to be more silica-rich, whereas Eagle Ford shale rocks are generally carbonate-rich containing relatively smaller amounts of silica and clays. Formations in these shale gas reservoirs also exhibit a wide range of composition within a single reservoir. Another source of complexity is their mechanical anisotropy. These shales exhibit significant mechanical anisotropy due to its organized distribution of platy clay minerals (Hornby et al., 1994) and compliant organic materials (Vernik and Nur, 1992; Vernik and Liu, 1997; Sondergeld, 2000; Vernik and Milovac, 2011). There are also indications that it is not only the amount of clay or organics, but also the maturity of the shales that control the anisotropy of these organic rich shales (Vanorio et al., 2008; Ahmadov, 2010).

Understanding the anisotropy and its causes is crucial as they strongly influence interpretations in seismic exploration, sonic logs, and microseismic monitoring. However there is still a shortage of laboratory data reported in the literature for shale gas reservoir rocks, especially those dataset that span across different reservoirs.

There is also a lack of laboratory shale data that relates the small-strain elastic properties (rock physics) and the large strain deformational properties (rock mechanics). Linking between the two is crucial for the exploitation of shale gas reservoirs since these reservoirs do not produce unless stimulated by hydraulic fracturing. The short-term brittle deformation may dictate how the formation is fractured, or the long-term ductile deformation may determine how the transport properties of the formation change during production. If we can understand how these deformational properties relate to the elastic properties, we can better optimize operational procedures for the economical production from these reservoirs.

We report laboratory core measurements on the mechanical properties of shale gas reservoir rocks (gas shale) collected from several different reservoirs in North America. Chapter 2 focuses on the static/dynamic elastic properties and its anisotropy, to delineate the basic parameters that control gas shale mechanical properties. In Chapter 3, we also discuss the deformational properties (creep strain and rock strengths) of these rocks to gain some information about the large-strain and long-term behavior of these rocks. Finally we attempt to understand the link between the elastic and deformational properties of these rocks.

2.2 Sample Characterization

2.2.1 Mineralogy, Organic Content, and Porosity

Samples used in our experiments come from four different shale gas reservoirs: Barnett, Bossier/Haynesville, Eagle Ford, and Fort St. John shale. Samples come from various depths and the in-situ effective stress estimated from the overburden stress and the pore pressure range between 15-35 MPa (Table 2.1). The mineralogy and the

organic content were determined through powder XRD analysis and pyrolysis conducted either on the samples used in the experiments or on nearby core samples no more than 2 feet apart in depth. The results are also summarized in Table 2.1 and displayed in a ternary plot in Figure 2.1. Volume fractions were determined by assuming the kerogen density of 1.3 g/cc (Mavko et al., 2009). Clay minerals in these rocks were mostly either illite or mixed layer illite-smectite (10-25% expandability), with minor amounts of kaolinite and/or chlorite in some samples. Minor constituents identified from XRD analysis such as apatite, marcasite, and barite are ignored in our interpretation as they sum to less than a few % of the whole rock volume. Samples from Barnett, Haynesville, and Eagle Ford shale are further divided into two sub-groups based on its mineralogy; sub-group 1 having more clay and kerogen volume compared to sub-group 2. Rocks from sub-group 1 are typically the better reservoir quality rocks in each reservoir. Note that the compositions reflect some characteristic features of each reservoir, but they do not necessary represent the full range of the rock composition in each reservoir.

Table 2.1: Summary of reservoir conditions and material compositions.

Sample Group	Estimated in-situ stress [MPa]	Density [g/cc]	QFP [%]	Carbonate [%]	Clay [%]	Kerogen [%]	Porosity [%]
Barnett-1	Sv: 65 Pp: 30 σ_{eff}: 35	2.39-2.47	50-52	0-3	36-39	9-11	4-9
Barnett-2		2.63-2.67	31-53	37-60	3-7	2-3	1-2
Haynesville-1	Sv: 85 Pp: 60-70 σ_{eff}: 15-25	2.49-2.51	32-35	20-22	36-39	8-8	6-6
Haynesville-2		2.60-2.62	23-24	49-53	20-22	4-4	3-4
Eagle Ford-1	Sv: 90 Pp: 65 σ_{eff}: 25	2.43-2.46	22-29	46-54	12-21	9-11	0-3
Eagle Ford-2		2.46-2.54	11-18	63-78	6-14	4-5	3-5
Fort St. John	Sv: 25-30 Pp: 10-12 σ_{eff}: 13-20	2.57-2.60	54-60	3-5	32-39	4-5	5-6

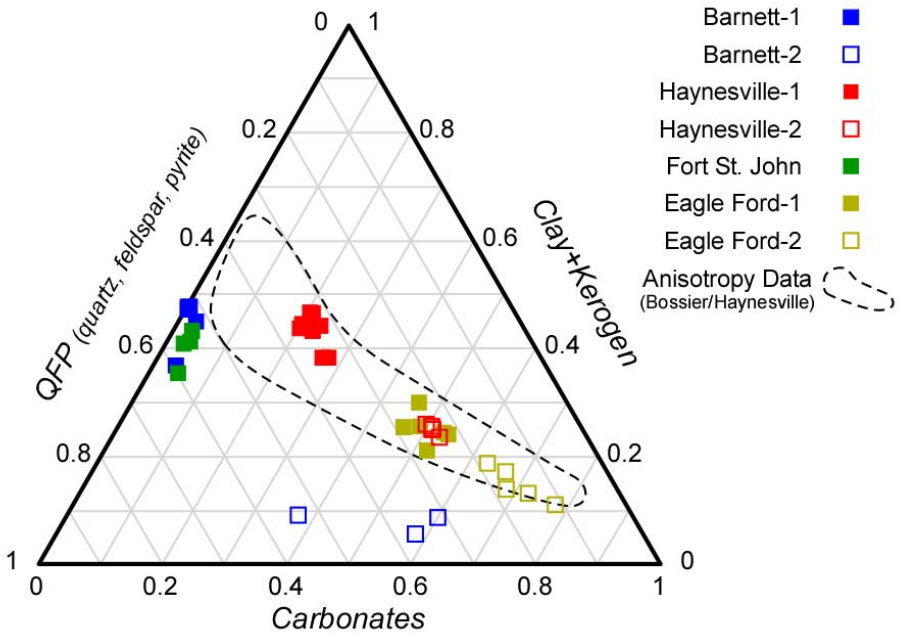

Figure 2.1: Ternary plot representation of the sample material composition.

Figure 2.2a shows the kerogen volume plotted against clay volume. Although the data seem to scatter over a wide region, when samples from the same reservoir are compared against each other (group 1 vs. group 2), we see that there is a positive correlation between kerogen and clay volume. Therefore it seems that the positive correlation between kerogen and clay content is a general characteristic seen in shale gas reservoirs.

We also estimated the porosity of the samples by comparing the bulk density of the rock with their average grain density determined from the mineralogy. The results are plotted against kerogen and clay volume in Figure 2.2b and 2.2c, respectively. From both plots, we recognize that there is a positive correlation between porosity and kerogen or clay volume. Again the trend is more clear when comparing samples from the same reservoir, although the Eagle Ford samples have fairly close porosities despite their difference in composition. These data confirm the observations made by previous studies that the pore volume mainly reside within the solid organics and/or between the clay platelets in these gas shales (Loucks et al., 2009; Sondergeld et al., 2010; Curtis et al., 2010). We cannot necessarily differentiate whether one tends to

carry more pore volume than the other due to the positive relation between their volumes, but previous studies suggest that they depend on the reservoir.

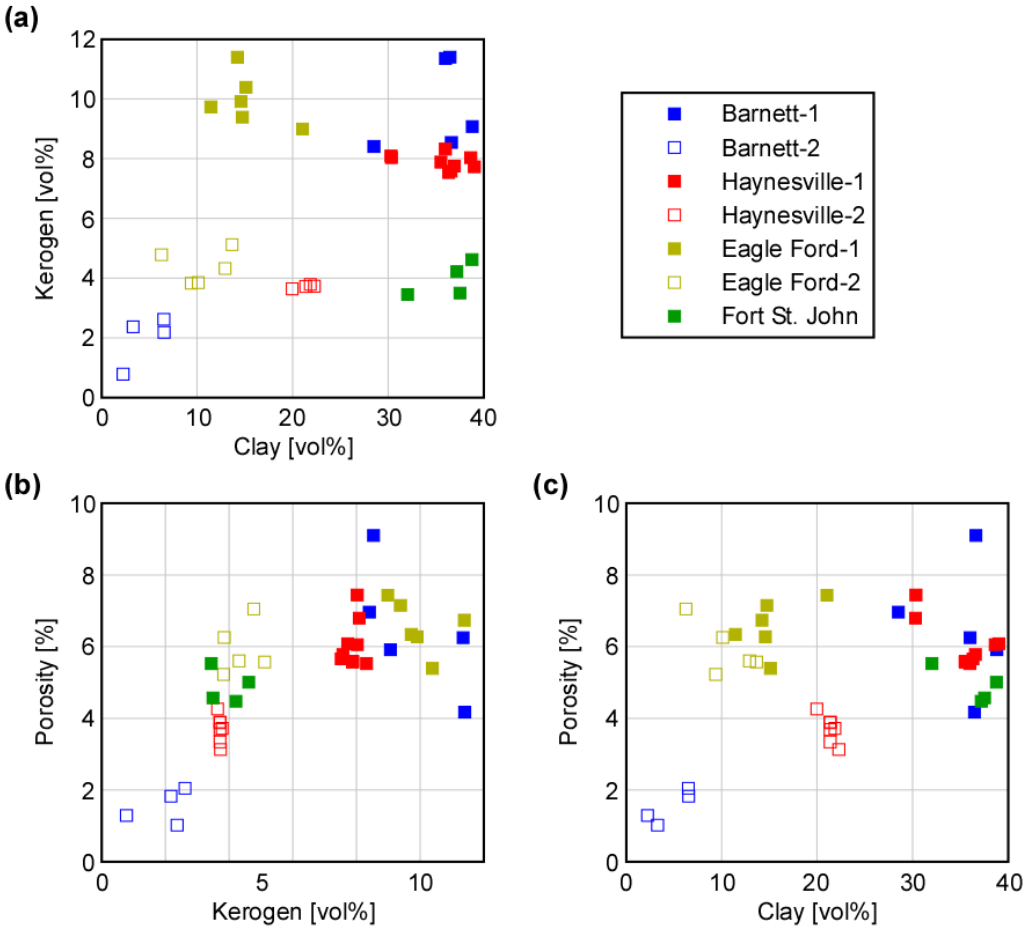

Figure 2.2: Relation between kerogen volume, clay volume, and porosity. (a) Kerogen volume vs. Clay volume. (b) Porosity vs. Kerogen volume. (c) Porosity vs. Clay volume.

2.2.2 Microstructural Observations

Optical microscope images of some representative samples used in the experiments are shown in Figure 2.3. The microstructures are mainly constructed of extremely fine grain clayey and/or calcareous matrix, silt-size detrital grains, biotic grains, and solid organic materials of various aspect ratio (aspect ratio, α, defined as the short axis divided by the long axis). However Barnett-2 samples were an exception to this general structural configuration since they appeared to be dominated by large carbonate crystals and had little fine grain matrix components.

At this scale, fabric anisotropy forming the bedding planes is defined by the combination of the followings: preferred orientations of matrix clay, shape/distribution of organics, and preferred alignment of elongated fossils. Aggregates of aligned clay minerals are always observed in the local scale in all samples when observed under the scanning electron microscope (Figure 2.4). But whether the preferred orientation of these clay aggregates persist at a larger scale is checked by observing the extinction/ diagonal positions under the optical microscope with a cross-polarized light (Figures 2.3, Fort St. John shale images). We find that some samples do not show preferred clay orientation under the optical microscope although aligned clay aggregates are observed under the scanning electron microscope. Shapes of organics vary from nearly round patches (α = 0.5–1) to thin layers (α < 0.05), and they become a strong source of fabric anisotropy especially when the aspect ratio is low. Fossil types consisting the biotic grains are not thoroughly identified, but they are believed to contain foraminifera, calcisphere, and bivalves.

Observations from each sample group are summarized in Table 2.2. In general, both Eagle Ford samples and Haynesville-2 samples showed pronounced anisotropic fabric due to the low aspect ratio organics. On the other hand, organic materials in Barnett-1, Haynesville-1, and Fort St. John samples had higher aspect ratio, but they all exhibited preferred clay orientation. Again we emphasize that samples in this study do not necessary represent the full spectrum of rocks found in each shale gas reservoir.

Comparison between the thin section observations and sample mineralogy suggests that preferred clay orientation under the optical microscope vanishes when clay volume is lower than about 30%. It is known that clay preferred orientation decreased with silt content in the rock (Gipson, 1966; Curtis et al., 1980).Therefore we interpret that the clay fabric is losing its preferred orientation at some critical volume content, below which the framework of load-bearing grain dominate the rock fabric.

Vernik and Nur (1992) observed the texture of organic-rich Bakken shale samples and characterized it to be consisting of lenticular shale laminae imparted by a continuous network of organic matter. Since then, many authors have studied rock

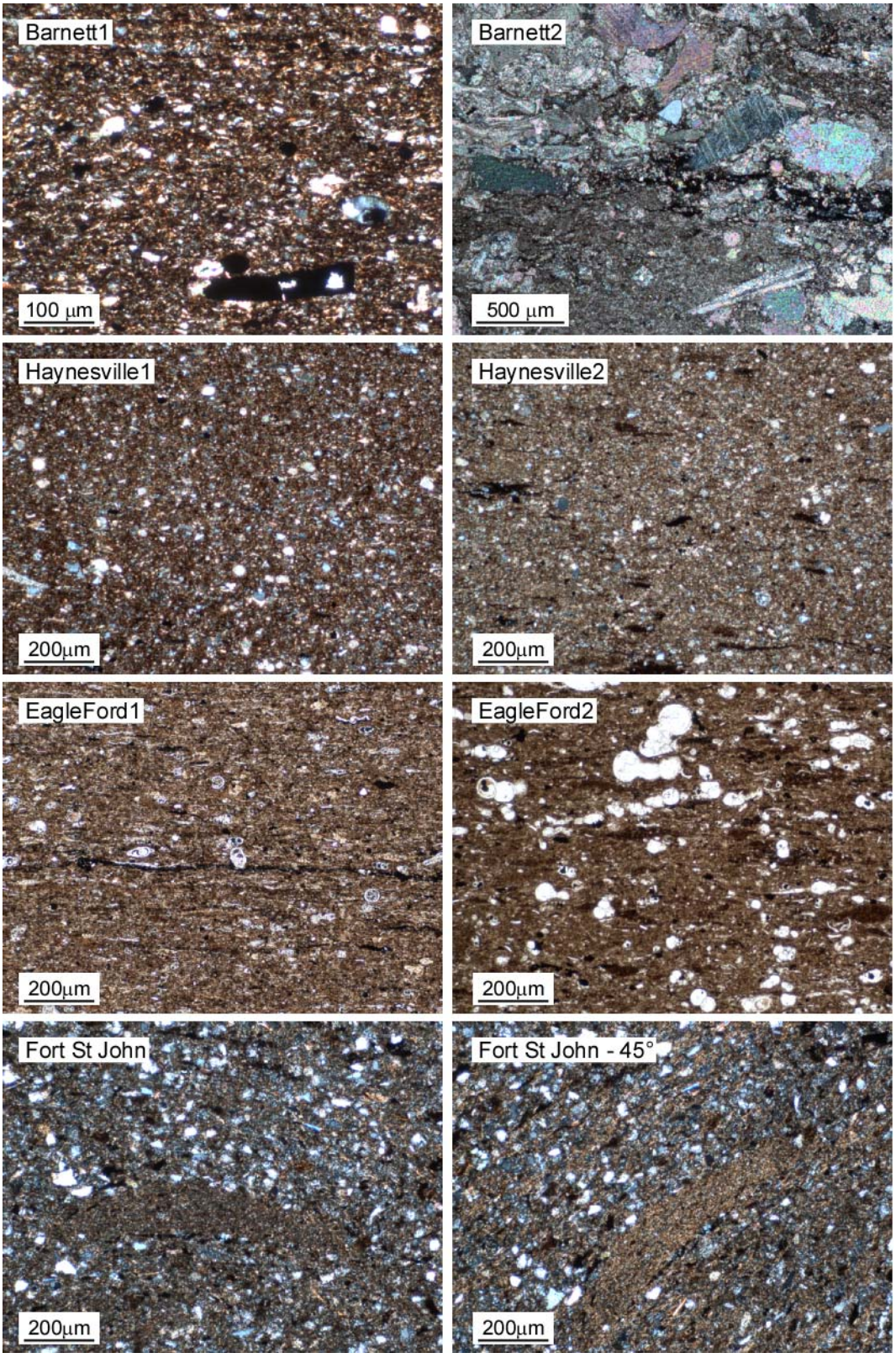
Barnett1
100 μm
Barnett2
500 μm
Haynesville1
200μm
Haynesville2
200μm
EagleFord1
200μm
EagleFord2
200μm
Fort St John
200μm
Fort St John - 45°
200μm

Figure 2.3: Thin section images of several representative samples used in the experiments under the optical microscope. All images were taken under cross-polarized light. Two images of the Fort St. John show the extinction/diagonal positions at the same location to show where the oriented clays are distributed (bright orange spots in the diagonal position).

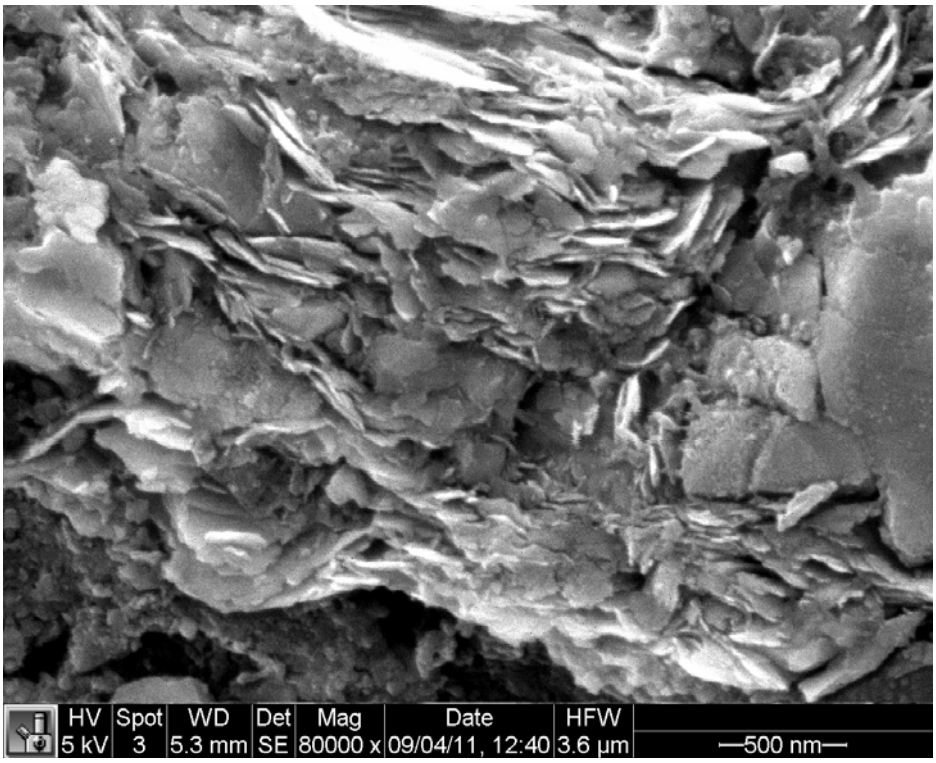

Figure 2.4: Secondary electron SEM image of an Eagle Ford-1 sample.

physics models of organic rich shales honoring the connectedness of the organic materials (Vernik and Nur, 1992; Bandyopadhyay, 2009; Carcione et al., 2011). However we did not see clear evidences of such features in our samples at the observation scale of an optical microscope. At best we saw low-aspect ratio organic materials merging at places but this was not a persistent feature. This may be due to the limited kerogen volume present in our samples (0-12 %) compared to the shales studied by Vernik and Nur (1992) (0-42 %).

Ahmadov (2011) suggested that shapes of organic matters evolve with maturation. It is suggested that as maturation progresses and hydrocarbon is expelled,

low-aspect ratio organics become disconnected and remains as patches organic materials. It was not clear if we saw such trend in our samples. This perhaps suggests that the distribution and aspect ratio of the organic matter is not only influenced by the maturation process, but also due to the origins of the organic matters.

Table 2.2: Summary of thin section observations under the optical microscope.

Sample	Structure	Clay preferred orientation	Shape of organics[*1]	Maturity (Ro/Tmax)
Barnett-1	Silt grains in clayey matrix	Yes	patches to lenses	Mature (oil to wet gas) Tmax=445-465 Ro=0.85-0.91
Barnett-2	Carbonate rock	No	Very few patches	
Haynesville-1	Silt grains in clayey matrix	Yes	Lenses	Overmature (dry gas) Tmax=525-545
Haynesville-2	Silt grains in clayey/ calcareous matrix	No	lenses to layers	
Eagle Ford-1	Calcareous biotic grains in clayey/calcareous matrix	No	lenses to layers	Mature (wet gas) Ro~1.39 Tmax=478-481[*2]
Eagle Ford-2	Calcareous biotic grains in clayey/calcareous matrix	No	lenses to layers	Mature (wet gas) Ro~1.29 Tmax=480[*2]
Fort St. John	Silt grains in clayey matrix	Yes	Patches	Mature (oil to wet gas) Tmax=450-460

[*1] Shapes defined based on aspect ratio: patches 0.5~1, lenses 0.05~0.5, layers <0.05
[*2] Average values of nearby samples (James Packwood, personal communication)

2.3 Laboratory Procedures

Experiments were conducted in a servo-controlled triaxial apparatus, in which cylindrical samples of 1" diameter were deformed under hydrostatic and triaxial pressure condition. A heat-shrink Viton jacket was used to seal the sample from the confining fluid. The sample deformation in the axial direction was measured by a pair of LVDT displacement transducers and the deformation in the direction perpendicular to the samples axis (lateral direction) was measured by a pair of spring-mounted strain gauge transducer to recover the static elastic properties. The velocities of ultrasonic P-

wave and (fast) S-wave generated by piezo-electric crystals were also measured at various timing of the experiments to measure the dynamic elastic properties. See Appendix A for more details on the apparatus and experimental setup.

The axes of the cylindrical samples were either perpendicular or parallel to the bedding, hereon referred to as vertical and horizontal samples, respectively. Vertical and horizontal samples were available from all sample groups except the Fort St. John samples, from which only horizontal samples were available. When both vertical and horizontal samples were available, this allowed us to obtain some measures of the mechanical anisotropy. We treat the shale as a vertical transversely isotropic (VTI) medium with the x_3-axis being the axis of symmetry, where the stiffness tensor in the Voigt notation is given by:

$$\begin{pmatrix}\sigma_1\\ \sigma_2\\ \sigma_3\\ \sigma_4\\ \sigma_5\\ \sigma_6\end{pmatrix} = \begin{pmatrix} c_{11} & c_{12} & c_{13} & 0 & 0 & 0\\ c_{12} & c_{11} & c_{13} & 0 & 0 & 0\\ c_{13} & c_{13} & c_{33} & 0 & 0 & 0\\ 0 & 0 & 0 & c_{44} & 0 & 0\\ 0 & 0 & 0 & 0 & c_{44} & 0\\ 0 & 0 & 0 & 0 & 0 & c_{66}\end{pmatrix}\begin{pmatrix}\varepsilon_1\\ \varepsilon_2\\ \varepsilon_3\\ \varepsilon_4\\ \varepsilon_5\\ \varepsilon_6\end{pmatrix}, \; c_{66} = (c_{11} - c_{12}) / 2 \qquad (2.1)$$

Thus the ultrasonic velocity measurements allowed us to determine the dynamic C_{33}/C_{44} and dynamic C_{11}/C_{66} stiffness constants from the vertical and horizontal samples, respectively. The slope of the stress-strain relations allowed us to determine the static Young's moduli E_{33} and E_{11} from the vertical and horizontal samples, respectively. Finally, the lateral-to-axial strain ratio gave the Poisson's ratio ν_{31} from the vertical samples, and Poisson's ratios ν_{13} and ν_{12} from the horizontal samples. Note that lateral strain was measured both parallel and perpendicular to the bedding plane for horizontal samples.

Experiments were carefully designed so as to accommodate the simultaneous measurement of various mechanical properties from a single sample. First the confining pressure (P_{conf}) was applied in several steps, of 30 seconds duration, up to a

target confining pressure (hydrostatic stage). The target confining pressure varied between experiments from 10-60 MPa to accommodate strengths measurements discussed in Chapter 3. Then the axial differential pressure ($P_{diff} = P_{axial} - P_{conf}$) was also applied in several steps, of 60 seconds duration, up to a pressure that was kept below 50% of the ultimate rock strength (triaxial stage). Between each pressure step in the hydrostatic and triaxial stages, pressure was kept constant for a sustained period of time (>3 hours) to observe creep deformation, which is discussed in Chapter 3. Then the pressure was partially unloaded and reloaded before moving on to the next pressure step (Figures 2.5a and 2.5b). These procedures allowed us to measure the dynamic and static elastic properties at various stress levels. Also dynamic elastic properties were obtained for both before and after the creep, and static elastic properties were determined under both 1st-loading and unloading/reloading pressure steps. Finally, samples were taken to failure to measure its intact and residual strengths (failure stage). The strengths measurements are discussed in Chapter 3. Magnitudes of the pressure steps used in each experiment and the measured elastic properties are summarized in Appendix B.

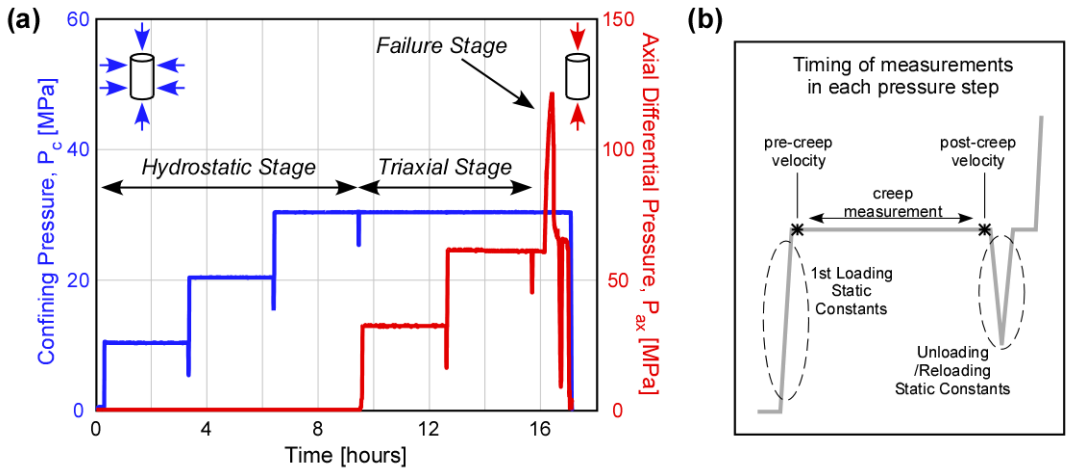

Figure 2.5: (a) The pressure-time history during an experiment. (b) Schematic showing the timings of each mechanical property measurements during a single pressure step. The gray curve represents pressure as a function of time.

All experiments were conducted under room-dry, room-temperature, and drained conditions. Since Haynesville and Eagle Ford samples were sealed in wax

after coring but Barnett and Fort St. John samples were not, samples had been exposed to room-humidity conditions for varying amounts of time. Therefore amounts of residual in-situ fluid present in the pore spaces at the time of the experiments may have been different between samples. However, we did not attempt to actively dry off the residual fluids so that we can preserve the clay-bound water in the samples. This is because we wanted to best preserve the original hydration states of clay minerals in the samples since hydration state of clay minerals can drastically affect their mechanical properties (Moore and Lockner, 2004). Judging from the fluid saturation measured for some samples after recovery from the subsurface (typically less than 40% including clay-bound water) and the dry appearance of the samples before and after the experiments, we believe that the mechanical behavior of the samples were free of any poroelastic effects that may have been caused by the remaining in-situ pore fluid.

We also report some results from laboratory measurements conducted elsewhere using Bossier/Haynesville shale samples, whose data we will explicitly refer to as the "anisotropy dataset". In these experiments, a set of samples from a certain depth was cored so that the cylinder axes were angled at 0, 30, 45, 60, and 90 degrees with respect to the bedding normal axis. This allowed the characterization of the full mechanical anisotropy of the samples. All samples were loaded axially at a constant strain rate of 10^{-5} s^{-1} under a constant confining pressure of 17.2 MPa (=2500 psi), during which the static and dynamic elastic constants were obtained from the stress-strain relation and ultrasonic velocity measurements, respectively. A total of 16 sets of samples from 2 different wells were tested in this manner.

2.4 Laboratory Results

2.4.1 Dynamic P-wave and S-wave Moduli

All pre-creep dynamic moduli measured in the experiments are shown in Figures 2.6 and 2.7, plotted against pressure. Displaying the dynamic properties as a function

of pressure required some careful consideration since the confining pressure during the triaxial stage was different between experiments; therefore, each experiment followed different stress paths. We chose to plot the dynamic moduli as a function of the total axial pressure, $P_{axial} = P_{conf} + P_{diff}$, since P_{axial} is the one quantity that varied during both hydrostatic and triaxial stages. This allowed us to plot the data from both stages continuously within a figure. Although rock moduli are likely not a unique function of P_{axial}, plotting the dynamic data against P_{axial} seemed to capture the pressure dependence of the sample fairly well. In Figures 2.6 and 2.7, transition from hydrostatic to triaxial stage in an experiment is indicated by the dashed lines. We find no abrupt changes in the pressure-dependent trend between stages.

Both p-wave modulus and s-wave modulus show monotonic stiffening against pressure for all samples. When the data is compared with the estimates of the in-situ effective stress magnitude shown in Table 2.1 (black dashed lines in Figures 2.6 and 2.7), we find that the stiffening against pressure is more rapid at pressures below the in-situ effective stress, but levels off beyond that with the exception of some vertical Haynesville and Eagle Ford samples which continue to stiffen. This transitional behavior seems to be more evident for the p-wave modulus. This transitional behavior is reflecting the closure of soft pore spaces that opened as the sample was de-pressurized from the subsurface. Judging from the pressure dependent trend, the closure pressure of the soft pore spaces seem to be about 40-50 MPa for most samples.

The dynamic moduli data from the same sample groups are fairly consistent with each other. We observe from comparison between sample groups that subgroup 2 samples are stiffer than the subgroup 1 samples. This is because the subgroup 2 samples contain more stiff minerals (quartz and carbonates) and less compliant materials (clay and organics). Also the dynamic moduli are stiffer in horizontal samples than in vertical samples. This is consistent with the anisotropy of these gas shale samples as a VTI medium. However, we interpret that the Barnett-2 samples exhibits no anisotropy since data from vertical and horizontal samples overlap. The

one Barnett-2 sample with the lowest p-wave modulus had a different mineralogy compared to the other Barnett-2 samples.

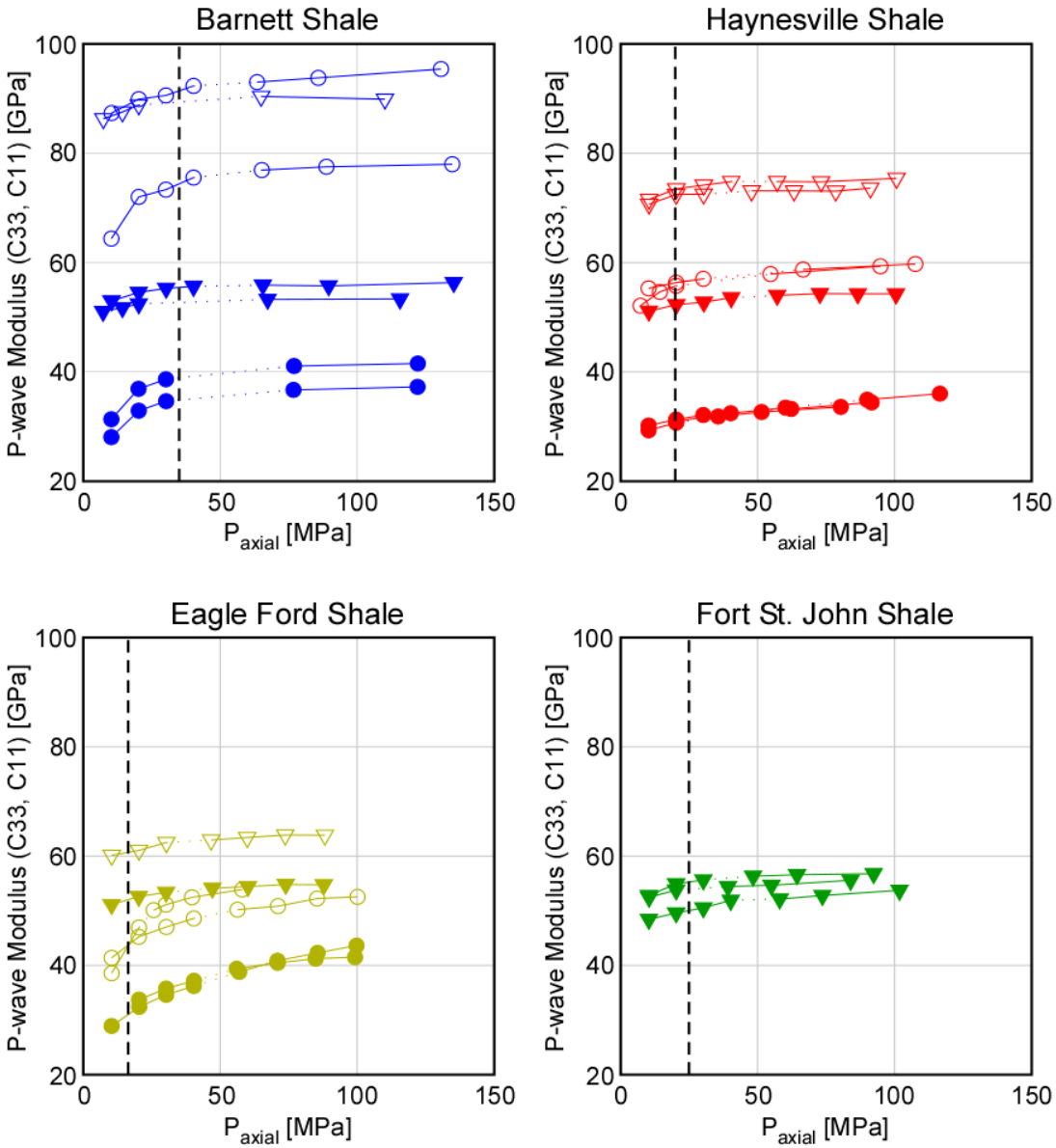

Figure 2.6: All P-wave modulus data plotted against total axial pressure. Circles represent vertical samples and triangles represent horizontal samples. Open symbols are the relatively clay- and organic- poor samples (subgroup 2) within a reservoir.

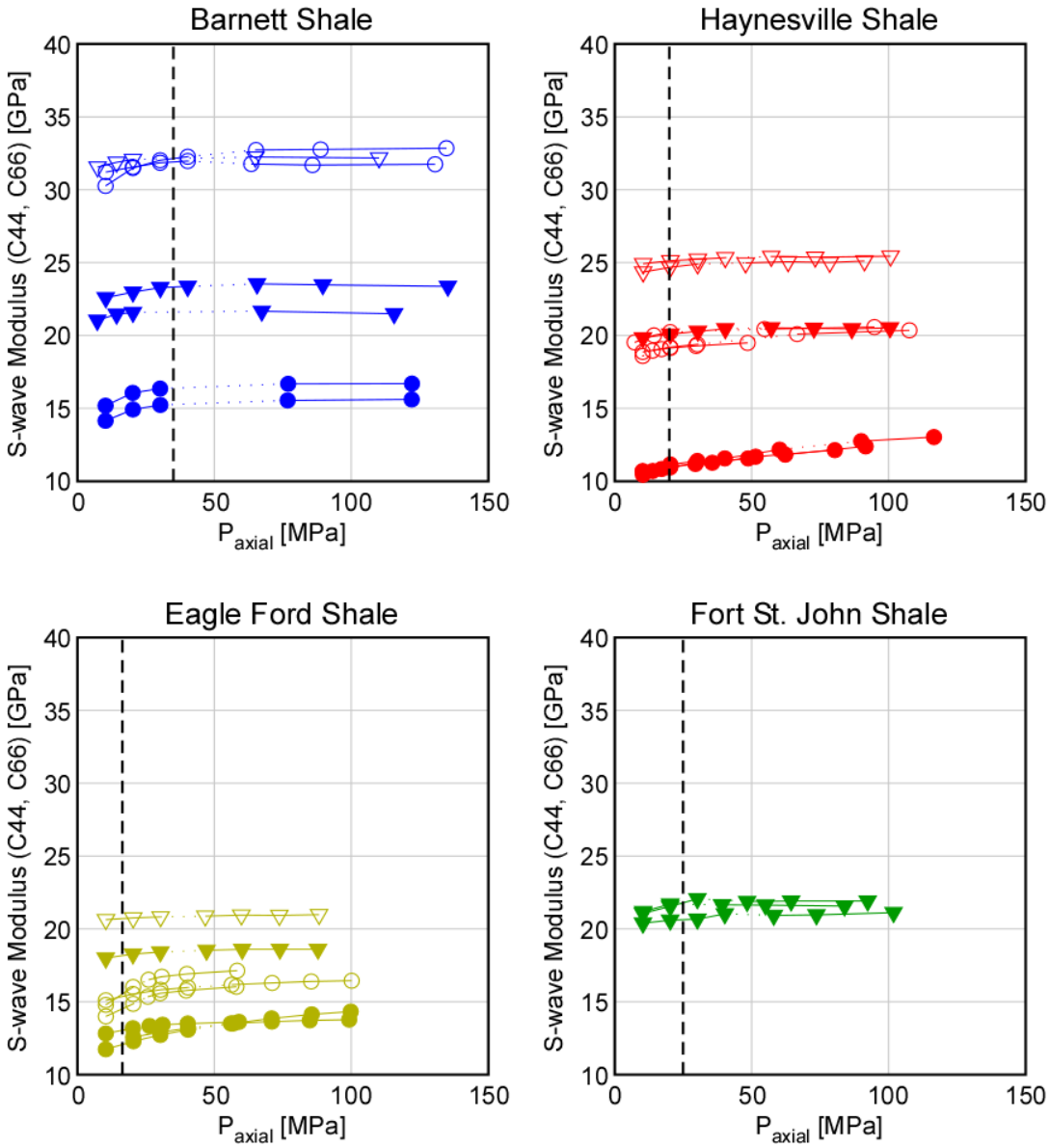

Figure 2.7: All S-wave modulus data plotted against total axial pressure. Circles represent vertical samples and triangles represent horizontal samples. Open symbols are the relatively clay- and organic- poor samples (subgroup 2) within a reservoir.

2.4.2 Static Young's Modulus

All static Young's modulus measured during 1st-loading is shown in Figure 2.8. The data is plotted against the average total axial pressure during the pressure steps. Note that these data come only from the triaxial stage since Young's modulus is not

measured under hydrostatic pressure. Compared to the dynamic moduli data in Figures 2.6 and 2.7, the trends depicted by the static data are not as smooth and consistent as in the dynamic data especially in the lower pressure range. Part of this is explained by the error due to the limited resolution in the strain measurements. Also static elastic properties simply exhibit nonlinear behavior as will be discussed later.

Many features observed from the Young's modulus are similar to what was observed from the dynamic moduli data. Subgroup 2 samples (right column in Figure 2.8) are stiffer than the subgroup 1 samples (left column in Figure 2.8) due to its relative abundance of quartz and carbonates, and the horizontal modulus is stiffer than the vertical modulus except for the Barnett-2 samples. But the pressure dependence of the static and dynamic moduli shows different characteristics. Although limited data are available at lower pressures, static moduli also seem to show a stage of rapid stiffening with axial pressure at pressures below 40-50 MPa. This can be understood as the closure of soft pores. However beyond 40-50 MPa axial pressure, Young's modulus decreases with pressure. The trend is observed for all samples except some vertical Eagle Ford-1 samples.

2.4.3 Static Poisson's Ratio

The static Poisson's ratio measured during 1st-loading is plotted against the average total axial pressure during the pressure steps in Figure 2.9. For the horizontal Poisson's ratio, ν_{12} is not shown but the data is provided in Appendix B. As with the Young's modulus (Figure 2.8), Poisson's ratios data was also affected by the limited resolution of strain measurements, especially when measured during small pressure steps. Measurement error is doubled for Poisson's ratio measurements since they are calculated from the ratio of two independent strain measurements. Therefore results are not shown in Figure 2.9 for those with large errors (R^2<0.9). Again data only comes from the triaxial stage.

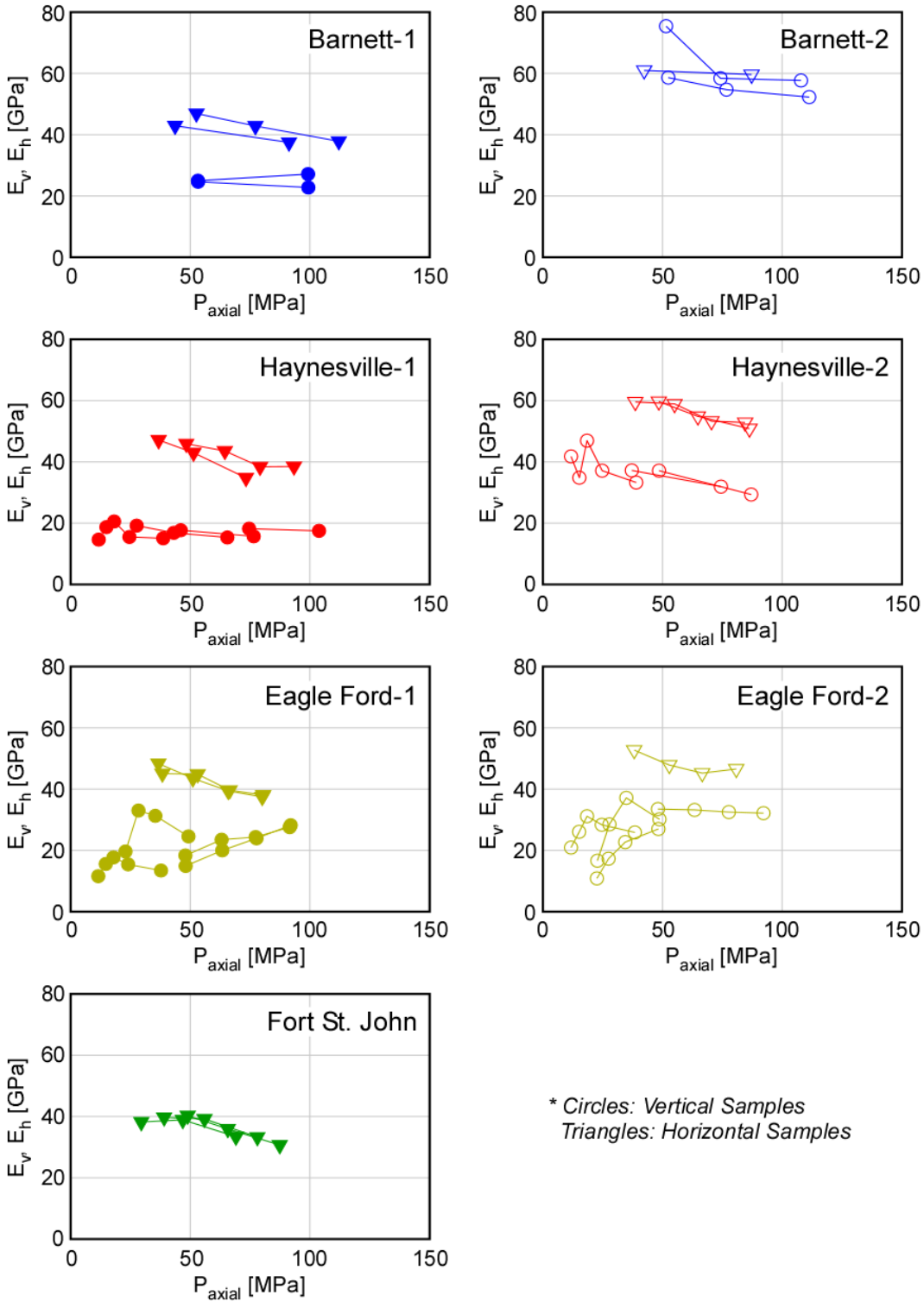

Figure 2.8: All 1st-loading Young's modulus data plotted against total axial pressure.

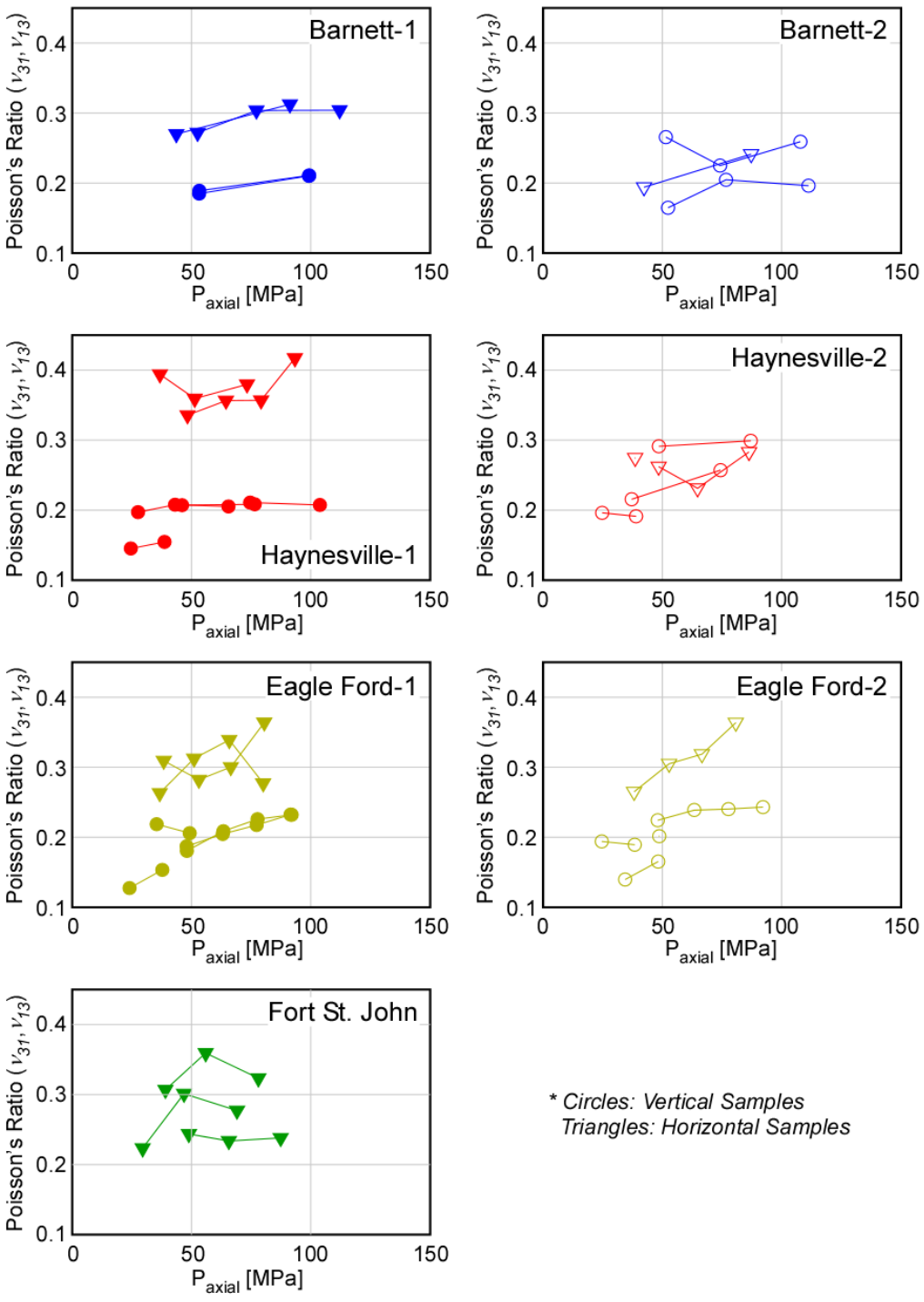

Figure 2.9: Poisson's ratio data, ν_{31} and ν_{13}, plotted against total axial pressure. Circles represent vertical samples (ν_{31}) and triangles represent horizontal samples (ν_{13}). ν_{12} is not plotted here, but the data is provided in Appendix B.

It is difficult to make any inference about the dependence of Poisson's ratio on material composition. However, there seems to be a clear anisotropy in Poisson's ratio. Values of the horizontal Poisson's ratio, ν_{13}, is generally larger compared to the vertical Poisson's ration, ν_{31}. This is consistent with results from Figure 2.8 since it follows from the symmetry of the elastic compliance tensor that:

$$\frac{\nu_{31}}{\nu_{13}} = \frac{E_3}{E_1} \tag{2.2}$$

However, Haynesville-2 samples do not show a clear anisotropy in Poisson's ratio as expected from the Young's modulus anisotropy. This may be due to the large error involved in the measurements.

It is also difficult to make inference about the pressure dependence of Poisson's ratio. But we suggest that there is a slight increase in Poisson's ratio with increasing axial pressure.

2.4.4 1st-loading vs. Unloading/Reloading Static Elastic Properties

Static elastic properties were measured during the stress-strain relation during the first time the sample was loaded to a certain axial pressure (1st-loading) and also during the partial unloading and reloading of the axial pressure (unloading/reloading) before moving on to the next pressure step. The Young's modulus and the Poisson's ratio measured at these two different timings are compared in Figure 2.10. Measurements from all pressure steps and all samples are plotted in Figure 2.10. We find from the comparison that the Young's modulus is consistently lower during 1st-loading compared to the Young's modulus during unloading/reloading. Although there is some scatter in the correlation, on average, the 1st-loading Young's modulus is about 20% lower than the unloading/reloading. On the other hand, comparison between the 1st-loading and unloading/reloading Poisson's ratio does not yield a clearly relation between them. On average, 1st-loading Poisson's ratio may seem to be

lower than the unloading/reloading Poisson's ratio, but the data scatters widely about the 1-to-1 correspondence line.

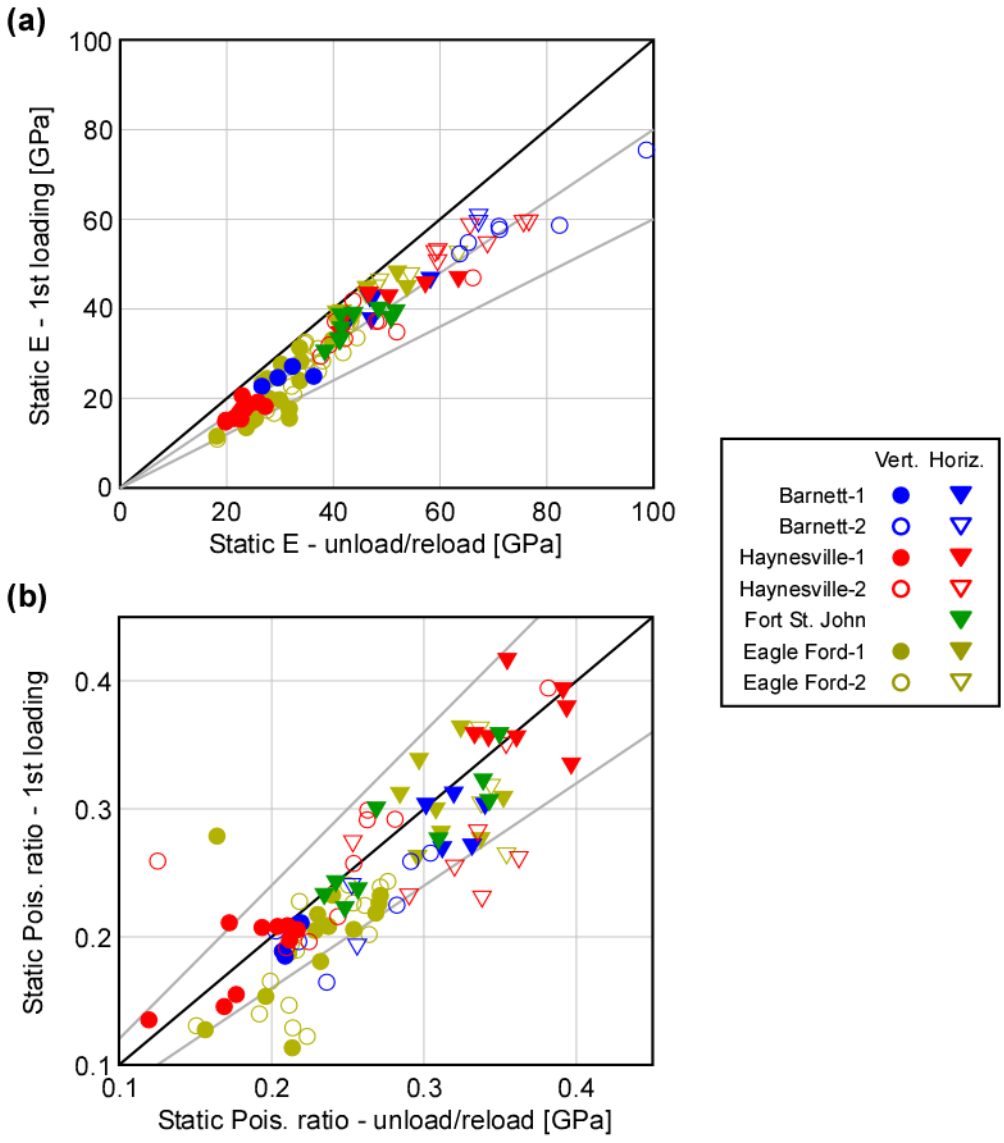

Figure 2.10: Comparison between 1st-loading and unloading/reloading elastic properties. (a) Comparison of static Young's modulus. The black line indicates 1-to-1 correspondence. The two grey lines indicated 20% and 40% deviation. (b) Comparison of static Poisson's ratio. The black line indicates 1-to-1 correspondence. The two grey lines indicated 20% deviation.

2.4.5 The Anisotropy Dataset

Figure 2.11 shows an example of velocity data from the anisotropic dataset conducted on a group of samples from a certain depth in Haynesville shale. In a VTI medium, the p-wave and (fast) s-wave velocity changes with incidence angle, measured from the symmetry axis (x_3), as in the following equations (Mavko et al., 2009):

$$V_p(\theta) = \sqrt{\frac{c_{11}\sin^2\theta + c_{33}\cos^2\theta + c_{44} + \sqrt{M}}{2\rho}} \qquad (2.3)$$

$$\text{where} \quad M = \left[(c_{11} - c_{44})\sin^2\theta + (c_{33} - c_{44})\cos^2\theta\right]^2 + (c_{13} + c_{44})^2 \sin^2 2\theta$$

$$V_{SH}(\theta) = \sqrt{\frac{c_{66}\sin^2\theta + c_{44}\cos^2\theta}{2\rho}} \qquad (2.4)$$

Equation 2.3 and 2.4 was fit to the velocity data measured at various orientations by least square method to obtain the best set of 5 stiffness constants (c_{11}, c_{33}, c_{44}, c_{66}, c_{13}) that represent the samples from that depth. In the anisotropy dataset, 15 more sets of velocity measurements similar to Figure 2.11 were analyzed to obtain 15 more sets of stiffness constants that represent various formations within the Bossier and Haynesville shale (Appendix C).

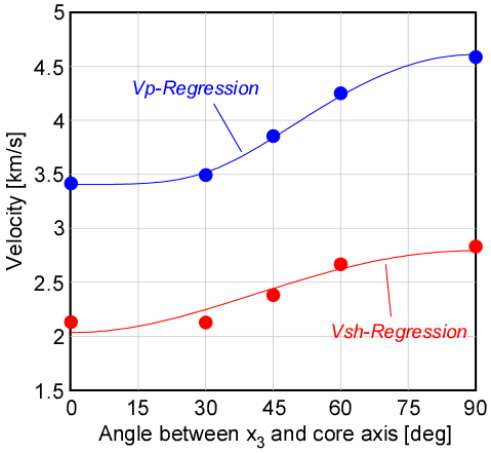

Figure 2.11: Example of a set of velocity measurement conducted in the anisotropy dataset.

2.5 Discussion

2.5.1 Vp-Vs Relation

A common way to interpret velocity data from reservoirs is to observe the relationship between p-wave and s-wave velocities. To look at this relation, we plotted velocity data from our experiments in Figure 2.12 along with some known empirical Vp-Vs relations from the literature (Castagna et al., 1993; Vernik et al., 2002) and constant Vp-Vs ratio lines. We only plotted the velocity data from when P_{axial} was closest to 45 MPa from each sample, in order to compare data that are free of soft-pore effects. Note that our data represent both vertical and horizontal velocity of a VTI medium whereas some of these trends are derived from vertical velocities. When focusing on the reservoir quality samples (Barnett-1, Haynesville-1, Eagle Ford-1), we see that the P-wave velocity is lower relative to the empirical shale line by Vernik et al. (2002), but perhaps rather closer to the sandstone line. This trend is consistent with other velocity data reported from Bossier /Haynesville shale sonic-log data (Lucier et al., 2011) and both core-ultrasonic and sonic-log data from Bossier, Bakken, and Woodford shale data (Vernik & Milovac, 2011).

The discrepancy is not surprising provided that gas shale rocks are clearly different from the shales used to establish the known shale empirical trend. Gas shales contain much more organic materials and have much lower fluid saturation. However, the mechanical explanation for why the Vp/Vs trend for gas shales differs from those of in-organic shales is still under debate. Organic materials can lower the rock velocities significantly due to their extreme compliance compared to other mineral constituents (Ahmadov et al., 2009; Bandyopadhyay, 2009). But their presence should affect both the p-wave and s-wave moduli simultaneously. Therefore it is not clear if the presence of organic materials explain the departure of gas shale velocity data from the empirical trend. Lucier et al. (2011) performed Gassmann's fluid substitution (Mavko et al., 2009) to the Bossier/ Haynesville sonic log data and demonstrated that such correction for the fluid saturation state can shift the gas shale velocity back to empirical shale trends. However frequency-dispersion effects also need to be

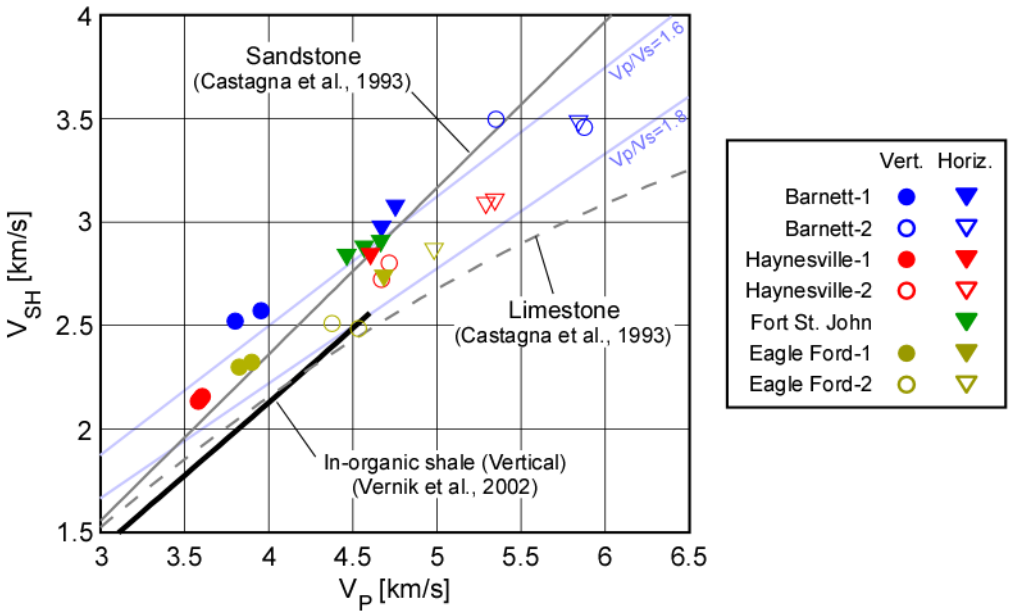

Figure 2.12: Vp vs. Vs at 45 MPa axial pressure for all samples tested. Note that Vs in the horizontal samples is the velocity of the fast s-wave (V_{SH}), polarized parallel to the bedding.

evaluated for a complete validation of their conclusion since it is not customary to apply a low-frequency theory, such as Gassmann's relations, to impermeable shales. Nonetheless, the results by Lucier et al. (2011) suggest that fluid substitution is one of the necessary steps towards bridging the gap between gas shale rocks and brine-saturated inorganic shale, and it can in fact be the most important step.

2.5.2 Pressure Dependence of Elastic Moduli

Both the dynamic and static elastic moduli showed stiffening trends against axial pressure at low pressures which can be attributed to the closure of soft pore space (e.g. cracks). However at higher pressures beyond 40-50 MPa axial pressure, the dynamic moduli continued to stiffen slightly, whereas static moduli showed a weakening trend (Figures 2.6-2.8). The difference indicates that the types of sample deformation involved in the two measurements are different although they are both measures of elastic mechanical properties.

Strain magnitudes involved in the passage of ultrasonic waves during dynamic measurements are on the order of 10^{-7} (Mavko et al., 2009). Since elastic moduli is on

the order of 10 GPa, such small deformation cause stress perturbations on the order of 1 kPa, assuring only purely elastic mineral deformation. Observing the change in dynamic moduli will tell how the elastic pore structure changes with pressure, but will not provide information about the deformation itself that is changing the pore structure. Therefore dynamic measurements are snapshot measurements of the elastic structure at a certain point in the experiment. Stiffening of dynamic moduli seen beyond 40-50 MPa in Figures 2.6 and 2.7 therefore simply reflects that stiffer pore spaces are closing at higher pressures.

On the other hand, stress changes are much larger during static measurements, on the order of 10 MPa. This not only causes mineral elastic deformation, but also induces additional energy-dissipative inelastic deformation, such as frictional sliding and microcrack growth, which changes the pore structure of the rock (Zoback et al., 1975). Static deformation captures all of the above deformations. Thus, softening of Young's modulus and increase of Poisson's ratio (enhancement of lateral material extrusion) seen in Figures 2.8 and 2.9 reflects the material degradation (increase in damage) with increasing axial pressure. Note that this material degradation is accommodated by the free-surface boundary condition at the side wall of the cylindrical samples in our experiments. During the triaxial stage, P_c is simply kept constant and lateral deformation is not suppressed. However, for instance, if the static bulk modulus was measured under hydrostatic pressure conditions, there should be much less, if any, degradation of bulk modulus due to pressure increase until grain crushing starts to occur (Zimmer, 2003).

2.5.3 Static-Dynamic Relation

Explorative industry technologies see dynamic moduli of the formation whereas reservoir deformations at longer time scales obey its static mechanical properties. Since these properties are different as explained in the previous section, industry applications often seek for correlations between static and dynamic properties in order to infer reservoir deformation from seismic- and log-derived elastic properties. In this context, the difference between the 1st-loading and unloading/reloading static

Young's modulus found in Figure 2.10a poses a question on which static moduli is the appropriate static modulus to be used in these applications.

The difference between the 1st-loading and unloading/reloading properties is a well-known hysteresis effect seen in soil mechanics and rock mechanics. As soil/rocks compact with pressure, soil/rock structures remember the highest stress it has been exposed to, and they will only deform elastically unless exposed to an even higher stress. Therefore the onset of hysteretic behavior reflects the maximum stress the rock has been exposed to. However, this simple idea of hysteresis does not explain our laboratory results for two reasons. First, we did not see any "onset" of hysteretic behavior as pressure conditions exceeded the current in-situ stress condition. Difference in 1st-loading and unloading/reloading modulus was observed consistently even at pressures lower than the current in-situ condition. Secondly, these gas shale samples were once at much greater depths, and much higher stress, where hydrocarbon generation took place. Thus, in theory, we should not see any hysteretic behavior. These observations suggest that the gas shale rocks have undergone some sort of a de-compaction process over geological time scale during uplift and also since the time cores were recovered from the subsurface a few years ago. De-compaction over geological time is conceivable given that these reservoirs are typically over-pressured from hydrocarbon generation, which would act to expand pore spaces. The shorter term de-compaction is probably a result of anelastic strain recovery (ASR; Blanton, 1983; Warpinski and Teufel, 1986), a well-known phenomenon sometime used to collect information about the in-situ stress state. While the exact contribution of these processes is not understood, the persistent hysteretic behavior of the gas shale samples alerts us to carefully consider which laboratory data, 1st-loading or unloading/reloading, is more relevant to the problem we are interested in.

Acknowledging the differences between the two static moduli can be quite important when considering static-dynamic relations. Figure 2.13 shows the 2 static-dynamic relations derived from our data using 1st-loading and unloading/reloading

static Young's moduli. The dynamic Young's modulus was approximated by simply applying the following isotropic equations to the measured p- and s-wave modulus:

$$E_{11}^{apparent} = \frac{c_{66}\left(3c_{11} - 4c_{66}\right)}{c_{11} - c_{66}}, \quad E_{33}^{apparent} = \frac{c_{44}\left(3c_{33} - 4c_{44}\right)}{c_{33} - c_{44}} \tag{2.5}$$

This equation is not precisely correct to apply to a VTI medium, but it was found that the error of using this isotropic equations rather than the anisotropic equations was found to be small (See Appendix D). Figure 2.13 shows that the 1st-loading static modulus is consistently lower than the dynamic modulus, in agreement with many static-dynamic relations published to date (Mavko et al., 2009). This is commonly understood to be the consequence of the additional inelastic deformation captured in the static modulus measurements. However the unloading/reloading static modulus plots around the 1-to-1 correspondence line. This suggests that most of the inelastic

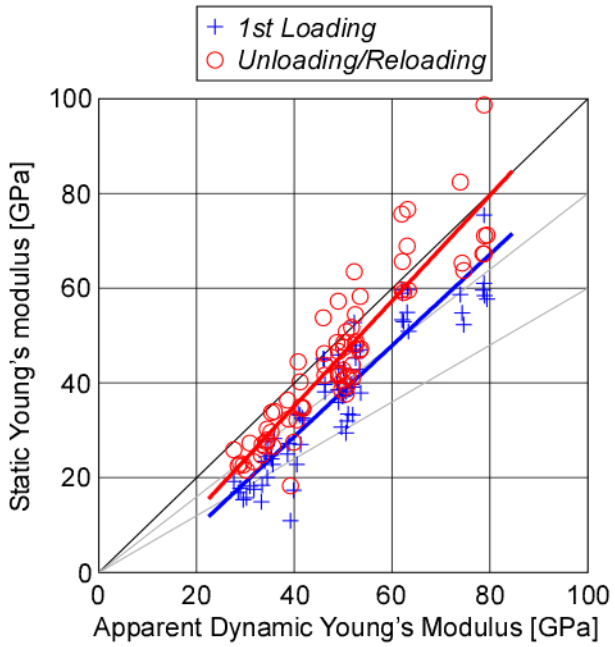

Figure 2.13. Static vs. dynamic relation for Young's modulus derived from our experimental data using 1st-loading and unloading/reloading static modulus. The black solid line represents 1-to-1 correspondence, and the 2 grey lines represent 20% and 40% deviation from 1-to-1 correspondence. Apparent dynamic Young's modulus is defined by Equation 2.5.

deformation captured in the static modulus measurements showed hysteretic behavior and was not recoverable at least in the laboratory time scale. Also, failing to choose the proper static-dynamic relation can lead to substantial errors, up to about 20-30%, in the estimation of static modulus from the dynamic modulus.

During completion and production of a shale gas reservoir, pore pressure is raised close to the overburden stress during hydraulic fracturing and then drawn down below the initial pore pressure as hydrocarbon is produced. Honoring these dramatic stress changes within the reservoir, perhaps the static-dynamic relation from unloading/reloading static modulus may be more relevant during hydraulic fracturing, whereas for later times during production, static-dynamic relation from the 1st-loading may become more relevant. Most published static-dynamic relations do not specify how the static moduli were measured. But we suggest that distinguishing between the two static moduli may be of substantial importance in utilizing static-dynamic relations to analyze reservoir deformation from dynamic data.

2.5.4 Inter-reservoir Comparison and Comparison with Theoretical Bounds

Laboratory data presented in sections 2.4.1 and 2.4.2 suggested that in each reservoir, both dynamic and static moduli were dependent on the material composition, namely on the amount of the compliant materials, clay and organics. As an inter-reservoir comparison of the moduli data, we have combined the information from each reservoir in Figure 2.14. Each panel shows the comparison of the p-wave, s-wave, and 1st-loading static Young's modulus obtained when P_{axial} was closest to 45 MPa, plotted against the sum of clay and kerogen volume. In each panel in Figure 2.14, we roughly observe that dynamic and static modulus decrease with increasing clay and kerogen volume and there is a separate trend for vertical and horizontal samples. Thus gas shale moduli are a strong function of the clay and kerogen volume. However, it also stands out that Eagle Ford samples showed anomalously low moduli values despite their low clay and kerogen content compared to other samples.

In order to check how the laboratory data compare with the upper and lower theoretical bounds predicted from the rock compositions, we have also drawn in the Voigt and Reuss averages calculated based on the compositional data (Figure 2.14). The bounds were calculated by viewing gas shales as a mixture of the *stiff* component, composed of quartz and calcite, and the *soft* component, composed of clay and kerogen. The stiff component property was approximated by taking the Hill's average

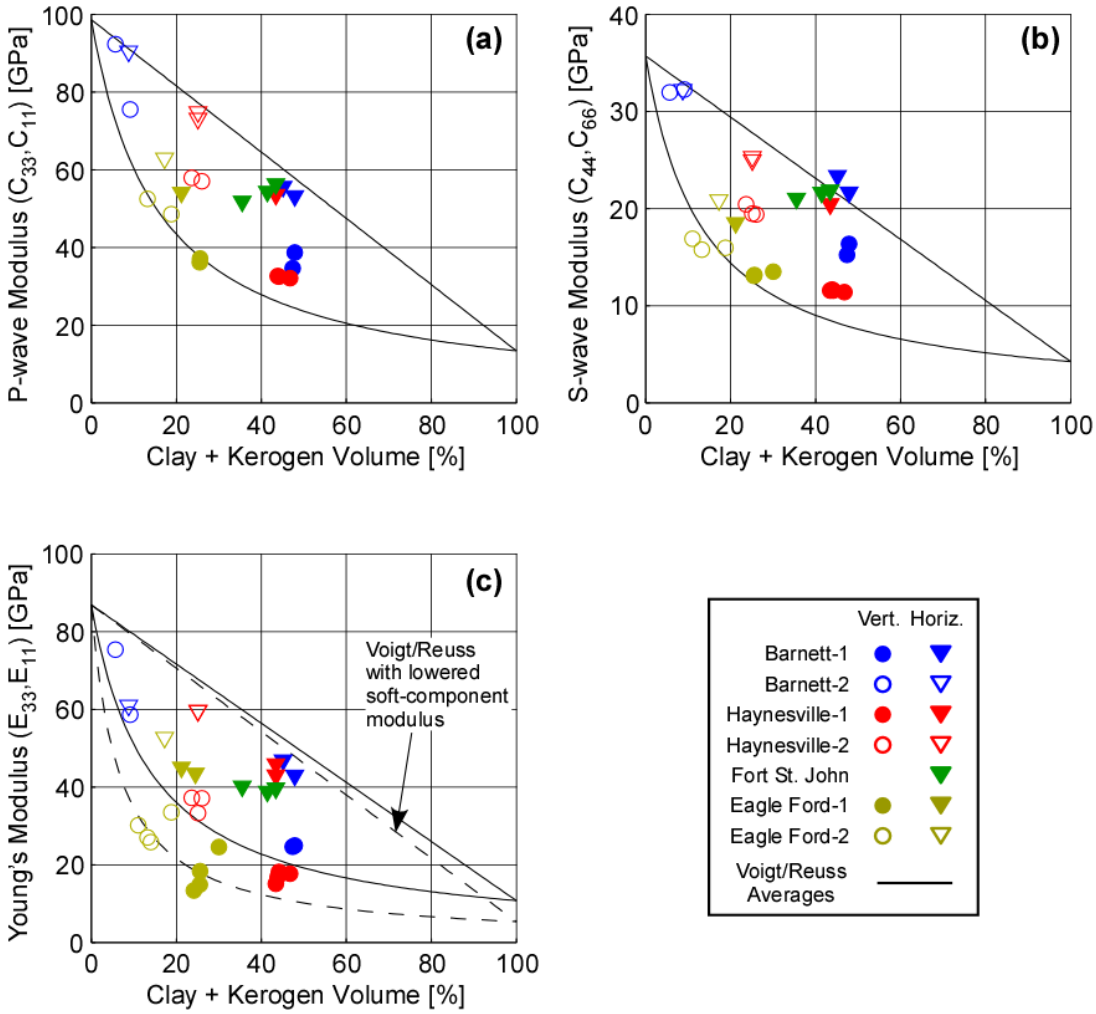

Figure 2.14: Inter-reservoir comparison of dynamic and static moduli data plotted against clay and kerogen volume, and comparison with Voigt and Reuss averages. (a) P-wave modulus. (b) S-wave modulus. (c) Static Young's modulus. Voigt and Reuss bounds were calculated using values from Table 2.3. The dashed lines in panel (c) is drawn by lowering the soft-component Young's modulus to 5.4 GPa.

(Mavko et al., 2009) of equal amounts of quartz and calcite, and the soft component similarly by the Hill's average of equal amounts of clay and kerogen (Table 2.3). Note that there are some approximations involved in this shale model. For instance, not all samples have the same proportions of quartz/calcite or clay/kerogen in its stiff and soft component. Eagle Ford-2 has more calcite than quartz in its stiff component, while Barnett-1 has much more quartz than calcite (Figure 2.1). Also there are still some uncertainties in our understanding of clay and kerogen mechanical properties. For the clay and kerogen properties, we honored those values collected or inferred from laboratory data (Vanorio et al., 2003; Bandyopadhyay, 2009).

Table 2.3: Elastic properties used to calculate the Voigt and Reuss bounds in Figure 2.14.

	K [GPa]	μ [GPa]	M [GPa]	E [GPa]
Quartz [*1]	37	44	-	-
Calcite [*1]	70.2	29	-	-
"Stiff" component	51.0	35.7	98.6	86.9
Clay [*2]	12	6	-	-
Kerogen [*3]	5	3	-	-
"Soft" component	7.8	4.3	13.4	10.8

References: [*1] Mavko et al. (2009), [*2] Vanorio et al. (2003), [*3] Bandyopadhyay (2009). Stiff and soft component properties are calculated by the Hill's average of Quarts/Calcite and Clay/Kerogen, respectively.

Comparison of the laboratory data with the theoretical bounds shows that the laboratory data generally falls within the upper and lower bounds, validating our shale model and the approximations therein. However for the static modulus, some data falls below the theoretical bounds. Various reasons can be invoked as the cause of this mis-prediction (e.g. lab measurement error, insufficient shale model), but we believe that the major reason is the fact that the clay and kerogen properties shown in Table 2.3 were collected by dynamic methods. As discussed in sections 2.5.2 and 2.5.3, static measurements involve inelastic deformations not captured by dynamic methods. It is also most likely that this inelastic deformation is concentrated in the clay and kerogen content where the pore volume resides in these rocks. Thus the soft-component Young's modulus should be lowered to reflect the inelastic deformations. We re-drew the Voigt and Reuss average curves after lowering the soft-component Young's

modulus to 5.4 GPa, half of its original value of 10.8 GPa (dashed line in Figure 2.14c). This allowed every static modulus data to reasonably fit within the theoretical bounds. Note that we also tried lowering the stiff-component modulus, but lowering the stiff-component modulus has much less effect on the Reuss average lower bound than lowering the soft-component modulus (Figure 2.15).

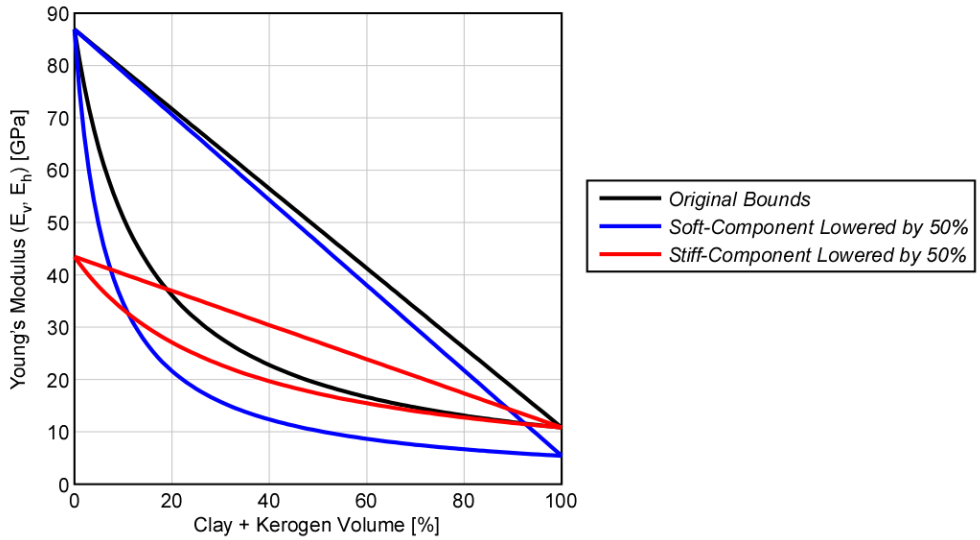

Figure 2.15: Comparison of theoretical Young's modulus bounds calculated with original set of end-member modulus, lowered soft-component modulus, and lowered stiff-component modulus.

From the comparison of the data with the theoretical bounds, the anomalously low moduli values of the Eagle Ford samples, despite its low clay and kerogen volume, could interpreted to be the consequence of its extreme fabric anisotropy. Voigt and Reuss averages correspond to the most extreme case of anisotropy represented by a completely layered rock. Thus the fact that the Eagle Ford vertical data lies on the Reuss average prediction suggests that the fabric anisotropy is strong in Eagle Ford samples. This inference is consistent with our micro-structural observations (Figure 2.3, Table 2.2) that organic materials in Eagle Ford sample show the lowest aspect ratio out of all the samples. Therefore the results depict that the mechanical properties of the gas shales are not only dependent on the volumetric fraction of the constituents, but also strongly dependent on the fabric anisotropy of the rocks.

2.5.5 Mechanical Anisotropy

The mechanical anisotropy of a VTI medium is oftentimes described using Thomsen anisotropy parameters (Thomsen, 1986). Several previous authors have compiled laboratory velocity data of shales to understand the controls on the Thomsen parameters and also develop empirical relations between the Thomsen parameters and other rock properties.

Tsuneyama and Mavko (2005) compiled laboratory velocity measurements of dry and brine-saturated sandstone and shale, and developed some empirical relationships through which the Thomsen anisotropy parameters ε and γ can be predicted from the vertical velocity (α and β) and porosity (ϕ). Li (2006) compiled laboratory velocity measurements of shales and developed a graphical method in the velocity/clay-volume space for determining anisotropy parameters ε and γ. Bandyopadhyay (2009) expanded the shale database from Li (2006), and found several linear relationships between the bedding parallel and bedding normal stiffness which generally yields higher anisotropy for lower velocities. However all authors did not find any strong correlation of the anisotropy parameter δ with the other constants or rock properties, except for a possible weak correlation with ε and γ. It is still unknown whether this owes to the larger errors involved in the determination of δ from laboratory measurements or whether δ simply is independent of other parameters.

In this section, we present the anisotropy parameters ε, γ, δ, and E_h/E_v constrained from our laboratory results, and discuss the factors that affect the mechanical anisotropy. We also compare our results with other laboratory data collected from organic-rich shales. Anisotropy parameters from our experiments were calculated for each sample group by averaging the obtained properties within each sample group. Anisotropy parameters were also obtained from the anisotropy dataset using the best set of stiffness constants obtained from the directional velocity data. Anisotropy of the static Young's modulus was evaluated by simply taking the ratio of the horizontal modulus to vertical modulus.

2.5.5.1 Causes of Mechanical Anistropy

Figure 2.16 shows the anisotropy parameters plotted against clay volume in the samples for both dynamic and static moduli data. We see from the data that mechanical anisotropy increases with clay content. Such trend is consistent with Li (2006) and is naturally understood to be caused by the preferred alignment of clay minerals and the anisotropy of the clay minerals itself. In panels a and b of Figure 2.16, the dashed lines show the estimate of anisotropy predicted from the graphical method in Li (2006) as a function of clay volume:

$$\varepsilon = 0.6 * V_{clay} \quad , \quad \gamma = 0.67 * V_{clay} \tag{2.6}$$

Since anisotropy is a function of V_{clay} and porosity in Li (2006), we derived the above relation by setting the porosity to 0% which yields their highest estimate of anisotropy. We find that our gas shale data plot higher than predicted by the Equation 2.6. This suggests that clay is not the only source of anisotropy in these shales. We interpret this discrepancy to be the additional anisotropy caused by the presence of compliant organic materials. Solid organic materials are much compliant compared to other shale-forming materials and their shapes and distribution are usually anisotropic. This makes organic materials a strong source of anisotropy in organic-rich shales (Vernik and Nur, 1992, Vernik and Liu, 1997). Since clay and organic content generally has a positive correlation, it is difficult to understand their relative contribution to the mechanical anisotropy of the bulk rock. But we learn from Figure 2.16 that clay minerals and organic contents are both sources of anisotropy in the studied shale gas reservoir rocks consistent with past studies on organic-rich shales.

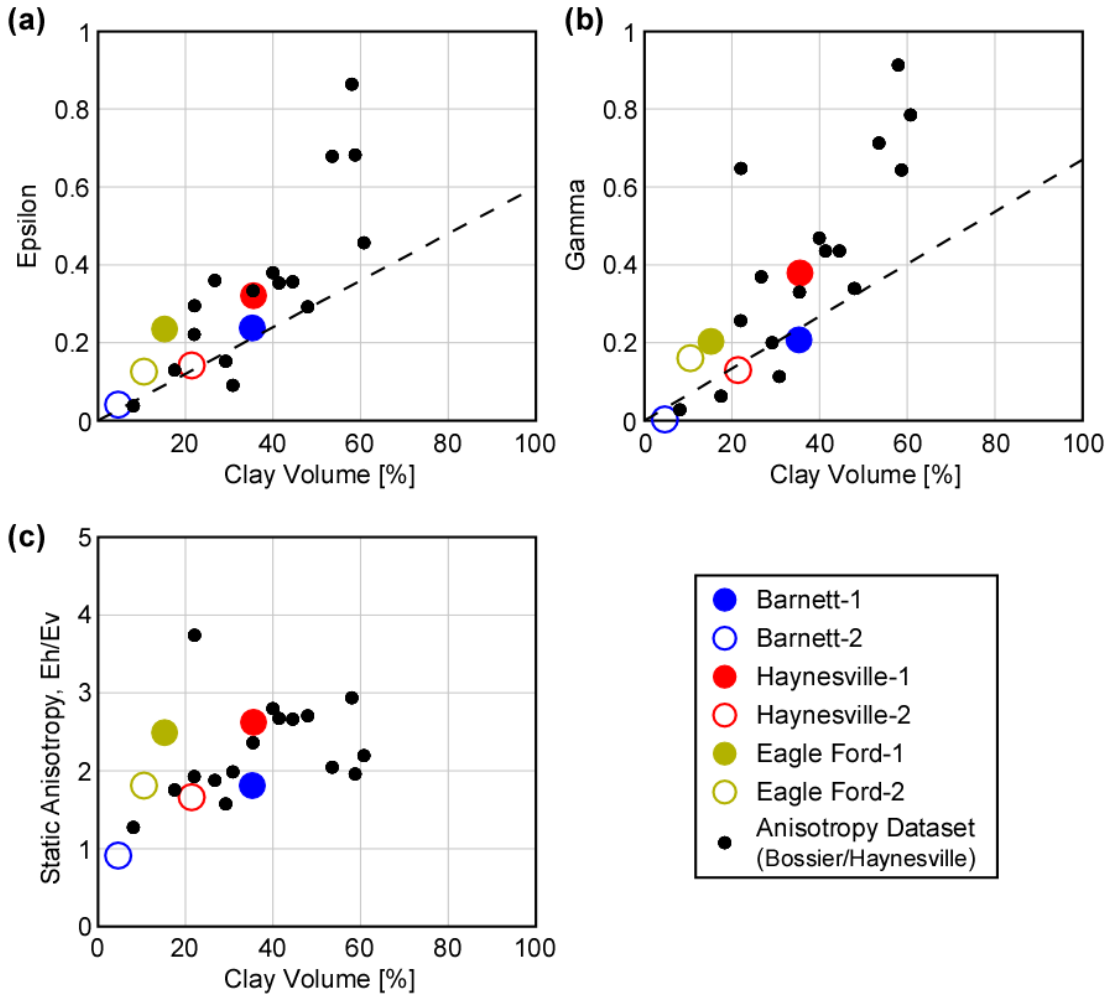

Figure 2.16: Comparison of anisotropy parameters with clay content. (a) Epsilon vs. clay volume. (b) Gamma vs. clay volume. (c) Young's modulus anisotropy vs. clay volume. Dashed line in panels (a) and (b) are estimates from Li (2006) assuming 0% porosity.

2.5.5.2 Comparison with Other Laboratory Data

We also compared the anisotropy parameters with the vertical velocities (Figure 2.17) since other studies have observed correlations between them (Tsuneyama and Mavko, 2005; Bandyopadhyay, 2009). Note that in terms of Thomsen parameters, vertical p-wave and s-wave velocities are defined as α and β, respectively. We also find a strong and confined correlation in our data although our laboratory data comes from number of shale gas reservoirs. This trend is interpreted to be the simultaneous effect of clays and organics to enhance anisotropy and lower velocity.

When our results are compared with data from organic-rich shales in Vernik and Liu (1997) (gray crosses in Figure 2.17), we find that our data show much less scatter and also tends to fall on the highest-anisotropy margin of their dataset. This is somewhat contrary to expectations since our samples have less kerogen volume (0-12%) compared to those studied in Vernik and Liu (1997) (0-42%), and anisotropy is expected to increase with kerogen volume from their study. Understanding this apparent paradox will require further examination of the samples, but we suggest that there may be two major factors involved, microstructure and kerogen property.

First, there was a difference in the microstructures observed in our samples and those invoked in Vernik and Liu (1997). The gas shales we studied do not have a continuous network of organic materials as observed in the Bakken shale samples (Vernik and Nur, 1992). Also, constituents of the gas shale rocks we studied may have lower aspect ratio than those samples used in Vernik and Liu (1997). Bandyopadhyay (2009) performed a regression of a DEM shale model to the Bakken shale velocity data from Vernik and Liu (1997) and found that the optimum aspect ratio that fitted the velocity data was 0.1. However, we observed much thinner constituents in our gas shale samples.

We also note that the gas shale rocks we studied only come from “mature” producing reservoirs, whereas the sample collection in Vernik and Liu (1997) span maturation levels from immature to overmature organic-rich shales. Vanorio et al. (2008) suggests that organic-rich shales may exhibit the highest degree of anisotropy at peak maturity due to crack alignment and kerogen distribution. This is perhaps reflected in the narrower anisotropy-velocity trend shown by our data in Figure 2.17. We do not have enough information to argue the cause of this confined trend, but we speculate that the kerogen in our samples were more compliant due to the decompaction effects caused by the presence of over-pressured gas in these reservoirs. As Figure 2.15 demonstrates, enhancing the modulus contrast between the stiff and soft component promotes anisotropy. Since kerogen is a major source of anisotropy in these rocks, a more compliant kerogen in our samples would help explain why our

samples exhibit higher anisotropy despite its limited kerogen volume. Expanding nano-indentation studies (Ahmadov et al., 2009) to organic-rich shales with various levels of maturity would help understand this problem.

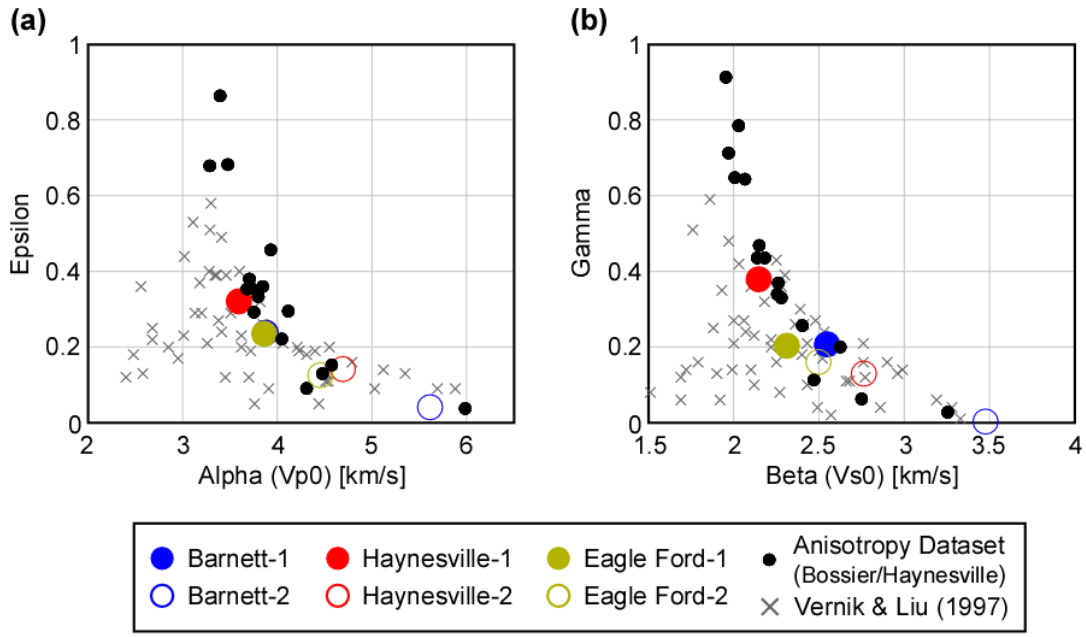

Figure 2.17: Comparison of anisotropy parameters with vertical modulus. (a) Epsilon vs. vertical p-wave velocity. (b) Gamma vs. vertical s-wave velocity. Gray crosses are data from Vernik and Liu (1997).

2.5.5.3 Empirical Relationships

Although our gas shale dataset is still limited, we tentatively attempt to derive an empirical relation between the anisotropy (ε, γ, E_h/E_v) and the vertical velocity/modulus (α, β, E_v). We find that an exponential and a power-law expression of the following form work quite well in capturing the trends:

$$y = a * \exp(b * x) \tag{2.7}$$

$$y = c * x^{d} \tag{2.8}$$

The results of the least-square regression of these equations to our data are shown in Figure 2.18, and the best-fitting constants are summarized in Table 2.4.

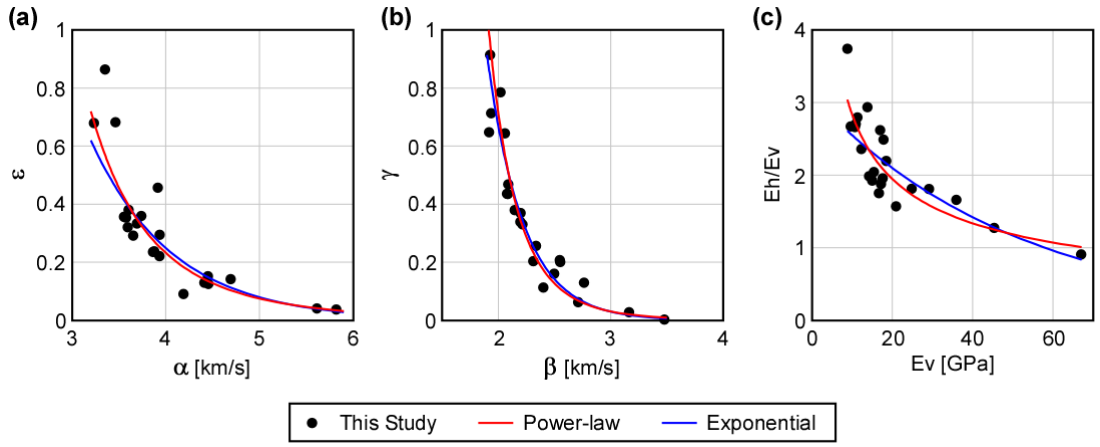

Figure 2.18: Empirical trends constrained from our laboratory data. (a) ε vs. α. (b) γ vs. β. (c) E_h/E_v vs. E_v.

Table 2.4: Best-fitting constants

x	y	a	b	c	d
α [km/s]	ε	23.8	-1.14	262	-5.07
β [km/s]	γ	329.7	-3.10	154	-7.75
E_v [GPa]	E_h/E_v	3.10	-0.0195	9.91	-0.543

We also obtained the δ Thomsen parameter which approximately describes the near-offset NMO velocity from the anisotropy dataset. δ was not obtained from our experiments since measurements were only conducted using vertical and horizontal samples. Figure 2.19 displays δ plotted against ε and γ. As previous authors have found (Thomsen, 1986; Vernik & Liu, 1997; Li 2006; Bandyopadhyay, 2009), we do not see any strong correlation of δ with other anisotropy parameters. Whether this is due to measurement error or truly due to the intrinsic property of the rock is unclear. The range of values we obtain for δ is consistent with previously reported data.

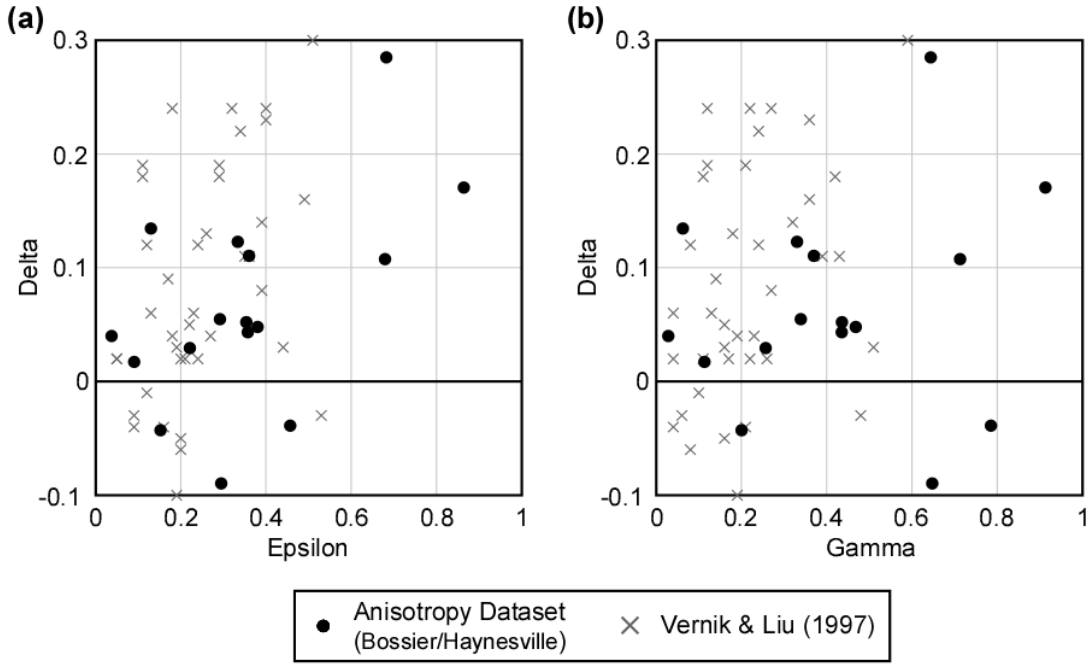

Figure 2.19: Anisotropy parameter delta plotted against epsilon and gamma. (a) Delta vs. epsilon. (b) Delta vs. gamma. Gray crosses are data from Vernik and Liu (1997).

2.6 Conclusions

Our laboratory results reveal the wide variation of elastic mechanical properties of shale gas reservoir rocks both between reservoirs and within a reservoir. As expected from basic rock physics principles, elastic properties of these rocks are a strong function of their material composition. A simple shale model dividing the shale composition into its stiff- and soft- component successfully describes the theoretical range of elastic moduli expected from their composition. Comparison of the data with the theoretical bounds also depicted how widely the shale moduli data scatters within the theoretical bounds. This reflects the how variable the microstructure can be in these shale rocks. As confirmed from microstructural observations, some gas shales exhibit extremely high degree of fabric anisotropy whereas some do not exhibit any fabric anisotropy. Therefore elastic properties of gas shales are strong functions of material composition and fabric anisotropy.

The anisotropy of the gas shale samples, described by Thomsen parameters, was found to increase with clay and organic content. The anisotropy was also found to correlate fairly well with the vertical velocities and modulus, from which we derived a empirical relation between the two quantities. These trends are consistent with past finding. However, comparison of our data with other organic-rich shale data (Vernik and Liu, 1997) shows that the anisotropy is relatively high in the studied gas shale samples despite their relatively low organic content. We suggest that the higher anisotropy observed in our samples have to do with the difference in the microstructures and possibly also the difference in kerogen mechanical properties between our gas shale samples and the organic-rich shales studied in Vernik and Liu (1997).

We also studied the static-dynamic relations of the samples. The significant difference in static modulus measured during the 1st-loading and the unloading/reloading stages suggest that one may either over- or under-estimate the static modulus from the dynamic modulus by as much as 20-30% if they fail to choose the proper static-dynamic relationships. Since most laboratory measurements of static elastic properties focus only on the stress-strain relationship during 1st-loading, we suggest that future studies also collect stress-strain data during unloading/reloading in order to better understand the static reservoir behavior at production time scales.

2.7 References

Ahmadov, R., Vanorio, T., and Mavko, G., 2009, Confocal laser scanning and atomic-force microscopy in estimation of elastic properties of the organic-rich Bazhenov Formation: The Leading Edge, **28**, 18-23.

Ahmadov, R., 2011, Micro-textural, elastic and transport properties of source rocks: Ph.D. thesis, Stanford University.

Bandyopadhyay, K., 2009, Seismic anisotropy: geological causes and its implications to reservoir geophysics: Ph.D. thesis, Stanford University.

Blanton, T. L., 1983, The relation between recovery deformation and in situ stress magnitudes: SPE/DOE Symposium on Low Permeability Gas Reservoirs, 11624.

Castagna, J. P., Batzle, M. L., and Kan, T. K., 1993, Rock physics – The link between rock properties and AVO response, in Offset-Dependent Reflectivity – Theory and Practice of AVO Analysis, Castagna, J. P., and Backus, M. M., eds, Society of Exploration Geophysicists, Tulsa, OK., 135-171.

Carcione, J. M., Helle, H. B., and Avseth, P., 2011, Source-rock seismic-velocity models: Gassmann versus Backus: Geophysics, **76**, N37-N45.

Curtis, C. D., Lipshie, S. R., Oertel, G., and Pearson, M. J., 1980, Clay orientation in some Upper Carboniferous mudrocks, its relationship to quartz content and some inferences about fissility, porosity and compactional history: Sedimentology, **27**, 333-339.

Curtis, M. E., Ambrose, R. J., Sondergeld, C. H., and Rai, C. S., 2010, Structural characterization of gas shales on the micro- and nano-scales: CUSG/SPE Canadian Unconventional Resources & International Petroleum Conference, 137693.

Gipson, M., 1966, A study of the relations with depth, porosity and clay-mineral orientation in Pennsylvanian Shales: Journal of Sedimentary Petrology, **36**, 888-903.

Hornby, B. E., Schwartz, L. M., Hudson, J. A., 1994, Anisotropic effective-medium modeling of the elastic properties of shales: Geophysics, **59**, 1570-1583.

Li, Y., 2006, An empirical method for estimation of anisotropic parameters in clastic rocks: The Leading Edge, **25**, 706-711.

Loucks, R. G., Reed, R. M., Ruppel, S. C., and Jarvie, D. M., 2009, Morphology, Genesis, and Distribution of Nanometer-Scale Pores in Siliceous Mudstones of the Mississippian Barnett Shale: Journal of Sedimentary Research, **79**, 848-861.

Lucier, A. M., Hofmann, R., and Bryndzia, T., 2011, Evaluation of variable gas saturation on acoustic log data from the Haynesville shale gas play, NW Louisiana, USA: The Leading Edge, **30**, 300-311.

Mavko, G., Mukerji, T., and Dvorkin, J., 2009, The Rock Physics Handbook Second Edition, Cambridge University Press.

Moon, C. F., 1972, The microstructure of clay sediments: Earth Science Reviews, **8**, 303–321.

Moore, D. E., and Lockner, D. A., 2004, Crystallographic controls on the frictional behavior of dry and water-saturated sheet structure minerals: Journal of Geophysical Research, **109**, B03401, doi:10.1029/2003JB002582.

Passey, Q. R., Bohacs, K. M., Esch, W. L., Klimentidis, R., and Sinha, S., 2010, From oil-prone source rocks to gas-producing shale reservoir – geologic and petrophysical characterization of unconventional shale-gas reservoir: CPS/SPE International Oil & Gas Conference and Exhibition in China, 131350.

Sondergeld, C. H., Rai, C. S., Margesson, R. W., and Whidden, K. J., 2000, Ultrasonic measurement of anisotropy on the Kimmeridge Shale, SEG Expanded Abstracts, **19**, 1858, doi:10.1190/1.1815791.

Sondergeld, C. H., Ambrose, R. J., Rai, C. S., and Moncrieff, J., 2010, Micro-Structural Studies of Gas Shales: SPE Unconventional Gas Conference, 131771.

Thomsen, L., 1986, Weak elastic anisotropy: Geophysics, **51**, 1954-1966.

Tsuneyama, F., and Mavko, G., 2005, Velocity anisotropy estimation for brine-saturated sandstone and shale: The Leading Edge, **24**, 882-888.

Vanorio, T., Prasad, M., and Nur, A., 2003, Elastic properties of dry clay mineral aggregates, suspensions and sandstones: Geophysical Journal International, **155**, 319-326.

Vanorio, T., Mukerji, T., and Mavko, G., 2008, Emerging methodologies to characterize the rock physics properties of organic-rich sahles: Leading Edge, **27**, 780-787.

Vernik, L., and Nur, A., 1992, Ultrasonic velocity and anisotropy of hydrocarbon source rocks: Geophysics, **57**, 727–735.

Vernik, L., and Liu, X., 1997, Velocity anisotropy in shales: A petrophyscial study: Geophysics, **62**, 521-532.

Vernik, L., Fisher, D., and Bahret, S., 2002, Estimation of net-to-gross from P and S impedance in deepwater turbidites: The Leading Edge, **21**, 380-387.

Vernik, L., and Milovac, J., 2011, Rock physics of organic shales: The Leading Edge, **30**, 318-323.

Warpinski, N. R., and Teufel, L. W., 1986, A viscoelastic constitutive model for determining in situ stress magnitudes from anelastic strain recovery of core: SPE 61st Annual Technical Conference and Exhibition, 15368.

Zimmer, M. A., 2003, Seismic velocities in unconsolidated sands: Measurements of pressure, sorting, and compaction effects: Ph.D. thesis, Stanford University.

Zoback, M. D., and Byerlee, J. D., 1975, The effect of cyclic differential stress on dilatancy in Westerly Granite under uniaxial and triaxial conditions: Journal of Geophysical Research, **80**, 1526-1530.

2.8 Appendix

2.8.1 Appendix A: Details of the Triaxial Apparatus and Experimental Setup

Experiments were performed in a fully servo-controlled triaxial machine, Autolab 2000 by New England Research (Figure 2A-1a). A 1-2" diameter sample is placed between 2 titanium coreholders which are set inside a pressure vessel for deformational testing. Inside the pressure vessel, isotropic confining pressure is applied to the sample by the confining fluid, and axial differential pressure is applied by the piston present inside the vessel, where both pressures are generated by servo-controlled hydraulic intensifiers. The confining pressure was controlled by a feedback from a pressure transducer with a 0.05 MPa resolution. The axial differential pressure was controlled by a feedback from an internal load cell attached on the internal piston with about a 0.3 MPa resolution (for a 1" diameter sample).

While the samples were deformed under pressure, the deformation of the sample was measured in the axial and lateral direction (Figure 2A.1b). A pair of LVDT transducers (1 micron resolution) attached to the coreholders was used to measure the change in distance between the coreholders, so that the sample axial deformation is inferred by subtracting the coreholder deformation from the observed LVDT displacements. The sample deformation in the lateral direction was measured by a pair of spring-mounted strain-gauge transducers (only one is drawn in Figure 2A.1b; 0.6 micron resolution) which clamped on to the samples 90 degrees apart from each other to measure the lateral deformation in two directions. The ultrasonic velocities were also measure by recording the travel time of ultrasonic waves generated by a piezoelectric crystal attached in the internal surface of the coreholder (Figure 2A.1b). Ultrasonic waves recorded by the other piezoelectric crystal had a time resolution of 0.04 microseconds, and they were high-pass filtered above 0.3 MHz before analyses. P-wave and cross-polarized S-wave velocities are measured but only the fast S-wave velocity is reported in this study.

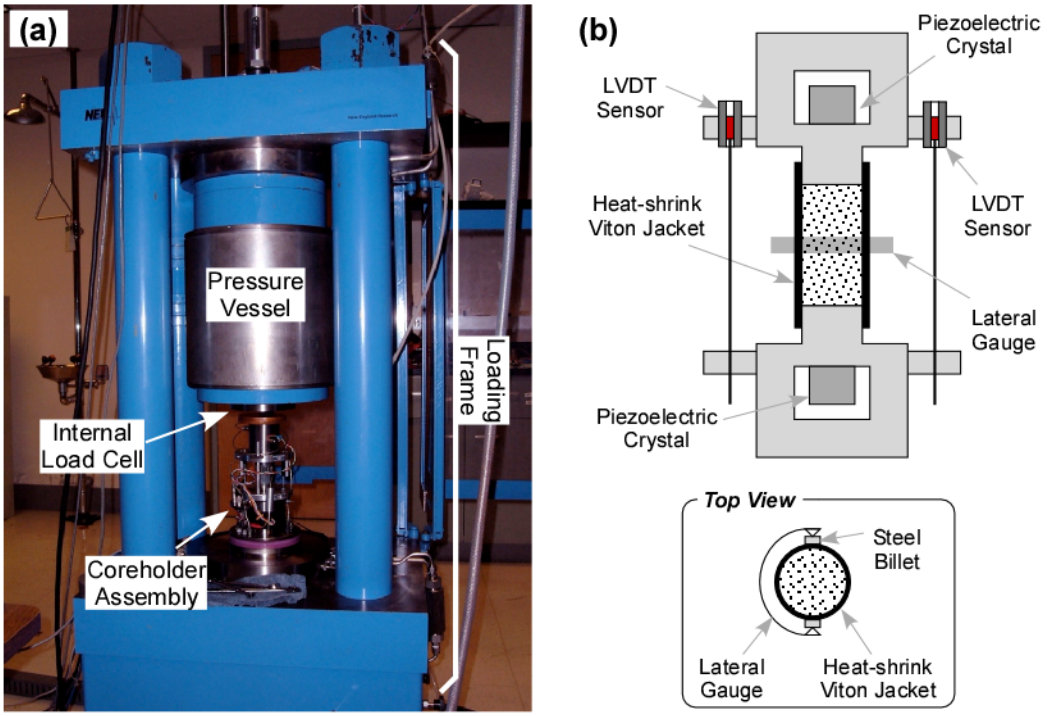

Figure 2A.1: (a) photograph of the Autolab 2000 triaxial apparatus. (b) Schematics of the sample coreholder assembly.

2.8.2 Appendix B: Database of Experimental Data

Table 2A.1: Petrophysical properties of the gas shales samples used in the experiments.

Group	Orientation	Density [g/cc]	QFP [%]	Carbonate [%]	Clay [%]	Kerogen [%]	Porosity [%]
Barnett1	V	2.466	49.7	0.4	36.5	11.4	4.2
	V	2.393	52.4	0.3	36.0	11.4	6.2
	H	2.431	52.1	0.0	38.8	9.1	5.9
	H	2.447	50.5	2.7	36.6	8.5	9.1
Barnett2	V	2.632	53.2	37.2	6.5	2.6	2.0
	V	2.671	35.9	57.8	3.3	2.4	1.0
	H	2.644	31.3	59.9	6.6	2.2	1.8
Haynesville1	V	2.503	35.0	20.8	36.6	7.6	5.8
	V	2.494	31.9	20.2	39.0	7.7	6.1
	V	2.501	35.0	20.1	36.3	7.5	5.7
	V	2.508	33.2	22.3	35.5	7.9	5.6
	H	2.508	33.2	22.3	35.5	7.9	5.6
	H	2.508	33.2	22.3	35.5	7.9	5.6
Haynesville2	V	2.610	23.9	49.3	22.3	3.7	3.1
	V	2.599	22.6	52.6	20.0	3.6	4.3
	V	2.600	23.1	50.8	21.4	3.7	3.9
	H	2.606	23.1	50.8	21.4	3.7	3.7
	H	2.615	23.1	50.8	21.4	3.7	3.3

Fort St. John	H	2.573	53.7	2.9	38.8	4.6	5.0
	H	2.591	59.8	4.7	32.0	3.5	5.5
	H	2.595	55.0	3.6	37.2	4.2	4.5
Eagle Ford1	V	2.426	25.9	48.5	14.2	11.4	1.1
	V	2.456	28.6	45.9	15.1	10.4	0.2
	V	2.447	23.8	46.2	21.0	9.0	3.2
	V	2.431	21.7	53.8	14.7	9.4	2.6
	H	2.430	22.6	52.9	14.6	9.9	1.4
	H	2.454	26.5	51.9	11.5	9.7	1.6
Eagle Ford2	V	2.525	18.0	62.8	13.7	5.1	3.2
	V	2.535	14.7	72.1	9.4	3.8	3.4
	V	2.460	11.4	77.6	6.3	4.8	4.8
	V	2.521	17.6	68.2	10.1	3.9	4.5
	H	2.525	16.3	66.5	12.9	4.3	3.6

Table 2A.2: Confining pressure and measured velocities during the hydrostatic stage.

Group	Orientation	Pc [MPa]	Vp [km/s]	Vsh [km/s]
Barnett1	V	10.2/20.3/30.2	3.56/3.86/3.95	2.48/2.55/2.57
	V	10.3/20.3/30.3	3.42/3.71/3.80	2.43/2.50/2.52
	H	7.3/14.3/20.3	4.58/4.61/4.64	2.94/2.97/2.97
	H	10.3/20.3/30.3/40.3	4.64/4.71/4.74/4.75	3.03/3.06/3.08/3.08
Barnett2	V	10.3/20.3/30.3/40.3	4.94/5.23/5.27/5.35	3.39/3.46/3.48/3.50
	V	10.3/20.3/30.3/40.3	5.72/5.80/5.82/5.88	3.42/3.44/3.45/3.46
	H	7.3/14.3/20.3	5.71/5.75/5.79	3.45/3.47/3.48
Haynesville1	V	20.3/40.3/60.2	3.52/3.59/3.65	2.09/2.15/2.20
	V	10.3/20.3/30.2	3.48/3.54/3.58	2.07/2.11/2.13
	V	10.3/20.3	3.42/3.50	2.06/2.10
	V	10.4	-	2.04
	H	10.4/20.4/30.4	-	-
	H	10.3/20.4/30.4/40.4	4.51/4.56/4.57/4.61	2.81/2.83/2.84/2.85
Haynesville2	V	10.2/20.3/30.2	4.60/4.64/4.67	2.69/2.71/2.72
	V	7.3/14.3/20.3	4.48/4.58/4.63	2.74/2.77/2.79
	V	10.4	-	2.67
	H	10.4/20.4/30.4	5.21/5.27/5.27	3.06/3.08/3.09
	H	10.4/20.4/30.4/40.4	5.23/5.30/5.32/5.34	3.09/3.10/3.10/3.11
Fort St. John	H	10.3/20.3/30.2	4.52/4.61/4.64	2.86/2.89/2.92
	H	10.3/20.3/30.2/40.3	4.32/4.37/4.41/4.46	2.80/2.82/2.82/2.84
	H	10.3/20.3	4.49/4.54	2.85/2.89
Eagle Ford1	V	10.4/20.4/30.4/40.4	-/3.72/3.83/3.90	-/2.27/2.30/2.32
	V	10.4/20.4/30.4/40.4	3.42/3.62/3.74/3.82	2.18/2.23/2.27/2.30
	V	10.3/20.4	-	2.28/2.32
	V	10.4	-	-
	H	10.4/20.4/30.4	-	-
	H	10.4/20.4/30.4	4.56/4.62/4.65	2.70/2.72/2.73
Eagle Ford2	V	10.4/20.4/30.4/40.4	4.04/4.22/4.31/4.38	2.44/2.48/2.50/2.51
	V	10.4/20.4	3.89/4.29	2.34/2.41
	V	10.4/20.4	-	2.45/2.54
	V	10.4	-	-
	H	10.4/20.4/30.4	4.87/4.91/4.97	2.86/2.86/2.87

Table 2A.3: Differential pressure and measured velocities during the triaxial stage.

group	Orientation	Q [MPa]	Vp [km/s]	Vsh [km/s]
Barnett1	V	46.5/92.0	4.07/4.09	2.59/2.60
	V	46.6/92.1	3.91/3.94	2.55/2.55
	H	47.3/95.2	4.67/4.67	2.98/2.97
	H	25.2/49.2/94.9	4.76/4.75/4.78	3.09/3.09/3.08
Barnett2	V	24.9/48.6/94.0	5.40/5.42/5.43	3.52/3.52/3.53
	V	23.1/45.4/90.4	5.90/5.92/5.97	3.45/3.44/3.44
	H	44.7/89.7	5.84/5.82	3.49/3.48
Haynesville1	V	29.2/58.4	3.72/3.78	2.25/2.27
	V	32.1/61.0	3.64/3.70	2.17/2.22
	V	15.2/31.0/60.0	3.56/3.61/3.65	2.12/2.16/2.20
	V	3.4/6.6/9.9/19.2/38.2	-	2.06/2.08/2.08/2.11/2.14
	H	13.6/29.2/57.4	-	-
	H	16.7/32.1/46.3/60.4	4.62/4.63/4.63/4.63	2.85/2.85/2.84/2.85
Haynesville2	V	37.1/77.1	4.74/4.78	2.77/2.79
	V	34.4/74.5	4.72/4.77	2.80/2.81
	V	3.6/6.8/10.1/19.5/38.5	-	2.70/2.71/2.71/2.72/2.73
	H	17.3/32.8/48.3/60.8	5.29/5.29/5.29/5.31	3.09/3.10/3.09/3.10
	H	17.0/32.4/60.3	5.34/5.34/5.36	3.11/3.11/3.11
Fort St. John	H	18.1/33.9/62.2	4.67/4.68/4.68	2.91/2.91/2.91
	H	17.9/33.4/61.4	4.47/4.50/4.54	2.83/2.84/2.85
	H	19.1/34.8/63.4	4.57/4.58/4.61	2.88/2.88/2.87
Eagle Ford1	V	15.9/30.2/44.4/58.7	4.01/4.07/4.10/4.12	2.35/2.36/2.37/2.37
	V	16.2/30.6/44.8/59.1	3.95/4.06/4.13/4.19	2.34/2.36/2.39/2.40
	V	6.0/10.8/20.0/38.6	-	2.33/2.34/2.34/2.35
	V	3.1/6.2/9.5/18.5/37.0	-	-
	H	13.4/28.8/42.9/57.1	-	-
	H	16.8/29.5/43.5/57.5	4.68/4.70/4.71/4.71	2.74/2.74/2.75/2.75
Eagle Ford2	V	16.2/30.6/44.9/59.4	4.45/4.48/4.53/4.55	2.52/2.53/2.54/2.54
	V	5.1/9.8/19.1/37.6	4.43/4.47/4.53/4.59	2.45/2.47/2.49/2.51
	V	5.5/10.2/19.5/38.0	-	2.58/2.60/2.61/2.63
	V	3.7/6.7/10.2/19.2/37.8	-	-
	H	16.3/29.5/43.7/57.8	4.98/5.00/5.02/5.02	2.87/2.87/2.87/2.88

Table 2A.4: Differential pressure and Young's modulus measured during the triaxial stage.

group	Orientation	Q [MPa]	E – 1st loading [GPa]	E – unloading/reloading [GPa]
Barnett1	V	46.5/92.0	24.9/27.1	36.3/32.3
	V	46.6/92.1	24.6/22.7	29.6/26.6
	H	47.3/95.2	42.9/37.4	47.5/42.7
	H	25.2/49.2/94.9	46.9/42.8/37.8	58.2/46.8/47.2
Barnett2	V	24.9/48.6/94.0	58.6/54.7/52.3	82.4/65.3/63.7
	V	23.1/45.4/90.4	75.4/58.4/57.7	98.7/71.0/71.2
	H	44.7/89.7	61.0/59.6	67.2/67.2
Haynesville1	V	29.2/58.4	18.2/17.5	27.2/23.3
	V	32.1/61.0	17.7/15.7	23.0/21.5
	V	15.2/31.0/60.0	19.2/16.9/15.3	25.8/22.4/22.6
	V	3.4/6.6/9.9/19.2/38.2	14.7/18.7/20.6/15.5/15.1	19.8/24.2/22.9/21.4/19.8
	H	13.6/29.2/57.4	47.1/43.0/34.8	63.5/50.3/41.3
	H	16.7/32.1/46.3/60.4	45.9/43.6/38.4/38.5	57.2/46.6/42.1/41.7

Haynesville2	V	37.1/77.1	37.2/29.4	40.4/37.6
	V	34.4/74.5	37.3/32.0	48.5/39.2
	V	3.6/6.8/10.1/19.5/38.5	41.8/34.8/46.9/37.2/33.3	43.7/51.9/66.2/48.0/42.2
	H	17.3/32.8/48.3/60.8	59.6/58.9/53.3/52.9	75.6/65.6/59.6/59.1
	H	17.0/32.4/60.3	59.7/54.9/50.9	76.6/68.9/59.5
Fort St. John	H	18.1/33.9/62.2	39.7/39.1/33.2	51.7/43.8/41.1
	H	17.9/33.4/61.4	40.2/35.9/30.6	48.5/41.5/38.4
	H	19.1/34.8/63.4	38.1/38.9/33.4	50.8/41.4/41.3
Eagle Ford1	V	15.9/30.2/44.4/58.7	18.4/23.5/24.4/27.6	27.0/26.6/27.6/30.2
	V	16.2/30.6/44.8/59.1	14.9/20.0/23.9/28.2	24.7/27.9/33.7/33.9
	V	6.0/10.8/20.0/38.6	19.7/33.0/31.3/24.6	29.9/39.8/33.7/29.6
	V	3.1/6.2/9.5/18.5/37.0	11.6/15.5/17.7/15.4/13.4	18.2/31.8/31.8/25.4/23.6
	H	13.4/28.8/42.9/57.1	48.4/43.6/39.4/37.4	52.0/46.2/40.7/40.5
	H	16.8/29.5/43.5/57.5	45.1/44.9/39.7/38.1	53.8/46.2/41.6/43.7
Eagle Ford2	V	16.2/30.6/44.9/59.4	33.5/33.2/32.6/32.2	44.4/40.2/34.8/34.6
	V	5.1/9.8/19.1/37.6	10.9/17.3/22.7/27.0	18.2/27.4/32.2/34.9
	V	5.5/10.2/19.5/38.0	16.6/28.5/37.2/30.2	28.9/34.9/43.3/41.8
	V	3.7/6.7/10.2/19.2/37.8	20.9/26.1/31.2/28.3/25.9	32.5/37.2/37.1/38.0/33.3
	H	16.3/29.5/43.7/57.8	52.7/47.9/45.2/46.6	63.4/54.4/48.0/48.7

Table 2A.5: Differential pressure and Poisson's ratio measured during the triaxial stage.

group	Orientation	Q [MPa]	ν_{31} (vertical samples) or ν_{13} (horizontal samples)	ν_{12} (horizontal samples)
Barnett1	V	46.5/92.0	0.185/0.210	-
	V	46.6/92.1	0.189/0.211	-
	H	47.3/95.2	0.270/0.313	0.177/0.184
	H	25.2/49.2/94.9	0.272/0.304/0.304	0.155/0.173/0.156
Barnett2	V	24.9/48.6/94.0	0.165/0.204/0.196	-
	V	23.1/45.4/90.4	0.265/0.225/0.259	-
	H	44.7/89.7	0.194/0.241	0.214/0.226
Haynesville1	V	29.2/58.4	0.211/0.208	-
	V	32.1/61.0	0.207/0.209	-
	V	15.2/31.0/60.0	0.197/0.208/0.205	-
	V	3.4/6.6/9.9/19.2/38.2	-/-/-/0.145/0.155	-
	H	13.6/29.2/57.4	0.394/0.359/0.380	0.194/0.179/0.148
	H	16.7/32.1/46.3/60.4	0.336/0.357/0.357/0.417	0.160/0.205/0.161/0.196
Haynesville2	V	37.1/77.1	0.291/0.299	-
	V	34.4/74.5	0.216/0.257	-
	V	3.6/6.8/10.1/19.5/38.5	-/-/-/0.196/0.191	-
	H	17.3/32.8/48.3/60.8	0.275/-/-/-	0.227/0.203/0.212/0.197
	H	17.0/32.4/60.3	0.262/0.231/0.283	0.141/0.216/0.219
Fort St. John	H	18.1/33.9/62.2	0.307/0.359/0.323	0.164/0.194/0.170
	H	17.9/33.4/61.4	0.244/0.233/0.238	0.179/0.171/0.211
	H	19.1/34.8/63.4	0.223/0.301/0.277	0.163/0.171/0.207
Eagle Ford1	V	15.9/30.2/44.4/58.7	0.187/0.205/0.217/0.232	-
	V	16.2/30.6/44.8/59.1	0.181/0.209/0.226/0.232	-
	V	6.0/10.8/20.0/38.6	-/-/0.219/0.206	-
	V	3.1/6.2/9.5/18.5/37.0	-/-/-/0.127/0.153	-
	H	13.4/28.8/42.9/57.1	0.263/0.313/0.339/0.277	0.169/0.250/0.204/0.191
	H	16.8/29.5/43.5/57.5	0.309/0.282/0.300/0.364	0.227/0.257/0.204/0.206
Eagle Ford2	V	16.2/30.6/44.9/59.4	0.224/0.239/0.240/0.243	-

	V	5.1/9.8/19.1/37.6	-/-/0.140/0.165	-
	V	5.5/10.2/19.5/38.0	-/-/-/0.202	-
	V	3.7/6.7/10.2/19.2/37.8	-/-/-/0.194/0.189	-
	H	16.3/29.5/43.7/57.8	0.265/0.305/0.319/0.364	0.249/0.293/0.273/0.240

2.8.3 Appendix C – Database for the Anisotropy Dataset

Table 2A.6: Static and dynamic elastic properties of samples from Bossier and Haynesville shale determined from measured from 3-5 orientations.

Locality		Well 1								Well 2							
Formation (B: Bossier, H: Haynesville)		B	B	B	B	H	H	H	H	B	H	H	H	H	H	H	H
Average Density (g/cc)		2.646	2.661	2.659	2.554	2.587	2.522	2.497	2.518	2.565	2.532	2.534	2.492	2.518	2.516	2.582	2.66
Static Moduli	E33 [GPa]	13.8	17.6	18.5	15.4	16.7	10.9	10.7	8.8	14.2	15.0	12.3	11.3	9.7	17.2	21.0	45.4
	E11 [GPa]	40.4	34.4	40.5	31.5	29.2	29.4	28.4	33.0	28.2	28.9	29.0	31.7	25.8	32.2	33.0	57.8
	v31	0.130	0.191	0.167	0.138	0.214	0.186	0.156	0.262	0.221	0.229	0.149	0.179	0.172	0.144	0.139	0.267
	v12	0.338	0.297	0.273	0.19	0.235	0.241	0.239	0.315	0.277	0.252	0.285	0.434	0.267	0.341	0.265	0.291
Dynamic velocity	Vp-0 [km/s]	3.35	3.46	3.92	3.23	4.41	3.65	3.55	3.94	4.19	3.93	3.69	3.60	3.58	3.74	4.45	5.82
	Vp-45 [km/s]	4.36	4.35	4.42	3.99	4.69	4.00	3.96	4.18	4.31	4.21	4.14	4.05	3.99	4.22	4.59	5.93
	Vp-90 [km/s]	5.54	5.33	5.42	4.97	4.95	4.60	4.65	4.96	4.55	4.73	4.77	4.78	4.67	4.90	5.08	6.03
	Vs-0 [km/s]	1.93	2.06	2.02	1.94	2.71	2.19	2.09	1.92	2.40	2.34	2.21	2.09	2.08	2.20	2.55	3.16
	Vs-45 [km/s]	2.50	2.44	2.50	2.50	2.71	2.41	2.34	2.02	-	-	-	-	-	-	-	-
	Vs-90 [km/s]	3.24	3.11	3.24	3.02	2.87	2.84	2.85	2.91	2.66	2.87	2.85	2.91	2.84	2.90	3.02	3.25
Best fit dynamic stiffness and Thomsen parameters	C11 [GPa]	83.2	76.0	78.7	65.1	65.3	56.3	59.2	67.8	56.3	59.8	60.9	60.3	58.2	64.0	70.5	102.5
	C33 [GPa]	30.5	32.2	41.1	27.6	51.9	35.5	34.5	42.6	47.6	41.5	36.5	34.2	34.1	37.2	54.1	95.4
	C44 [GPa]	10.1	11.4	10.9	9.9	19.6	12.8	11.9	10.1	15.7	14.6	13.1	11.5	11.5	12.9	17.8	28.2
	C66 [GPa]	28.5	26.0	28.1	24.0	22.0	21.5	22.2	23.2	19.2	22.1	21.8	22.3	21.5	22.4	24.9	29.8
	C13 [GPa]	15.0	17.2	17.6	10.5	19.1	11.7	12.2	18.3	17.2	13.4	14.4	12.8	12.8	15.3	16.1	42.7
	Epsilon	0.864	0.682	0.457	0.679	0.130	0.292	0.357	0.295	0.091	0.221	0.334	0.380	0.354	0.360	0.152	0.038
	Gamma	0.914	0.644	0.785	0.713	0.063	0.340	0.436	0.648	0.113	0.257	0.330	0.469	0.436	0.370	0.201	0.028
	Delta	0.171	0.285	-0.039	0.108	0.134	0.055	0.043	-0.090	0.017	0.029	0.123	0.048	0.052	0.110	-0.043	0.040

2.8.4 Appendix D – True vs. Apparent Young's modulus ia a VTI Medium

For an isotropic medium, the dynamic Young's modulus is determined precisely from the p- and s-wave moduli by the equation.

$$E = \frac{\mu(3M - 4\mu)}{M - \mu} \tag{A-1}$$

For a VTI medium, as in horizontally layered shales, equations relating the Young's modulus and the stiffness constants depend on the orientation and involve 4 independent stiffness constants as shown below.

$$\begin{aligned} E_{vertical} &= E_{33} = c_{33} - \frac{2c_{31}^2}{c_{11} + c_{12}} \\ E_{horizontal} &= E_{11} = c_{11} + \frac{c_{31}^2(-2c_{11} + c_{12}) + c_{12}(-c_{33}c_{12} + c_{31}^2)}{c_{33}c_{11} - c_{31}^2} \end{aligned} \tag{A-2}$$

However, in many laboratory studies, this equation cannot be used since the stiffness constant c_{31} is not determined due to technical difficulty.

Using the anisotropy dataset which contains complete sets of stiffness constants for 16 different samples (Appendix B), we evaluated the error of simply using the isotropic relations by Equation A-1 to calculate the apparent dynamic Young's modulus rather than using Equation A-2 to calculate the true dynamic Young's modulus in a VTI medium.

Figure 1A.1 shows the apparent dynamic Young's modulus against the true dynamic Young's modulus for both vertical and horizontal directions. The plot shows a quite good agreement between each other. With the exception of several vertical samples the agreement is within 5%. Although this is what we find for just the Bossier/Haynesville shales in the dataset, we judged it is reasonable to expect a similar agreement for the other shale samples we used in our experiment and used the apparent dynamic Young's modulus to discuss the static-dynamic relations in section 1.5.3.

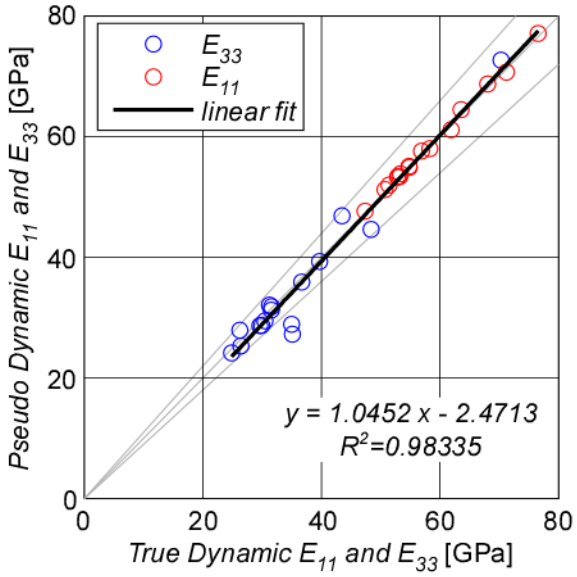

Figure 2A.2: Apparent dynamic Young's modulus vs. true dynamic Young's modulus. The grey lines show 1-to-1 correspondence and 10 % deviation.

Chapter 3

MECHANICAL PROPERTIES OF SHALE GAS RESERVOIR ROCKS– PART 2: DUCTILE CREEP, BRITTLE STRENGTH, AND THEIR RELATION TO ELASTIC ANISOTROPY

Abstract

We studied the ductile creep behavior and brittle strengths of shale gas reservoir rocks from the Barnett, Haynesville, Eagle Ford, and Fort St. John shale, and find that these deformational properties correlate with the elastic modulus of the rock although they are fundamentally different mechanical properties. Laboratory experiments show that creep deformation is approximately linear against the applied pressure, and the tendency to creep generally increases with the total clay and organic content in the samples. Creep deformation is also more pronounced in the bedding perpendicular direction than in the bedding parallel direction. The intact and sliding strengths of the

gas shale rocks were also dependent on material composition, and the intact rock strengths exhibited weak anisotropy. However, the strongest correlation of these deformational properties is found with their elastic modulus. The tendency to creep correlated negatively with the sample Young's modulus, and various parameters describing rock strengths (UCS, internal and sliding frictional coefficient) correlated positively with the sample Young's modulus. We explain the apparent correlation between creep behavior and elastic modulus by appealing to the stress partitioning that occurs between the soft components (clay and kerogen) and stiff components (quartz, feldspar, pyrite, carbonates) of the shale rock due to the fabric anisotropy. Anisotropic DEM modeling was performed for a shale rock model, composed of a stiff matrix and soft inclusions of various aspect ratios, to calculate the elastic properties, stress partitioning, and the resulting whole rock creep behavior. Results show that the DEM shale modeling can predict the correlation between creep and elastic properties observed in the laboratory data. The results provide a mechanical explanation for why long-term ductile deformational properties can correlate with the short-term elastic properties. We also make suggestions on why anisotropic rocks are stronger against loading in the bedding parallel direction by referring to the stress partitioning results obtained from the DEM modeling.

3.1 Introduction

Recent success in producing from unconventional shale gas reservoirs are made possible by reservoir stimulation via multi-stage hydraulic fracturing along horizontal wells. In these settings, geophysicists and petrophysicists are not only asked to precisely locate these resources, as in most conventional hydrocarbon reservoirs, but also to gain information about how these shale respond mechanically to fluid/proppant injection as hydraulic fracturing proceeds. The latter is a great challenge since large-strain deformational properties of rocks are not captured by the small-strain elastic properties collected by seismic exploration or well logging. Difference between static and dynamic elastic properties studied in Chapter 2 is only an entrance to this problem, as rock deformational properties span as far as how a rock ultimately fails. Studies on

empirical relations of rock strength (Chang et al., 2006) illustrate how difficult it is to accurately predict deformational properties from other petrophysical parameters. Time-dependent ductile deformation is another class of deformational properties that will influence the production of these reservoirs. For instance, fractures once opened by proppants can close over time lowering the effective permeability of the reservoir after stimulation (proppant embedment).

A common approach now popular in the industry is to evaluate the "brittleness" (Rickman et al., 2008) of the formations encountered in these shale gas reservoirs, in order to indentify well intervals that are relatively easier to fracture. "Brittleness" is an empirical parameter usually computed from the dynamic elastic constants derived from sonic logs. While this approach is practical and may be successful to some extent, it is not defined nor justified through basic observations of rock deformation. Since rock failure is a highly nonlinear process, certainly not described by consolidating its behavior into a single parameter, it is important to evaluate how well elastic properties relate to rock deformational behavior in the lab in order to understand to what extent these approaches can be useful or not.

In light of these issues, we studied the deformational properties of various shale gas reservoir rocks through laboratory experiments to acquire some fundamental properties that may be relevant to shale gas production. Intact and frictional strength is collected to understand how brittle strengths vary between samples. We also observed the time-dependent creep deformation of these rocks as one measure of ductility. Finally, we attempt to demonstrate how these deformational properties are related to the anisotropic elastic property found in Chapter 2. Such relation will help understand why small-strain elastic properties can be used in some cases to infer high-strain deformational properties.

3.2 Samples and Methods

3.2.1 Sample Description

Samples used in the experiments come from Barnett, Haynesville, Eagle Ford shale, and Fort St. John shales. Mineralogy of the samples constrained by powder XRD analysis show that clay, QFP (=quartz+feldspar+pyrite), carbonate contents vary between 5-50 vol%, 5-60 vol%, and 0-80 vol%, respectively, representing a wide range of mineralogy (Figure 3.1). Samples from Barnett, Haynesville, and Eagle Ford shale are further divided into 2 subgroups of distinct mineralogy where subgroup 1 contains more clay and organic contents than subgroup 2. Total organic contents range from 0.4-5.8 wt% and porosities estimated from the mineral and bulk density range between 1.5-9 %. As described in Chapter 2, clay content, organic content, and porosity correlate with one another supporting the idea that pore volumes in these shale mostly reside within the clay aggregates and solid organics in the sample (Loucks et al., 2009; Sondergeld et al., 2010). Also from Chapter 2, these samples

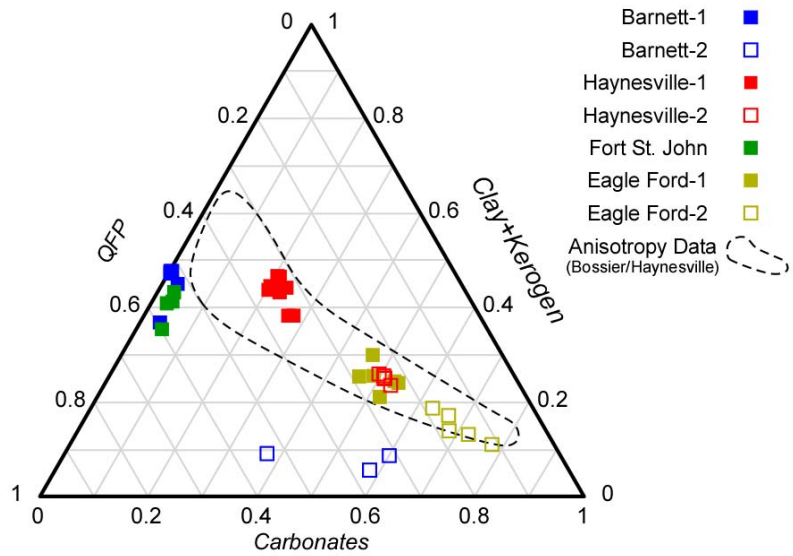

Figure 3.1: Ternary plot representation of the sample material composition.

were also found to exhibit a wide range of fabric anisotropy, which is reflected on the anisotropy of their elastic properties. Further details on the mineralogy and the microstructure of these samples are described in Chapter 2.

3.2.2 Laboratory Procedures

Laboratory experiments discussed here are the same experiments as those discussed in Chapters 2. Cylindrical plugs of 1" diameter and 1.2-2.1" length from each sample groups were prepared with its axes either perpendicular (vertical) or parallel (horizontal) to the bedding planes. These samples were pressurized in a servo-controlled triaxial deformation apparatus to observe its static and dynamic elastic properties and creep properties. A heat-shrink Viton jacket was used to seal the sample from the confining fluid. Hydrostatic confining pressure, P_c, was first applied in 1-4 steps (hydrostatic stage), and then axial differential pressure, P_{diff}, was applied in 2-5 steps while P_c was held constant (triaxial stage). Duration of each pressure step was either 30 or 60 seconds, after which the pressure was held constant for 3 hours to observe the creep response. During the experiments, the sample deformation in the direction parallel to the sample cylindrical axis was measured by a pair of LVDT displacement transducers, and the deformation perpendicular to the sample cylindrical axis (lateral deformation) was measured by a pair of spring-mounted strain-gauge transducers attached outside of the Viton jacket.

An example of the strain response to some pressure steps during the triaxial stage is shown in Figure 3.2. In our interpretation of the laboratory data, we divide the total strain response to a pressure step into 2 parts, elastic strain ($\varepsilon_{elastic}$) and creep strain (ε_{creep}). $\varepsilon_{elastic}$ was used to determine the static elastic constants, and ε_{creep} was used to quantify the amount of creep strain that occurs after 3 hours of constant pressure. Note that we will only focus on the 1st-loading elastic behavior of the rock in this chapter. After the triaxial stage, the samples were taken to failure by loading the samples at a constant axial strain rate of 10^{-5} s^{-1} to measure rock strengths (failure stage). After the ultimate rocks strength was reached and a macroscopic failure plane

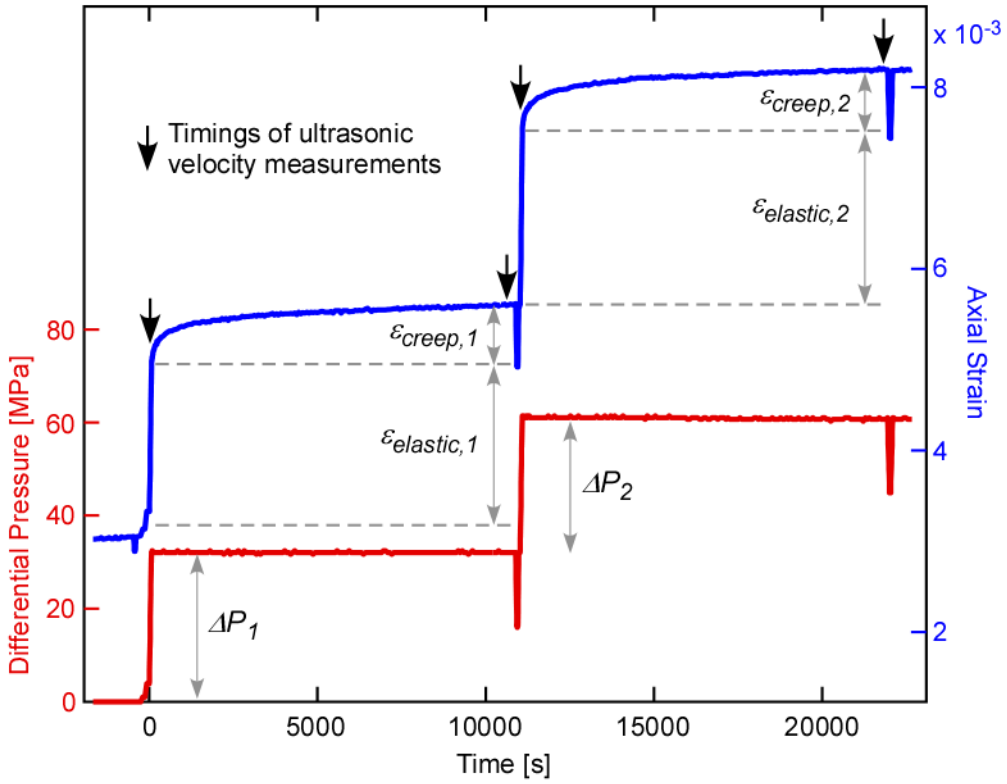

Figure 3.2. Illustration of how elastic and creep strain is measured from each pressure step.

was formed, we continued to slide the failure plane for a while to measure the residual strengths of the rock.

P_c during the triaxial and failure stages was varied between 10-60 MPa so that the P_c dependence of rock strengths could be evaluated. It was necessary to observe the P_c dependence of both ultimate and residual rock strengths to obtain the internal and sliding frictional coefficients of the rock. This also helped to check if the creep behavior was dependent on P_c.

The maximum axial differential pressure during the triaxial stage was kept below 50 % of the ultimate rock strengths to assure that creep deformation did not enter its tertiary creep stage (Lockner, 1993). In the tertiary creep stage, strain rate starts to increase and leads to unstably rock failure. We avoided the tertiary creep stage because our focus in the triaxial stage was to observe the long-term ductile

property of the samples. The appearance of the tertiary creep in the triaxial stage would contaminate the ductile behavior with a shorter-term brittle response of the rock.

We believe that the measured strain responses were free of any poroelastic effects since the original fluid saturation was no more than 40% (including clay-bound water) and all experiments were conducted under dry (no introduction of pore fluid), room-temperature, drained conditions. Also, samples were either sealed in wax or kept at room humidity condition but never oven-dried prior to the experiments. Therefore clays in the samples were likely associated with clay-bound water.

3.3 Laboratory Results

3.3.1 Results from the Hydrostatic Stage

Interpreting results from the hydrostatic stage proved to be very difficult. We did observe varying amounts of creep strain during the hydrostatic stage, but the accurate quantification of the behavior was extremely difficult due to several erratic instrument responses created by the confining pressure change. The detail description of these instrument responses are provided in Appendix A; but in summary, the rapid confining pressure change during the pressure step and the associated temperature fluctuation created several artificial signals that could not be removed from the data effectively. These effects could be ignored if the sample deformation was large relative to these instrument responses. But creep strains observed in some samples were at comparable magnitudes as the instrument responses. Thus in most cases, the true rock behavior could not be extracted from the data. However, we still performed the hydrostatic stage since the process of gradually raising the confining pressure during the hydrostatic stage helped to achieve a stable condition inside the pressure vessel prior to the triaxial stage. During the triaxial stage, there were no significant changes in the confining fluid pressure or temperature, thus the mechanical data were free of the above mentioned artificial responses.

3.3.2 Creep during the Triaxial Stage

Figure 3.3 shows examples of creep strain responses during the triaxial stage from an experiment using a Haynesville-1 vertical and a Barnett-1 horizontal sample. The plots show that the direction of the creep strain is consistent with what would happen during a regular triaxial experiment. Sample shrinks in the axial direction, and dilates in the lateral direction. However lateral strain seems to stabilize after about 10

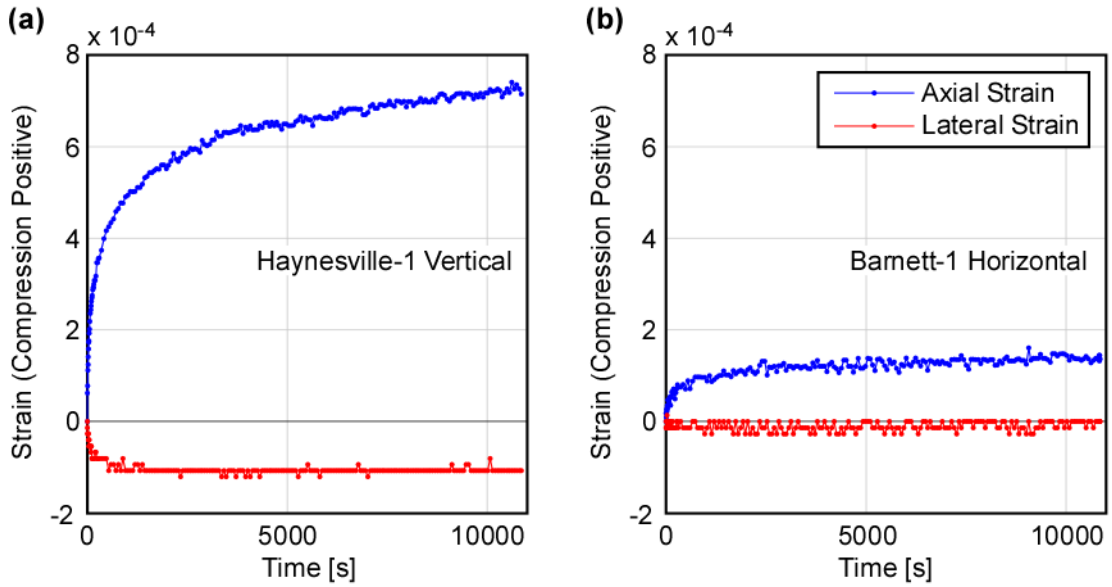

Figure 3.3: Axial and lateral creep strain responses during the triaxial stage. (a) An experiment using a Haynesville-1 vertical sample. (b) An experiment using a Barnett-1 horizontal sample.

minutes or so and stay constant although the axial strain continues to creep. The plots also show that the creep strain response is much greater in the axial direction than in the lateral direction. When the sample does not creep so much (Figure 3.3b), the lateral creep strain response is only within few measurement resolutions making it difficult to analyze. For these reasons, we judge that we cannot consistently recover useful information from the lateral strain data. Therefore, from hereon, we will only analyze the axial strain data to characterize the creep behavior of the rocks. This will also become convenient later since we will be comparing the creep behavior with the Young's modulus. Young's modulus is also measured from experiments by only looking at the axial strain response.

Figure 3.4 displays several representative axial creep strain data observed during the triaxial stage. As shown in the plots, samples exhibited varying degree of creep behavior. Note that the aluminum alloy data (Al7075, black data) tested under similar conditions showed no creep behavior which verifies that we were observing real rock time-dependent deformation, rather than some instrument response. From comparison with the aluminum alloy data, we confirm that even the sample that exhibited the least amount of creep (Barnett-2) shows some creep behavior although the magnitude is very small. Although Figure 3.4 shows the difference in creep behavior between samples, each triaxial creep data was collected under different magnitudes of pressure steps. Since, intuitively, creep strain is expected to increase with the magnitude of differential pressure, we probably cannot directly compare the strain responses to infer the tendency to creep of each sample.

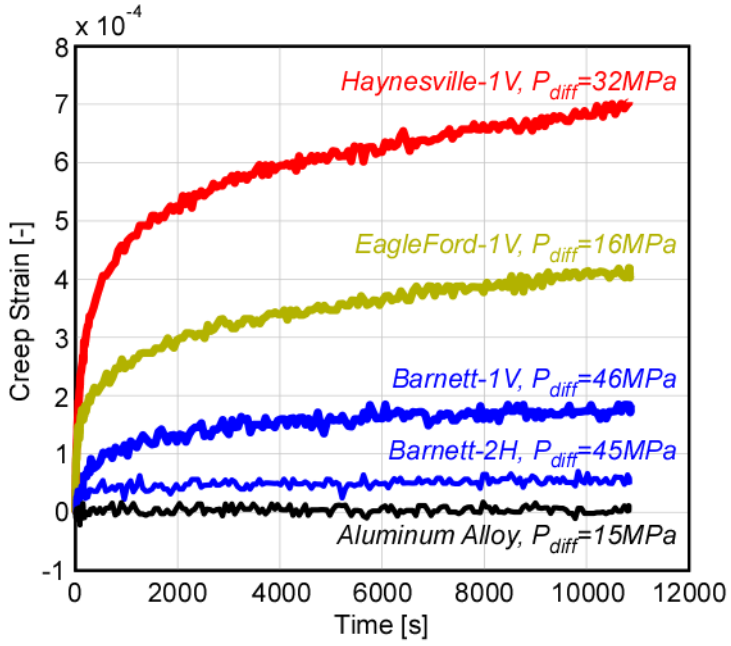

Figure 3.4: Several representative axial creep strain data. V: vertical samples, H: horizontal samples.

In Figure 3.5, the cumulative amount of creep strain, $\Sigma\varepsilon_{creep,i}$, after each step is plotted against cumulative differential pressure at each step. Each connected set of data points represents a single experiment. All samples show an approximately linear trend, despite the varying magnitudes of pressure steps applied in each step. This

suggests that the magnitude of creep after 3 hours scales linearly with the magnitude of differential pressure. Thus the amount of creep is more or less proportional to the applied differential pressure. Under this assumption, if a line is fit to each set of data

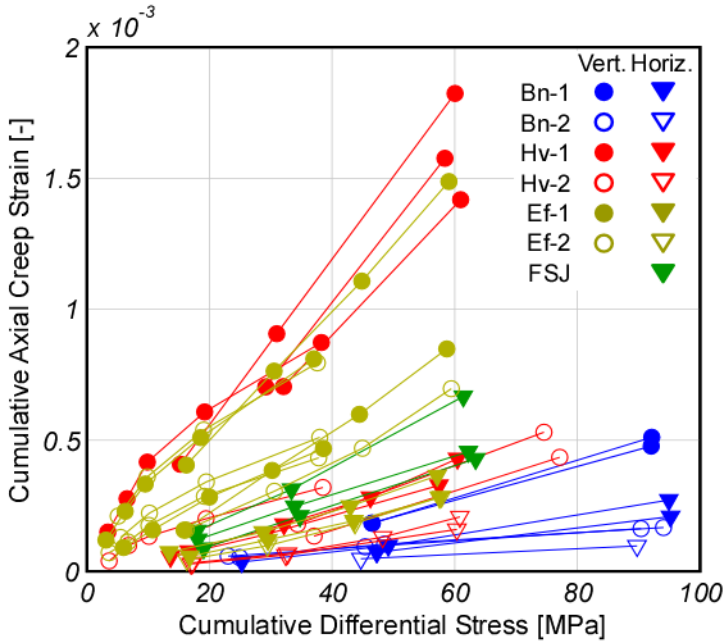

Figure 3.5: Cumulative creep vs. cumulative differential pressure. Bn: Barnett, Hv: Haynesville, Ef: Eagle Ford, FSJ: Fort St. John.

representing a single sample, the slope can be interpreted to be an approximate measure of the tendency to creep for that sample. We refer to this slope as the 3-hour creep compliance, S_{creep}, or simply the creep compliance from hereon. S_{creep} has units of MPa^{-1}. Note that the value of S_{creep} we recover from the data only has the predictive capability for how much creep will take place after 3 hours. The 3-hour creep compliance does not carry information about the constitutive relation between strain and time. Nonetheless, S_{creep} becomes a useful proxy for us to infer the ductility of a sample.

By comparing the slopes of the data in Figure 3.5, we observe several important observations about what controls the creep behavior. First, we observe that samples with more clay and organic contents have higher 3-hour creep compliances. When comparing data from the same reservoir, the subgroup-1 samples show a higher slope

than the subgroup-2 samples. We also observed that the creep behavior is anisotropic. Vertical samples always exhibit higher 3-hour creep compliance than the horizontal samples from the same sample group. Finally, the 3-hour creep compliance seems to be insensitive to the magnitude of the constant confining pressure applied during the triaxial stage. For instance, the constant confining pressures during the triaxial stage varied from 10-60 MPa in the Haynesville-1 vertical samples, but the slopes representing the 3-hour creep compliance are more or less the same. The same is observed from all sample groups except for the Eagle Ford vertical samples. The inconsistency of the slopes from Eagle Ford vertical samples may be caused by sample variability, which will become more evident later when observing the strength data. Nonetheless, the results indicate that the magnitude of the creep strain response in the triaxial stage is a function of the applied differential stress, but not a function of the isotropic stress.

We also note that the amount of creep per unit stress is much lower than observed from creep of unconsolidated reservoir rocks. Laboratory results from Hagin and Zoback (2004) using Wilmington sands show that the 6-hour volumetric creep strain per MPa of hydrostatic pressure was about 6e-4 MPa^{-1}, whereas the sample that crept the most in our experiments showed 3-hour creep compliance of about 3e-5 MPa^{-1}. Thus the creep strain of gas shales we observed is about an order of magnitude smaller than those of typical sand reservoir rocks.

3.3.3 Ultimate and Residual Strength Data

From the failure stage, we obtained the dependence of ultimate and residual strengths on the confining pressure. Figure 3.6 shows the ultimate strength data plotted against the confining pressure. In order to characterize the uniaxial compressive strength (UCS) and the internal coefficient of friction (μ_i), we fit a line to the strength data from each experiment by least square method. The y-intercept of the fitted line represents the UCS, and the slope, n, is used to calculate the internal friction coefficient through the following equation (Zoback, 2007):

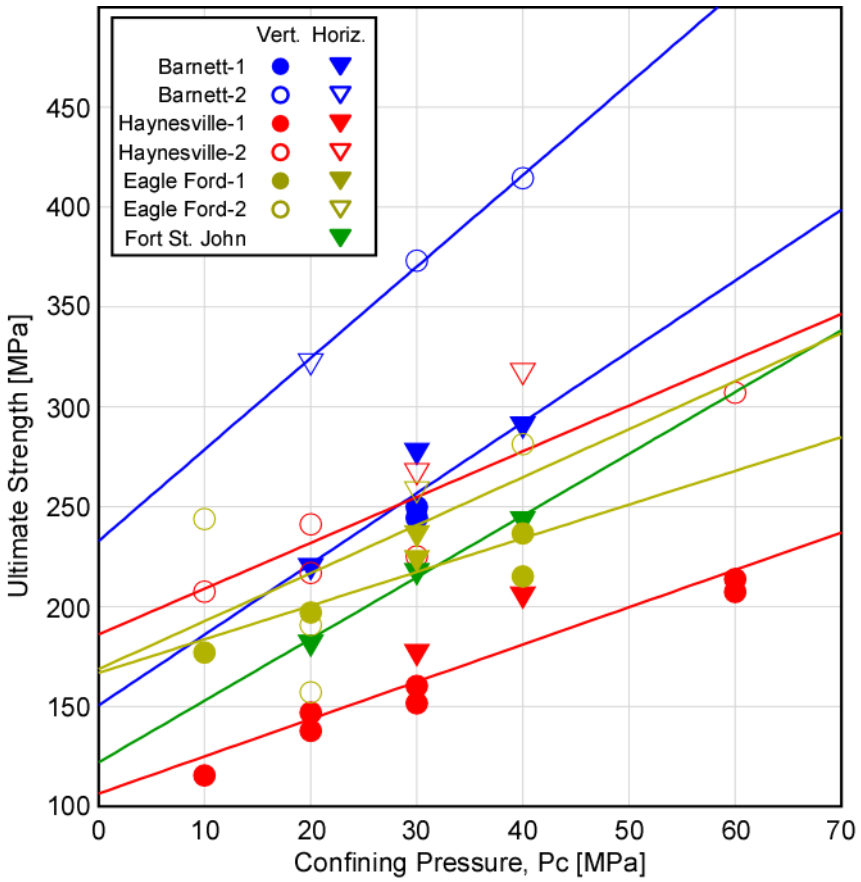

Figure 3.6: Ultimate strength data plotted against confining pressure.

$$\mu_i = \frac{n-1}{2\sqrt{n}} \tag{3.1}$$

Note that we have treated the strength data from vertical and horizontal samples equally, although our samples exhibit significant anisotropy. This is because it is generally regarded, to the first order, that ultimate strength parallel to and perpendicular to the bedding plane will not be affected by the plane of weakness (bedding plane) as long as the plane of weakness is not oriented diagonally to the principal stress directions (Paterson and Wong, 2005; Zoback, 2007). However, as the triangle data points shows in Figure 3.6, the horizontal strength data tends to plot above the general trend determined by the linear regression. This suggests that the

ultimate rock strengths in our samples are actually stronger in the direction parallel to the bedding plane.

Figure 3.7 summarizes the residual strength data collected in the failure stage. After each experiment, the angle of the failure plane relative to the sample cylindrical axis was measured by a protractor. This angle was used to calculate the normal and shear tractions resolved on the failure plane when the residual strength stabilized towards the end of the experiments. Similar to the ultimate strength data, we fit a line to the shear traction versus normal traction data to obtain the sliding coefficient of friction, μ_s, and the cohesion. The slope of the linear fit gives us the sliding frictional coefficient, and the y-intercept gives us the cohesion.

Frictional sliding surfaces generally do not carry a significant amount of cohesion. But we consistently see about 5-15 MPa of cohesion. This reflects the sliding resistance due to the rough failure plane created by the experiment. Fault displacement along the failure plane reached at most about 2.5 mm in our experiments, and this was not enough to smooth out the failure plane.

Note that there does not seem to be a tendency for the horizontal sample data to fall above the average trend in Figure 3.7. Sliding strength is governed by the frictional strength of the gouge material present at the fault interface, which is naturally a product of high shear strain deformation. Therefore it is not affected by the original fabric of the rock, unless the roughness of the surface is affected by the sample orientation. We do not see a systematic tendency for one orientation to be stronger than the other, therefore there seems to be minimal influence of sample orientation on the sliding strength of the samples.

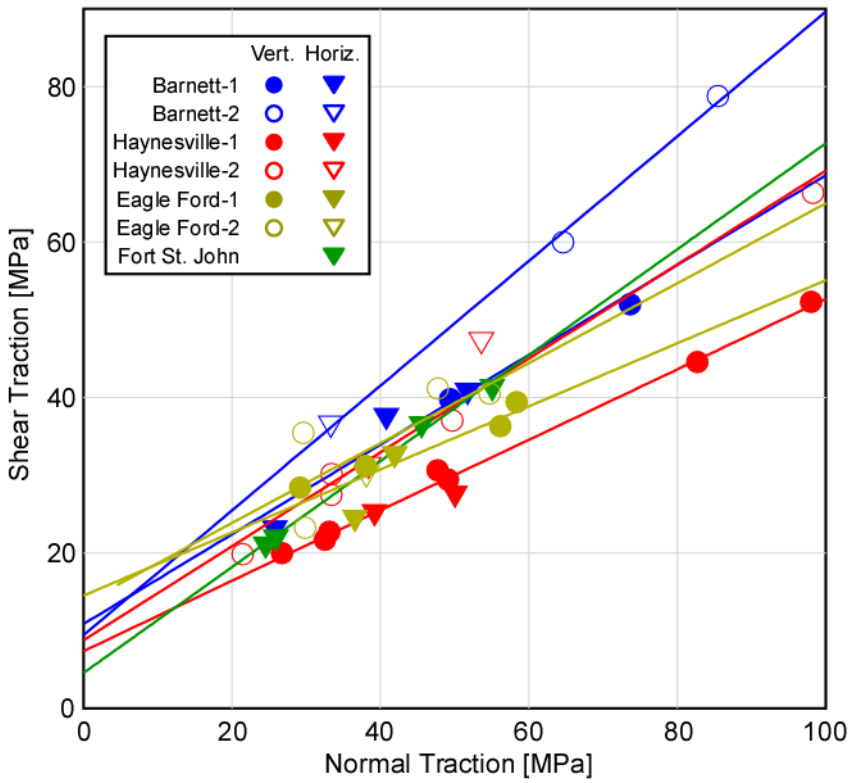

Figure 3.7: Residual strength data. Resolved shear traction plotted against resolved normal traction.

3.4 Observations on Relation between Deformation Properties and Other Properties

In this section, we compare the 3-hour creep compliance data, S_{creep}, and the strength related information against other rocks properties to gain insight about what controls those deformational behaviors and what proxies may exist for those properties. Specifically, we will focus on relating the deformational properties to the material composition and static elastic properties.

3.4.1 3-hour Creep Compliance versus Composition and Elastic Properties

From Figure 3.5, it was suggested that samples with more clay and organic content has a higher tendency to creep. In Figure 3.8, the 3-hour creep compliance of each sample is plotted against the sum of clay and kerogen volume in the sample. We

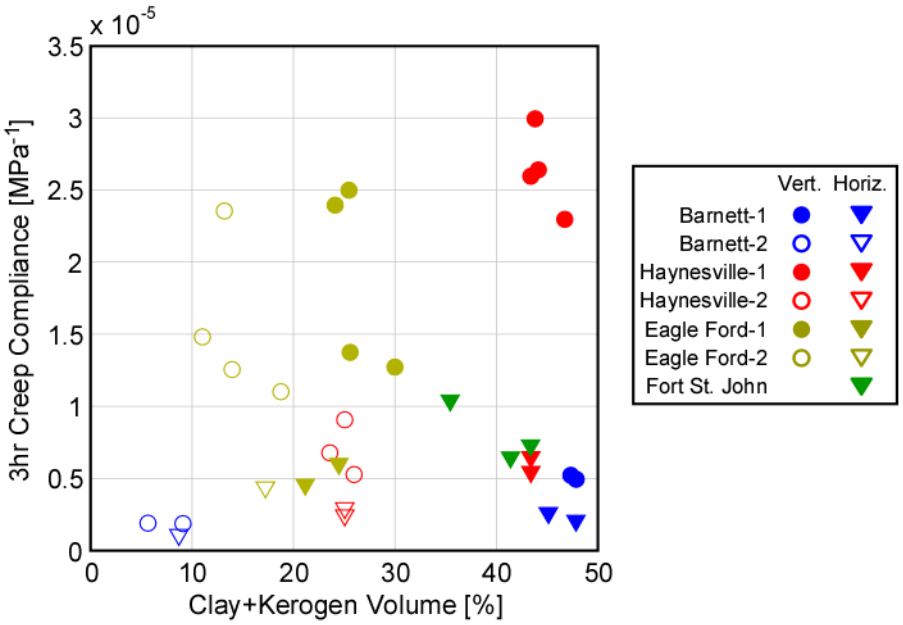

Figure 3.8: 3-hour creep compliance plotted against sample clay + kerogen volume.

generally find that the creep compliances of vertical samples are higher than those of horizontal samples, suggesting that creep compliance is anisotropic just like the elastic properties of these gas shale samples (Chapter 2). But there does not seem to be any universal inter-reservoir trend between creep compliance and the total clay/kerogen volume contrary to our expectation from Figure 3.5. Eagle Ford vertical samples specifically have relatively low clay and kerogen volume, but exhibit one of the highest creep compliance values. Although we grouped together samples with similar compositions, expecting that they will have similar mechanical behavior, Eagle Ford samples tend to show wider ranges of creep compliances. This suggests there are some variations within the Eagle Ford sample groups.

Figure 3.9 shows the 3-hour creep compliance data plotted against some static elastic properties. The static elastic constants were those presented in Chapter 2, and they are the 1st-loading elastic properties obtained at when the total axial pressure was closest to 45 MPa. The pressure value of 45 MPa was chosen because it was found from Chapter 2 that the closure pressures of the soft pore space was about 40-50 MPa.

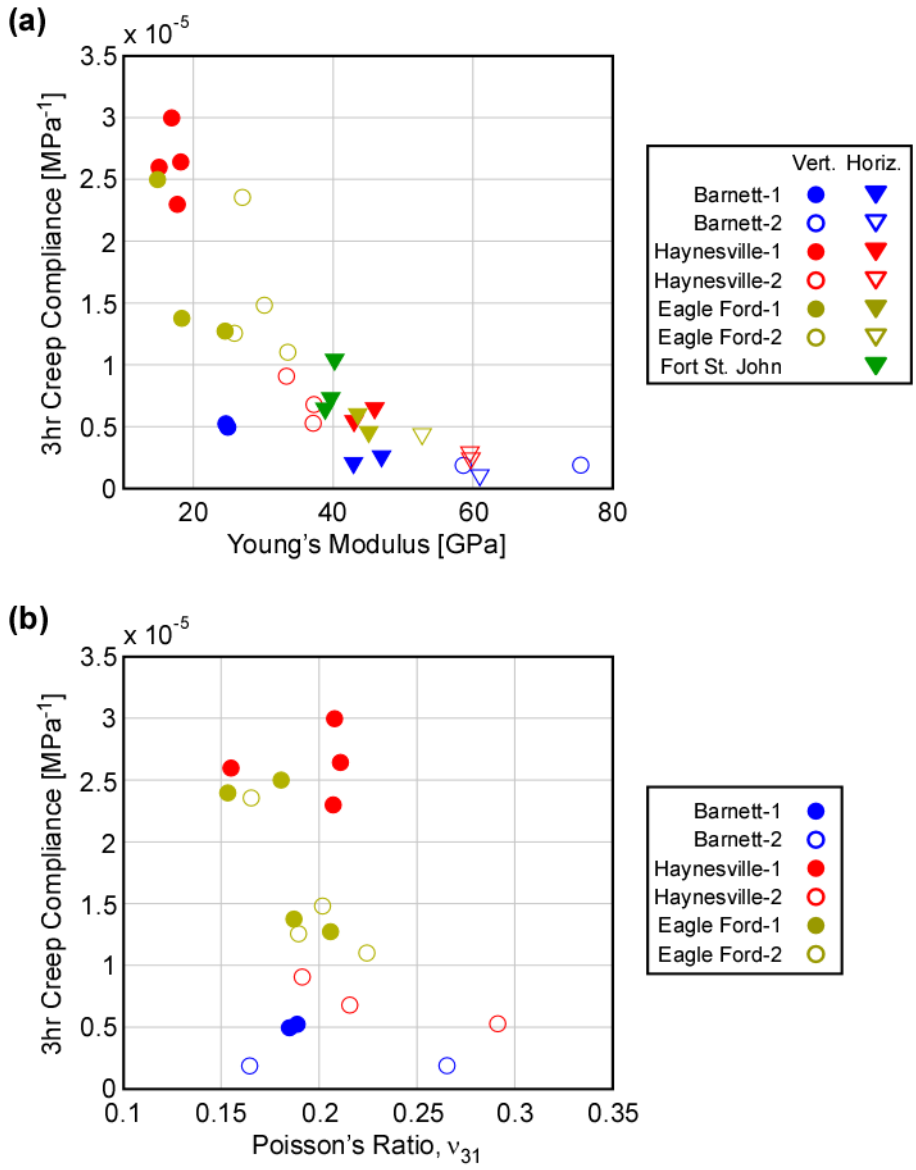

Figure 3.9: 3-hour creep compliance plotted against elastic properties. (a) 3-hour creep compliance plotted against static Young's modulus. (b) Vertical 3-hour creep compliance plotted against static vertical Poisson's ratio, ν_{31}.

Figure 3.9a shows that there is a fairly confined correlation between the creep compliance and the static Young's modulus. Although the Barnett-1 vertical samples tend to show lower creep compliances compared to the average trend, there seems to be a universal trend between the creep compliance and the Young's modulus regardless of the sample orientation. Note that the Eagle Ford vertical samples, which exhibited a relatively wide range of creep compliance values, also follow this trend

within the sample group. The samples with higher creep compliances within the Eagle Ford samples have lower static Young's modulus values.

On the other hand, the static Poisson's ratio does not seem to correlate with creep compliance. As in the empirical relation shown in Rickman et al. (2008), "brittleness" is usually expected to increase with decreasing Poisson's ratio. But we cannot make any inference from out static Poisson's ratio data.

3.4.2 Strength and Friction versus Composition and Elastic Properties

Figure 3.10 compares the UCS with the average total clay-kerogen volume and the average static Young's modulus at 45 MPa axial pressure of each sample groups. The pressure 45 MPa for the axial pressure was chosen since the soft crack closure pressures were found to be around 40-50 MPa from Chapter 2. We find that UCS generally decreases with increasing clay-kerogen volume, and has a positive correlation with the Young's modulus. As the error bars indicate, some of these values were poorly constrained, especially those from Eagle Ford-2. The uncertainty in the regression was caused by the scatter in the strength data with respect to the fitted line, which may be a result of sample variability within a sample group.

Figure 3.11 compares the internal coefficient of friction, μ_i, against the average total clay-kerogen volume and the average static Young's modulus of each sample groups. As the error bars indicate, there was much more uncertainty in the obtained μ_i values compared to the UCS values, especially the Eagle Ford-2 samples. However if we read the center values, μ_i seem to have a fairly well correlation with the average static Young's modulus, but there is not a correlation with the clay-kerogen volume.

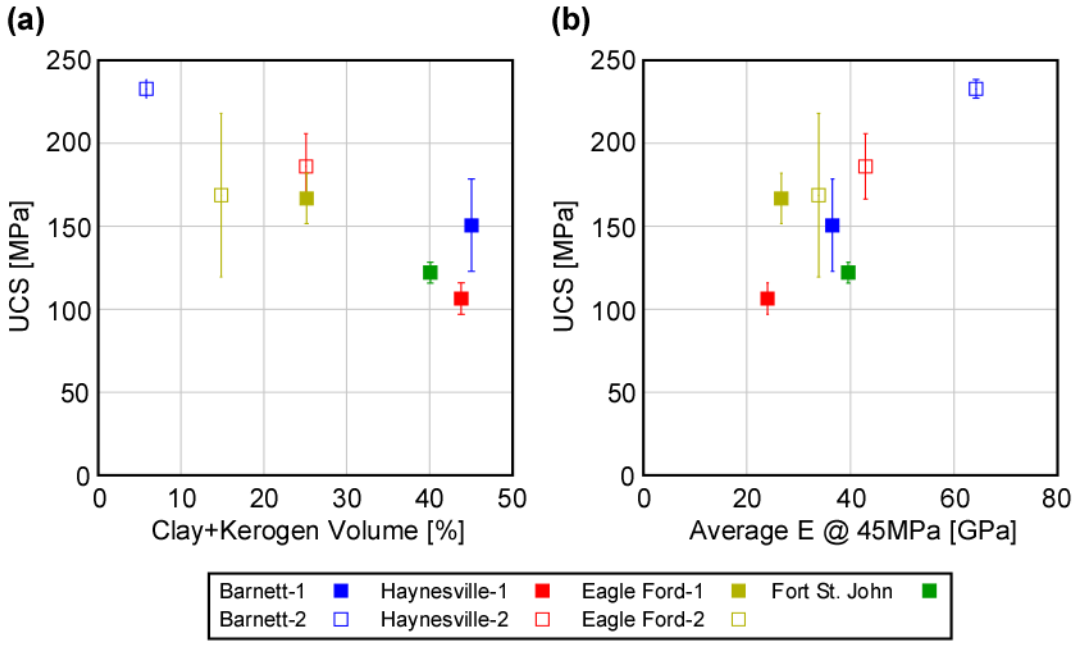

Figure 3.10: (a) UCS plotted against average clay + kerogen volume. (b) UCS plotted against average Young's modulus at 45MPa axial pressures. Error bars indicate one standard deviation confidence intervals.

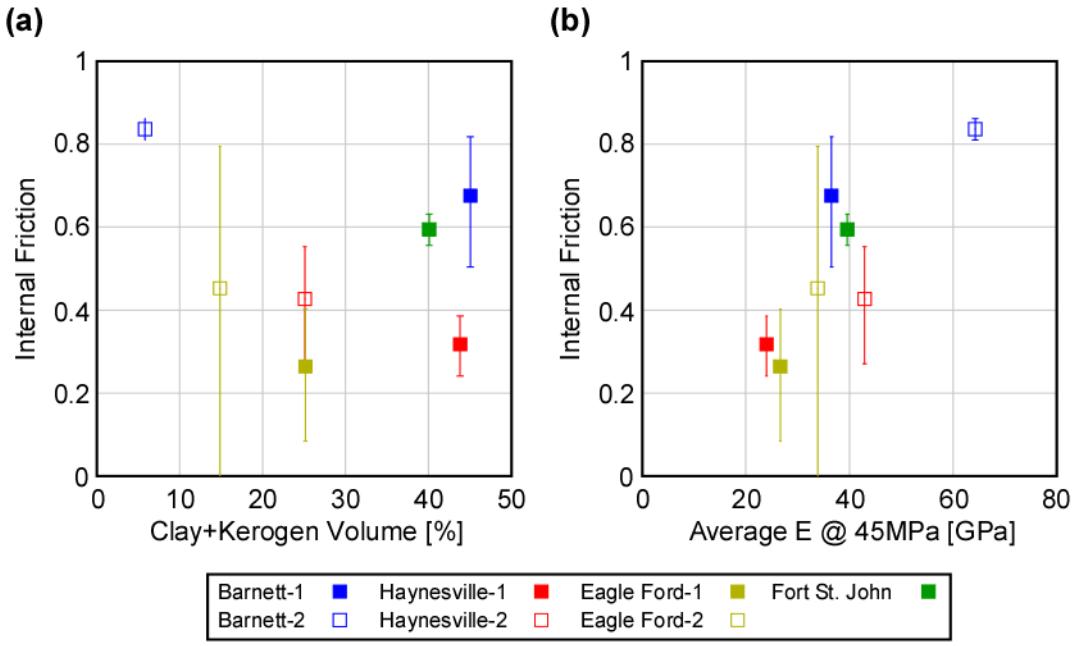

Figure 3.11: (a) Internal friction coefficient plotted against average clay + kerogen volume. (b) Internal frictional coefficient plotted against average clay volume. Error bars indicate one standard deviation confidence intervals.

Finally, Figure 3.12 compares the sliding coefficient of friction, μ_s, with the average clay volume and the average static Young's modulus of each sample groups. μ_s was compared against clay volume, instead of clay-kerogen volume, since sliding friction is expected to depend on the gouge material composition (Tembe et al., 2010) and clay minerals are known to have anomalously low frictional coefficients (Moore and Lockner, 2004). The correlation of μ_s with clay volume is not as robust as expected, but if we ignore the poorly constrained data points, our results generally agree with past findings that μ_s weakens with increase in clay volume. More data is needed to understand why the Eagle Ford samples show low μ_s despite its relatively low clay content. μ_s has a fairly well correlation with the elastic modulus. This is somewhat surprising since sliding friction should be governed by the properties and composition of the gouge material, rather than the mechanical property of the host rock. Whether this is a coincidence or not is not known from our data.

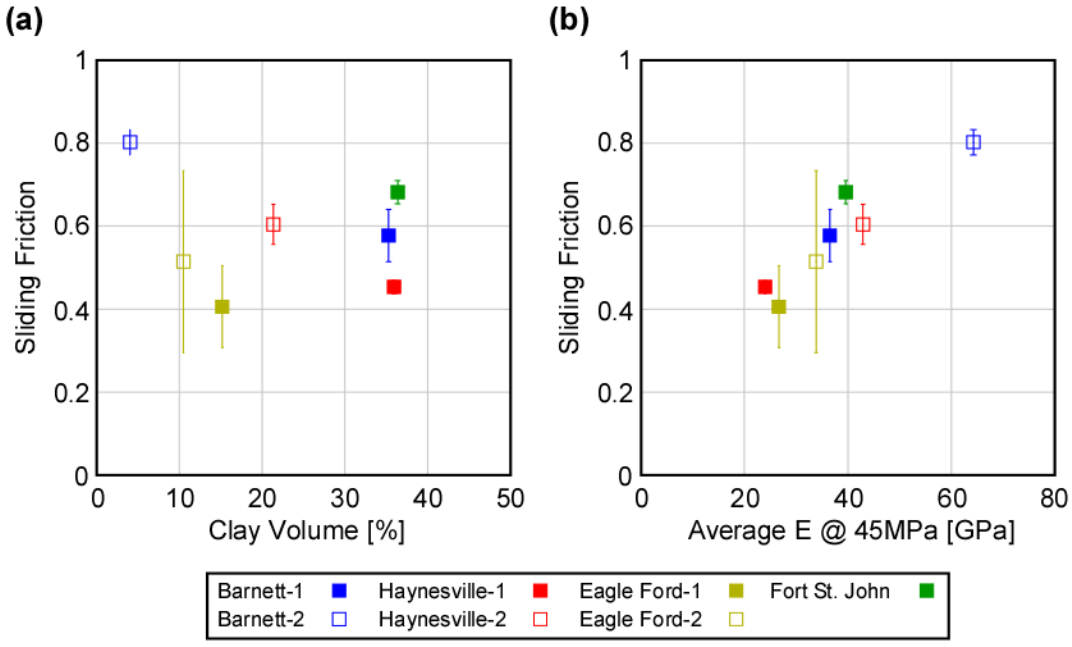

Figure 3.12: (a) Sliding friction coefficient plotted against average clay + kerogen volume. (b) Sliding frictional coefficient plotted against average clay volume. Error bars indicate one standard deviation confidence intervals.

3.5 Discussion

3.5.1 Where the Creep Deformation is Occurring

As seen from Figure 3.3, the creep strain in the lateral direction is much smaller than the creep strain in the axial direction. Thus we could tell that the sample is losing volume through creep deformation during the triaxial stage. Since creep occurs under constant stress, the volume loss is most likely accommodated by pore volume loss, or compaction. This is also inferred by the observation that the 3-hour creep compliance correlated with the change in dynamic moduli measured by ultrasonic velocities (Figure 3.13). For a dry rock, the whole rock modulus, K_{dry}, is a function of the average mineral modulus, K_m, pore stiffness, K_ϕ, and porosity, ϕ, given by the following equation (Mavko et al., 2009):

$$\frac{1}{K_{dry}} = \frac{1}{K_m} + \frac{\phi}{K_\phi} \tag{3.2}$$

where the equation is shown for bulk modulus here, but the same applies to the p-wave and s-wave moduli. Thus, if the mineral properties are not changing during creep, the overall stiffening of the rock is caused by either porosity reduction or pore modulus stiffening, both explained as results of compaction.

Since microstructural observations by many studies (Loucks et al., 2009; Sondergeld et al., 2010; Curtis et al., 2010) reveal that most of the pore space in these shale gas reservoir rocks reside in the clays and solid organics, this suggests that compaction responsible for the creep deformation is predominantly occurring within the clays and organics in the rock. This is conceivable as increase in clay content is known to enhance creep deformation in unconsolidated shale sediments (Chang et al., 1997) and clay minerals are known to have anomalously low frictional coefficients (Moore and Lockner, 2004), which would help facilitate grain rearrangement. Also coal materials, often considered as a proxy for solid organic materials, are known to exhibit significant creep behavior from laboratory experiments (Hagin and Zoback,

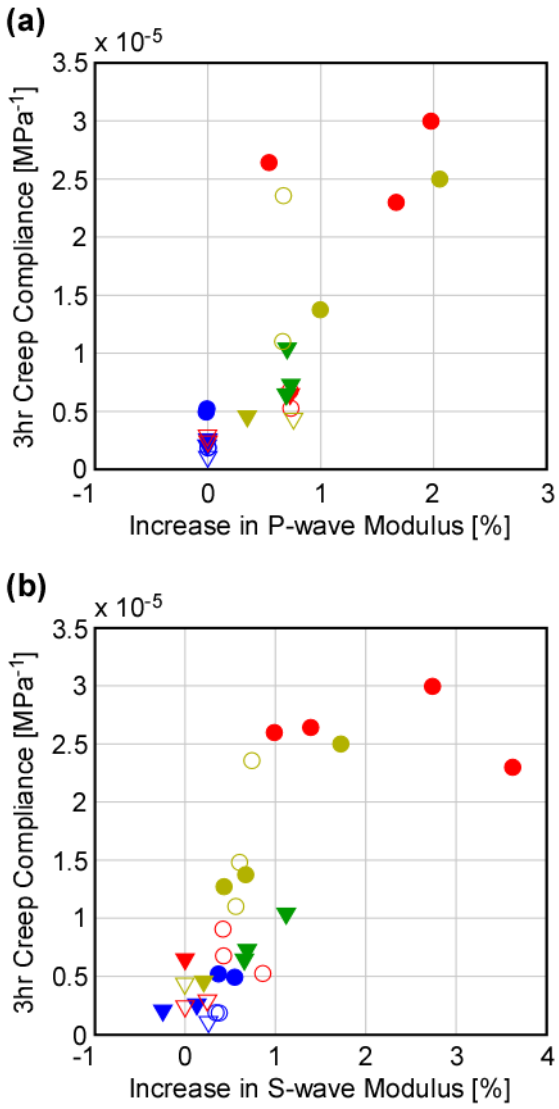

Figure 3.13: 3-hour creep compliance plotted against % increase in dynamic moduli. (a) Creep compliance vs. change in p-wave modulus. (b) Creep compliance vs. change in s-wave modulus.

2010; Yang and Zoback, 2011). Thus the key to understanding the overall creep behavior of these gas shale rocks seem to reside in how the clays and organics deform in these rocks.

If majority of the creep deformation takes place within the clays and organics, it is easily expected that the tendency for the bulk rock to creep depends on the amount of clays and organics in the sample. While such trend was confirmed by comparing samples within a single reservoir (Figure 3.5), a universal trend was not observed by

comparing all samples (Figure 3.8) suggesting that material composition is not the only control on creep. Eagle Ford-1 vertical samples particularly demonstrate this point well, as they have relatively low clay and organic content but have high creep compliance (Figure 3.8).

3.5.2 Effect of Sample Orientation (Anisotropy) on Creep Behavior

We also observed that sample orientation consistently affected the creep behavior where vertical samples crept much more compared to horizontal samples (Figure 3.5 and 3.8). To explain this observation, we refer to a simple model in which an anisotropic gas shale rock is represented by a composite of soft and stiff layers, where the soft layers represent the clay and kerogen contents, and stiff layers represent the QFP and carbonate contents (Figure 3.14a,b). For simplicity, we treat the layer properties to be mechanically isotropic and ignore shear tractions at the boundaries between bedding planes.

We first consider a case where this hypothetical shale is loaded by a far-field uniaxial stress, σ, perpendicular to the layers, which represents a vertical sample being tested in the lab (Figure 3.14a). This is a so-called *iso-stress* condition where the stresses carried by each layer are identical to the far-field stress:

$$\sigma_{soft} = \sigma_{stiff} = \sigma \tag{3.3}$$

where σ_{soft} and σ_{stiff} are the stresses carried by the soft and stiff layers, respectively. In this case the overall elastic stiffness of the rock is the Reuss (harmonic) average of the elastic stiffness of each layer. However when the loading direction is parallel to the layers (Figure 3.14b), an *iso-strain* condition, the stresses carried by each layer will be different from the far-field stress as follows:

$$\sigma_{soft} = \frac{C_{soft}}{C}\sigma, \quad \sigma_{stiff} = \frac{C_{stiff}}{C}\sigma, \qquad \therefore \sigma_{soft} < \sigma < \sigma_{stiff} \tag{3.4}$$

where C_{soft} and C_{stiff} are the stiffness of the soft and stiff layers, respectively, and C is the average stiffness of the whole rock which is equal to the Voigt (arithmetic) average of the stiffness of each layer. Thus, the stiff layers act somewhat like pillars in the rock structure. If creep predominantly occurs in the soft layer, and creep is proportional to the magnitude of stress, we expect that the shale would creep less in this setting representing a horizontal sample, consistent with laboratory results.

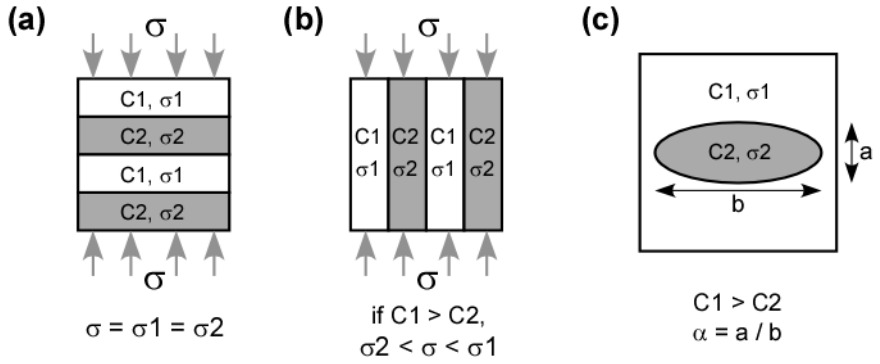

Figure 3.14: Schematics of shale models used in the stress partitioning analyses. (a) A layered shale model being loaded by a uniaxial far-filed stress perpendicular and parallel to the bedding, representing a vertical and horizontal sample in the lab, respectively. *C1* and *C2* are the stiffness of the stiff and soft components, respectively. (b) A shale model with soft ellipsoidal inclusion embedded in a stiff matrix. Aspect ratio α is defined as the ratio of the short axis, a, to the long axis, b.

We see from this simplified conceptual shale model that orientation, which is inherently related to anisotropy, affects the overall creep compliance of the rock because it determines how the far-field stress partitions within a sample. It is this stress partitioning that determines the stress acting on the soft components, and thus determines the magnitude of creep in the soft component, and ultimately the creep behavior of the whole rock. We also note that the average elastic moduli of the rock are also determined through these fundamental calculations of stress partitioning (and strain-partitioning). This evokes a close relation between the creep compliance and elastic moduli. In fact, at least from the layered shale model above, we see that the stiffer rock (horizontal sample) has lower creep compliance, consistent with laboratory observations.

However, the above scenarios only represent the most extreme case of anisotropy, when the elastic moduli lie on the Voigt and Reuss theoretical bounds (or more strictly, the bounds calculated by Backus average (Backus, 1962) if tractions between the boundaries are fully considered). In reality, the elastic moduli of the gas shale samples scatter widely between the two theoretical bounds as observed in Chapter 2 (Figure 3.15). This means that the condition in the shale samples is neither *iso-stress* nor *iso-strain*, but somewhere in between. Equations by Hill (1963) provide a simple and useful way of evaluating the stress/strain partitioning in these intermediate states, but the equations are one dimensional and do not address bulk anisotropic elastic properties. Therefore if we wish to generalize the above argument to rocks that lies between the *iso-stress* and *iso-strain* end members, a more involved treatment of anisotropy is required.

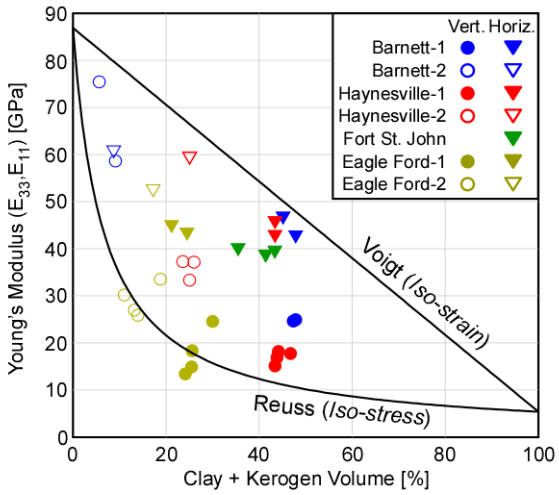

Figure 3.15: Static Young's modulus data compared against theoretical bounds by Voigt and Reuss averages.

Table 3.1: Elastic properties of the soft and stiff components used to calculate the Voigt and Reuss bounds in Figure 3.15, and also in the DEM modeling.

	K [GPa]	μ [GPa]	E [GPa]
"Stiff" component	51.0	35.7	86.9
"Soft" component	3.6	2.0	5.0

3.5.3 Stress Partitioning from Anisotropic DEM Shale Modeling

3.5.3.1 DEM Modeling Methods

In order to study the general relation between elastic properties and stresses carried by the soft/stiff components in the shale samples, we performed an anisotropic differential effective medium (DEM) modeling of the elastic properties for a rock consisting of aligned soft oblate ellipsoidal inclusions embedded in a stiff matrix (Figure 3.14c). Here we take the soft component to be the inclusion within the stiff matrix, since microstructural observations showed lenses of solid organics and clay domains embedded in a siliceous/calcareous matrix (Chapter 2, Figure 2.3). In the DEM modeling, we start with a rock composed entirely of the stiff component, and then add incremental amounts of soft inclusions as we keep track of the change in the elastic stiffness of the bulk rock. We used the same equations as those used in Bandyopadhyay (2009), where the change in elastic moduli with respect to the addition of incremental amounts of inclusions is modeled by:

$$dC^{DEM}(v_i) = \frac{dv_i}{1-v_i}\left(C^i - C^{DEM}(v_i)\right)Q_i \tag{3.5}$$

where v_i is the volume fraction of the inclusion, C^i is the stiffness tensor of the inclusion, C^{DEM} is the resulting stiffness tensor of the effective medium. Q_i is a fourth rank tensor that relates the inclusion strain tensor, ε_i, to the overall rock strain tensor, ε, by the following relation.

$$\varepsilon_i = Q_i \varepsilon \tag{3.6}$$

Q_i is a function of $C^{DEM}(v_i)$, C^i, and the aspect ratio of the inclusion, α, updated at each step of the modeling, calculated by considering the response of an unbounded matrix of the effective medium (Eshelby, 1957; Mura, 1982).

This approach is convenient for us since the modeling will not only output $C^{DEM}(v_i)$, but also the corresponding Q_i tensors, which can be used to relate the inclusion stress to the far-field stress by:

$$\sigma_i = C_i \varepsilon_i = C_i Q_i \left(C^{DEM}(v_i) \right)^{-1} \sigma \tag{3.7}$$

Also since the overall average strain is the volume weighted average of the inclusion strain and matrix strain,

$$\varepsilon = v_i \varepsilon_i + v_m \varepsilon_m = \left(v_i Q_i + v_m Q_m \right) \varepsilon \tag{3.8}$$

where v_m is the volume fraction of the matrix, we can also obtain the tensor, Q_m, which relates the matrix strain to the overall rock strain by:

$$Q_m = \frac{\left(I - v_i Q_i \right)}{v_m} \quad (I \text{ is a 4th-rank identity tensor}) \tag{3.9}$$

Now Q_m can be used to calculate the average stress in the stiff matrix. Note that the matrix stress calculated by using Q_m above is the average matrix stress, rather than the exact values within the matrix, since strain is constant inside the inclusion but not outside of it in Eshelby's (1957) solution. Nonetheless, it will provide a useful measure for the stress carried by the stiff matrix.

3.5.3.2 DEM Modeling: Verification of Results

Figure 3.16 shows the vertical and horizontal Young's moduli calculated from the DEM modeling for inclusion aspect ratios 10^{-4}, 0.325, and 1, overlain on laboratory data of the studied gas shales. The modeling was done by assuming isotropic mechanical properties for the soft and stiff components provided in Table 3.1, which were chosen based on values in Table 2.3 of Chapter 2, but the soft component properties scaled down to represent static behavior. Calculations were done for 0.1% inclusion volume increments, but results are shown for every 2% volume increments. As seen in Figure 3.16, DEM modeling can produce Young's modulus vs. soft component fraction curves that span the entire region enclosed by the Backus average of the soft and stiff component properties by taking α between 1e-4 ($\approx$0) and 1. When $\alpha \approx 0$, the calculated vertical and horizontal Young's moduli coincide with those predicted by the Backus average. As α increases, the rock becomes less anisotropic,

and the Young's moduli values depart away from the Backus average until they eventually collapse into one trend that represents an isotropic rock at α=1.

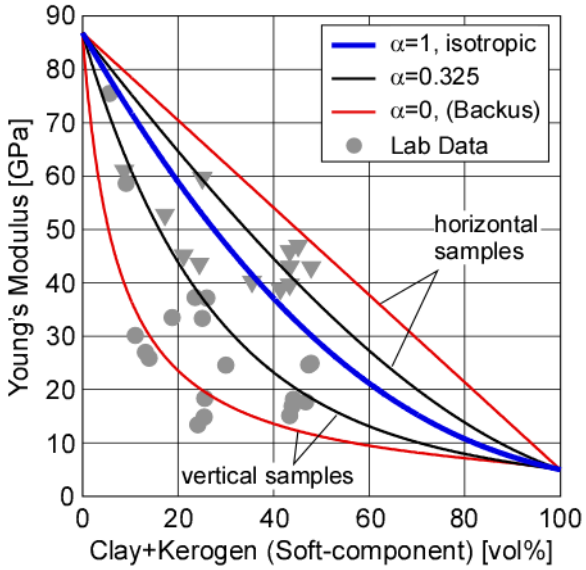

Figure 3.16: Examples of Young's modulus vs. soft-component volume curves modeled by DEM modeling. Model results are overlain on experimental data. Aspect ratios of the modeled curves are α = [1e-4, 0.325, 1].

Note that although the DEM results cover almost all of our experimental data, which roughly demonstrates the validity of the modeling, the approach is a strongly simplified treatment of the micromechanical causes of rock anisotropy. Rock anisotropy is not only affected by the aspect ratio of the constituents, but also the orientation distribution of the components (e.g. cracks, inclusion, fossils) and the intrinsic anisotropy of the constituents. However, as Bandyopadhyay (2009) showed through DEM modeling, these effects are practically indistinguishable when forward modeling the elastic properties of an anisotropic rock. Thus if we are eventually most interested in exploring how the stress partitioning behavior changes with anisotropy, it may not necessary require us to consider all mechanisms and understand their contributions. Here, aspect ratio is considered as a convenient proxy for anisotropy that allows us to explore the change in stress partitioning behaviors between the isotropic (α=1) and anisotropic (α=0) end members.

Other shortcomings of our modeling approach include the fact that the end member properties of the soft and stiff components are not necessary the same for all samples. The ratios of quartz to carbonate content vary between sample groups, as well as the ratio of clay to kerogen content. Also solid organics properties may not necessary be the same between each sample groups.

3.5.3.3 DEM Modeling: Stress Partitioning in the DEM Shale Model

After performing the DEM modeling for 12 different realizations of aspect ratios ranging from 1e-4 to 1, the stress carried by the soft and stiff components were computed using Equation 3.7 for every point in the moduli-composition space considered by the DEM modeling. A uniaxial far-field stress, σ, of magnitude 1 MPa was applied to the effective medium, and then the magnitude of differential stress in the inclusion and the matrix was evaluated by calculating the absolute value of σ_{11}-σ_{33} (Figure 3.17). Results show a stress partitioning behavior consistent with those suggested from the simple layered model in Figures 3.14a and 3.14b. Stresses carried by the soft and stiff components are both close to the far field stress of 1 MPa at the bottom end of the color-coded region (*iso-stress*). But they are much different from each other at the top end of the mapped region, indicating severe stress partitioning. The DEM modeling also provides us a continuous image of how the stress partitioning behavior changes between the upper and lower bound as the degree of anisotropy (α) and material composition changes.

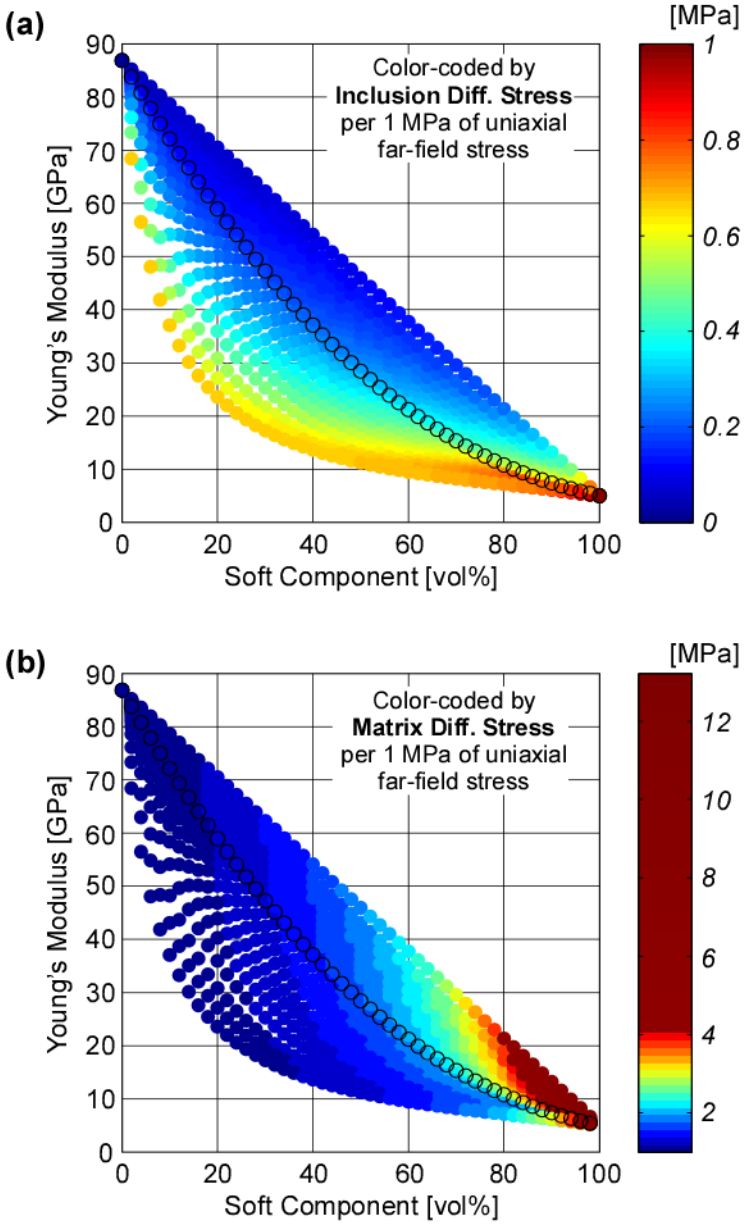

Figure 3.17: Modeling results of differential stresses carried by the soft-inclusion and stiff-matrix. (a) Young's modulus vs. soft-component volume curves modeled for various aspect ratios, color-coded by the differential stress in the soft inclusion resulting from a 1 MPa uniaxial far-field stress. (b) Young's modulus vs. soft-component volume curves, color-coded by the differential stress in the stiff matrix resulting from a 1 MPa uniaxial far-field stress. The black circles are the Young's modulus vs. soft-component volume curve calculated for aspect ratio α=1, thus no anisotropy.

3.5.4 3-hour Creep Compliance from the DEM Shale Model

Next, the overall rock creep compliance is estimated using the stress information obtained above. Honoring the definition of strain in Equation 3.8, we assume that the total 3 hour creep strain of the rock can be represented similarly by:

$$\varepsilon_{creep} = \sigma S_{creep} = v_{soft}\sigma_{soft} S_{soft} + v_{stiff}\sigma_{stiff} S_{stiff} \tag{3.10}$$

where S_{soft} and S_{stiff} is the creep compliance of the components. Then the overall creep compliance of the rock becomes:

$$S_{creep} = v_{soft}\frac{\sigma_{soft}}{\sigma} S_{soft} + v_{stiff}\frac{\sigma_{stiff}}{\sigma} S_{stiff} \tag{3.11}$$

Note that there is an important assumption made here that the stress remains the same during creep deformation. We believe this is a valid assumption, although not strictly true, because the creep strains are on the order of 1e-4 and thus small enough to preserve the elastic structure of the rock. The fact that the dynamic elastic moduli more or less stayed the same between pressure steps in the triaxial stage (Chapter 2 Figures 2.6 and 2.7) validates this assumption.

There exists no direct observation for the values of S_{soft} and S_{stiff}, but these can be inferred from the laboratory data. Since Young's modulus of some Eagle Ford-1 samples lie on the Reuss average of the end members (Figure 3.15), stress on the soft component in these samples are likely very close to the far-field stress (σ_{soft}/σ=1). Ignoring the creep contribution by the stiff component, and taking values from the Eagle Ford-1 sample with the highest creep compliance (Figure 3.9b):

$$S_{soft} \approx \frac{S_{creep}}{v_{soft}} \approx \frac{2.5*10^{-5}}{0.25} = 1*10^{-4}\ [MPa^{-1}] \tag{3.12}$$

Similarly for S_{stiff}, we refer to the Barnett-2 creep compliance data. Since the soft components likely do not carry much stress in Barnett-2 samples, we ignore its contribution to creep and reach an estimate of:

$$S_{stiff} \approx \frac{S_{creep}}{v_{stiff}} \approx \frac{0.1*10^{-5}}{0.9} \approx 1*10^{-6}\ [MPa^{-1}] \tag{3.13}$$

Although these are rough estimates of the individual creep compliances, the magnitudes are different by 2 orders of magnitudes which conform to the idea that majority of the creep occurs in the soft components.

The estimates of the creep compliance values calculated from Equations 3.11-3.13 are shown in Figure 3.18 for every point in the moduli-composition space considered by the DEM modeling. By observing the trend of the contours, we see that they are roughly horizontal. This is an important observation as it suggests that the creep compliance more or less correlates with Young's modulus, consistent with observations from Figure 3.9a.

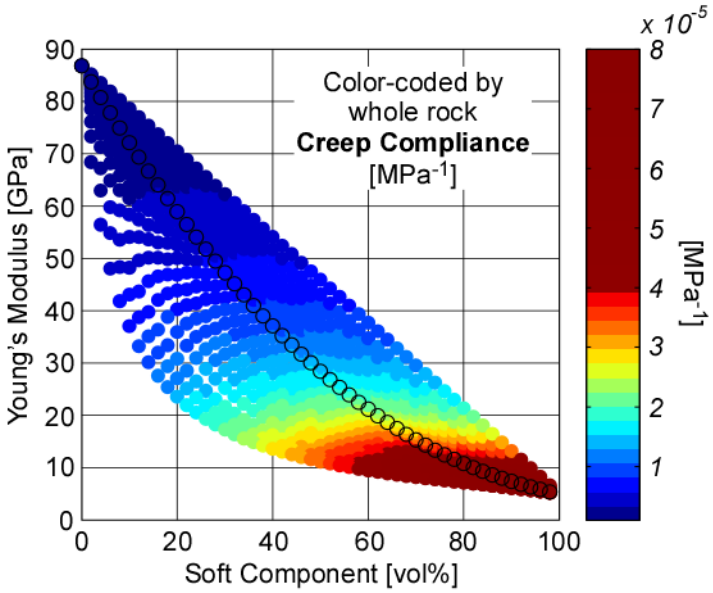

Figure 3.18: Young's modulus vs. soft-component volume curves, color-coded by the total 3-hour creep compliance. The black circles are the Young's modulus vs. soft-component volume curve calculated for aspect ratio α=1, thus no anisotropy.

Now we make comparisons between the laboratory data and the calculated results by plotting the S_{creep} vs. Young's modulus relation calculated for a fixed v_{soft} value of 10%, 30%, and 50% (Figure 3.19a). This is equivalent to keeping track of the Young's modulus and S_{creep} value while moving vertically in Figure 3.18. From Figure

3.19a, we see that the predicted relation captures the trend of the laboratory data remarkably well, validating our DEM model and creep compliance calculations.

We also recognize that the calculated trend roughly resembles an inverse proportionality, which would be the trend arising from the comparison between elastic compliance and elastic modulus. This similarity arises because we treated creep to be linear against stress and used creep compliance, which is treated much similarly to an elastic compliance. Thus we can say that it is, more deeply, the linear relationship between creep strain and applied stress observed in our experiments (Figure 3.5) that gave rise to the apparent unique trend between creep compliance and Young's modulus observed in our data.

We also compared the S_{creep} vs. v_{soft} trends calculated for a fixed aspect ratio of α=[1e-4, 0.325, 1] with the laboratory data in Figure 3.19b. All trends show that S_{creep} increases with increasing v_{soft}, but the values vary over a wide range. Therefore we understand from this comparison that, although creep does increases with total

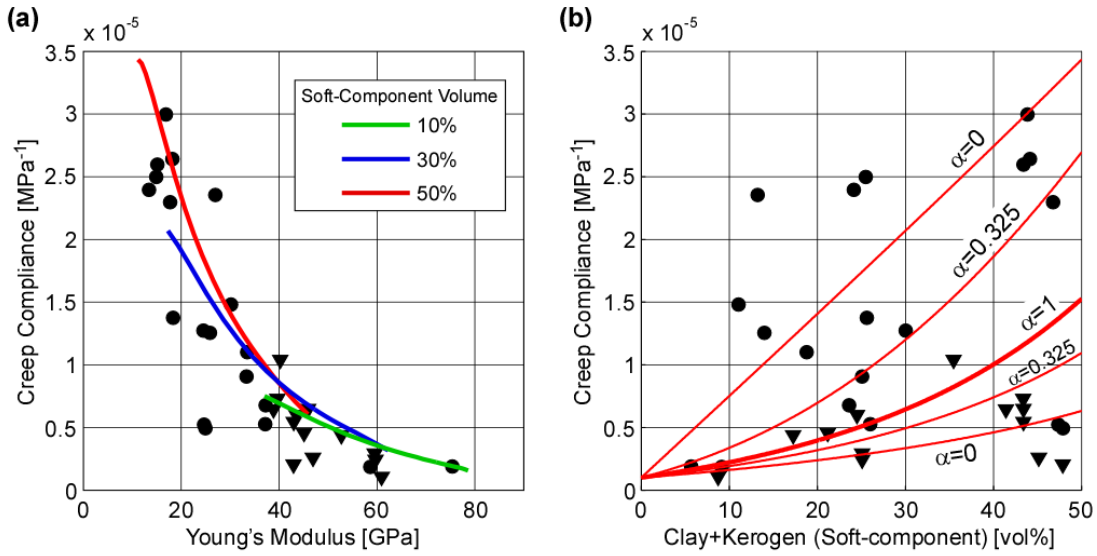

Figure 3.19: (a) Total creep compliance vs. Young's modulus trends calculated by DEM modeling for soft-component volumes 10%, 30%, 50%, overlain on laboratory data. (b) Total creep compliance vs. soft-component volume trends calculated by DEM modeling for aspect ratios, α = [1e-4, 0.325, 1], overlain on laboratory data.

clay/kerogen volume, the scatter in the inter-reservoir comparison (S_{creep} vs. ν_{soft}) in Figure 3.8 was caused by the variation in the degree of anisotropy of the rock.

3.5.5 Insights on Intact Strength Anisotropy from DEM Modeling

Despite the apparent success of the DEM modeling in predicting the creep behavior, it is quite difficult to apply the modeling results to discuss the relation between rock strength and elastic properties. The discussion from the previous section was possible since creep deformation was small enough to preserve the elastic structure of the rock, and thus the elastic calculation of stress partitioning was valid throughout the creep process. However, rock strengths are measured at the point of rock failure, and processes leading up to rock failure does not preserve the elastic structure of the rock. As observed from acoustic emissions, rocks first start to fail by hosting micro-scale failures at micro-cracks distributed all over the rock specimen (Lockner et al., 1992). Then as the number of micro-crack increases, they gradually coalesce into larger fractures which ultimately develop into a macroscopic failure plane. These micro-cracks are permanent damages to the elastic structure of the rock, and process of fracture coalescence is a highly non-linear process not captured by simple elastic models. Therefore it seems impossible at this point to argue why the apparent correlation between UCS and Young's modulus exist as in Figure 3.10b and observed elsewhere in the literature (Chang et al., 2006; Fjaer et al., 1992).

However, we speculate that the stress partitioning calculations by DEM modeling provide some insights into why horizontal samples are usually stronger than vertical samples as observed here and in many other data in the literature (Paterson and Wong, 2005). If we limit our discussion to rocks with identical compositions and fabric, we may expect that the fracture coalescence characteristics would be the same between vertical and horizontal samples. If so, we might expect that rock strength is affected by the timing of the onset of micro-fracturing. That is, the earlier the onset of micro-fracturing, the earlier the coalescence into a macro-fracture plane, thus weaker the eventual ultimate strength. If we further assume that it is the soft component in the rock that fails before the stiff components, we may expect that the stress carried by the

soft component controls the onset of micro-fracturing. This assumption may not be too unreasonable since clay-rich shales are generally found to be weaker than carbonates, and porosity reduces rock strength significantly (Paterson and Wong, 2005). Recall that clays and solid organics host most of the porosity in the studied gas shale rocks.

The DEM modeling from the previous section shows that the stress carried by the soft component is always larger when an anisotropic rock is loaded perpendicular to the bedding plane compared to when it is loaded parallel to the bedding. Therefore, under all assumptions made above, a vertical sample will lead to macroscopic failure earlier than a horizontal sample when loaded at similar strain rates. This would result in a weaker vertical strength compared to the horizontal strength for anisotropic rocks.

3.6 Conclusions

We have shown through laboratory experiments that deformational properties of the studied shale gas reservoir rocks, ductile creep and brittle strength, are a function of both material composition and sample anisotropy. Ductile creep deformation increases with increasing clay and organic content but is also strongly affected by the direction of loading with respect to the axis of symmetry. Brittle rock strengths were also found to be a function of the clay and organic content and intact rock strengths were also affected by the direction of loading. We also found an apparent correlation between elastic moduli and these deformational properties.

We showed through DEM modeling of the gas shale elastic properties that the contrast in elastic properties of the rock constituents (soft and stiff components) and their anisotropic fabric creates a highly heterogeneous stress distribution within the rock. We find that it is this stress heterogeneity that gives rise to the composition and anisotropy dependency of rock deformational properties. We further found that the apparent correlation between elastic moduli and ductility (creep properties) can be predicted from the DEM model by considering that majority of the creep deformation

takes place in the clay and organic contents and that magnitude of creep is linear against the applied stress.

However, the apparent relation between brittle strengths and elastic properties of the shale rock remains unanswered. We can speculate their relations by appealing to the internal stress heterogeneity predicted from the DEM model, but further detail observation of brittle rock deformation is required to fully explain their relation.

3.7 References

Backus, G. E., 1962, Long-wave elastic anisotropy produced by horizontal layering: Journal of Geophysical Research, **76**, 4427-4440.

Bandyopadhyay, K., 2009, Seismic anisotropy: geological causes and its implications to reservoir geophysics: Ph.D. thesis, Stanford University.

Chang, C., Moos, D., and Zoback, M. D., 1997, Anelasticity and dispersion in dry unconsolidated sand: International Journal of Rock Mechanics and Mining Sciences, **34**, Paper No. 048.

Chang, C., Zoback, M. D., and Khaksar, A., 2006, Empirical relations between rock strength and physical properties in sedimentary rocks: Journal of Petroleum Science and Engineering, **51**, 223-237.

Curtis, M. E., Ambrose, R. J., Sondergeld, C. H., and Rai, C. S., 2010, Structural characterization of gas shales on the micro- and nano-scales: CUSG/SPE Canadian Unconventional Resources & International Petroleum Conference, 137693.

Eshelby, J. D., 1957, The determination of the elastic field of an ellipsoidal inclusion and related problems: Proceedings of the Royal Society of London, Series A, **241**, 376-396.

Fjaer, E., Holt, R. M., Horsrud, P., Raaen, A. M., and Risnes, R., 1992, Petroleum related rock mechanics, Elsevier Science Publishers B.V.

Hagin, P. N., and Zoback, M. D., 2004, Viscous deformation of unconsolidated sands-Part 1: Time-dependent deformation, frequency dispersion, and attenuation: Geophysics, **69**, 731-741.

Hagin, P. N., and Zoback, M. D., 2010, Laboratory studies of the compressibility and permeability of low-rank coal samples from the Powder River Basin, Wyoming, USA: ARMA 44th US Rock Mechanics Symposium and 5th U.S.-Canada Rock Mechanics Symposium, Salt Lake City, UT, June 27-30, 10-170.

Hill, R., 1963, Elastic properties of reinforced solids: Some theoretical principles: Journal of the Mechanics and Physics of Solids, **11**, 357-372.

Lockner, D. A., Byerlee, J. D., Kuksenko, V., Ponomarev, A., and Sidorin, A., 1992, Observations on quasistatic fault growth from acoustic emissions, in Fault mechanics and transport properties of rocks. International Geophysics Series, Evans, B., and Wong, T., eds, Academic Press, London, 3-32.

Loucks, R. G., Reed, R. M., Ruppel, S. C., and Jarvie, D. M., 2009, Morphology, Genesis, and Distribution of Nanometer-Scale Pores in Siliceous Mudstones of the Mississippian Barnett Shale: Journal of Sedimentary Research, **79**, 848-861.

Mavko, G., Mukerji, T., and Dvorkin, J., 2009, The Rock Physics Handbook Second Edition, Cambridge University Press.

Moore, D. E., and Lockner, D. A., 2004, Crystallographic controls on the frictional behavior of dry and water-saturated sheet structure minerals: Journal of Geophysical Research, **109**, B03401, doi:10.1029/2003JB002582.

Mura, T., 1982, Micromechanics of Defects in Solid: Martinus Nijhoff Pub.

Paterson, M. S., and Wong, T., 2005, Experimental rock deformation – The brittle field, second edition, Springer-Verlag Berlin Heidelberg.

Rickman, R., Mullen, M., Petre, E., Grieser, B., and Kundert, D., 2008, A practical use of shale petrophysics for stimulation design optimization: All shale plays are not clones of the Barnett Shale: SPE Annual Technical Conference and Exhibition, Denver, Co, September 21-24, 115258.

Sondergeld, C. H., Ambrose, R. J., Rai, C. S., and Moncrieff, J., 2010, Micro-Structural Studies of Gas Shales: SPE Unconventional Gas Conference, 131771.

Tembe, S., Lockner, D. A., and Wong, T., 2010, Effect of clay content and mineralogy on frictional sliding behavior of simulated gouges: Binary and ternary mixtures of quartz, illite, and montmorillonite, Journal of Geophysical Research, **115**, B03416, doi:10.1029/2009JB006383.

Yang, Y., and Zoback, M. D., 2011, The effects of gas adsorption on swelling, visco-plastic creep and permeability of sub-bituminous coal, ARMA 45th US Rock Mechanics Symposium, San Francisco, CA, June 26-29, 11-433.

Zoback, M. D., 2007, Reservoir Geomechanics, Cambridge University Press.

3.8 Appendix

3.8.1 Appendix A: Data Acquisition Issues during the Hydrostatic Stage

When a pressure step is introduced during the hydrostatic stage, the pressure change causes a temperature change in the confining fluid (mineral oil) due to the near-adiabatic compression of the oil. Figure 3A.1a shows the temperature change inside the pressure vessel measured by a thermocouple, which shows about a degree of temperature increase for 10 MPa of pressure increase over 30 seconds. This temperature change fades away over about 30 minutes (Figure 3A.1b) as the heat conducts into the metal pressure vessel and eventually emitted outside of the system to room air. While this transient temperature change is occurring, the axial strain measured by LVDT transducers shows the elastic shrinkage of the sample in response to the pressure, then shows a slight creep behavior as pressure is held constant (Figure 3A.1a). However in the long term, the axial strain also shows an overall expansion of the rock over several hours. This long-term *negative creep* signal cannot be reflecting real rock deformation.

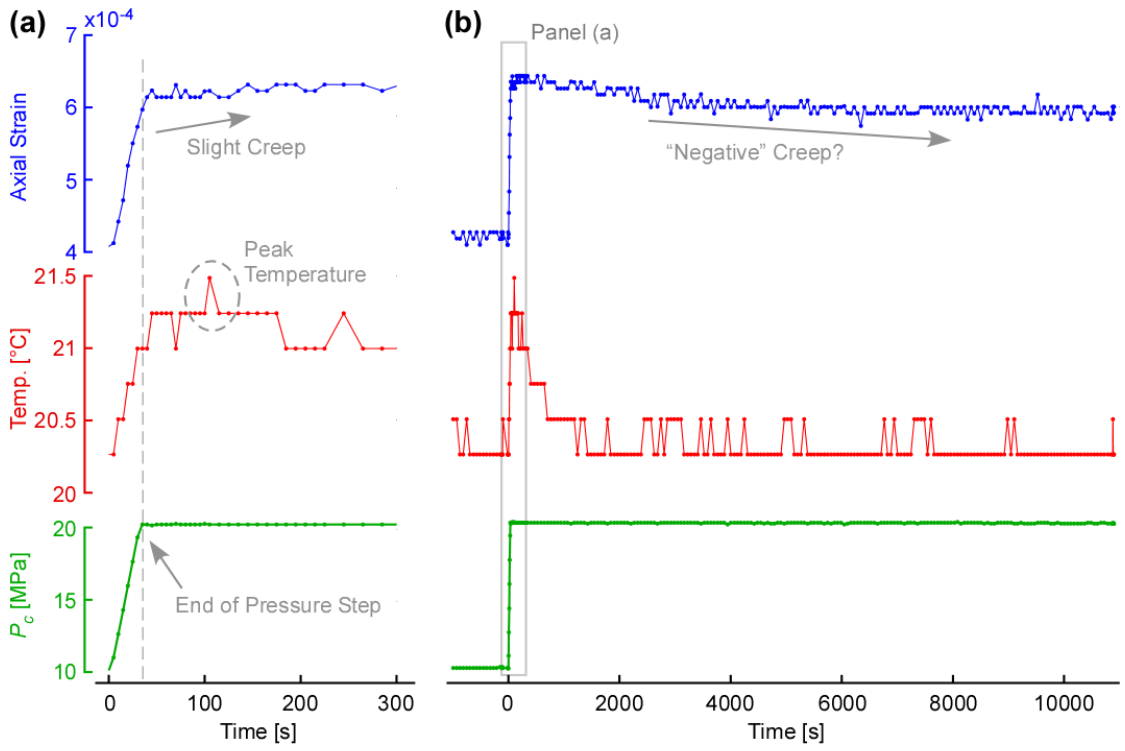

Figure 3A.1: Data from a pressure step during the hydrostatic state. (a) Axial strain, thermocouple temperature, and confining pressure during the pressure step and first 5 minutes thereafter. (b) Axial strain, thermocouple temperature, and confining pressure during the entire 3 hour after the pressure step.

Associated with the transient temperature change is a temperature related instrument response of the axial displacement reading by a LVDT transducers. This instrument response can come from two mechanisms; 1) change in resistance of the coils inside the LVDT transducer caused by the temperature change, and 2) thermal expansion/contraction of the sample, core-holder, steel-rod holding the LVDT core (Figure 3A.2). It requires an extensive investigation of the instrument characteristics to evaluated the contributions by each of the above factors, but we know from weeks-long experiments (discussed in Chapter 5) that there is a positive correlation between the LVDT reading and the intra-vessel temperature. Therefore we understand that the apparent long-term *negative creep* suggested by the LVDT reading is likely the instrument response of the LVDT measurement to the slow temperature decrease after the initial spike.

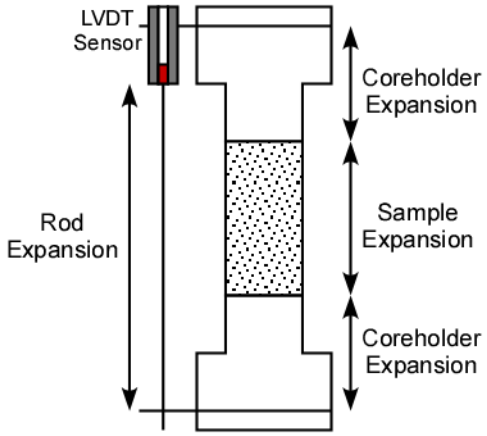

Figure 3A.2: Schematic showing the temperature related expansion/contraction signals that may be caught by the LVDT displacement transducer.

In theory, if we can calibrate the LVDT instrument response to temperature change, we can correct for this to isolate the signal only related to sample deformation. But this is not possible here with the 3-hour long experiments since the temperature inside the pressure vessel is not in an equilibrium condition and the thermocouple temperature reading does not necessarily reflect the actual temperature of the LVDT sensors, rock sample, and the core-holders. As seen from Figure 3A.1a, the thermocouple reading reaches its peak temperature a minute after the pressure step was completed. This suggests that there is a delay in the thermocouple reading with respect to the true temperature change in the confining fluid. Also, the time-scale at which the temperature-spike decays and the artificial *negative creep* take place is somewhat different. The *negative creep* is slower. This probably reflects the fact that it takes longer for the sample/core-holder/LVDT system to reach thermal equilibrium than the thermocouple. We do not have information to take these factors into account to perform a temperature correction of the axial strain measurement. However, note that temperature correction is done in Chapter 5 in the weeks long experiments. It is possible to do so in the long experiments because there weren't such drastic temperature changes during the experiments and the system was thermally quasi-static.

The rapid change in the confining pressure also affects the lateral strain measurements. Figure 3A.3 shows the lateral strain measured by the pair of spring-

mounted strain-gauge displacement transducers in the hydrostatic stage during an experiment using an aluminum alloy (Al7075) sample. Since the aluminum alloy does not creep, the time-dependent signatures shown, especially in the 2nd lateral strain reading, are artificial response not related to the sample deformation. We consistently saw that one lateral displacement transducer had more time-dependent signature than the other, which we can only understand it to be a gauge-specific instrument response. The measured lateral displacement also includes the deformation of the Viton jacket in response to the change in confining pressure. We do not know if the jacket deformation is time-dependent or not, but this jacket deformation will affect the measurement of elastic deformation during change in hydrostatic pressure. This is also difficult to correct for, since each time a Viton jacket is shrunk onto the sample, the thickness of the jacket may vary.

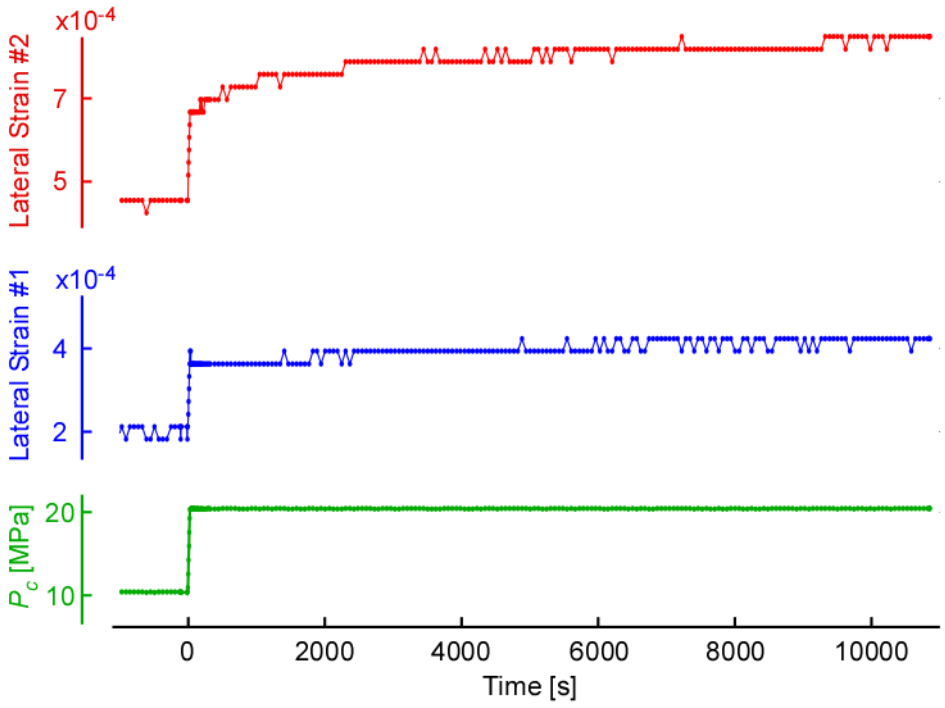

Figure 3A.3: Lateral strain responses measured by a spring-mounted strain-gauge displacement transducer during hydrostatic-stage in an experiment using an aluminum alloy sample (Al7075).

Chapter 4

IN-SITU STRESS VARIATIONS OBSERVED IN BARNETT SHALE, TX

Abstract

We observed the occurrences of wellbore failure in a vertical well from Barnett Shale to investigate the in-situ state of stress within the shale gas reservoir and found that stress state is highly variable within the reservoir. The occurrences of drilling-induced tensile fractures (DITFs) indicate that the reservoir is in the strike-slip faulting regime and the direction of the maximum horizontal stress is estimated to be N20E. We observed many inclined DITFs in the lower Barnett Shale (approximately 8000-8740 ft depth) which indicated that, on average, the vertical principal stress is tilted by about 5 degrees from vertical in the ESE direction in the lower Barnett Shale. We also observed that the inclination angle (ω) and the angular span (θ_t) of the inclined DITFs fluctuated dramatically within the lower Barnett Shale. Forward modeling of the inclination angle and the angular span of the inclined DITFs implies that: 1) the tilt angle of the vertical principal stress, ϕ_{tilt}, varies between 0-30 degrees in the lime wash section (approximately 8000-8350 ft depth) where the formation is highly interbedded,

2) the pore pressure is locally high within the basal hot shale section (approximately 8500-8740 ft depth). We also find that the frequent appearance and disappearance of the DITFs in the lower Barnett Shale roughly correlate with the lithological variation such that DITFs are more likely to be absent in the relatively clay- and organic-rich layers. We suggest that such correlation between lithology and DITF occurrence is caused by the relaxation of the horizontal stress anisotropy due to ductile deformation in the clay- and organic-rich layers.

4.1 Introduction

Economic natural gas production from unconventional shale gas reservoirs is achieved by the combination of horizontal drilling and reservoir stimulation by multi-stage slick-water fracturing. Ideally, every fracture treatment at every stage of the well is successful, but experiences from the Barnett Shale and other shale gas reservoirs have shown that not all stages are stimulated equally. The regions of stimulated reservoir volume, as seen by the clouds of micro-seismicity, can be fairly different between stages in size and shape, sometimes confined along a plane or sometimes dispersed widely in the reservoir (Figure 4.1; Waters et al., 2006; Maxwell, 2011). Operators also observe that fracturing pressure (fracture gradient) can vary between stages, sometimes to a point where pump pressures can not reach the fracturing pressure required to propagate a fracture (Daniels et al., 2007). These variations in the outcome of hydraulic fracturing are caused by the heterogeneity in the rock mechanical/deformation properties, presence of natural fractures, and/or the variations in in-situ stress within the reservoir.

Amongst the factors affecting the outcome of hydraulic fracturing operations, understanding the in-situ state of stress and its variation along a horizontal well is extremely important since it directly affects the planning of a shale gas stimulation program in several ways. First, the direction of the principal stresses determines the direction of the horizontal drilling since fractures propagate perpendicular to the minimum principal stress (Hubbert and Willis, 1957). Secondly, the magnitude of the

stress directly controls the fluid pressure needed to propagate a fracture (Zoback, 2007). Therefore understanding the magnitude of stress and its variation is crucial in deciding where to perforate and inject fluid in order to optimize production and also to identify where the fracture barrier is within the reservoir. Lastly, the anisotropy of the stress state (i.e. the relative magnitude of the principal stresses) could affect the mode of failure (i.e. single vs. network of fractures, opening vs. shearing) during stimulation, and ultimately how effectively a reservoir is stimulated by the fluid injection.

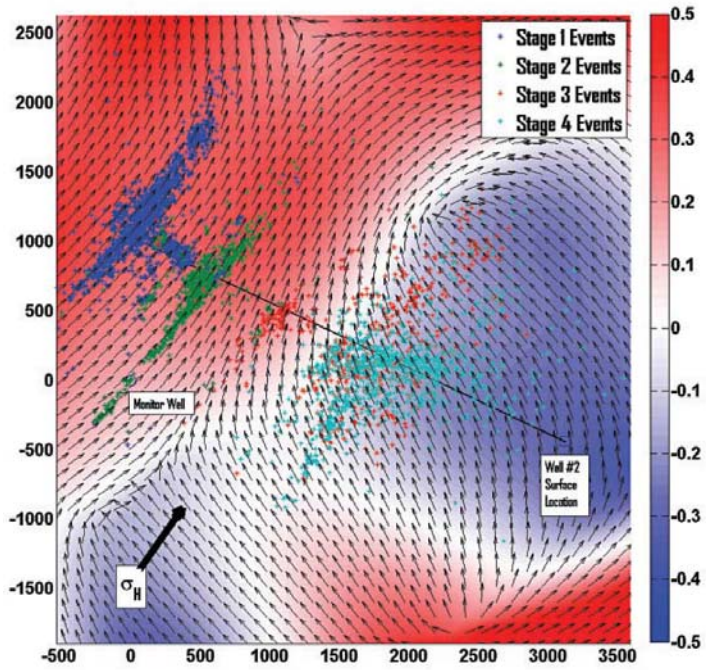

Figure 4.1: A map view of located microseismic events from a four-stage hydraulic fracturing in Barnett Shale overlain on relative probability of nature fracture presence calculated based on seismic attributes (color-scale), and predicted natural fracture orientations (arrows). Figure from Maxwell (2011), after Rich and Ammerman (2010).

In this chapter, we studied an FMI image log from a vertical well in Barnett Shale, TX, to obtain basic information on the in-situ state of stress from observations of wellbore failures. We also analyzed the variable occurrence of the wellbore failures by forward modeling to understand the in-situ stress variations within the reservoir. Finally interpretations are made in relation to the observed geology and laboratory data obtained in the previous chapters.

4.2 Geological Setting

4.2.1 Regional Geology

Barnett Shale is a major shale gas play located in central-eastern TX (Figure 4.2). This middle- to late- Mississippian organic-rich shale was identified to be the primary source rock for oil and gas produced from the Paleozoic reservoirs in the Bend Arch – Fort Worth Basin area, but it was also discovered to be productive since the early 2000's. The Fort Worth Basin in this region is bounded by the Ouachita Thrust Front to the east-southeast, the Muenster Arch to the northeast, the Bend Arch to the west, and Llano Uplift to the south. The basin itself also hosts numerous structural features as well including the Mineral Wells-Newark East fault system, thrust-fold structures, and minor horst/graben type structures related to the Mineral Wells-Newark East fault and the Ouachita structural front (Montgomery et al., 2005; Pollastro et al., 2007). Natural fractures associated with these structures are found from conventional cores and they are commonly filled with carbonate cement (Bowker, 2003).

In this region, the Fort Worth Basin deepens to the northeast as outlined by the top of the underlying Ellenburger group (Figure 4.2). Also following the deepening trend, the Barnett Shale also thickens to the northeast where the thickness varies from about 50-100 ft in the southwest, up to 1000 ft in the northeast by the Muenster Arch. Close to the deepest and thickest part of the Barnett Shale at the northeast margin is the Newark East Field area, where much of the production from the high-thermal maturity gas-producing Barnett Shale started in the early 2000's. Barnett Shale is generally bounded by the overlying Pennsylvanian Marble Falls Limestone and the underlying Ordovician Ellenburger group throughout the basin, but around the Newark East Field, the Forestburg limestone divides the Barnett Shale into its upper and lower layer, and the Viola limestone enters between the Barnet Shale and the Ellenburger

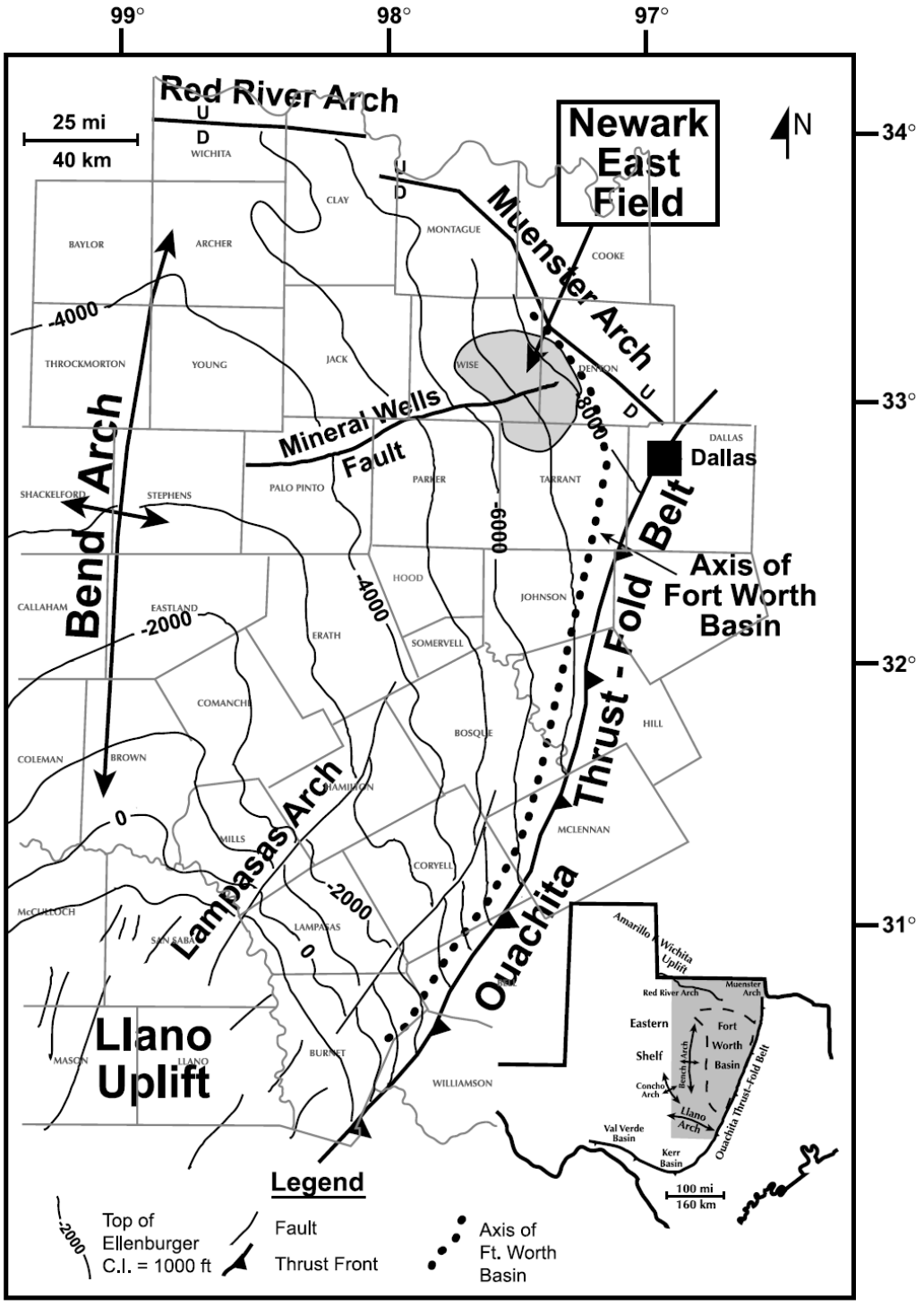

Figure 4.2: Map showing the extent of the Fort Worth Basin and major structural features. Figure from Montgomery et al. (2005). Contours represent the top of the Ellenburger Group.

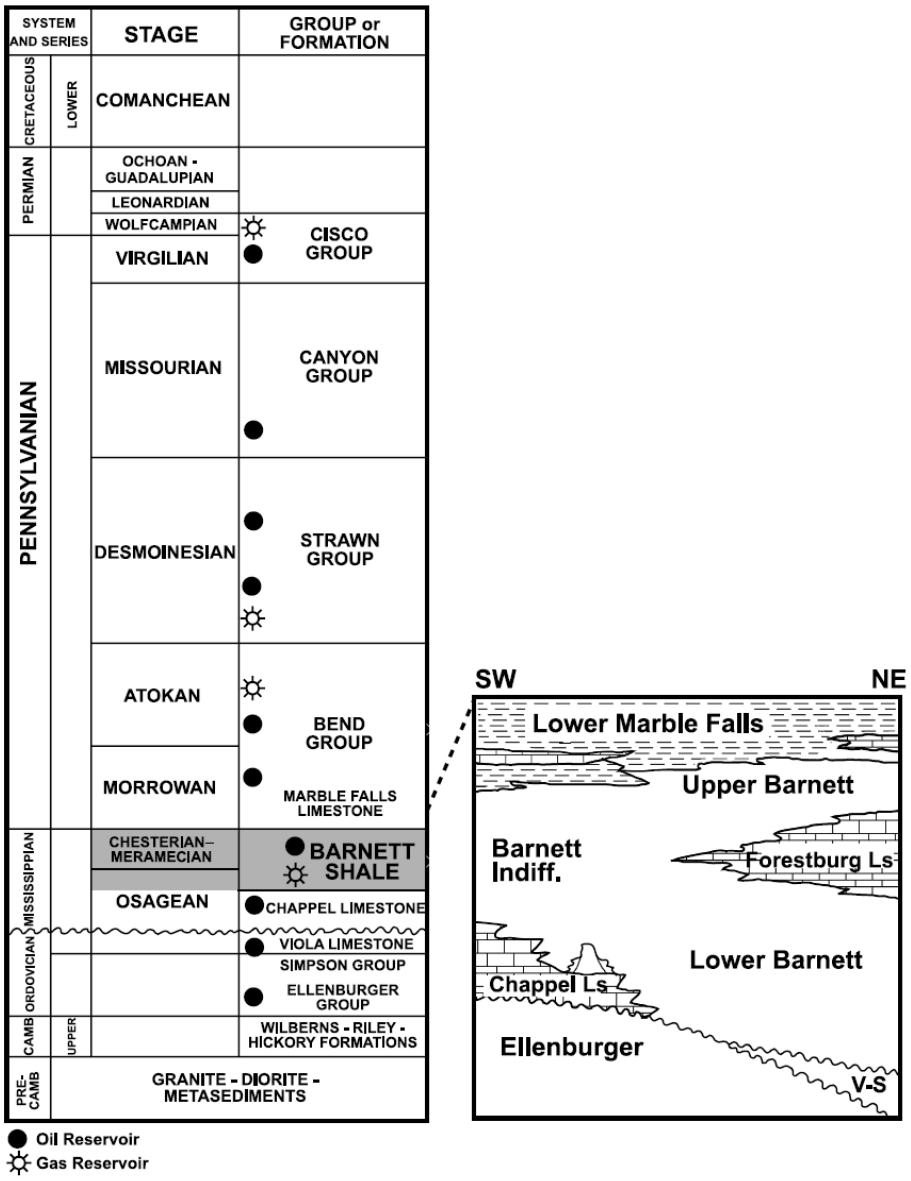

Figure 4.3: A generalized stratigraphic column of the Fort Worth Basin. Figure from Montgomery et al. (2005).

group (Figure 4.3). This Viola limestone is an important structure for hydraulic fracturing since it serves as a frac-barrier to the porous, water-bearing Ellenburger formation. It helps to prevent a hydraulic fracture from penetrating into the Ellenburger which leads to water production and well abandonment in the worst case scenario.

4.2.2 Geology of the Studied Well

Figure 4.4 shows the well log response from the vertical well we study in this Chapter, located close to the Newark East Field area, close to the Muenstar Arch. At this location, the Barnett Shale is over 1000 ft in thickness, divided by the Forestburg limestone, and overlies the Viola limestone consistent with the general stratigraphic column Figure 4.3.

We identify the upper Barnett Shale to be the quartz/clay rich unit that starts from about 7650 ft to 7840 ft depths. The lower extent of the underlying Forestburg limestone is unclear, but we believe that it extends down to about 8000 ft depth where the rapid inter-layering of high- and low-resistivity units starts to appear in the FMI image log. This would be consistent with the fact that the Forestburg thickness reaches over 200 ft near the Muenster Arch but thins rapidly to the south and west (Pollastro et al., 2007). Also the highly interbedded unit below the Forestburg likely represents part of the lower Barnett Shale that is referred as "lime wash" (Pollastro et al., 2007) found only near the Muenster Arch.

Thickness of the lime wash unit in this area is thought to reach as high as 500 ft, but it is difficult to identify the bottom limit from our data. Nonetheless, this lime wash unit is responsible for the highly heterogeneous nature within the lower Barnett Shale. The mineral compositions obtained through analysis of elemental capture spectroscopy show that the rocks in this interbedded unit range from almost completely carbonates (>90%), to QFM- (quartz, feldspar, mica) and clay- dominated shales with no carbonates. Core material analyses confirm these observations as well (See Chapter 2 Figure 2.1). Material analyses also show that TOC roughly correlates with clay content (Also see Chapter 2 Figure 2.1), thus TOC concurrently fluctuates with the lithology in the lime wash unit, ranging between 0-5 % by weight.

We also see the presence of a high gamma-ray layer at the base of the lower Barnett. This is referred as the "basal hot shale", which can be tracked throughout most of the Fort Worth Basin (Pollastro et al., 2007). The high gamma values are

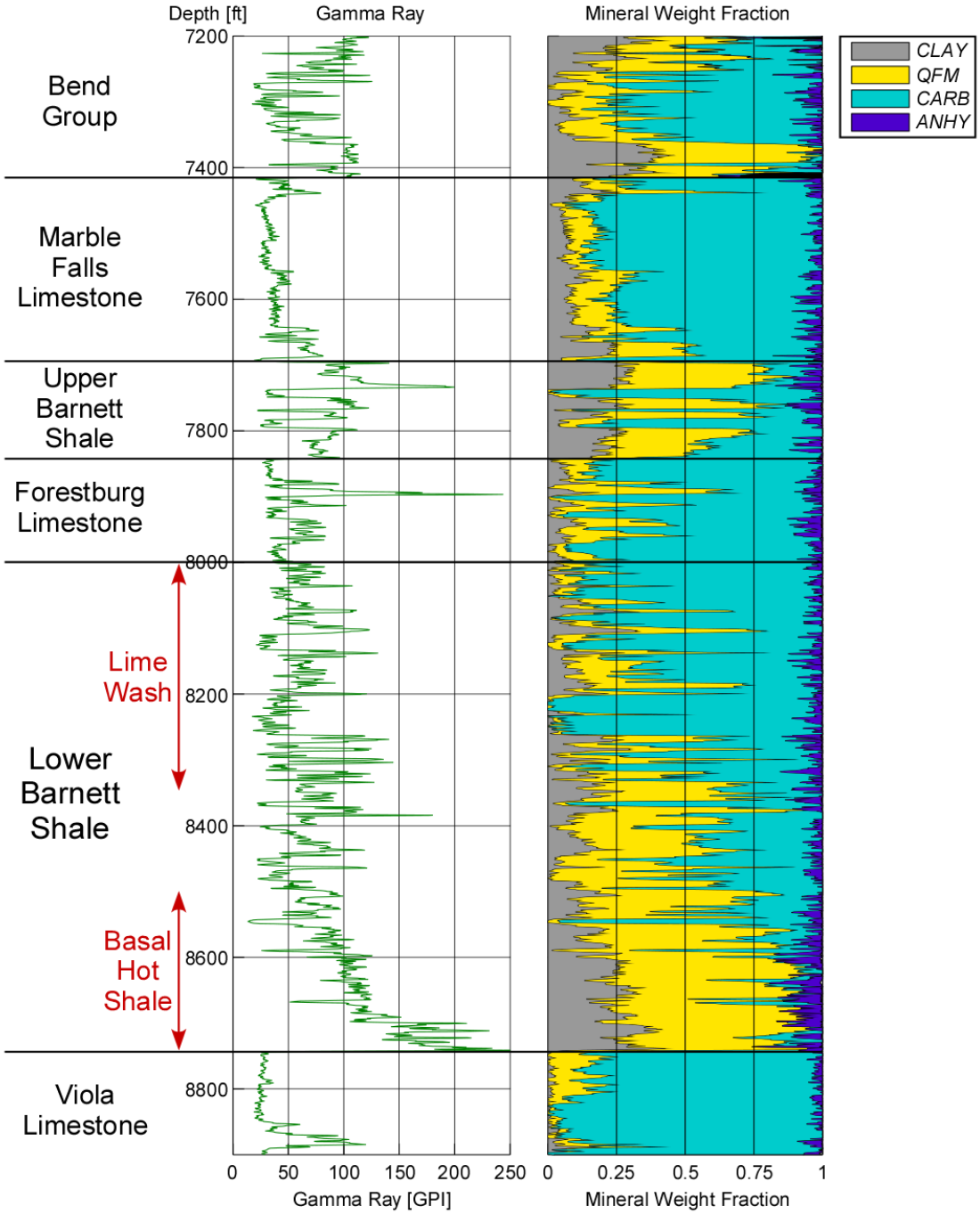

Figure 4.4: Petrophysical log data from the studied vertical well close to the Newark East Field. Lithological boundaries are approximate.

attributed to the abundance of organic- and phosphate-rich shale zones that are inter-bedded with laminated siliceous mudstone (Tian, 2010). The locally high shale content, specifically the presence of glauconite, is also suggested from the high-gamma, high-potassium, low-thorium responses in this unit which indicate slow and quiet deposition under reducing conditions (Mapel et al., 1979; Pollastro et al., 2007; Tian, 2010).

4.3 Wellbore Failures and In-situ Stress

FMI image logs provide a continuous unwrapped image of the borehole wall in terms of the formation electrical resistivity. Observations of these images not only provide information about the distribution of natural fractures, but also the distribution of wellbore failures, such as breakouts and drilling-induced tensile fractures (abbreviated as DITF from hereon). After the passage of the drilling bit, the in-situ tectonic stress will no longer be supported by the drilling bit and the wellbore wall becomes a free surface exposed only to the drilling mud weight. This perturbs the stress field around the wellbore, and wellbore failures will occur if the perturbed stress field around the wellbore meets the failure criterion of the rock. Thus the presence and location of wellbore failures provide information about the orientation and magnitude of the in-situ principal stresses given sufficient knowledge of the formation strengths.

The circumferential stress around a vertical wellbore whose axis is aligned with the vertical stress is given by elastic solutions extending from Kirsch (1898) as follows:

$$\sigma_{\theta\theta} = S_{h\min} + S_{H\max} - 2\left(S_{H\max} - S_{h\min}\right)\cos 2\theta - P_m - P_p - \sigma^{\Delta T} \tag{4.1}$$

In Equation 4.1, S_{Hmax} and S_{hmin} are the magnitudes of the far-field maximum and minimum horizontal stresses, θ is the circumferential position relative to the azimuth of S_{Hmax}, $\sigma_{\theta\theta}$ is the effective circumferential stress, P_m is the pressure exerted on the wellbore wall by the drilling mud (mud weight) , P_p is the pore pressure, and $\sigma^{\Delta T}$ is the

thermal stress induced by the difference in mud and formation temperature. The solutions at $\theta = 0$ and $\theta = 90$ degrees give the minimum and maximum circumferential stress magnitudes as follows:

$$\sigma_{\theta\theta}^{\min} = 3S_{h\min} - S_{H\max} - P_m - P_p - \sigma^{\Delta T} \tag{4.2}$$

$$\sigma_{\theta\theta}^{\max} = 3S_{H\max} - S_{h\min} - P_m - P_p - \sigma^{\Delta T} \tag{4.3}$$

If $\sigma_{\theta\theta}$ from Equation 4.3 exceeds the compressive strength of the rock, the borehole wall will collapse to form a breakout. If $\sigma_{\theta\theta}$ from Equation 4.2 becomes negative, the tensional stress pulls apart the borehole wall to form a vertical DITF, assuming the tensile strength of a rock is essentially zero (Figure 4.5a). Therefore, the position of breakouts and DITFs carry information about the direction of the far-field horizontal stresses, and their presence or absence provide information on the upper or lower bounds for the magnitudes of the far-field horizontal stresses.

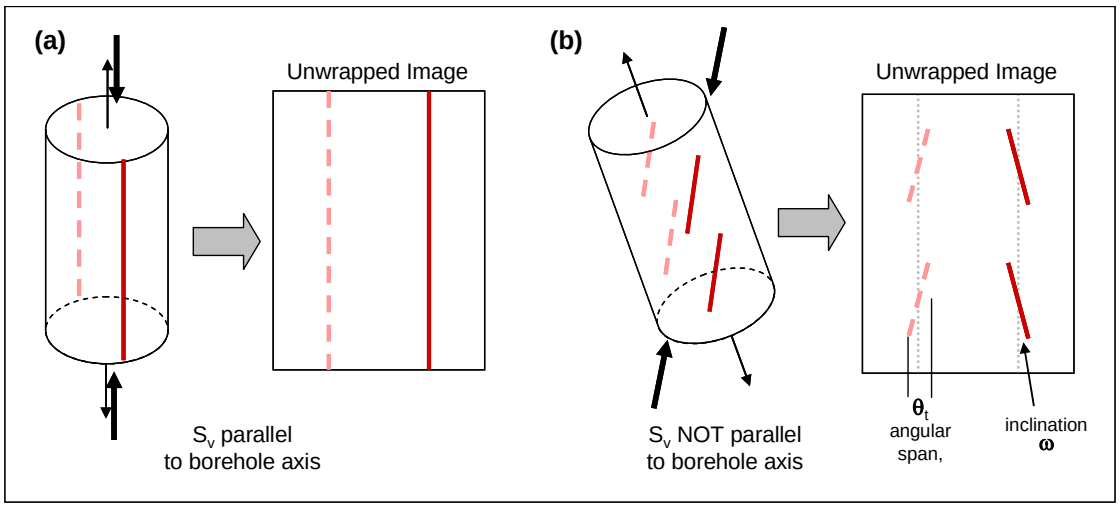

Figure 4.5: Schematics of appearance of drilling-induced tensile fractures in an image log. (a) Borehole axis is aligned with a principal stress. (b) Borehole axis not aligned with principal stress.

However when the borehole axis is not aligned with one of the principal stress axes, the direction of maximum tension becomes oblique relative to the borehole axis, resulting in an inclined DITF (Figure 4.5b). In this case, after transforming the principal stresses (i.e. S_1, S_2, S_3) into the borehole Cartesian coordinates (i.e. S_{ij}) (See

Peska and Zoback (1995) for detail explanations of the coordinate transformation), and adding the effect of P_p to obtain effective stresses (i.e. S_{ij} to σ_{ij}), the perturbed stress field around a misaligned borehole at the borehole wall is given by (Hiramatsu and Oka, 1962):

$$\sigma_{zz} = \sigma_{33} - 2\nu(\sigma_{11} - \sigma_{22})\cos 2\theta - 4\nu\sigma_{12}\sin 2\theta \tag{4.4}$$

$$\sigma_{\theta\theta} = \sigma_{11} + \sigma_{22} - 2(\sigma_{11} - \sigma_{22})\cos 2\theta - 4\sigma_{12}\sin 2\theta - P_m + P_p \tag{4.5}$$

$$\tau_{\theta z} = 2(\sigma_{23}\cos\theta - \sigma_{13}\sin\theta) \tag{4.6}$$

where the stress components in the borehole cylindrical coordinate system (L.H.S.) are expressed by the stress components in a borehole Cartesian coordinate system (R.H.S.), θ is the angle around the borehole wall in the cylindrical coordinate system, and ν is the static Poisson's ratio of the medium. Then by looking at the principal stresses at the borehole wall, the magnitude and orientation of the tangential stress becomes (Peska and Zoback, 1995):

$$\sigma_{t\max}(\theta) = \frac{1}{2}\left(\sigma_{zz} + \sigma_{\theta\theta} + \sqrt{(\sigma_{zz} - \sigma_{\theta\theta})^2 + 4\tau_{\theta z}^2}\right) \tag{4.7}$$

$$\sigma_{t\min}(\theta) = \frac{1}{2}\left(\sigma_{zz} + \sigma_{\theta\theta} - \sqrt{(\sigma_{zz} - \sigma_{\theta\theta})^2 + 4\tau_{\theta z}^2}\right) \tag{4.8}$$

$$\omega(\theta) = \frac{1}{2}\arctan\left(\frac{2\tau_{\theta z}}{\sigma_{zz} - \sigma_{\theta\theta}}\right) \tag{4.9}$$

The value ω is the inclination of the maximum tangential principal stress from the borehole axis, therefore determines the inclination of the DITF relative to the borehole axis (Figure 4.5b). The angular span of the inclined DITF around the wellbore circumference, θ_t, is predicted from Equation 4.8 by observing the range of θ angle that gives a negative σ_{tmin} value (Figure 4.5b).

4.4 Observed Wellbore Failures

In order to observe the in-situ state of stress within and around the Barnett Shale reservoir, we analyzed a FMI image log from a vertical well spanning from 6750-8950 ft depths. From the image log, we find that there are no breakouts, but only DITFs were present along the wellbore wall. Also some natural fractures were found. Figure 4.6 shows some examples of DITFs found in the image log.

Figure 4.6a is a DITF found in the Forestburg limestone. The alignment of the DITF with the borehole axis indicates that the wellbore axis is parallel with the vertical principal stress direction.

In Figures 4.6b and 4.6c, some examples of DITFs from the lime wash and basal hot shale section from the lower Barnett Shale are shown. In contrast to Figure 4.6a, the DITFs are not aligned with the borehole axis, but are rather inclined, forming an en-echelon pattern. These inclined DITFs indicate that the wellbore axis is not aligned with one of the principal stresses. In Figure 4.6c, we also see examples of natural fractures observed in the image log. The natural fractures appear relatively faint compared to the inclined DITF since they are not open fractures like the DITFs. These natural fractures are healed fractures likely filled with calcites as observed in core materials recovered from the Barnett Shale (Bowker, 2003; Gale et al., 2007). The material inside the fracture has less resistivity contrast with the host rock compared to an open fracture which makes them appear faint.

Finally in Figure 4.6d is an example image from the Viola limestone below the lower Barnett Shale. In the Viola limestone, we also see some inclined DITFs but less compared to the overlying Barnett Shale formation. They also seemed to co-exist with normal vertical DITFs.

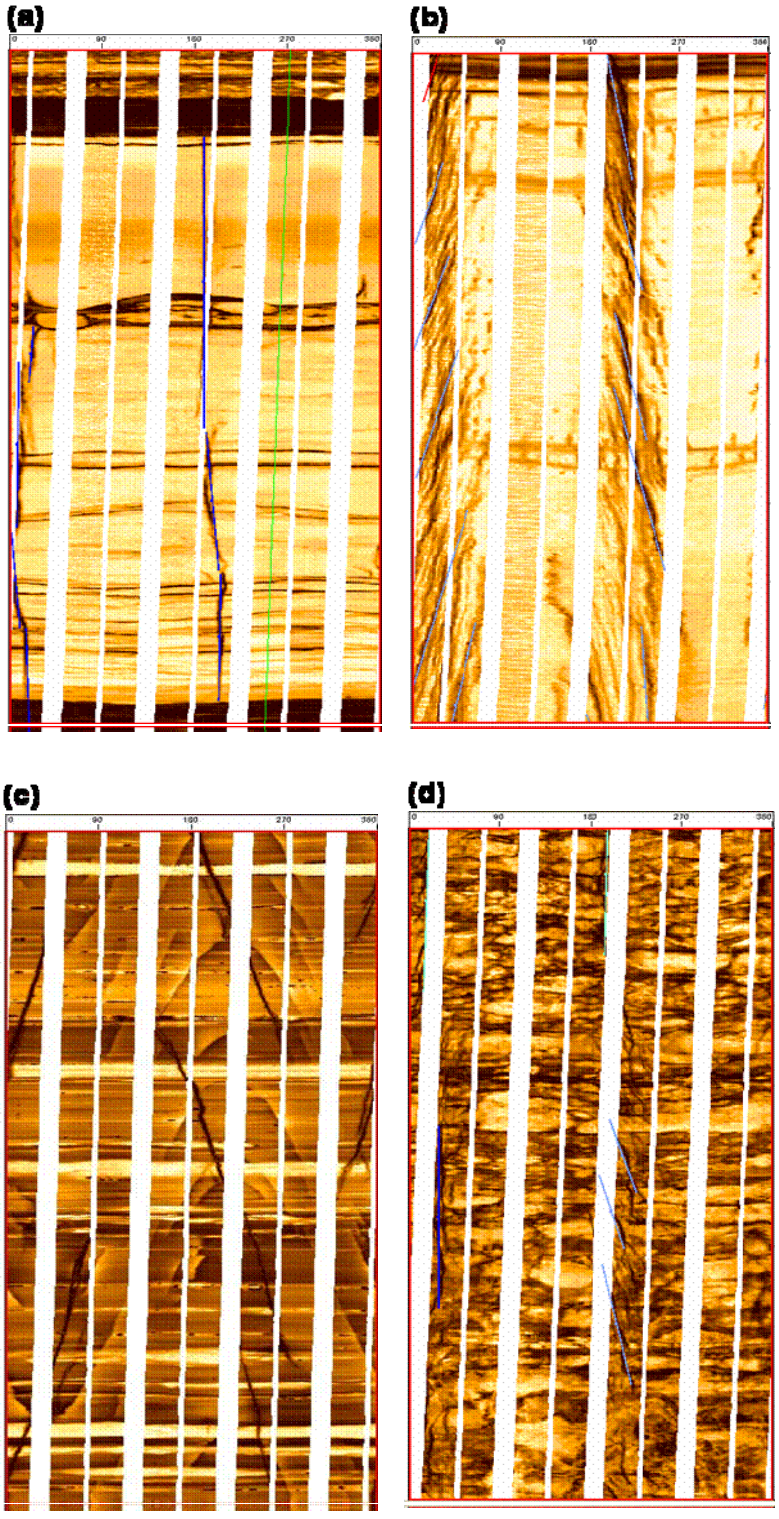

Figure 4.6: Examples of DITFs observed in the image log. All examples show approximately 8.5 ft of image along the vertical well.

4.4.1 Direction of S_{Hmax} and Natural Fractures

Figure 4.7 summarizes the azimuth at which the DITFs are observed and the strike of the natural fractures. Except for the Marble Falls limestone, DITF is observed throughout the image log and its azimuth appears to be consistent. From the Rose diagram plot (Figure 4.7b), we see that the azimuths of DITFs are scattered around N20E and N200E, indicating that the direction of S_{Hmax} is in the NNE/SSW direction. This S_{Hmax} direction is roughly consistent, but slightly northerly, with those found from other studies in the Barnett Shale (Gale et al., 2007; Vermylen, 2011) and also inferred from the World Stress Map data in northeast Texas (Heidebach, 2008), which all show NE/SW to ENE/WSW directions.

Most of the natural fractures were found from the basal hot shale section and the upper Barnett Shale. These fractures had strikes and dips focused around N50W and 80-85 degrees, respectively (plane dips to the right when looking in the direction of strike). Natural fractures were also found in the Forestburg limestone and in the Bend group formation, but their orientation were not as consistent as in the basal hot shale fractures (Figures 4.7b, c). These observations agree fairly well with natural fractures observed in cores reported by Gale et al. (2007). From 2 wells in the Newark East Field they studied, they observed that fractures in the shale section all strike in the WNW/ESE direction and were steeply dipping, whereas in the Forestburg limestone, at least 2 fracture sets of different orientations were identified.

4.4.2 Inclination and Angular Span of the Drilling-Induced Tensile Fractures

Along with the depths and azimuths of the DITFs, their inclination (ω) and angular span (θ_t) around the borehole circumference was recorded. Analyzing how these parameters vary with depth allows us to examine where anomalous stress states are occurring.

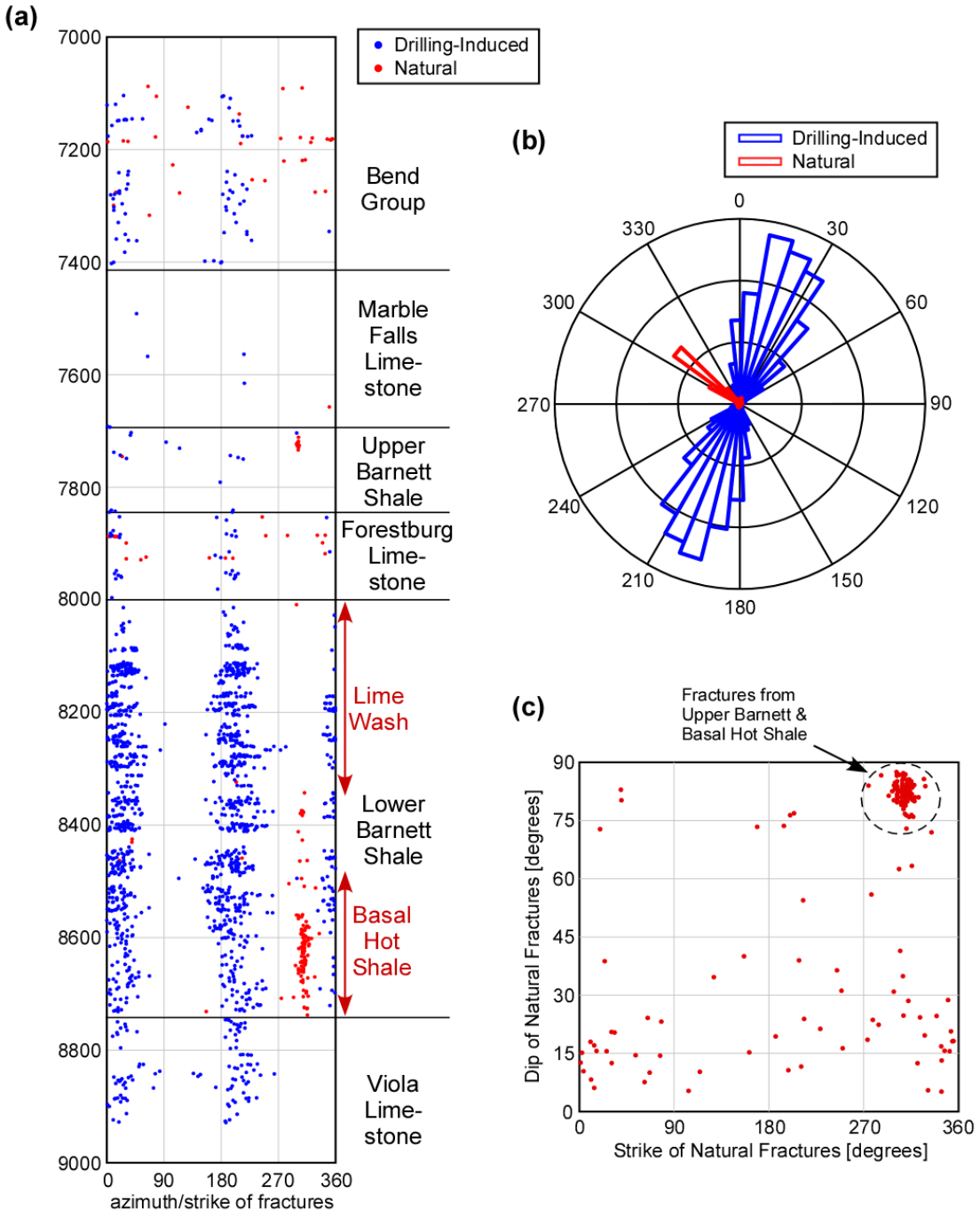

Figure 4.7: (a) Azimuth of DITFs and strike of natural fractures against depth. (b) Rose diagram of DITF azimuth and strike of natural fractures. (c) Strike vs. dip of natural fractures.

Figure 4.8a shows the inclination, ω, of the DITFs plotted against depth. ω is usually described to vary between 0-180 degrees (Zoback, 2007), but here we assign numbers between -90 to 90 degrees. ω takes positive and negative values since DITFs located 180 degrees apart from each other will tilt in the opposite direction (Figure 4.5). We observe that ω is mostly less than 5 degrees, representing a vertical DITF, down to the Forestburg limestone, but becomes high within the lower Barnett Shale. After a peak value above 40 degrees is observed at around 8250 ft, ω stays at around 10-20 degrees throughout the shale layer, and then decreases as the borehole exit the Barnett Shale and enters the Viola limestone. We also see that the scatter of data is greater in the lime wash section where the lithology is more heterogeneous, but the ω values are much consistent in the basal hot shale section.

The θ_t versus depth trend in Figure 4.8b also shows some anomalous occurrence of the DITFs in the shale layer. θ_t is mostly confined within 20 degrees until the well enters the lower Barnett Shale layer, then the angular span continues to increase until it reaches a maximum above 150 degrees at the basal hot shale section. θ_t then decreases back to a lower value as the wellbore enters the Viola limestone. Similar to the ω values, θ_t scatters greatly in the lime wash section, but the trend of θ_t is more confined in the basal hot shale section.

These observations indicate that the vertical principal stress is rotated within the lower Barnett Shale. As shown in Figure 4.8c, the deviation of the borehole axis from vertical was smaller than few degrees, which is normally regarded to have indistinguishable effect on the inclination of DITFs (Zoback, 2007). Even if such small deviation were to affect the inclination of the DITFs, we see no correlation between the deviation and DITF inclination. Moreover, the borehole deviation direction, N200E, is parallel to the azimuth of the DITF which means that the borehole deviation is parallel to the S_{Hmax} direction. Such NNE/SSW trending deviation could not have caused the observed WNW/ESE trending inclination of the DITFs. Therefore, the change in DITF inclination can only be explained by the local tilt in the vertical

principal stress. Note that we will continue to call this principal stress the "vertical" stress although its orientation is actually tilted from vertical direction.

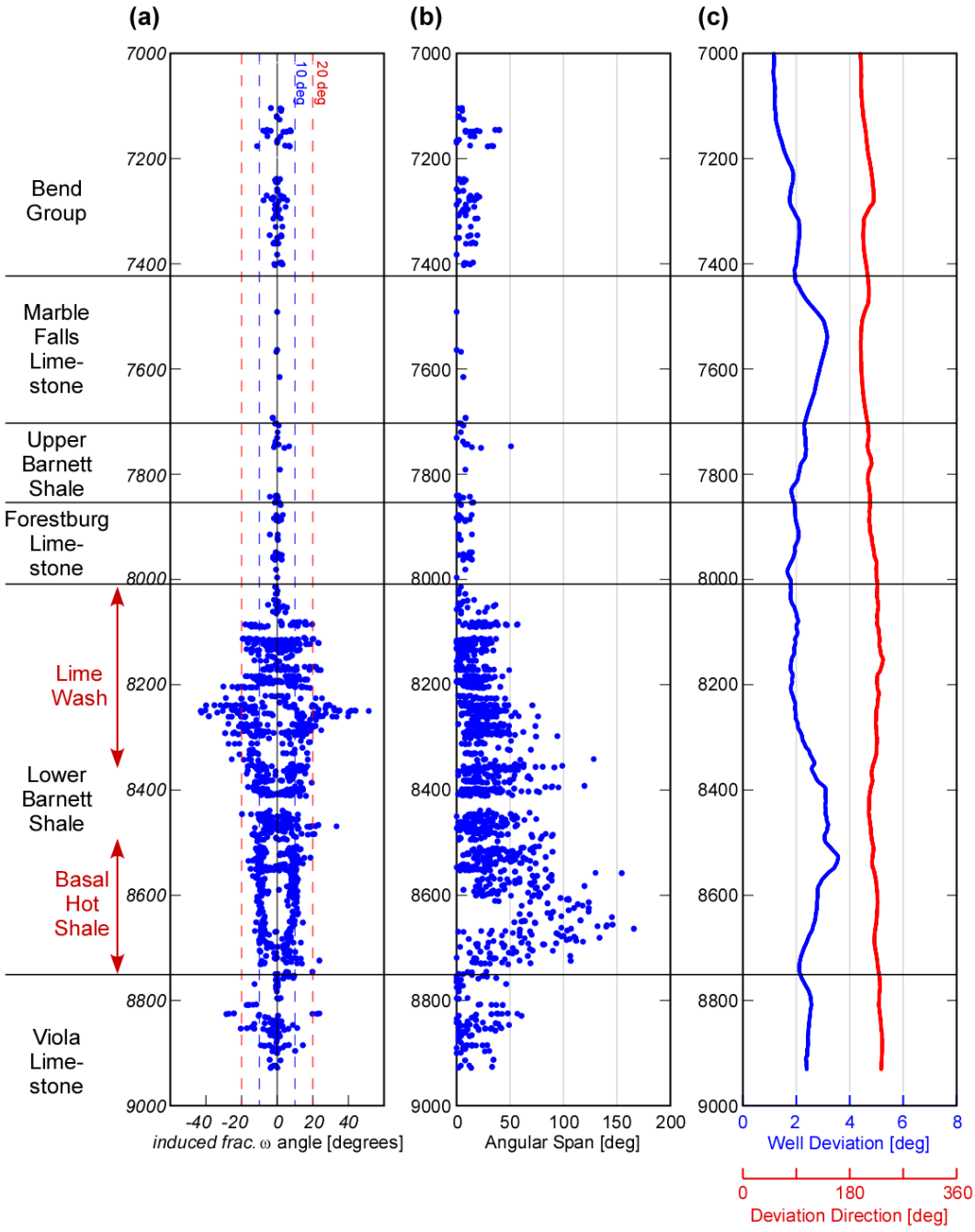

Figure 4.8: (a) Distribution of DITF inclination angle with respect to depth. (b) Distribution of DITF anglular span with respect to depth. (c) Well deviation and deviation direction.

4.4.3 Frequent Disappearance and Re-appearance of DITFs

In addition to how the inclination and angular span DITFs fluctuated within the lower Barnett Shale, we also observed a frequent disappearance and re-appearance of DITFs along the well. Figure 4.9 shows an example of such observation. Here DITFs are observed to disappear as the well enters a high-gamma ray section, but re-appear as the well re-enters a lower-gamma ray section. Although such features were not always observed at high-gamma ray sections, it was observed at many places within the lower Barnett Shale. High-gamma ray either represents high-clay content or high organic content, but since those two generally correlate (Chapter 2 Figure 2.1a), we understand that such feature occurred more in the clay- and organic-rich section.

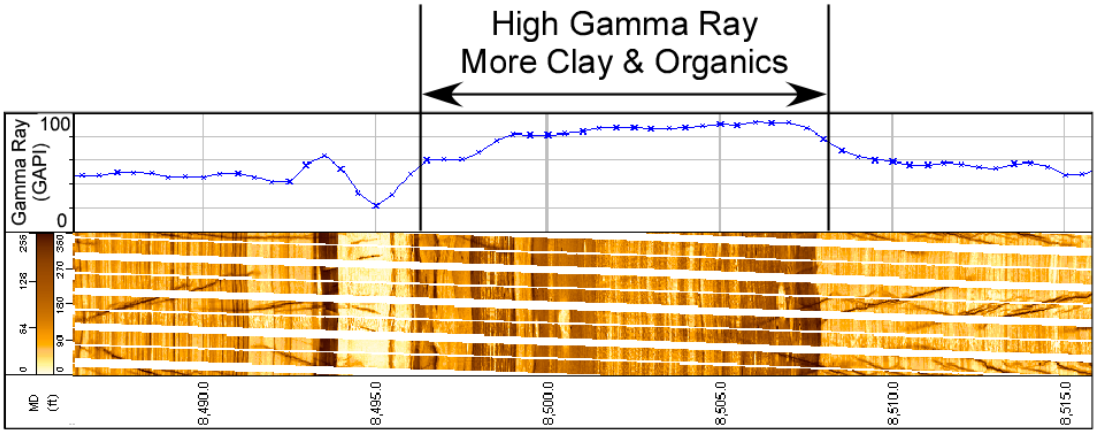

Figure 4.9: Example of a section within the lower Barnett Shale where DITF was observed to disappear in the high-gamma ray, clay- and organic-rich section. DITF reappeared in the lower-gamma ray section right below.

4.4.4 Summary of Observations

1. No breakouts were observed but DITFs were observed throughout the image.
2. DITFs were mostly vertical outside of the lower Barnett Shale, but inclined in the lower Barnett Shale
3. At depths between 8000-8350, roughly corresponding to the lime wash section, inclination and angular span of the DITFs scattered between 0-40 degrees and 0-100 degrees, respectively.

4. At depths between 8500-8740, roughly corresponding to the basal hot shale section, inclination and angular span of the DITFs was scattered between 5-10 degrees and 0-150 degrees, respectively, but showed much confined depth dependent trends compared to the lime wash section.
5. These inclined DITFs suggest that the vertical stress is tilted locally in the lower Barnett Shale.
6. Natural fractures mostly appeared in the basal hot shale and the upper Barnett Shale. The strike and dip of the fractures were consistent at N50W and 80-85 degrees.
7. DITF was observed to disappear in high-gamma ray section but re-appear in low-gamma ray sections many parts of the lower Barnett Shale.

4.5 Constraining the Far-field Stress

Before discussing the formation scale characteristics of the observed DITF patterns, we first constrain the far-field stress acting on the region. Generally, the vertical stress magnitude, S_v, is accurately determined by integrating the density log against depth. Also, the minimum horizontal stress magnitude, S_{hmin}, can be directly measured from fracturing operations by observing the fracture closure upon termination of fluid injection. But the maximum horizontal stress magnitude, S_{Hmax}, cannot be measured by any direct means, and thus is constrained from conditional information.

In the current study, the fact that breakouts are absent but DITFs are present can be used to constrain the magnitude of S_{Hmax} by referring to Equations 4.1 to 4.3. Environmental parameters necessary to conduct the analysis come from a hydraulic fracturing data in a nearby horizontal well, log data, and the literature. The rock mechanical properties come from laboratory data in chapters 2 and 3, and some common estimates. These are summarized in Table 4.1. Values were determined for 8500 ft depth where applicable. Calculations were conduct using the software SFIB by GeoMechanics International.

Table 4.1: List of parameters values used to constrain stress magnitudes and their sources.

Parameter	Values @ 8500ft	Source
S_v	65 MPa (1.1 psi/ft)	Integration of density log
S_{hmin}	44-47 MPa (0.75-0.80 psi/ft)	ISIP obtained nearby horizontal well
Pore Pressure, P_p	30.5 MPa (0.52 psi/ft)	Montgomery et al. (2005)
Mud Pressure, P_m	28.5 MPa (9.4 ppg, 0.49 psi/ft)	Log file header
Biot's Coefficient	1	Common estimate
Mud Temp.	30.5 C°	Log file header
Formation Temp.	70 C°	Log data
Thermal Expansivity, α	4e-6 C^{o-1}	Rock with 50% quartz
Young's Modulus	40 GPa	Barnett-1 lab data from Chapter 2
Poisson's Ratio	0.25	Barnett-1 lab data from Chapter 2
UCS of Formation	150 MPa	Barnett-1 lab data from Chapter 3
Internal Friction	0.75	Barnett-1 lab data from Chapter 3
Sliding Friction	0.65	Barnett-1 lab data from Chapter 3

Figure 4.10 shows the stress polygon representation of allowable stress states calculated based on the input parameters in Table 4.1. Here, for simplicity, we are considering a vertical well with no tilt in the vertical stress. Presence of DITFs forces the stress state to be on the left side of the blue T_0=0 contour, and absence of breakouts forces the stress state to be below the red C_0=150 MPa contour. The magnitude of S_{Hmax} is constrained to be between S_{Hmax}=64-85.5 MPa for S_{hmin}=44-47 MPa and S_v=65MPa. As a result, the allowable stress state mostly lies in the strike-slip faulting regime, but extending into the boundary with the normal faulting regime.

Next, we also tested the effect of the misalignment between the borehole axis and principal stress on the estimates of S_{Hmax}. This is because we observed from the previous section that the vertical stress is likely tilted from the vertical direction. To simulate the effect of tilt in vertical stress, we kept the stress orientations fixed, but intentionally deviated the borehole in the S_{Hmax} and S_{hmin} direction by 15 degrees (Figure 4.11). When the wellbore axis was tilted in the S_{Hmax} direction (N20E/N200E), there was only 0.5 MPa increase in the upper estimate of S_{Hmax} but no change in the lower estimate (Figure 4.11a). When the wellbore axis was tilted in the S_{hmin} direction,

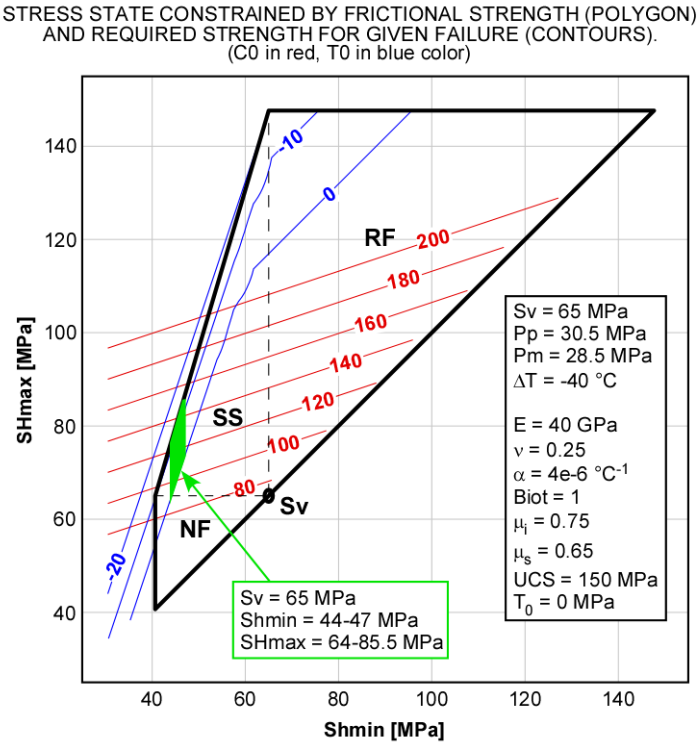

Figure 4.10: Stress polygon used to constrain the magnitude of S_{Hmax}. The green area describes the allowable stress state when DITFs are present and breakouts are not observed.

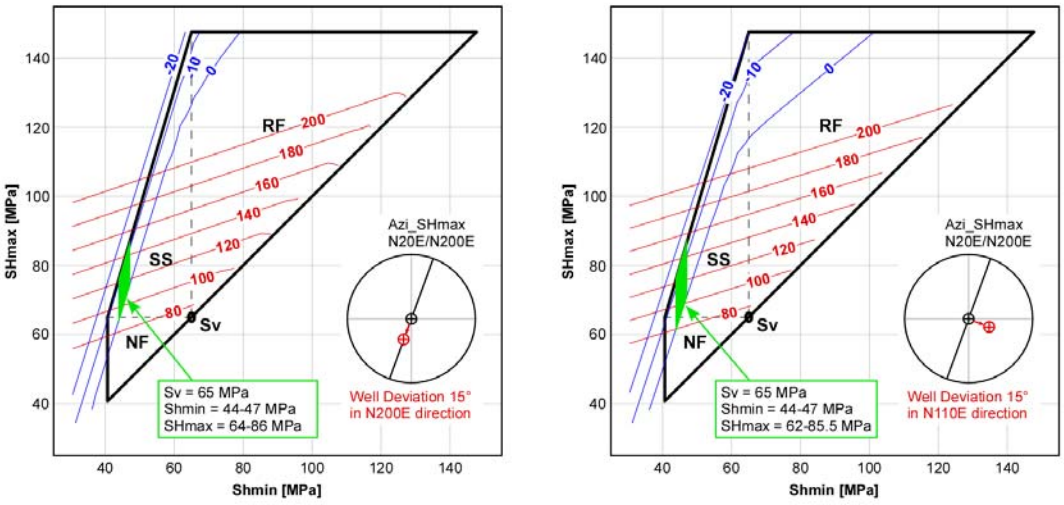

Figure 4.11: Stress polygon representation of constraints on principal stress magnitudes for deviated wells. (a) Well deviated by 15 degrees in the N200E direction. (b) Well deviated by 15 degrees in the N110E direction.

there was a 2 MPa decrease in the lower estimate of S_{Hmax}, but no change in the upper estimate (Figure 4.11b).

These observations suggest that the misalignment of the borehole axis and the principal stress, when less than 15 degrees, had little effect on the boundaries and contours drawn in the stress polygon. This means that the occurrence of DITF, just simply whether it occurs or not, will not be a function of the borehole/stress misalignment if the misalignment stays within about 15 degrees.

4.6 Implications for In-situ Stress Variation

4.6.1 Modeling Inclined DITFs: Base Case

Given constraints on principal stress magnitudes and the fact that the vertical stress is tilted, we are now interested in checking whether the observed inclination and angular span of the DITFs is consistent with these information. We do this by forward modeling the inclination, ω, and angular span, θ_t, of an inclined DITF using the constrained stress magnitudes and assuming some amount of tilt in the S_v direction. For simplicity, tilting of the vertical stress was assumed to occur in the plane spanned by the vertical and S_{hmin} direction, which is equivalent to the rotation of S_v and S_{hmin} directions about the S_{Hmax} axis (Figure 4.12a). We will call this tilt (rotation) angle ϕ_{tilt}. Modeling was performed using the BSFO module of the software SFIB by GeoMechanics International. An example of results obtained by the SFIB software is shown in Figure 4.12b.

As a starting point, we attempt to explain an average representative inclined DITF occurrence with ω=10 and θ_t=40 degrees at depth 8500 ft, which we call the "base-case". Since the parameters that we least understand are the magnitude of S_{Hmax} (64-85.5 MPa) and the ϕ_{tilt} angle, we treat these 2 variable as the free parameters and all of the rest constant as provided in Table 4.1. Figure 4.13 shows the results of ω and θ_t values obtained by varying the S_{Hmax} magnitude between 70-85 MPa and ϕ_{tilt}

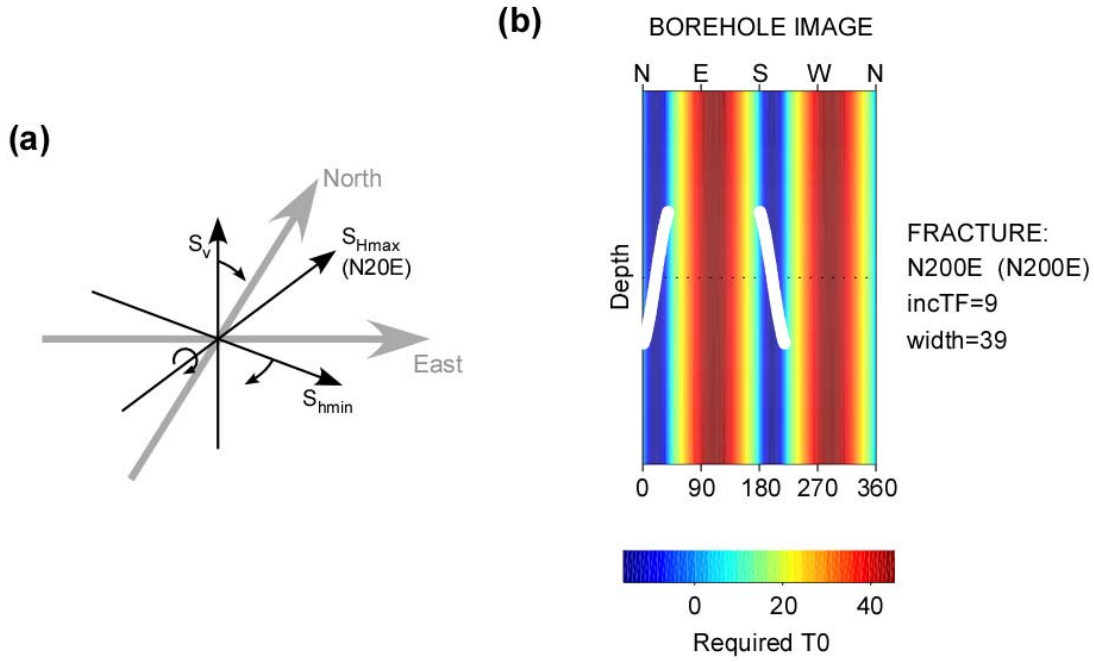

Figure 4.12: (a) Illustration of how the tilt in vertical stress is treated as a rotation of Sv and Shmin about the SHmax axis. (b) An example of results obtained by the SFIB software. The white curve shows the predicted geometry of the inclined DITF. The background color is the tensile strength of the rock required to prevent the formation of DITFs.

between 2-20 degrees. The plots show that the best combination of S_{Hmax} and ϕ_{tilt} values that matches the base-case scenario is about 85 MPa and 5 degrees, respectively. So we confirm from these forward modeling that the magnitude of inclination and angular span we observed in the FMI image logs are explained by reasonable estimates of S_{Hmax} and ϕ_{tilt} values. S_{Hmax}=85 MPa is within the range constrained from the stress polygon (Figure 4.10) and ϕ_{tilt}=5 degrees is of the same order as the well deviation. We may also say that we were able to further constrain the S_{Hmax} magnitude to be about 85 MPa, on the higher end of the range constrained by the stress polygon, since lower S_{Hmax} magnitudes did not yield θ_t values as high as 40 degrees. θ_t was insensitive to ϕ_{tilt} compared to S_{Hmax}.

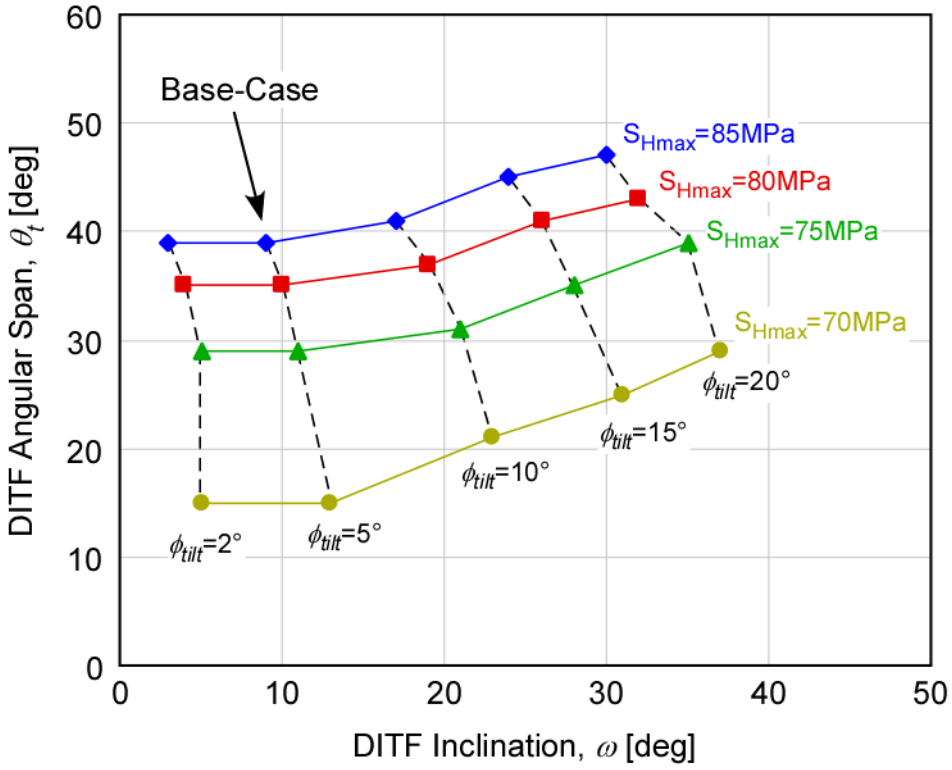

Figure 4.13: Modeled values of ω and θ_t by varying the S_{Hmax} magnitude and ϕ_{tilt}.

4.6.2 Modeling Inclined DITFs: Controls on Inclination and Span

In the previous section, we found that the base-case could be explained with a relatively high magnitude of S_{Hmax}, and only 5 degrees of tilt in the vertical stress. However, as Figure 4.8 shows, it is obvious that we see many occurrences of inclined DITFs that differ from the base-case. Inclination can be as high as 40 degrees and angular span as high as 150 degrees. Especially for the extremely high angular span values, we see from Figure 4.13 that increasing the S_{Hmax} magnitude within the allowable range does not achieve such high θ_t. This implies that there shall be other causes for the variability in ω and θ_t, other that just S_{Hmax} magnitude and ϕ_{tilt}. In this section, we attempt to understand the causes of the variable occurrences of the inclined DITFs.

As seen from Equations 4.4 to 4.9, the final prediction of the inclination, ω, and angular span, θ_t, is a fairly complicated function of numerous parameters. For example,

the mud pressure P_m affects the differential fluid pressure ΔP, which ultimately affects both ω and σ_{tmin}. The magnitude of the principal stresses will affect all of the stress components in the borehole cylindrical coordinate (i.e. σ_{zz}, $\sigma_{\theta\theta}$, and $\tau_{\theta z}$), but pore pressure P_p will only affect the diagonal components of the stress tensor in the borehole cylindrical coordinate (i.e. σ_{zz} and $\sigma_{\theta\theta}$). Thus it is not straight forward to understand how ω and θ_t are affect by the changes in each parameter.

We explored how ω and θ_t is affected by changes in various parameters by forward modeling ω and θ_t using the SFIB software while perturbing one parameter at a time from the base-case. The parameters we considered to vary were: S_{Hmax}, S_{hmin}, P_p, P_m, and ϕ_{tilt}. Other environmental parameters and rock properties were held constant. Figure 4.14 shows the results of the calculation.

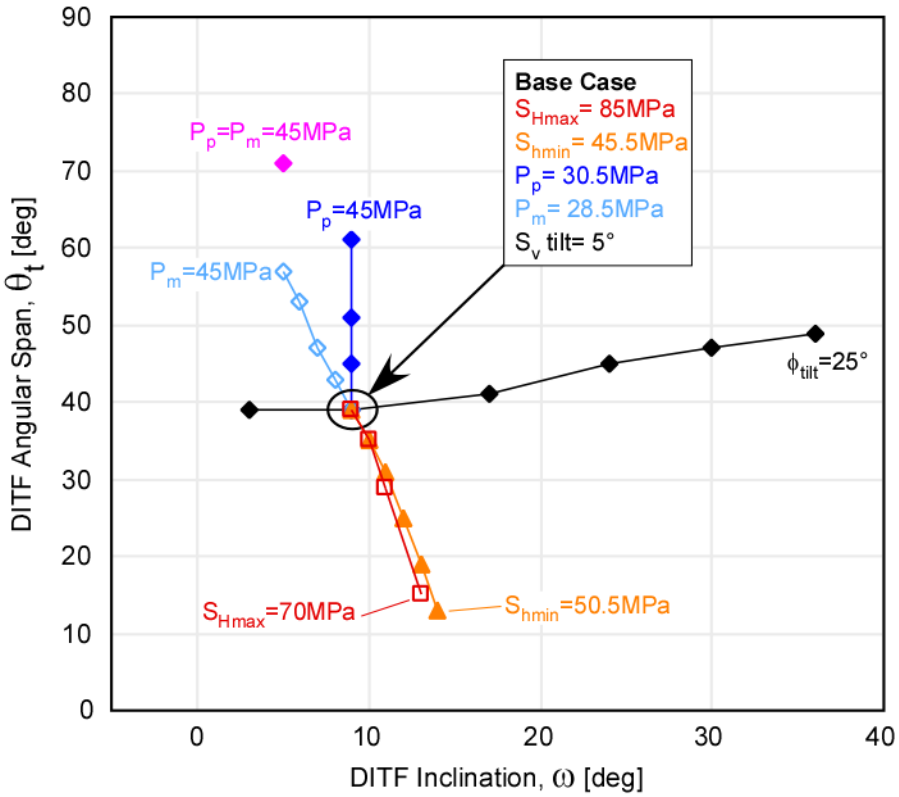

Figure 4.14: Modeled values of ω and θ_t by perturbing S_{Hmax}, S_{hmin}, P_m, P_p and ϕ_{tilt} from the base case. The magenta data point is an example of an extreme scenario with high P_m and P_p.

We see from the results that different parameters clearly have different effects on ω and θ_t. In general, changing stress and pressure magnitudes (S_{Hmax}, S_{hmin}, P_p, P_m) tends to affect θ_t more than ω as seen by the steep trend in the ω-θ_t space, whereas ϕ_{tilt} has a much greater effect on ω than on θ_t. Increasing S_{hmin} magnitude and decreasing S_{Hmax} essentially seem to have the same effect on ω and θ_t; however, note that a 5 MPa increase in S_{hmin} had a larger effect than a 15 MPa decrease in S_{Hmax}. P_m and P_p both affect ΔP, but since P_p also affects the effective stress magnitude of the diagonal components in the stress tensor, they follow a different path in the ω-θ_t space. But their ability to affect the magnitudes of ω and θ_t appears to about the same.

4.6.3 Stress Variations in the Lime Wash and Basal Hot Shale

Motivated by the picture in Figure 4.14, we cross-plot the values of ω and θ_t observed from the inclined DITF in Figure 4.15. The first panel, Figure 4.15a, shows all of the data obtained throughout the FMI image. From the plot, we see that there possibly exist two set of trends between ω and θ_t in the dataset. One is characterized by a gentle increase in θ_t as ω is increased, and the other is characterized by a more steep increase in θ_t as ω is increased. In Figures 4.15b and 4.15c, we show a similar plot but now with data only from the lime-wash and basal hot shale sections, respectively. The plots are also color-coded by the gamma ray values obtained from petrophysical logs observed at the depths of the DITFs. Interestingly, we find that the gentle slope in Figure 4.15a is represented by the data from the lime wash section, and the steeper slope in Figure 4.15a is represented by the data from the basal hot shale section.

These observations suggest different phenomena, that cause the variation in ω and θ_t values, are occurring within the two sections within the lower Barnett Shale. Since ω is most prominently influenced by the tilt angle of the vertical stress, the lime section maybe characterized by a frequent fluctuation in vertical stress tilt angle, ϕ_{tilt}, with depth. From Figure 4.13, we may also perhaps suggest that ϕ_{tilt} reaches up to 25-

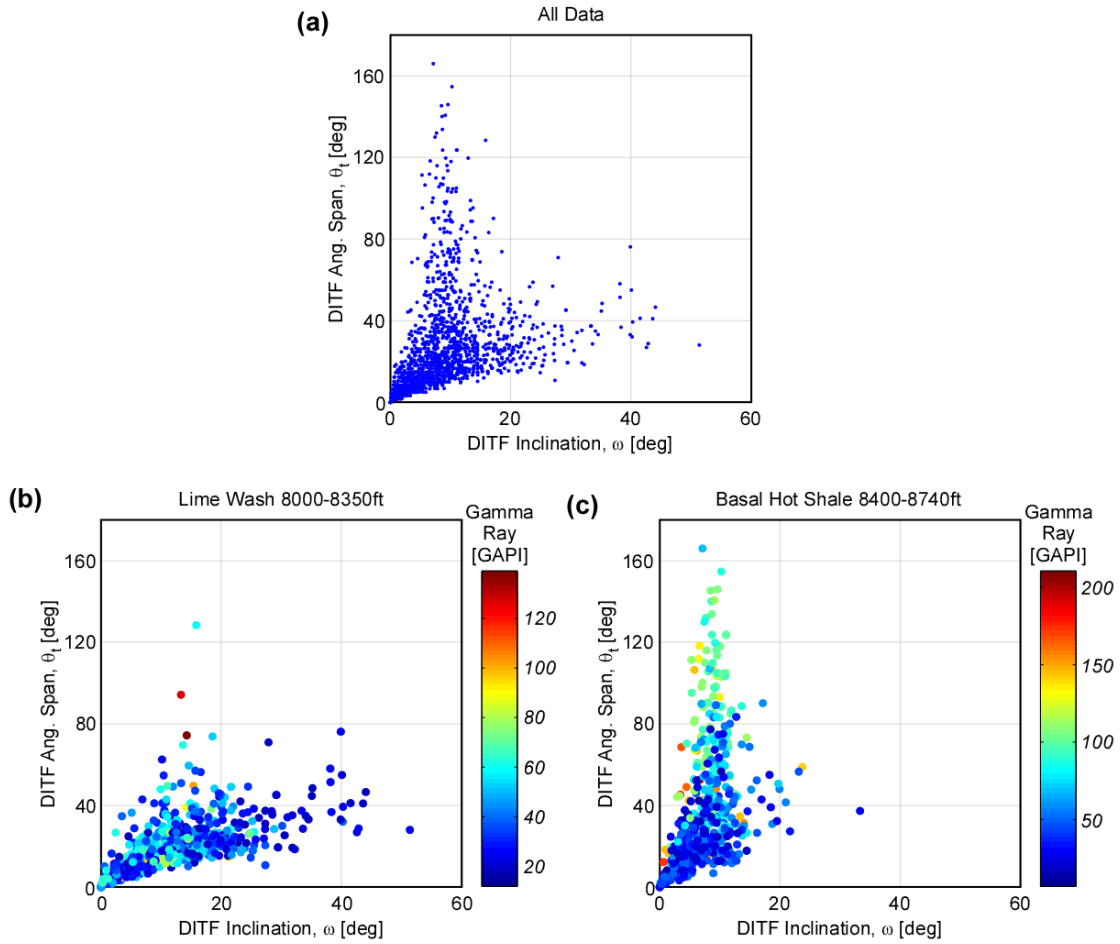

Figure 4.15: (a) Cross-plot of ω and θ_t values for all DITF data. (b) Cross-plot of ω and θ_t values for data from the lime wash section, color-coded by the gamma ray values. (c) Cross-plot of ω and θ_t values for data from the basal hot shale section, color-coded by the gamma ray values.

30 degrees at when ω is at its highest values above 40 degrees. However, comparison with the gamma ray values does not clearly imply what kind of rocks tend to host more tilted vertical stresses.

Since the trend between ω and θ_t is fairly steep in the basal hot shale section as seen from Figure 4.15c, it suggests that some anomalous change in principal stress magnitudes or fluid pressure has occurred in this section. Judging from the fact that the base-case S_{Hmax} magnitude was already close to its highest limit, we do not believe that it is the anomaly in S_{Hmax} magnitude. We also suggest that lowering the S_{hmin} magnitude from the base-case also does not help to explain the extremely high values

of θ_t. The argument is as follows. Lower S_{hmin} does produce larger θ_t as shown in Figure 4.14. However, lowering S_{hmin} also means that the allowable stress state shown by the green polygon in Figure 4.10 shifts to the left, which in turn lowers S_{Hmax} due to the finite frictional strength of the rock. If S_{Hmax} decreases simultaneously as S_{hmin} is decreased, the net effect on θ_t may be cancelled out to be insignificant. For these reasons, we suggest that either an anomalous high mud pressure occurred during drilling, or a locally high pore pressure was present in the basal hot shale section.

Another observation to note is the apparent correlation between gamma ray values and θ_t. As seen from the relatively bright cyan to yellow colored plots concentrated at the high θ_t end of the data in Figure 4.15c, the anomalously high angular span tends to occur in the high-gamma ray sections. This implies that the θ_t value is being influenced by some characteristic of the formation. If so, unless mud weight was controlled according to the gamma ray response, it is easier to believe that the P_p, rather than the P_m, is responsible for the steep relationship between θ_t and ω.

However, we note that our suggestion on what controls the ω and θ_t relation is merely qualitative. In the SFIB modeling, a P_m and P_p value as high as the minimum horizontal stress (45.5 MPa) could not produce a θ_t value as high as 150 degrees (magenta data point in Figure 4.14). It seemed impossible to create a reasonable scenario that yields θ_t as high as 150 degrees.

4.6.4 Variation in Horizontal Stress Anisotropy

We now revisit the observation that DITFs frequently disappeared in the clay- and organic-rich section of the lower Barnett Shale (section 4.4.3). Such feature can be caused by various drilling practices such as change in mud weight/chemistry, mud pressure surge due to drilling string movement during bit replacements, variations in ROP or weight on bit. Although we could not obtain drilling reports that describe these information, it is unlikely that these drilling practices took place frequent enough to explain all occurrences of DITFs. Therefore the mechanical significance of the

disappearance and re-appearance of the DITFs is that it implies a frequent change in the horizontal stress anisotropy. All stress analyses up to now were based on the existence of DITFs, thus the stress states were only allowed to exist to the left of the T_0=0 contour. However, the observed absences of DITFs suggest that locally, the in-situ stress state can be on the right side of the T_0=0 contour (Figure 4.16). One way such crossover can occur is by the change in fluid pressures, P_m and P_p. However, we do not believe these are the causes because the mud weight is not changed so frequently, and lowering the pore pressure to hydrostatic pressure had little effect on

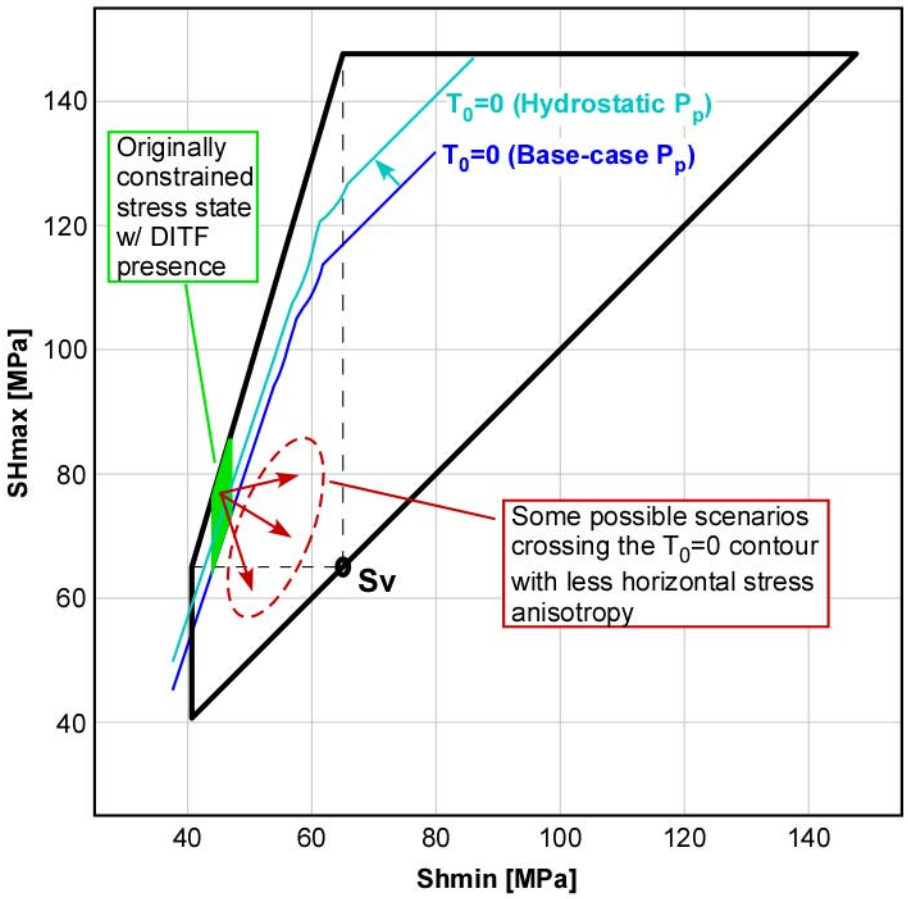

Figure 4.16: Schematic description in the stress polygon of how the stress states might cross over the T_0=0 contour line.

the position of the T_0=0 contour (Figure 4.16 blue lines). Therefore the most likely scenario that can create a rapid disappearance and re-appearance of DITFs is the rapid change in the horizontal stress magnitudes, either by the decrease in magnitude of S_{Hmax} and/or increase in magnitude of S_{hmin} (Figure 4.16 red arrows). Both of these effects make the stress state closer to the S_{Hmax}=S_{hmin} line, or in other words, decreases the horizontal stress anisotropy, making the stress state closer to isotropic.

In order to gain some insight on what is controlling the horizontal stress anisotropy, we look in detail where DITFs appears and disappear. Figure 4.17 shows histograms of gamma ray values at depths where DITF was observed (red bars) and not observed (cyan bars). The 2 panels represent data from the lime wash and basal hot shale sections. We observe from these histograms that, overall, the cyan histograms plot more to the right compared to the red histograms. This means that gamma ray values are higher on average at depths where DITF is absent compared to depths where DITF is observed.

Viewing the data in a slightly different manner, we calculate the relative frequency of DITF absence, $F_{absent}(GR)$, at a given gamma ray value as follows:

$$F_{absent}(GR) = \frac{N_{absent}(GR)}{N_{absent}(GR) + N_{present}(GR)} \times 100\% \tag{4.10}$$

where $N_{absent}(GR)$ and $N_{absent}(GR)$ are the number of times DITF was observed to be absent and present, respectively, when the gamma ray value at a certain depth was equal to GR. The results are plotted in blue, overlain on the histograms in Figure 4.17. Although there are some fluctuations in the data, especially when the total number of observation was small, we clearly see that F_{absent} increases with increasing gamma ray values. Thus, as the gamma ray becomes higher and the formation is more clay- and organic-rich, DITF is more likely to disappear suggesting less horizontal stress anisotropy. This trend is persistent throughout the lower Barnett Shale.

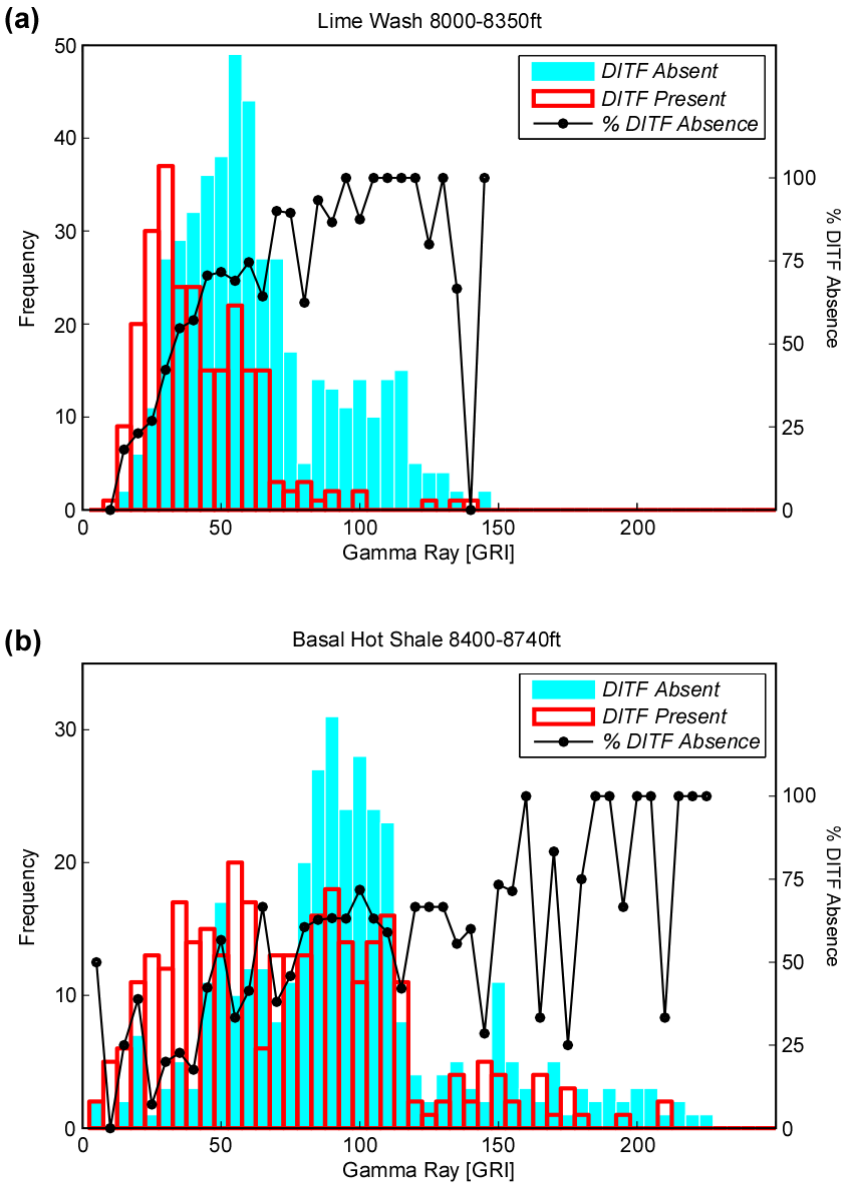

Figure 4.17: (a) Histograms of gamma ray values for depths at which DITF is present and absent for the lime wash section. (b) Histograms of gamma ray values for depths at which DITF is present and absent for the basal hot shale section. Black plots show how frequent (in %) DITF was absent for a give gamma ray value corresponding to the histogram bins.

4.6.5 Summary on Implied Stress Variation in the Lower Barnett Shale

1. The base-case scenario suggests that an average inclined DITF in the lower Barnett Shale is explained by a tilt in the vertical stress axis by 5 degrees to in the N110E direction.
2. In the lime wash section, the stress variation is characterized by a rapid fluctuation in the rotation angle of the principal stress axes, ϕ_{tilt}.
3. In the basal hot wash section, the stress variation is likely caused by the change in pore pressure, P_p, which correlated with the gamma ray values of the formation.
4. In the entire lower Barnett Shale, the appearance and disappearance of DITFs were likely cause by the rapid change in the horizontal stress anisotropy. Comparison with gamma ray data suggests that horizontal stress is more isotropic in clay-/organic-rich formations.

4.7 Possible Mechanisms Responsible for the In-Situ Stress Variations

4.7.1 Stress Refraction

Rotation of principal stress axes in a layered media is a well studied phenomenon, known as “stress refraction” (Treagus, 1973). When a media composed of layers with contrasting properties is loaded by a uniform far-field stress (or strain), a necessary boundary condition of traction continuity at the layer boundaries creates a discontinuous stress state between the layers. Bradshaw and Zoback (1988) studied the possible rotation of the principal stress axes in the Gulf Coast basin to suggest that the geometry of listric normal faults are caused by the enhanced stress rotation in the shale layer with relatively low effective viscosity compared to the overlying sand layers (Figure 4.18). Although not referred to as stress refractions, a similar phenomenon of stress discontinuity can occur by contrast in elastic properties as well in various settings (Bourne, 2003; Faulkner et al., 2006).

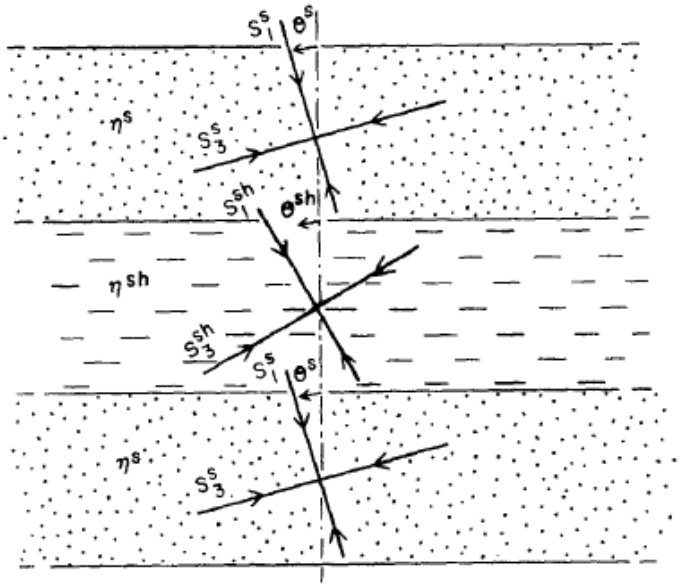

Figure 4.18: (a) Illustration of stress refraction in low viscosity shale layers. Figure from Bradshaw and Zoback (1988).

We suggest that the tilt in the vertical principal stress observed in the lower Barnett Shale may be caused by the relatively low effective viscosity of the whole section. Laboratory data from Chapter 3 suggests that these gas-bearing shales possess some ability to creep which is facilitated by deformation in the porous clay and porous organic components. Although we could not conduct similar experiments using samples from the overlying and underlying formations for comparison, the overlying and underlying formations do not contain as much organic materials as in the lower Barnett Shale section. Therefore one possible explanation for the local appearance of inclined DITFs in the lower Barnett Shale is that these rocks have relatively lower effective viscosity that induces formation scale stress refraction in the lower Barnett Shale layer.

We may also possibly appeal to a similar stress refraction mechanism to explain the rapid fluctuation in the ϕ_{tilt} angle observed within the lime wash section. This section is where the lithology variation was greatest and the greatest mechanical heterogeneity is expected. However, we did not observe a clear correlation between

the gamma ray response and the ϕ_{tilt} angle (Figure 4.15b). Thus we cannot conclude whether stress refraction caused the variation in the ϕ_{tilt} angle.

4.7.2 High pore pressure in the basal hot shale

Although we could not exactly match the observed θ_t values in our forward modeling, we implied that the anomalously wide angular spans, θ_t, of the inclined DITFs were caused by a locally high pore pressure in the basal hot shale section. Such notion may also be consistent with the fact that many natural fractures were observed specifically in the basal hot shale section.

Unfolding the exact tectonic history of the Barnett Shale and identifying the ages of each structural feature is challenging. However, we believe it is plausible that these natural fractures indicate where high pore pressure was generated through maturation of kerogen between late Paleozoic and late Mesozoic era. Fractures are obviously created by shear deformation as well, but the highly concentrated presence of these natural fractures specifically in the basal hot shale where high organic content is suggested from the gamma ray log leads us to believe that high pore pressure was present in this section. Since direct measurement of the pore pressure in these impermeable shales is challenging, we cannot verify whether such locally high pore pressure exists in the basal hot shale section. But this is an actively producing shale layer and it is plausible to believe that some over-pressure remains in the basal hot shale section.

4.7.3 Stress Relaxation

The disappearance of DITFs in the higher gamma ray section implied that the horizontal stress anisotropy is diminished in the more clay- and organic-rich layers. Inspired by the laboratory observations from Chapter 3 that clay- and organic-rich layers tend to exhibit ductile creep behavior, we suggest that the decrease in horizontal stress anisotropy is caused by the viscous stress relaxation over geological time scales. Stress relaxation due to viscous deformation is a commonly invoked idea in

geomechanical studies involving salt domes, where salts are essentially regarded as a fluid over geological time scales. Within the salt diaper, stress is assumed to be isotropic (all principal stress magnitudes equal to overburden stress) and no shear tractions exist at the boundary with the surrounding formations.

We observed from Chapter 3 that there is a clear contrast in creep behavior between samples from the same reservoir, and clay/organic content enhances the ductile behavior. Thus if clay/organic varied rapidly between layers in a shale gas reservoir, it is likely that each layer has undergone different amounts of stress relaxation. The result would be a more isotropic stress states in the clay- and organic-rich layers, and more anisotropic stress state in the clay- and organic-poor layers. This is consistent with our observations (Figure 4.16). We will explore this problem quantitatively in the next chapter (Chapter 5), by attempting to characterize the time-dependent constitutive relation of the studied gas shale rocks.

4.8 Conclusions

By observing the occurrences of wellbore failures in a vertical well in the Newark East Field, close to the Muenster Arch, we constrained the stress state and also characterized the stress variations observed within the lower Barnett Shale section. Conclusions are summarized below.

1. The stress state in the Barnett Shale at this region is in the strike-slip faulting regime.
2. The vertical principal stress in the lower Barnett Shale section is tilted by about 5 degrees in the N110E direction possibly due to stress refraction caused by the slightly ductile nature of the shale relative to the surrounding formation.
3. The tilt angle of the vertical principal stress, ϕ_{tilt}, fluctuates rapidly in the lime wash section of the lower Barnett Shale, but the mechanism is unknown.

4. The anomalously wide angular span of the inclined DITFs in the basal hot shale section of the lower Barnett Shale is suggested to be the result of a locally high pore pressure within the organic-rich basal hot shale section.
5. The horizontal stress anisotropy tends to be relaxed, closer to isotropic, in the more clay- and organic-rich shale layers in the lower Barnett Shale.

4.9 References

Bourne, S. J., 2003, Contrast of elastic properties between rock layers as a mechanism for the initiation and orientation of tensile failure under uniform remote compression: Journal of Geophyscial Research, 108, doi:10.1029/2001JB001725.

Bowker, K. A., 2003, Recent development of the Barnett Shale play, Fort Worth Basin: West Texas Geological Society Bulletin, 42(6), 4-11.

Bradshaw, G. A. and Zoback, M. D., 1988, Listric normal faulting, stress refraction, and the state of stress in the Gulf Coast Basin: Geology, 16, 271-274.

Curtis, J. B., 2002, Fractured shale-gas systems: AAPG Bulletin, 86(11), 1921-1938.

Daniels, J., Waters, G., LeCalvez, J., Lassek, J., and Bentley, D., 2007, Contacting more of the Barnett Shale through an integration of real-time microseismic monitoring, petrophysics and hydraulic fracture design: SPE Annual Technical Conference and Exhibition, Anaheim, CA, 110562.

Faulkner, D. R., Mitchell, T. M., Healy, D., and Heap, M. J., 2006, Slip on 'weak' faults by rotation of regional stress in the fracture damage zone: Nature, 444, 922-925.

Gale, J. F.W., Reed, R. M., and Holder, J., 2007, Natural fractures in the Barnett Shale and their importance for hydraulic fracture treatments: AAPG Bulletin, 91(4), 603-622.

Heidbach, O., Tingay, M., Barth, A., Reinecker, J., Kurfeß, D. and Müller, B., 2008, The World Stress Map database release 2008 doi:10.1594/GFZ.WSM.Rel2008.

Hiramatsu, Y., and Oka, Y., 1962, Stress around a shaft or level excavateion ground with a three-dimensionsal stress state, Memoir of Faculty of Engineering Kyoto University, XXIV(I), 56-76.

Hubbert, M. K., and Willis, D. G., 1957, Mechanics of Hydraulic Fracturing: Petroleum Transactions AIME, 210, 153-166.

Jarvie, D. M., Claxton, B. L., Henk, F., and Breyer, J. T., 2001, Oil and shale gas from the Barnett Shale, Ft. Worth basin, Texas (abs.): AAPG Annual Meeting, Program with Abstracts, p. A100.

Kirsch, G., 1898, Die Theorie der Elastizitat und die Bedurfnisse der Festigkeitslehre, Zeitschrift des Verlines Deutscher Ingenieure, 42, 707.

Mapel, W. J., Johnson, R. B., Bachman, G. O., and Varnes, K. L., 1979, Southern midcontinent and southern Rocky Mountains region, in Paleotectonic investigations of the Mississippian system in the United States, Craig, L. C. and Connor, C. W., coordinators, U. S. Geological Survey Professional Paper, v. P1010, p. 161–187.

Maxwell, S., 2011, Microseismic hydraulic fracture imaging: The path toward optimizing shale gas production: The Leading Edge, 30, 340-346.

Montgomery, S. L., Jarvie, D. M., Bowker, K. A., and Pollastro, R. M., 2005, Mississippian Barnett Shale, Fort Worth basin, north-central Texas: Gas-shale play with multi-trillion cubic foot potential: AAPG Bulletin, 89(2), 155-175.

Peska, P., and Zoback, M. D., 1995, Compressive and tensile failure of inclined well bores and determination of in situ stress and rock strength: Journal of Geophysical Research, 100, 12,791-12,811.

Pollastro, R. M., Jarvie, D. M., Hill, R. J., and Adams, C. W., 2007, Geologic framework of the Mississippian Barnett Shale, Barnett-Paleozoic total petroleum system, Bend arch-Fort Worth Basin, Texas: AAPG Bulletin, 91(4), 405-436.

Tian, Y., 2010, An investigation of regional variations of Barnett Shale reservoir properties, and resulting variability of hydrocarbon composition and well performance: Master's thesis, Texas A&M University.

Treagus, S. H., 1973, Buckling stability of a viscous single-layer system oblique to the principal compression: Tectonophysics, 19, 271-289.

Waters, G., Heinze, J., Jackson, R., Ketter, A., Daniels, J., and Bentley, D. 2006, Use of horizontal well image tools to optimize Barnett Shale reservoir exploitation: SPE Annual Technical Conference and Exhibition, San Antonio, TX, 103202.

Vermylen, J. P., 2011, Geomechanical studies of the Barnett Shale, Texas, USA: Ph.D. thesis, Stanford University.

Zoback, M. D., 2007, Reservoir Geomechanics, Cambridge University Press.

Chapter 5

VISCOELASTIC DEFORMATION OF SHALE GAS RESERVOIR ROCKS AND ITS RELATION TO THE STATE OF STRESS IN SHALE GAS RESERVOIRS

Abstract

We studied the viscoelastic properties of shale gas reservoir rocks through laboratory triaxial creep experiments and found that the viscoelastic stress relaxation behavior of these rocks may have a significant influence on the current variation of stress state in these reservoirs. Shale gas reservoir rocks exhibit varying degrees of time-dependent strain response in addition to their instantaneous elastic response. The time-dependent deformation is an inherent behavior of the dry rock as it occurs in the absence of pore fluid. The contribution of the time-dependent deformation is generally larger for rocks with more clay and organic content, and also when the rock is loaded perpendicular to the bedding plane rather than parallel to the bedding plane. The strain

response of the rock upon pressure input was adequately described by a power-law function of time, and its magnitude was approximately linear with the magnitude of the applied differential pressure but insensitive to the confining pressure. These observations suggest an approximately linear viscoelastic behavior of these gas shale rocks. Taking advantage of the linearity, we calculated the differential stress relaxation behavior from the observed creep behavior, and calculated the stress accumulation/relaxation that would occur in these reservoirs at geological time scales. The variation in viscoelastic properties within a reservoir can create differential stress variations on the order of one to tens of MPa. This is consistent with the variation in horizontal stress difference inferred from wellbore failures in a well in Barnett shale. Although time-dependent deformational behaviors of intact reservoir rocks are not studied routinely in the lab, we suggest that it can have a significant impact in determining the current in-situ state of stress when reservoir deformation takes place over geological time scales.

5.1 Introduction

Characterization of the mechanical properties of reservoir rocks often focuses on its elastic properties through analysis of seismic reflection data, sonic logs and laboratory tests on core samples. However, it is also important to understand the time-dependent (viscous) mechanical properties of rocks in order to predict the long-term reservoir behavior over time. Numerous laboratory studies have shown that deformation of very weak uncemented sands and shales occur through elastic-visco-plastic constitutive behavior (de Waal and Smits, 1985; Dudley et al., 1994; Chang et al., 1997; Hagin and Zoback, 2004a; Chang and Zoback, 2009a,b). A significant portion of the deformation of these types of rocks takes place by a time-dependent response not predicted by linear elasticity. Failing to address the time-dependent response of these reservoir rocks may lead to a significant under-estimation of reservoir compaction during depletion (Hagin and Zoback, 2004b; Hagin and Zoback, 2007). Such under-estimation will not only lead to inaccurate prediction of surface

subsidence, but also inaccurate forecasting of reservoir performance as compaction is a primary driving force for hydrocarbon production in unconsolidated reservoirs.

On the other hand, time-dependent viscous behavior of more intact reservoir rocks has not received much attention in the literature. This is an obvious consequence of the fact that intact rocks exhibit much less time-dependent characteristics compared to unconsolidated rocks, and they appear to behave more or less elastically at laboratory time scales. Shale gas reservoir rocks are an example of such relatively intact reservoir rocks, which we focus in our study.

We investigate the time-dependent viscous deformational properties of shale gas reservoir rocks not only because they may affect the transport properties of the reservoir over the lifetime of a reservoir, but also because they may be related to the in-situ stress variations observed in shale gas reservoirs. Understanding stress variations within shale gas reservoirs is crucial for the development of these reservoirs since these low-permeability reservoirs require stimulation by hydraulic fracturing whose outcome is greatly influenced by the in-situ state of stress. As studied in chapter 4, the intra-reservoir stress state was observed to vary dramatically within the Barnett Shale characterized by a frequent change in the direction and the magnitude of the principal stresses within the reservoir. Moreover, the variation in the in-situ stress state was found to correlate with the gamma ray log response which correlates with the abundance of clay minerals and organic contents in the rock. As studied in chapters 2 and 3, mechanical properties of these rocks are a strong function of the rock composition. These results lead us to believe that the stress variation is closely related to the mechanical heterogeneity of the reservoir rocks.

Some studies attempt to explain this relation between stress and mechanical properties by appealing to the heterogeneity in elastic properties (Suarez-Rivera et al., 2006; Higgins et al., 2008). But these methods are founded upon the questionable assumption that rocks behave as a linear-elastic medium in throughout the loading and unloading of stress. As studied in chapter 3, these rocks are not linear-elastic and they exhibit varying degrees of time-dependent deformational behavior. Since viscous

deformation relaxes differential stress, it may be more reasonable to consider the long-term viscous behavior of the rocks to understand the variation in the in-situ state of stress.

In this chapter, we focus on establishing a quantitative connection between the observed variation in horizontal stress anisotropy (Chapter 4) and the laboratory measured variation in viscous properties of gas shales. While time-dependent deformations of rocks are usually understood to be a highly non-linear process, we interpret the time-dependent viscous property of gas shales in the framework of linear viscoelastic theory. While such approach is difficult to fully justify, it allows us to perform a 1st-order quantitative analyses on whether the variation in the viscous properties of gas shales may have any relation to the observed stress variations. We start by reviewing relevant concepts in viscoelasticity, then attempt to describe the viscoelastic properties of gas shales from laboratory data, and finally extrapolate the results to geological time-scale to address the current state of stress in gas shale reservoirs.

5.2 Linear Viscoelasticity

5.2.1 General Behavior of Viscoelastic Materials

In an elastic material, the relation between applied stress and strain response is immediate and direct (Figures 5.1a and 5.1b dashed lines). Viscoelastic material is a material that exhibits time-dependent deformation behavior. Thus a viscoelastic material could exhibit either creep strain or stress relaxation behavior depending on the boundary condition (i.e. constant stress or constant strain) (Figures 5.1a and 5.1b solid lines). Creep and relaxation behavior are inherently related to one another. If a material creeps, it will also exhibit relaxation behavior, and vice versa. An intuitive way to understand this linkage is to first imagine a material that creeps under constant stress. Then if you were to deform that same material so that the amount of deformation remains constant, you will first apply some load but will have to release

the load subsequently to keep it from deforming further (keep it from creeping). This inherent relation can be described analytically under the assumptions of linear superposition behavior, discussed in the next section.

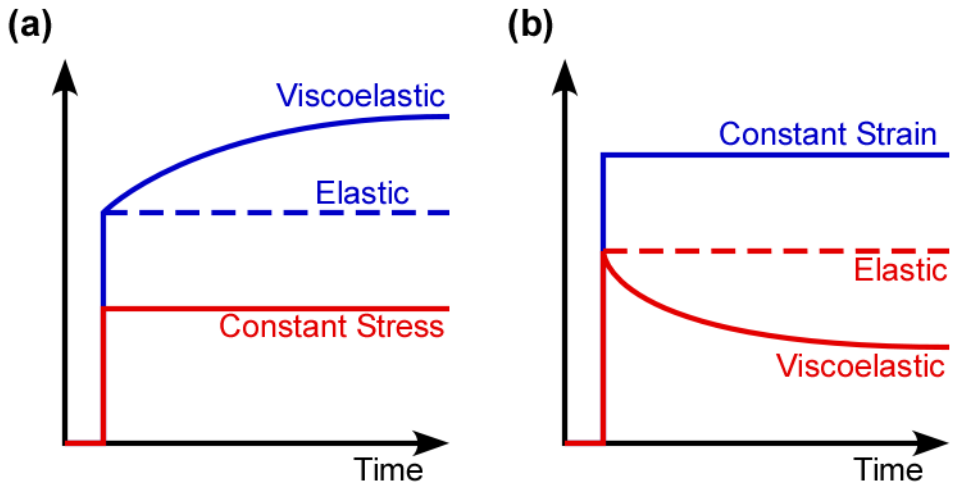

Figure 5.1: Schematic descriptions of some general viscoelastic behaviors and creep behavior. (a) Creep under constant stress. (b) Stress relaxation under constant strain. (c) The 3 stages of creep behavior.

5.2.2 Boltzmann Superposition

Here we review some concepts in viscoelasticity theory that is relevant to our problem. For a complete review of the theory, see Findley et al. (1976) or Lakes (2009). When a viscoelastic material is linear, the stress/strain response scales linearly with the strain/stress input and the principle of linear superposition holds. These requirements can be described mathematically as:

$$\varepsilon[c\sigma(t)] = c\varepsilon[\sigma(t)] \tag{5.1}$$

$$\varepsilon[\sigma_1(t) + \sigma_2(t-\tau_1)] = \varepsilon[\sigma_1(t)] + \varepsilon[\sigma_2(t-\tau_1)] \tag{5.2}$$

where ε and σ are the strain output and stress input, respectively, and c is a constant. The same relation holds when stress and strain are interchanged in these equations. The second requirement is specifically referred to as the Boltzmann superposition, a fundamental concept underlying much of the linear viscoelasticity theory. The idea is

that when a response to a step (Heaviside) input is known, the total response to a multiple-step input can be computed by taking the sum of the individual responses to each step (Figures 5.2a and 5.2c). By extending this idea to an infinite number of infinitesimal steps (Figures 5.2b and 5.2d), thus an arbitrary input history, the superposition principle can be expressed in an integral form as follows:

$$\varepsilon(t) = \int_0^t J(t-\tau)\frac{d\sigma(\tau)}{d\tau}d\tau \tag{5.3}$$

$$\sigma(t) = \int_0^t E(t-\tau)\frac{d\varepsilon(\tau)}{d\tau}d\tau \tag{5.4}$$

J(t) is the *creep compliance* function which describes the time-dependent strain response to a Heaviside input of stress, or a Dirac-delta input of stress rate. Similarly, *E(t)* is the *relaxation modulus* function which describes the time-dependent stress response to a Heaviside input of strain, or a Dirac-delta input of strain rate. Equations 5.3 and 5.4 states that if the kernel responses, *J(t)* and *E(t)*, are known in advance, one can predict the responses to any arbitrary input history by convolving the kernel functions with the derivative of the input history. Since we are eventually interested in predicting the stress accumulation in reservoirs over geological time, we can see from the equations that our goal will be to obtain the relaxation modulus, *E(t)*, of the reservoir material as well as the strain history of the reservoir to solve our problem.

The analytical relationship between *J(t)* and *E(t)* can be seen by taking the Laplace transforms of Equations 5.3 and 5.4 which yields:

$$\varepsilon(s) = sJ(s)\sigma(s) \tag{5.5}$$

$$\sigma(s) = sE(s)\varepsilon(s) \tag{5.6}$$

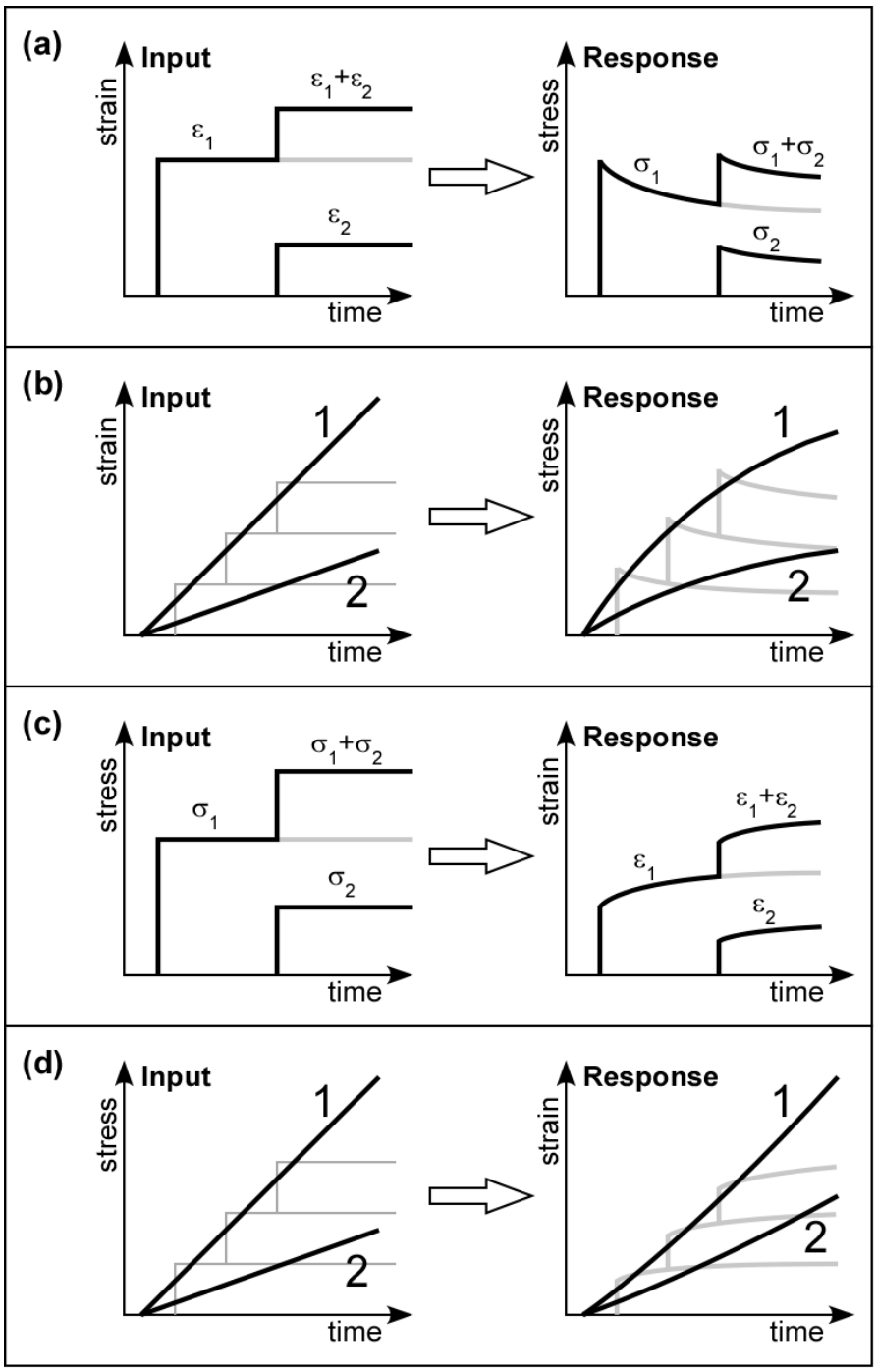

Figure 5.2: Illustration of linearity and Boltzmann superposition principle. (a) Superposition of stress relaxation behavior. (b) Stress response to a continuous strain input. (c) Superposition of creep behavior. (d) Strain response to a continuous stress input.

By eliminating ε and σ from these to equations, we obtain the following relation in the Laplace domain:

$$E(s)J(s) = \frac{1}{s^2} \tag{5.7}$$

Equation 5.7 is a useful relation, as it allows us to obtain, exactly, an unknown kernel function as long as its other counterpart is known. For example, if one knows the mathematical form of *J(t)*, *E(t)* can be determined by: 1) taking the Laplace transform of *J(t)* to obtain *J(s)*, 2) solving for the corresponding relaxation modulus, *E(s)*, in the Laplace domain using Equation 5.7, and 3) performing the inverse Laplace transform to obtain the relaxation modulus, *E(t)*, in the time domain. We will use this relation later to obtain the relaxation modulus of a sample from the creep compliance determined in the lab. However, note that successful determination of one kernel function from the other using Equation 5.7 requires that the Laplace transform and the inverse Laplace transform is analytically manageable. Thus, even though a certain expression for *J(t)* is found to be the best fitting model to a laboratory data, it may not be the ideal expression to carry out the analytical conversion from *J(t)* to *E(t)* using Equation 5.7.

5.3 Methods

5.3.1 Sample Description

We performed creep experiments using core samples collected from several shale gas reservoir rocks in North America to observe their creep behavior. Samples come from the Barnett, Haynesville, Fort St. John, and Eagle Ford shale. The material composition of these samples constrained by powder XRD analysis and pyrolysis is summarized in a ternary plot (Figure 5.3) with clay+kerogen, QFP (quartz, feldspar, pyrite), and carbonate volumes as the end members. The compositional data of each sample are compiled in Chapter 2 Appendix A. Samples from Barnett, Haynesville, and Eagle Ford shale are further divided into 2 subgroups of distinct mineralogy where

subgroup 1 contains more clay and organic contents than subgroup 2. In general, Barnett and Fort St. John shales samples are relatively QFP-rich and Eagle Ford samples are carbonate-rich. Sample porosity constrained by their mineral and bulk densities roughly correlates with the amount of clay and kerogen in the samples, and they range from 1.5 to 9%. More information on sample composition and their microstructures are described in Chapters 2.

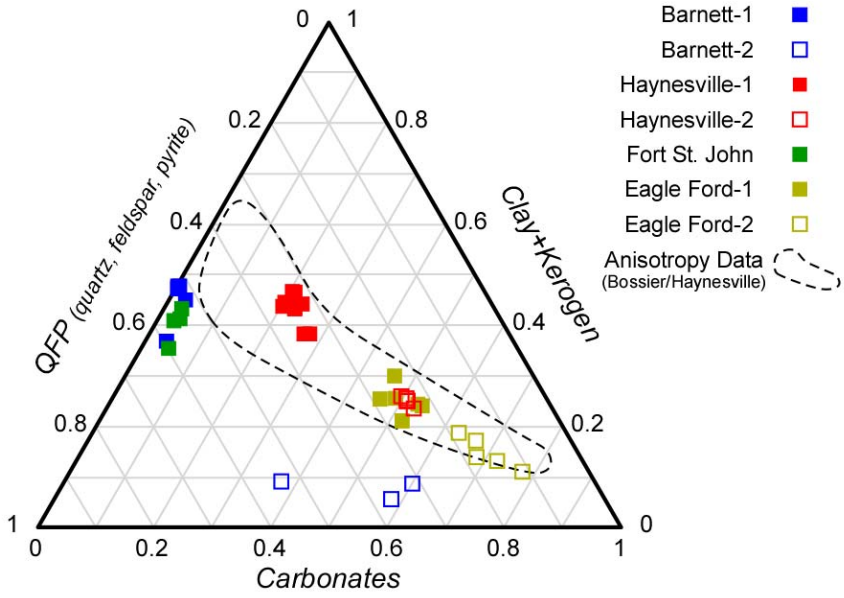

Figure 5.3: Ternary plot representation of the sample material composition.

5.3.2 Laboratory Procedures

Laboratory experiments discussed here are the same experiments as those discussed in Chapters 2 and 3. A more complete description of the experiments and measured properties are described in Chapter 2 sections 3. Here we only explain the relevant portion of the experiments.

We performed multi-step creep experiments in a servo-controlled triaxial apparatus to characterize the viscoelastic properties of gas shales. We used cylindrical samples with 1" diameter and 1.2-2.1" lengths. The cylindrical axes were either perpendicular (vertical samples) or parallel (horizontal samples) to the bedding planes. Samples were first subject to a constant confining pressure of 10-60 MPa and kept

under that condition for at least 3 hours to reach thermal equilibrium inside the pressure vessel. Then axial differential pressures, P_{diff}, of varying magnitudes were applied in 2-5 steps. Each of these P_{diff} step lasted 60 seconds, and P_{diff} was held constant for 3 hours to 2 weeks to observe the creep response of the sample. During the experiments, sample deformation in the axial direction was measured by a pair of LVDT transducers and the deformation in the direction perpendicular to the axis (lateral deformation) was measured by a pair of spring-mounted strain-gauge transducers.

The differential pressure applied during creep deformation was kept below 50% of the ultimate rock strength to prevent the transition of the creep behavior into tertiary creep. Creep deformation is typically characterized by a stable deformation with continuously decreasing strain rate. But under the triaxial boundary condition we employed in our experiments, creep may lead to a stage of increasing strain rate which ultimate leads to sample failure (tertiary creep; Lockner, 1993) if enough differential load is applied. Tertiary creep is a nonlinear process not described by linear viscoelasticity. Therefore we assured that our experiment did not enter the tertiary creep stage by applying low enough differential pressures.

Data from a representative experiment is shown in Figure 5.4. Most of the strain occurs in the initial 60 seconds of the data when the axial differential pressure is applied, and the rest is the creep response under constant differential pressure. The short term (60 seconds) unloading and reloading at the end of each creep deformation was done to measure the elastic properties of the rock before moving on to the next pressure step. From the slope of the stress-strain relation during the unloading and reloading, the Young's modulus was determined by least square linear regression.

We believe that the measured creep strain responses were free of any poroelastic effects since the original fluid saturation was at most 40% (including clay-bound water), and we made no effort to saturate the sample with any kind of fluid. We also did not actively dry the sample in an oven in an attempt to preserve the original

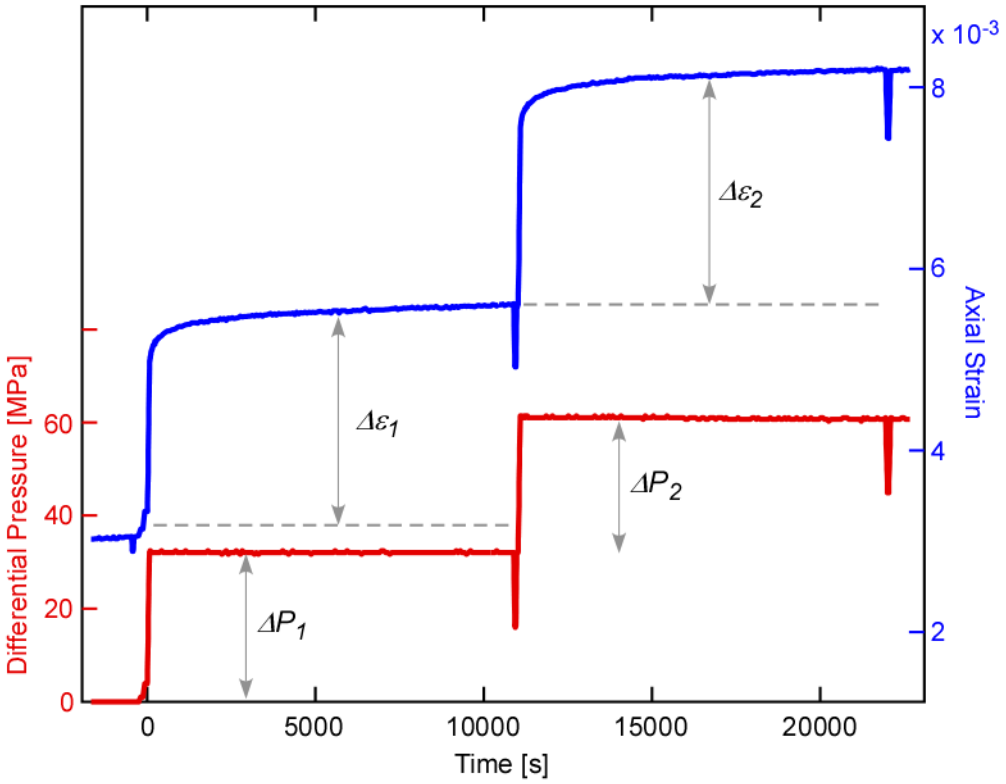

Figure 5.4: Data from a representative experiment. The sample used in this data is a Haynesville-1 vertical sample.

hydration state of the clay minerals. Changing the hydration state of clay minerals would drastically change the mechanical and frictional behavior of the clays (Moore and Lockner, 2004). All experiments were conducted at room-temperature, drained condition.

5.3.3 Geometry of the Deformation in This Study

While a complete analysis of material deformation requires tensor descriptions of stress and strain, many studies of viscoelastic mechanical behavior of materials simplify the problem into a one-dimensional problem (Equations 5.1 to 5.7) that suites their purpose of investigation. For instance, laboratory studies concerned with the compaction of unconsolidated reservoir rocks deal with isotropic volumetric deformation in response to hydrostatic pressures (de Waal and Smits, 1985; Dudley et al., 1994; Chang et al., 1997; Hagin and Zoback, 2004a; Chang and Zoback, 2009). On

the other hand, engineering studies concerned with deformation of metals or polymers oftentimes apply tensional or torsional deformation to the material (Findley et al., 1976; Lakes, 2009).

In this study, we are addressing the variability in horizontal differential stress observed in the Barnett Shale. Thus we are concerned with rock deformation under the application of a differential stress and strain. Thus we are treating our problem as a one-dimensional problem by using the axial differential pressure, P_{diff} or $\Delta P_{ax,}$ as the one-dimensional pressure variable, and the axial strain, ε_{ax}, as the one-dimensional strain variable in Equations 5.1 to 5.7.

5.4 Observations of Creep Behavior

5.4.1 Laboratory Data

Figure 5.5 shows several representative 3 hour creep data. A result from a test using an aluminum alloy sample is also shown in black as a reference for an elastic response. We see by comparing the data that the strain response varies between samples. For instance, Hanesville-1 and Eagle Ford-1 samples shows significant amounts of creep strain after 3 hours reaching up to about 30% of the instantaneous strain observed in the first 60 seconds, whereas other samples show much less creep strain relative to the instantaneous strain in the initial 60 seconds. We seen in general that when comparing samples from the same reservoir (e.g. Haynesville-1 vs. -2), the more clay- and organic-rich sample group tend to show much pronounced creep behavior. Also, vertical samples show more creep behavior than horizontal samples as illustrated by the two Eagle Ford samples in Figure 5.5. From comparison with the aluminum alloy data, we see that these rocks clearly exhibit time-dependent response not captured by linear elasticity.

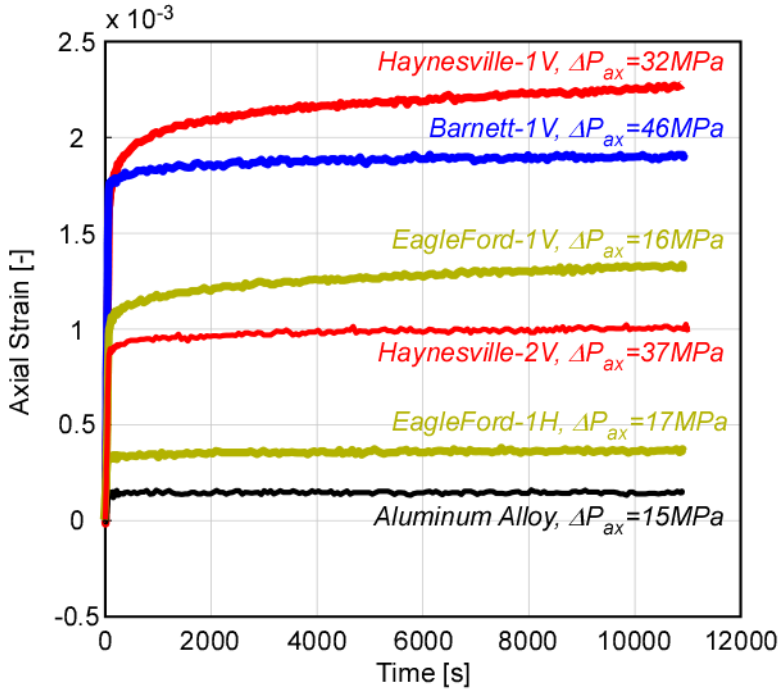

Figure 5.5: Several representative 3 hour creep data. ΔP_{ax} indicates the amount of axial differential pressure applied in the first 60 seconds. "V" denotes vertical samples, "H" denotes horizontal samples.

5.4.2 Pressure Dependence and First Order Linearity

In order to check the linearity of the strain responses against the pressure inputs, data from creep experiments with 3 hour hold times are plotted in Figure 5.6, where the cumulative axial strain after each step is plotted against the cumulative axial differential pressure. Each plot represents the total strain and total stress after each step. Each set of plots connected by lines represents data from a single experiment using a single sample. We first see from Figure 5.6 that the strain responses of these rocks are more or less proportional to the applied differential pressure. This roughly suggests a linear behavior described by Equation 5.1 and illustrated by Figure 5.2c. However, note that Figure 5.6 does not serve as a strict verification of linear behavior. We are neglecting the fact that creep strain from the previous steps continue on into the subsequent steps. The linear trend in Figure 5.6 can be suggestive of a linear behavior if we can assume that the creep response after 3 hours is negligibly small compared to the deformation superimposed by later pressure steps. The approximate

linear relation between the total strain response and the applied differential pressure verifies that the creep deformation did not enter the tertiary creep stage. If tertiary creep were to have happened, we should see a pronounced increase in the slope.

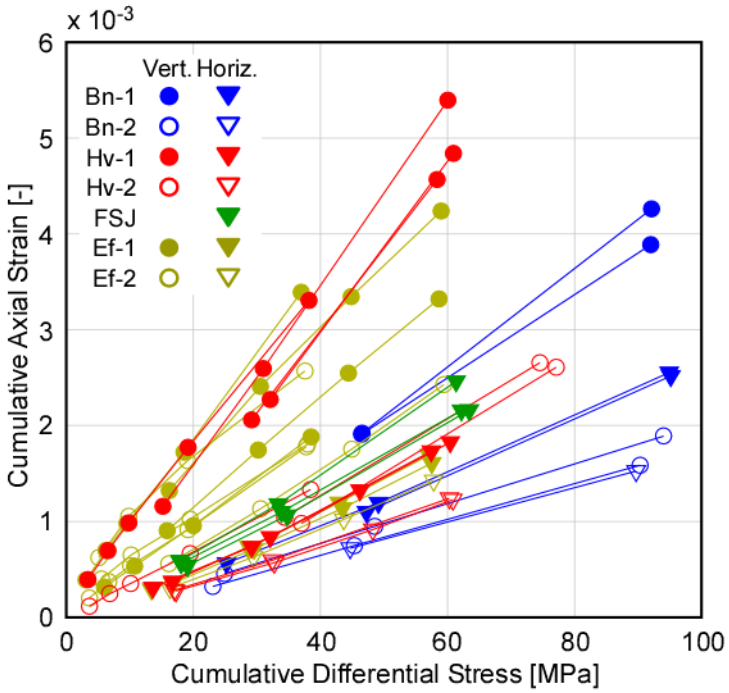

Figure 5.6: Cumulative total axial strain vs. cumulative differential pressure from 3 hour hold data. Each connected plots represent an experiment from a single sample. Bn: Barnett, Hv: Haynesville, FSJ: Fort St John, Ef: Eagle Ford, Vert.: vertical samples, Horiz.; horizontal samples.

We also observe that the slopes indicated by samples of the same rock type and same orientation are fairly consistent. This is despite of the significantly different confining pressure, P_c, employed in each experiment. For instance, P_c varied between 10-60 MPa for the 4 Haynesville-1 vertical sample experiments (red filled circles), but the data points nearly overlap with each other. This suggests that confining pressure is not a major control on the viscoelastic response of these gas shale rocks. Figure 5.7 further illustrates this point by comparing the 3 hour strain responses from several Haynesville-1 samples. In Figure 5.7, strain is normalized by ΔP_{ax} since strain responses are found to be proportional to the applied pressure. For both vertical and horizontal samples, the normalized strain responses nearly overlap with each other.

Therefore the viscoelastic strain response of the studied gas shale rocks is linear against axial differential pressure, ΔP_{ax}, but is not a function of the confining pressure, P_c.

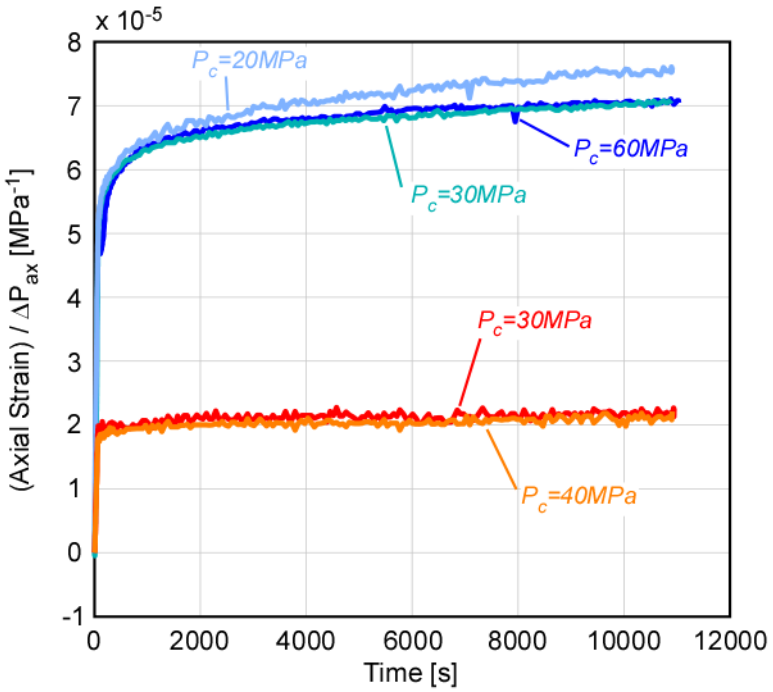

Figure 5.7: Strain responses of Haynesville-1 vertical and horizontal samples during the first pressure step normalized by the magnitude of the applied differential pressures.

5.5 Characterization of Viscoelastic Behavior

In this section, we focus on extracting the kernel functions $J(t)$ and $E(t)$ necessary to carry out a viscoelastic stress analysis from the laboratory data.

5.5.1 Obtaining the Creep Compliance Function, $J(t)$, from Laboratory Data

The laboratory strain data we obtain from each differential pressure step is not strictly the kernel strain response, $J(t)$, to an instant stress input because differential pressure is applied over 60 seconds. This is because the laboratory observed strain response corresponds to the left-hand-side of Equation 5.3, which is not equal to $J(t)$ unless $d\sigma/dt$ is represented by a Dirac-delta function, or $\sigma(t)$ is a Heaviside step

function. However, 60 seconds is a very short time interval compared to the total observation time of creep deformation (at least 3 hours ≈ 10^4 seconds). Thus as observation time increases, the observed strain approaches the strain response that would have resulted from a true instantaneous Heaviside stress input. Therefore it is customary in laboratory studies of viscoelastic creep behavior to discard the initial portion of the strain data and only analyze the remaining strain data to infer the creep compliance function, *J(t)* (Lakes, 2009). Following this approach, we discard the initial 100 seconds of the strain response data from each pressure step, and divide the remaining strain response data with the magnitude of the pressure step (shown later in Figure 5.10) to gain information about the creep compliance function, $J(t)$. Hereon, we will refer to the outcome of this "cut and scale" procedure as the *creep compliance* data, which will have the units of MPa^{-1}. We confirmed that this approach works very well in recovering information about the true creep compliance response. A complete verification of this approach is provided in Appendix A.

5.5.2 Constitutive Relations of the Creep Compliance: Implication from Long-Term Creep Experiments

The creep compliance data from each pressure steps give us the raw data for the creep compliance function, *J(t)*. We are now interested in finding an analytical representation of *J(t)* that will allow us to perform a quantitative stress analysis. Figure 5.8 shows some examples of creep compliance data obtained from 3 hour hold experiments plotted against the logarithm of time. The data in Figure 5.8 correspond to those in Figure 5.5. It is observed that the relation between the creep compliance and logarithm of time is fairly linear suggesting a logarithmic constitutive relation between strain and time of the following form:

$$\varepsilon = \sigma * A\log_{10}(t) \tag{5.8}$$

where A is a constant. This is generally consistent with the primary creep behavior observed in the study of brittle creep in rocks such as granite (Lockner, 1993). Since a secondary creep behavior that departs from this logarithmic relation is also observed

in brittle creeps of granites, we are motivated to check if this logarithmic relation holds for longer time periods in the creep of gas shales.

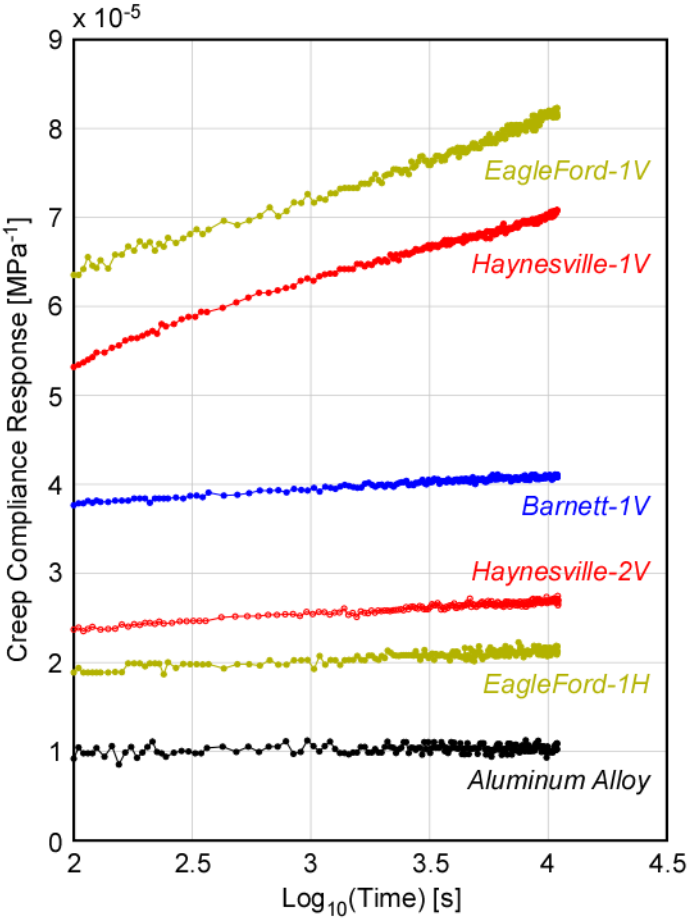

Figure 5.8: 3-hour creep compliance data vs. logarithm of time. All data come from the same samples and same pressure steps as those from Figure 5.5.

Figure 5.9 shows the creep compliance data from the longest hold time experiment (2 weeks) conducted with a Haynesville-1 vertical sample, plotted against the logarithm of time. When experiments last longer than about a day, the axial strain data collected by LVDT sensors is affected by the slight fluctuation in the temperature inside the pressure vessel. Thus, the temperature corrected strain data is plotted in Figure 5.9 (See Appendix B for the temperature correction method). From the 2 week creep compliance data, we see that there is some upward concavity not captured by a linear trend suggested from a logarithmic function. If we compared the 2 week data with the linear trend predicted from the initial 3 hours of data (the red straight line in

Figure 5.9) we observed that the blue data starts to depart from the red line at sometime between 10^4-10^5 seconds. In this case we find that the 2 weeks data is much better represented by a power-law function of time of the following form:

$$\varepsilon = \sigma * Bt^n \tag{5.9}$$

where B is a constant and n is the power-law exponent. For creep deformation, n is between 0 and 1. The black curve in Figure 5.9 is a regression of Equation 5.9 to the entire data up to 2 weeks. We can conclude from the fit that a power-law function is a better formulation than a logarithmic function at capturing the primary and secondary creep behavior altogether over longer time scales.

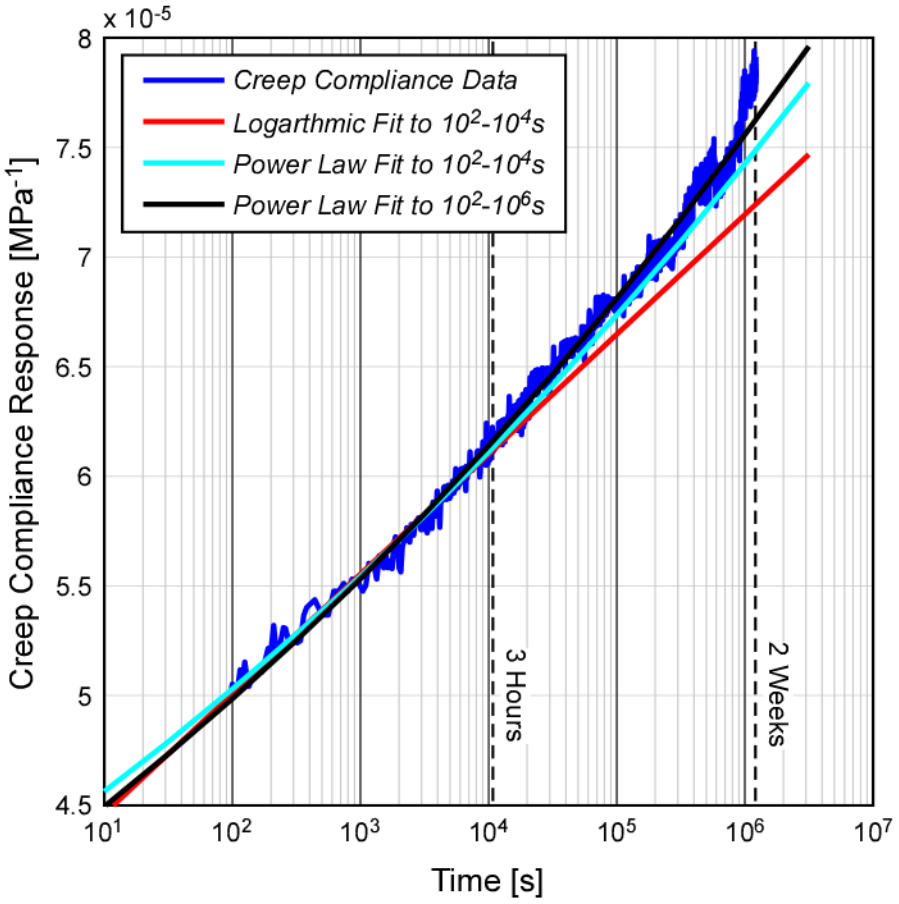

Figure 5.9: Two-week long creep compliance data of a Haynesville-1 vertical sample along with regressions of logarithmic and power-law constitutive relations.

We also examined the error of only having 3 hours worth of data since the departure from the logarithmic behavior was not necessary captured by the first 3 hours of creep compliance data (Figure 5.8). The cyan curve in Figure 5.9 is a regression of the power-law function to only the initial 3 hours of the creep compliance data. Although the cyan curve does not exactly overlap with the black curve obtained by fitting the power-law function to the entire data, it captures the overall trend better than a logarithmic function. Therefore, we will be using Equation 5.9 as our best analytical model to describe the creep compliance behavior of all of the gas shale samples studied although not all creep data lasts longer than 3 hours.

5.5.3 Constitutive Parameters from Laboratory Data

We now characterize all of our creep compliance data by utilizing the power-law expression shown in Equation 5.9 as the constitutive relation between creep strain and time. In order to recover the 2 constitutive parameters, B and n, in Equation 5.9 from laboratory data, each creep compliance data was fit by a straight line in the log(time)-log(strain) space (Figure 5.10). This greatly simplifies the regression procedure to obtain B and n, since the intercept of the linear fit (in the log-log space) with t=1s gives us the logarithm of the constant B, and the slope of the linear fit (in the log-log space) directly gives us the power-law exponent, n.

Figure 5.11 summarizes the results from the regression of Equation 5.9 to each creep compliance data. Each panel shows the power-law exponent, n, plotted against B for each sample group. Since several pressure steps were conducted using a single sample, several pairs of B and n values are obtained for a single sample. The average of those values is shown by the circle and triangle plots, for vertical and horizontal samples, respectively. The boxes surrounding the plots represent the variability of B and n values observed from a single sample. The horizontal and vertical span of the boxes is determined by the maximum and minimum values of B and n observed from a sample. Note that all axes are scaled equally in the figure.

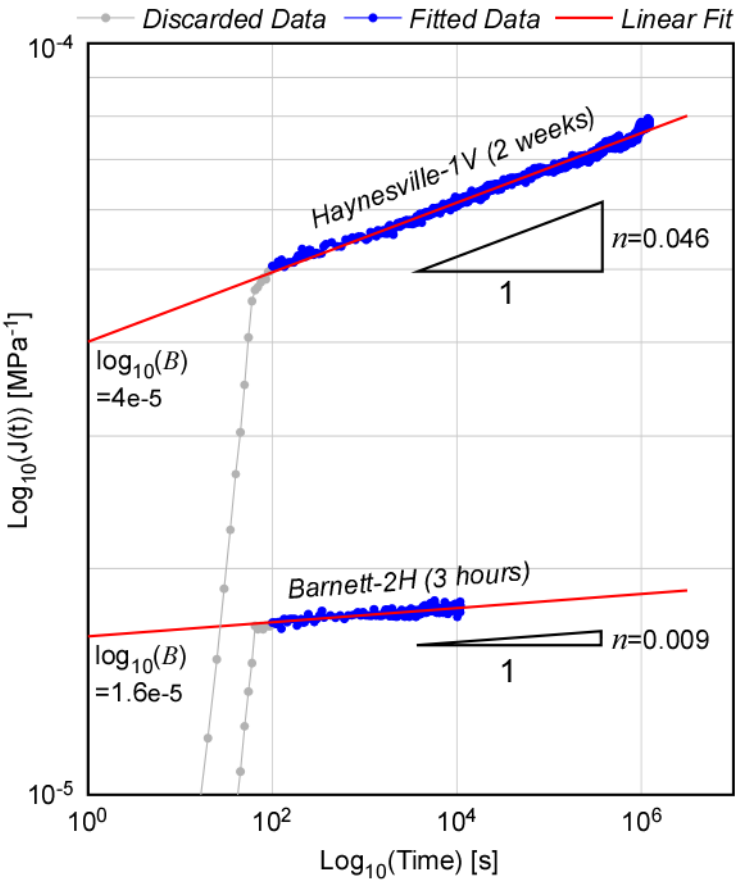

Figure 5.10: Some examples of linear regression performed in the log-log space to determine constitutive parameters, *B* and *n*. The grey data is the first 100 seconds which is not considered in the regression due to its proximity to the pressure step.

Comparison between each panel in Figure 5.11 shows that different sample groups clearly possess different ranges of values of *B* and *n*. For instance, Barnett shale samples possess relatively lower *B* and *n* values, whereas Haynesville and Eagle Ford samples show relatively higher *B* and *n* values. Within the same reservoir, it is generally seen that the relatively clay- and organic-rich sample group (subgroup 1) possess higher *B* and *n* values compared to the other. We also observe that vertical samples generally possess higher *B* and *n* values compared to the horizontal samples. Thus there is anisotropy in the viscoelastic behavior.

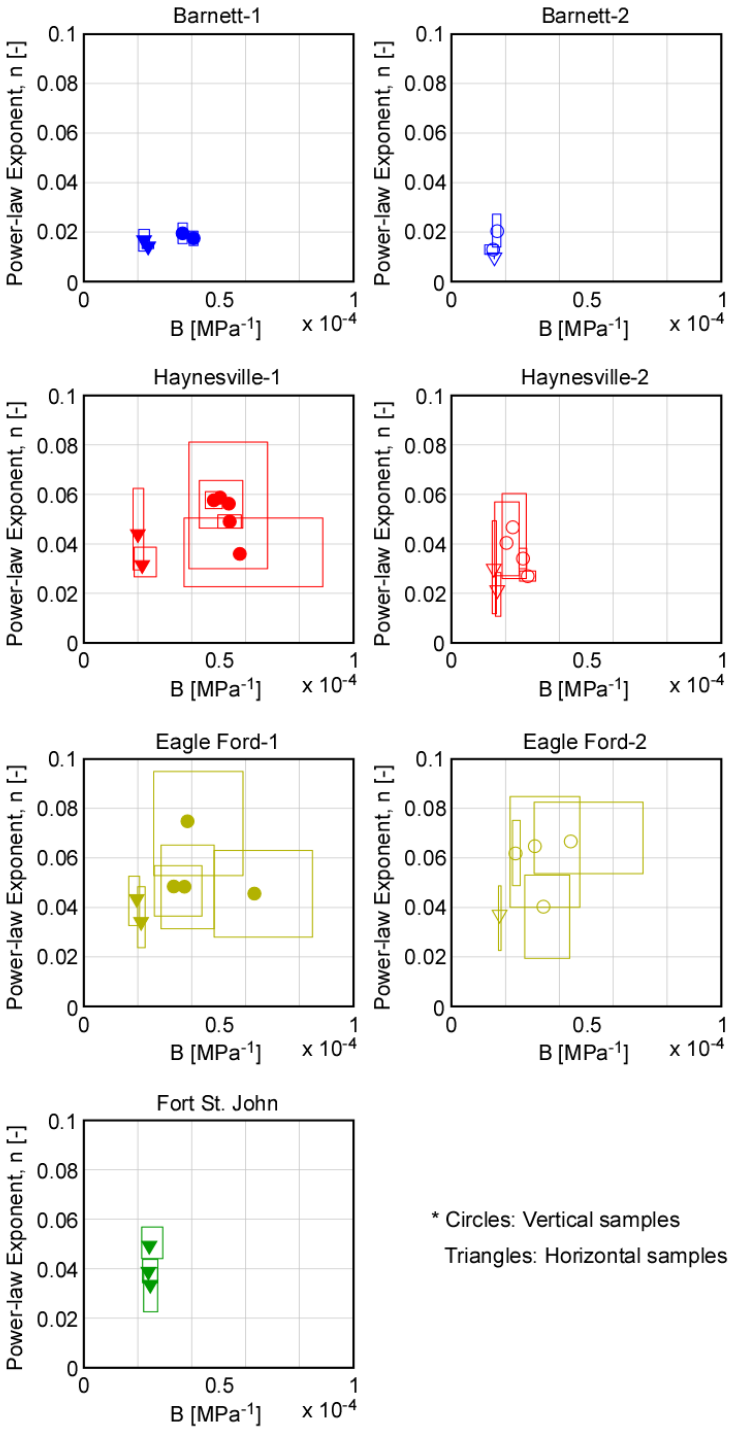

Figure 5.11: Summary of the constitutive parameters determined from the creep compliance data. Each panel shows data from each sample group. Each data point represents the average value of the constitutive parameters determined for a single sample. The boxes represent the variability of constitutive parameters determined for each sample.

Another important observation to make from Figure 5.11 is the consistency of the constitutive parameters determined within a sample group and within an experiment. The constitutive parameters determined for Barnett-1, Barnett-2, Fort St. John, and Haynesville-2 shale samples all show that the values are fairly consistent within those sample groups for a given orientation. The relatively small boxes in these samples groups also indicate that the constitutive parameters are consistent within an experiment. This is an important feature since it implies how consistent the viscoelastic behavior is against pressure, which is a requirement for linear viscoelastic behavior. However, samples from Haynesville-1, Eagle Ford-1, and Eagle Ford-2 shale samples exhibit a wide range of constitutive parameters, particularly for the vertical samples. This implies that the viscoelastic behavior of these samples is not truly consistent with pressure, violating the requirement for a linear viscoelastic behavior to a certain degree. For additional verifications of linearity, see Appendix C and D. Nonetheless, when constitutive parameters from all reservoirs are compared

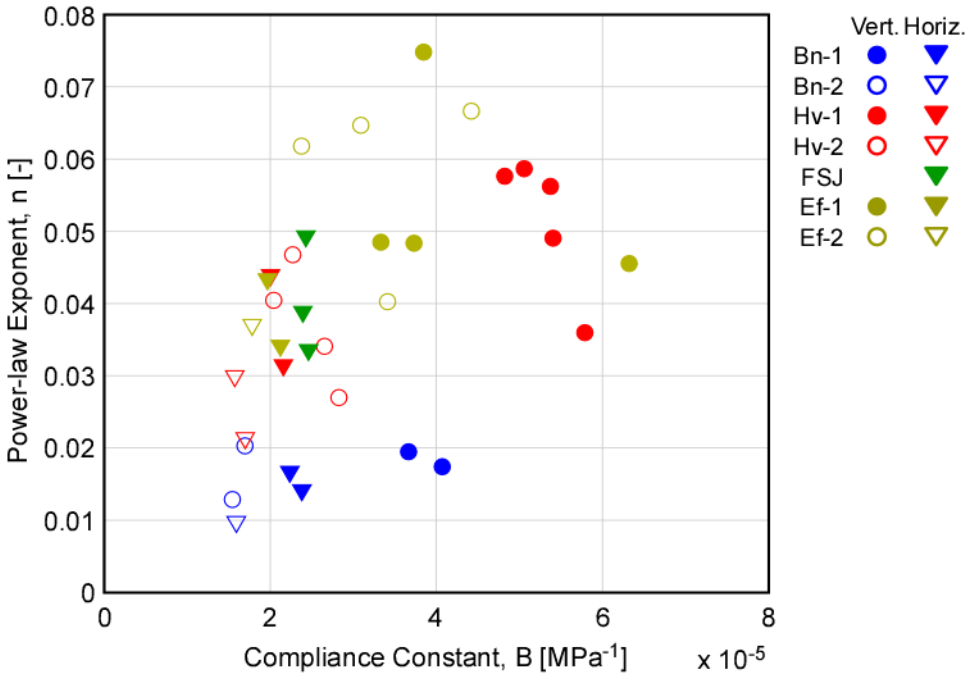

Figure 5.12: Compilation of the average constitutive parameter values determined for each sample.

against each other (Figure 5.12), we do find that data from each sample group span a different region in the *B*-*n* parameter space. Therefore, despite the scatter in data for some sample groups, characterization of the viscoelastic behavior through a power-law constitutive relation effectively differentiates the viscoelastic mechanical properties of the studied samples. We also note that from Figure 5.12, we may see a weak positive correlation between the two constitutive parameters *B* and *n*.

5.5.4 The Meaning of the Constitutive Parameters

Although the physical meaning of the parameters *B* and *n* are not defined in Equation 5.9, they reflect important characteristics of the viscoelastic behavior of the samples. A strict interpretation of Equation 5.9 indicates that constant *B* is the amount of strain that occurs after 1 second in response to a unit input of stress. *B* therefore has a unit of (pressure)$^{-1}$. We interpret that *B* essentially reflects the instantaneous elastic response of the rock, since, when $n<0.1$, strain rate drops by an order of magnitude after $t=1$s compared to the average strain rate during the first 1 second. That is, from Equation 5.9, for a unit input of stress $\sigma=1$:

$$\left.\begin{array}{c} \varepsilon(0) = B0^n = 0 \\ \varepsilon(1) = B1^n = B \\ \varepsilon(2) = B2^n < 1.07B \quad (n < 0.1) \end{array}\right\} \Rightarrow \begin{cases} \dot{\bar{\varepsilon}}(0 < t < 1) = B \\ \dot{\bar{\varepsilon}}(1 < t < 2) < 0.07B \quad (n < 0.1) \end{cases} \tag{5.10}$$

Thus the strain that takes place in the initial 1 second of the creep compliance response can essentially be regarded as instantaneous relative to the slow deformation that follows. Such interpretation is justified by the comparison of the elastic moduli inferred from the constant *B* and the Young's modulus that was measured after each observation of creep. Figure 5.13 plots the inverse of *B* against the measured Young's modulus. There is some scatter in the trend between the two quantities, but it is clear that they correlate with each other and the trend overlaps the 1-to-1 correspondence line. Therefore, *B* is roughly a measure of the elastic compliance of the rock and $1/B$ is a rough measure of the rock elastic stiffness. We will call *B* the compliance constant.

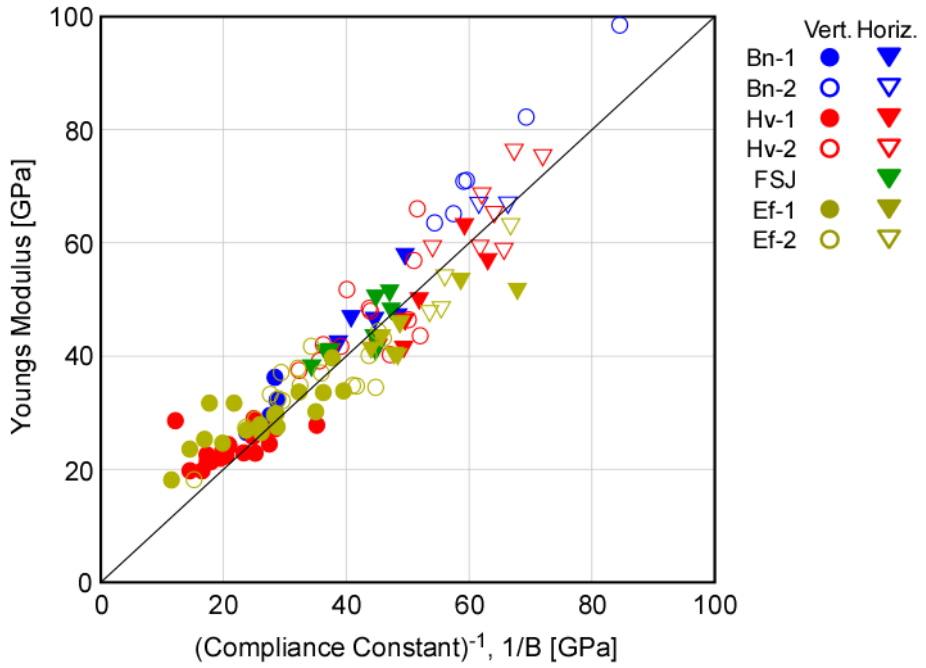

Figure 5.13: Comparison between Measured Young's modulus and stiffness of the rock inferred by the inverse of the compliance constant, *B*.

On the other hand, the power-law exponent, *n*, can be regarded as a parameter that describes the tendency to exhibit non-elastic deformation. If we regard the strain in the first 1 second as the elastic strain, *n* determines how much more time-dependent strain takes place after the first second relative to the elastic strain. Again for a unit input of stress σ=1, from Equation 5.9:

$$\varepsilon(t)_{non-elastic} = \varepsilon(t) - \varepsilon(1) = Bt^n - B1^n = B(t^n - 1)$$
$$\frac{\varepsilon(t)_{non-elastic}}{\varepsilon_{elastic}} = \frac{B(t^n - 1)}{B} = (t^n - 1) \qquad (5.11)$$

In other words, *n* determines the relative contribution of the time-dependent deformation to the total strain observed at a certain time. Larger *n* values will yield more pronounced creep behavior and *n*=0 will yield no time-dependent deformation, thus an elastic rock. Therefore the weak positive relation between *B* and *n* from Figure 5.12 could imply that in general, an elastically compliant rock tends to exhibit more time-dependent behavior.

5.5.5 Magnitude of Creep Strain over Geological Time

In order to obtain a physical sense of the magnitudes of deformation suggested by the constitutive parameters, we calculate the creep strain that would occur under a constant differential pressure of 50 MPa over 100 Ma for the combination of *B* and *n* parameter values represented by the gas shale samples. 100 Ma was chosen since the age of most shale gas reservoirs are on the order of 100 Ma. In Figure 5.14, the resulting axial creep strain is shown as contours in the *B*-*n* parameter space. Results show that rock deformation of these gas shales will be between 0.1-3% strain if the creep deformation is to be extended to geological time scales. Considering that the porosities of these rocks are about 1-8% and also that rocks generally fail at strains on the order of 1%, the magnitude of the predicted creep deformation are physically reasonable.

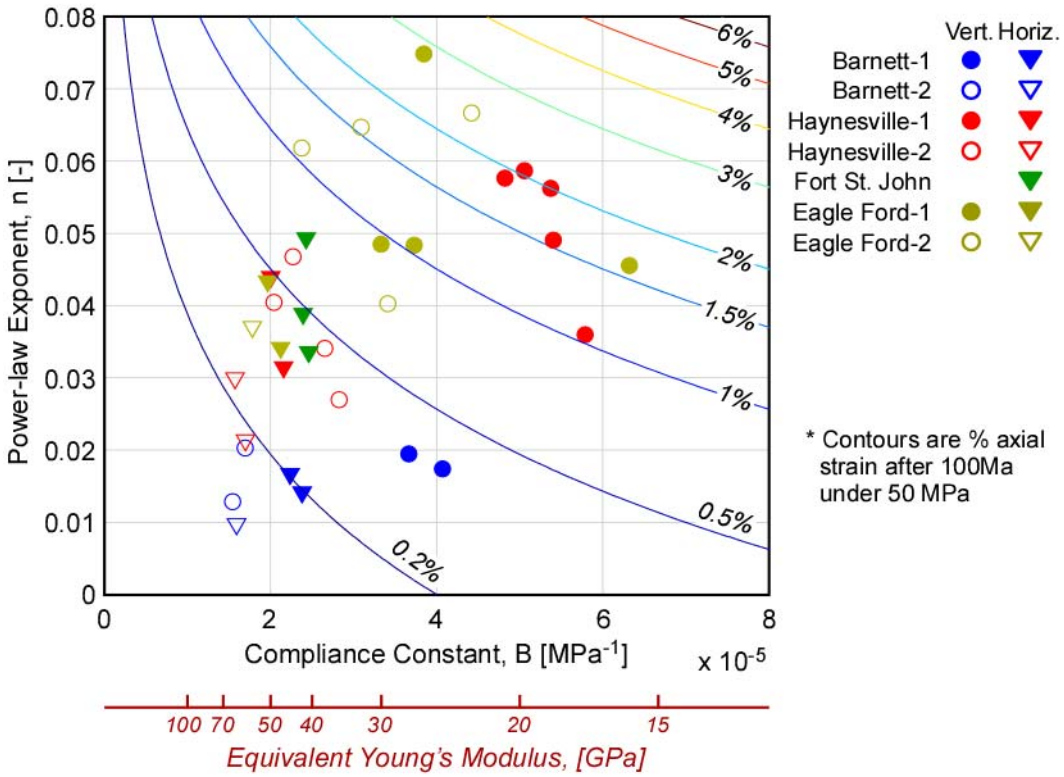

Figure 5.14: Creep strain over 100 Ma under 50 MPa differential stress.

5.6 Implications for Differential Stress Accumulation

5.6.1 Obtaining the Relaxation Modulus from Creep Compliance

Given parameter values that describe the power-law viscoelastic creep behavior of the gas shale samples, we analyze the differential stress bearing capacity of the samples. First we derive the corresponding analytical expression for the relaxation modulus of a material that exhibits power-law creep shown by Equation 5.9. Following the steps described in section 5.2.2, we perform a Laplace transform, use Equation 5.7, then perform an inverse Laplace transform:

$$
\begin{aligned}
J(t) &= Bt^n \\
J(s) &= \frac{B\Gamma(n+1)}{s^{1+n}} \\
E(s) &= \frac{1}{s^2 J(s)} = \frac{1}{B\Gamma(n+1)} \frac{1}{s^{1-n}} \\
E(t) &= \frac{1}{B\Gamma(1+n)\Gamma(1-n)} t^{-n} \approx \frac{1}{B} t^{-n}
\end{aligned}
\tag{5.12}
$$

$\Gamma(x)$ is the gamma function, and the final approximation is for $n \ll 1$. The error introduced by the approximation is 1.7% when $n=0.1$, a value greater than those measured. The result in Equation 5.12 indicates that we can directly take the constitutive parameters constrained from the creep experiments to predict the relaxation behavior of the rock. This simplicity for analyses was one of the advantages of employing a power-law function of the form described in Equation 5.9. With the relaxation modulus, *E(t)*, defined, we can now perform a stress analyses utilizing Equation 5.4.

5.6.2 Stress Accumulation and Relaxation under Constant Strain Rate

We are now interested in evaluating what kind of stress variation can be inferred from the differences in the viscoelastic properties possessed by the various shale gas reservoir rocks. Of our particular interest is whether the observed variation in the horizontal stress difference from a well in the Barnett shale (Chapter 4) can be

explained as the result of the variation in viscoelastic properties observed in Barnett shale. Stress analysis using Equation 5.4 requires us to construct a strain history of the Barnett shale reservoir. This is done ideally by a fine examination of the tectonic history of the reservoir, but such information is not always available. Therefore we may at best evaluate the viscoelastic stress history for a simple first order tectonic scenario. We will construct a model scenario based on information available for the Barnett shale.

Figure 5.15 shows the burial history of the Fort Worth Basin provided in Curtis (2002). Barnett shale deposited at around the Mississippian period and was buried down to roughly 3km of depths over the next 50 Ma. Maturation and hydrocarbon generation took place at this depth over about 100 Ma. The uplift started at around mid-Cretaceous period until it reached the current depth at around the end of the Paleogene period. Motivate by this burial history, we suggest that the Barnett shale acquired its current viscoelastic property at around the mid-point of its history when diagenesis and maturation likely completed at about 150 Ma. Under this assumption, we will evaluate how much horizontal stress difference, S_{Hmax}-S_{hmin}, would accumulate under a steady tectonic loading with a constant horizontal strain rate for 150 Ma. Note that we are ignoring the effect of uplift and the associated temperature change since stress changes caused by these factors will be horizontally isotropic and we are primarily interested in the horizontal stress differences.

When the strain rate in a viscoelastic material is constant, Equation 5.4 simplifies to:

$$\begin{aligned}\sigma(t) &= \int_0^t E(t-\tau)\frac{d\varepsilon(\tau)}{d\tau}d\tau \\ &= \dot{\varepsilon}\int_0^t E(t-\tau)d\tau \\ &= -\dot{\varepsilon}\int_t^0 E(T)dT \end{aligned} \qquad (5.13)$$

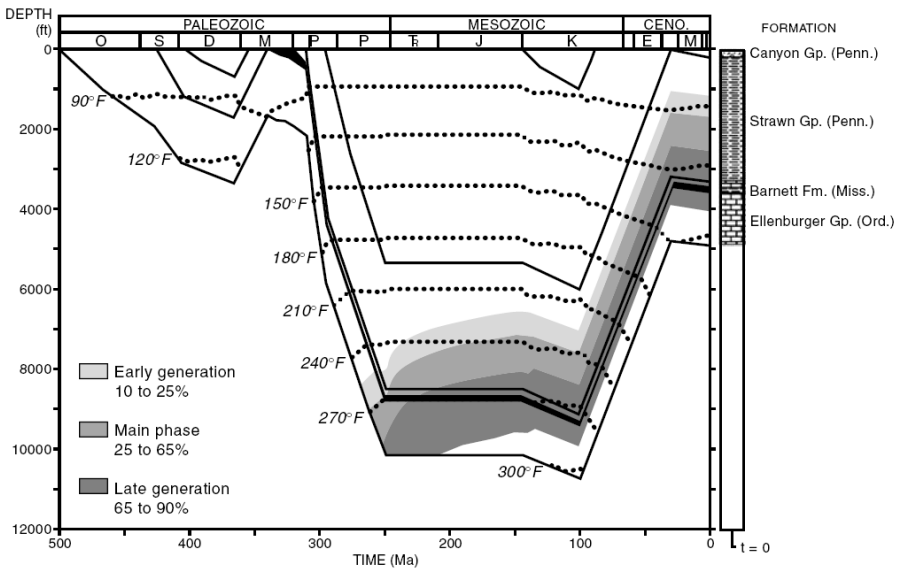

Figure 5.15: Burial history of the Fort Worth Basin. Figure from Curtis (2002), after Jarvie et al. (2001).

For a power-law relaxation modulus described by Equation 5.12, Equation 5.13 yields:

$$\begin{aligned}\sigma(t) &= -\dot{\varepsilon}\int_t^0 \frac{1}{B}T^{-n}dT \\ &= \dot{\varepsilon}\frac{1}{B(1-n)}t^{1-n}\end{aligned} \tag{5.14}$$

Therefore, by specifying the constant strain rate and the duration of the deformation, we can evaluate the stress accumulated in a rock with a certain value of B and n.

As discussed previously, we take the duration of the tectonic deformation as 150 Ma. For the strain rate, it will be appropriate to use those of plate interiors since all of the shale gas reservoirs studied here are located in a relatively stable intraplate region. The fact that plates are rigid over geological time provides an upper bound of intraplate strain rates at about 10^{-18} s^{-1} (Zoback and Townend, 2001; Sleep and Zoback, 2007). The lower bound can be estimated from the fact that there is about a 30 MPa horizontal stress difference observed in the reservoir from Chapter 4. Since the horizontal Young's modulus of the Barnett shale reservoir rocks were found to be between 40-60 GPa, it requires that there has been at least 5-7.5 $*10^{-4}$ horizontal strain

difference accumulated in the formation over the age of the Barnett shale (300Ma) in the absence of viscoelastic relaxation. These information yield a lower limit average strain rate of about 5-8 $*10^{-20}$ s^{-1} strain rate. Sleep and Zoback (2007) also estimates the lower bound of intraplate strain rates to be a few times 10^{-20} s^{-1} by acknowledging that intraplate stress orientation are dominated by "renewable stresses" owing to lithospheric body forces (Zoback et al., 1989) rather than "nonrenewable stresses" such as change in Earth's radius/ellipticity or changes in local geotherms. Honoring these bounds on intraplate strain rates, we take the constant strain rate to be 10^{-19} s^{-1} in our stress analyses.

Figure 5.16 shows the result of the calculation for the stress accumulated under strain rate of 10^{-19} s^{-1} over 150 Ma as a function of the constitutive properties, *B* and *n*, overlain on laboratory data. Where the contours intercept with the horizontal axis (*n*=0) shows what the stress accumulation would be if the rock were to behave elastically without any time-dependent deformation. However as *n* increases and time-dependent deformation becomes more pronounced, the stress-carrying capacity of the rock diminishes. For instance, the Eagle Ford-1 horizontal sample with *B* and *n* values of about 2e-5 MPa^{-1} and 0.04, respectively, would be predicted to carry more than 20 MPa of horizontal stress anisotropy if its time-dependent behavior was ignored, but in reality would only carry about 5 MPa of horizontal stress anisotropy under this loading condition. Figure 5.16 illustrates how the present state of stress cannot be inferred from only its elastic properties.

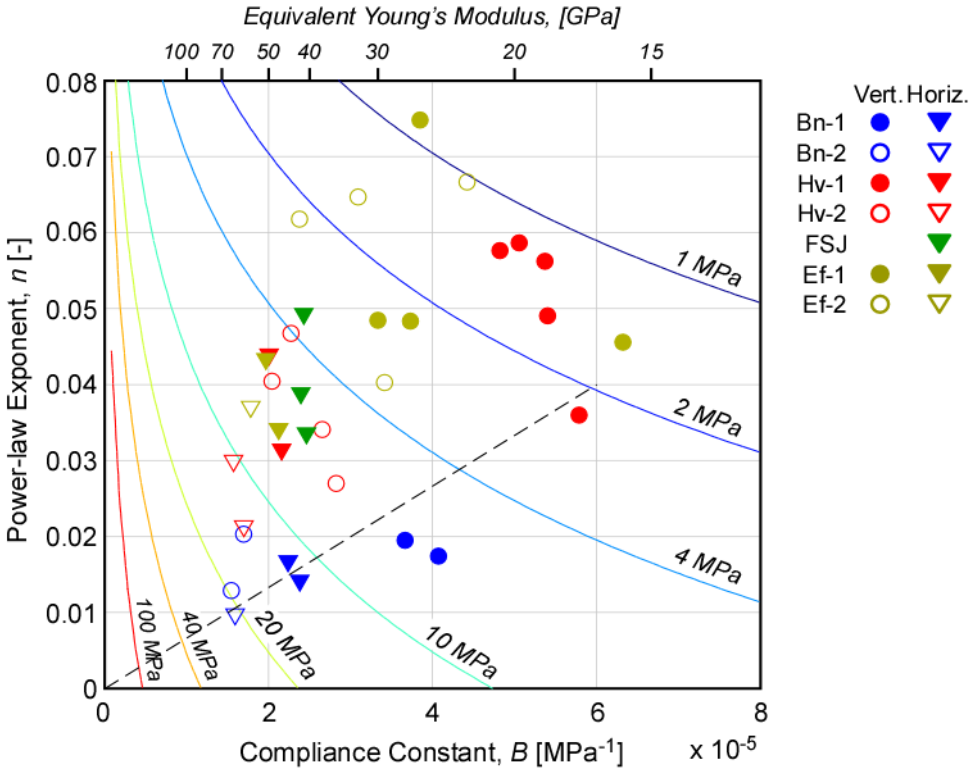

Figure 5.16: Stress accumulation calculated for a constant strain rate of 10^{-19} s^{-1} at 150 Ma described by contours overlain on *B* and *n* values determined from the experiments. The dashed line is a linear trend for Barnett horizontal samples used in a later analysis. The equivalent Young's modulus inferred from the inverse of *B* is also displayed at the top.

5.6.3 Stress Accumulation and Relaxation under Variable Strain Rates

Stress calculations from the previous section was simplified by assuming a constant strain rate throughout time, but actual strain rates likely vary in time. Since we are considering the process of time-dependent accumulation and relaxation of stress, it is important to evaluate how results may deviate from the previous section under various scenarios of tectonic strain rate history.

In order to cover the full spectrum of possibilities, we considered several tectonic strain rate histories as shown in Figure 5.17. In all cases, the total strain is fixed at ε_0 = [150 Ma] * [10^{-19} s^{-1}] = 0.000473, but the timing at which the tectonic strain occurs is varied. The "instantaneous-past" scenario represents all strain happening at the beginning and then strain remaining constant throughout time. The

"instantaneous-current" scenario represents all strain happening at the end of the history. The "rapid-recent" scenario represents all strain happening towards the end of the history at 10^{-18} s^{-1} strain rate.

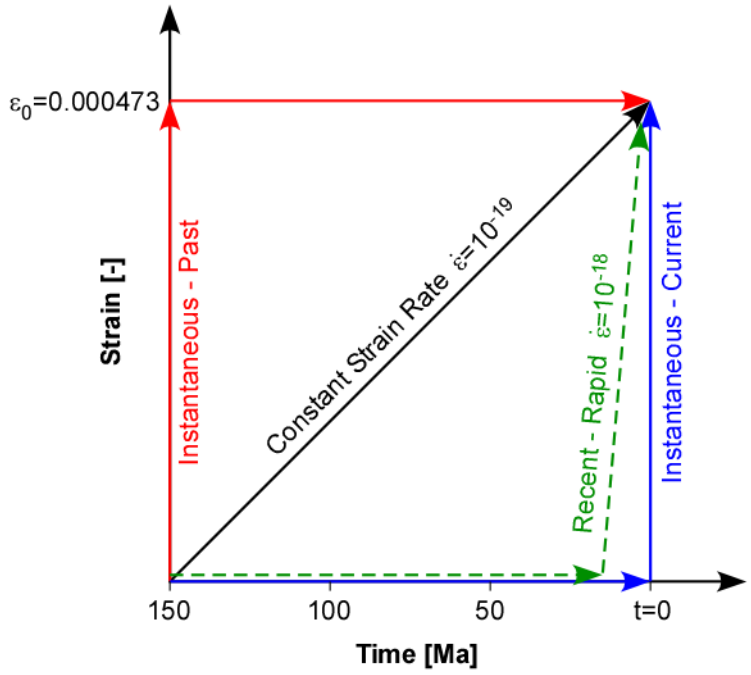

Figure 5.17: Strain rate histories considered in the stress analyses for non-constant strain rate histories.

Figure 5.18 compares the results of the stress calculations from the instantaneous-past, constant strain rate (10^{-19} s^{-1}), recent rapid (10^{-18} s^{-1}), and instantaneous-current scenarios. Results show that there is very little difference in the calculated stress between the instantaneous-past, constant strain rate, and recent-rapid scenarios (Figure 5.18a-5.18c). Thus, any strain history path that lies in between the instantaneous-past and recent-rapid strain paths practically has no difference in determining the current state of stress. The instantaneous-current result, however, is quite different from the others because it essentially shows the elastic response of the rock (Figure 5.18d). There is no time for the stress to relax after the application of strain in this scenario. Thus, if all horizontal tectonic strain were to take place at the very end of the strain history, results may appear different from those suggested from the constant strain rate scenario. However, unless we can obtain specific accounts on

evidence of a very rapid tectonic event in the past few million years, it is unlikely that this is the real case.

These results suggest that the effect of variable strain rates is minimal for the purpose of analyzing the stress accumulation/relaxation behavior of gas shale rocks. Therefore a stress calculation assuming a constant strain rate is sufficient enough to discuss the first order stress accumulation/relaxation in these shale gas reservoirs.

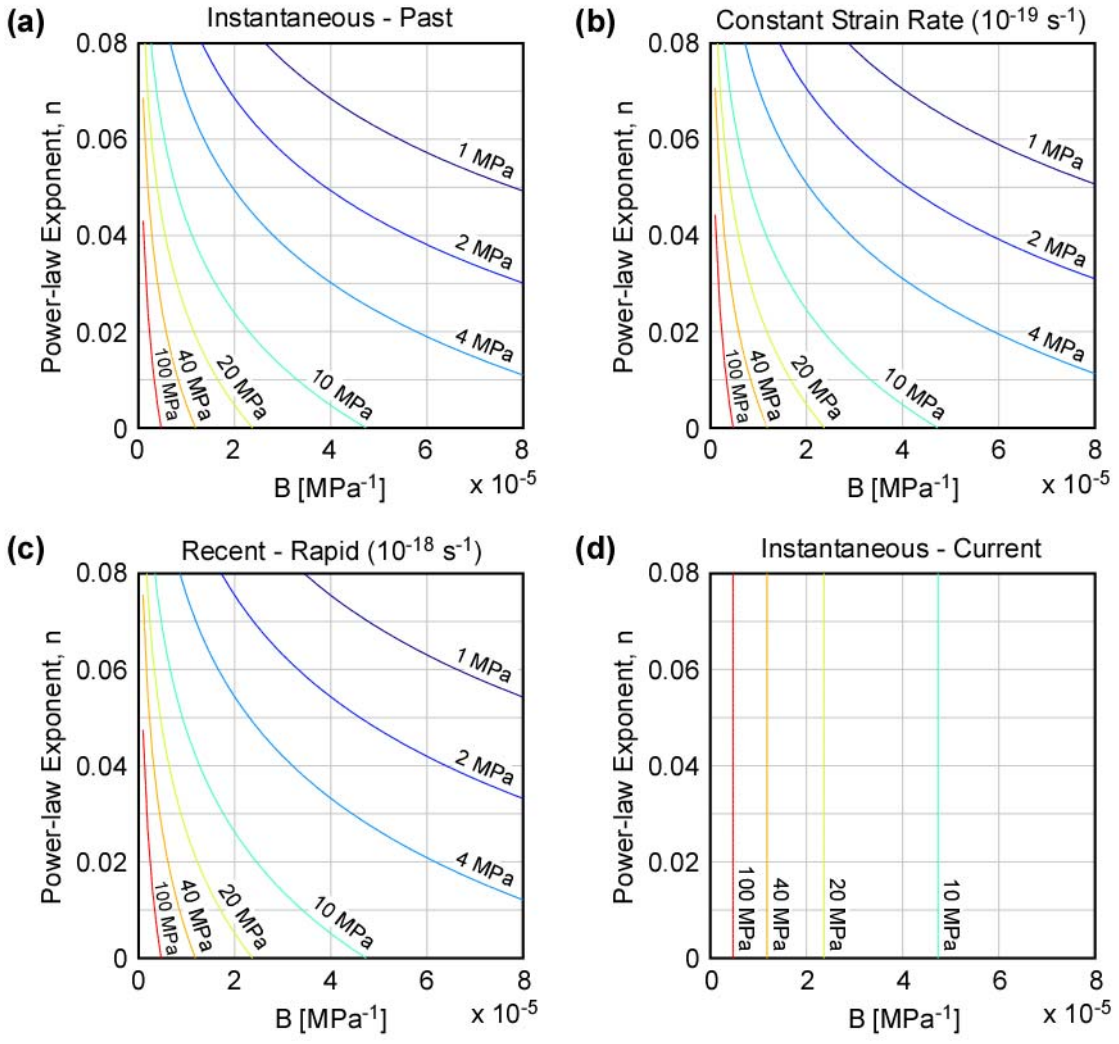

Figure 5.18: Differential stress calculated for the four strain rate histories shown in Figure 5.17. (a) Instantaneous-past, (b) Constant strain rate (10^{-19} s^{-1}), (c) Recent-rapid (10^{-18} s^{-1}), and (d) Instantaneous-current.

5.6.4 Variation in Horizontal Stress Differences in the Barnett Shale

In the Barnett shale, drilling-induced tensile fractures were observed to disappear at where gamma ray responses are high, and reappear at where gamma ray responses are low (Chapter 4, Figure 4.9). Barnett-1 and Barnett-2 samples in this study represent rocks from the high- and low-gamma ray regions, respectively, in the same well, thus we now focus on the stress differences carried by these rocks under the assume loading history. Figure 5.16 shows that a formation represented by Barnett-1 horizontal samples (filled blue triangles) would carry about 10 MPa of horizontal stress anisotropy under the assumed tectonic loading scenario. On the other hand, a formation represented by the Barnett-2 sample would carry about 20 MPa of horizontal stress anisotropy. Thus about a 10 MPa difference in the horizontal stress anisotropy is predicted from our calculation.

Figure 5.19 shows the stress polygon diagram at 8500 ft depth for the well studied in Barnett shale. The green area indicates the state of stress in the Barnett shale reservoir constrained from the presence of drilling-induced tensile fractures (DITFs). However observations from Chapter 4 suggested that DITF was absent in sections with higher clay and organic content, and the stress state at these layers shall fall some where to the right of the T_0=0 contour (blue line). The red lines represent contours of constant horizontal stress difference (hereon, S_H-S_h) drawn at 10 MPa intervals. We see from Figure 5.19 that the actual horizontal stress difference at where DITFs are present is about 30 MPa. This is 50% higher than what we calculated using Barnett-2 horizontal sample properties. However, the error in the absolute stress difference is not significant considering the simplifications involved in the assumed loading history. More importantly, we see that a 10 MPa variation in S_H-S_h inferred from the stress analysis is a reasonable magnitude change that would cause the reservoir state of stress to cross over the T_0=0 line, which could cause DITFs to appear and disappear with the variation in lithology as observed.

To put the above argument into perspective, we calculated the accumulated horizontal stress difference along the studied well using the sonic log data. In order to

obtain a continuous profile of the constitutive parameters B and n, several correlations and assumptions derived in this Chapter and in Chapter 2 were used.

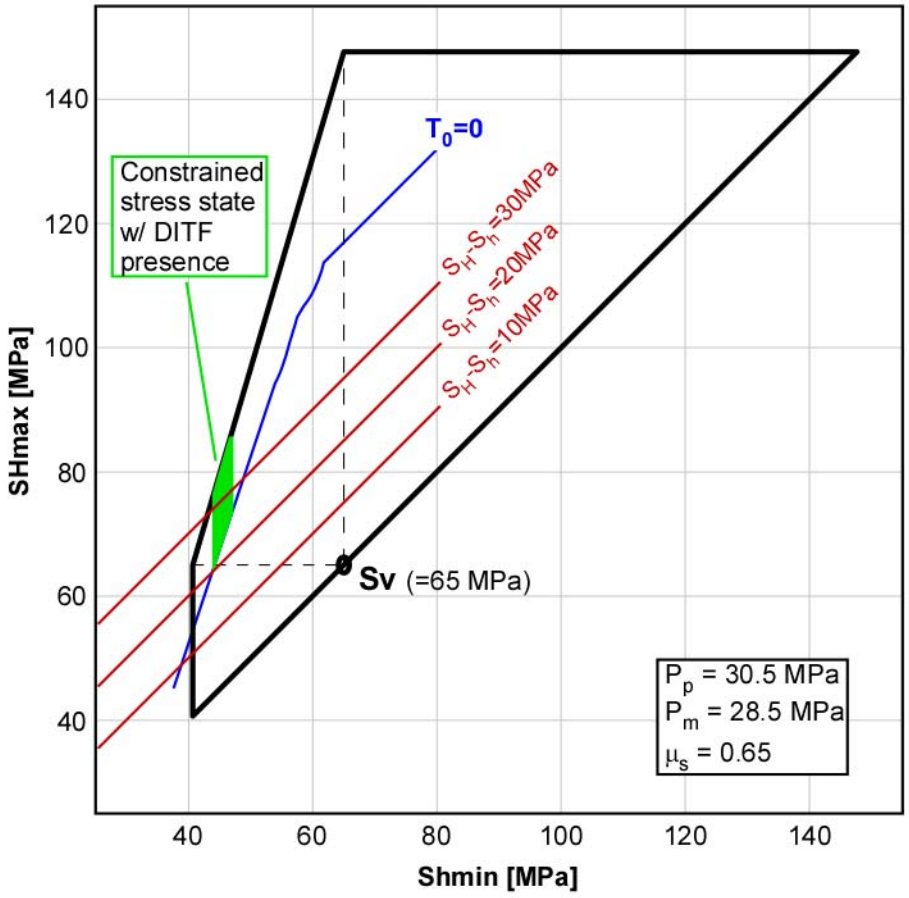

Figure 5.19: Stress polygon representation of the constrained state of stress in a well in Barnett shale at 8500 ft depth. The blue line indicates boundary of DITF occurrence when tensile strength is zero. Red contours indicate constant horizontal stress differences.

First the p-wave modulus, M, and the s-wave modulus, μ, can be used to obtain the vertical dynamic Young's modulus:

$$E_{vertical}^{dyn} = \frac{\mu(3M - 4\mu)}{(M - \mu)} \tag{5.15}$$

This is not strictly correct for an anisotropic rock, but it was found from Appendix C of Chapter 2 that the error for ignoring the anisotropy is very small. Then dynamic Young's modulus is assumed to be the same as the static Young's modulus following observations from Figure 2.9b that the unloading/reloading static modulus is more or less the same as the dynamic modulus ($E_{vertical}^{dynamic} \approx E_{vertical}^{static}$). Note that the static Young's modulus plotted in Figure 5.13 was measured from the unloading/reloading stress-strain relation. Then the horizontal Young's modulus is inferred from the vertical Young's modulus using the correlation between the Young's modulus anisotropy, $E_{horizontal}/E_{vertical}$, and vertical Young's modulus, $E_{vertical}$, (Figure 2.10e):

$$\frac{E_{horizontal}}{E_{vertical}} = 9.91 * E_{vertical}^{-0.543} \tag{5.16}$$

Since B is essentially the inverse of the static Young's modulus ($B \approx E^{-1}$, Figure 5.13), we now have a continuous estimate of B. Finally, from Figure 5.16, we can estimate the relation between the constitutive parameters B and n from a line that goes through the horizontal Barnett shale data points (black dashed line in Figure 5.16):

$$n = \frac{2000}{3} B \tag{5.17}$$

Now by applying the same loading conditions as before, a constant strain rate of 10^{-19} s^{-1} over 150 Ma, a continuous profile of the horizontal stress difference is obtained.

Figure 5.20 shows an example of the profile, which is the same depth range as the image log shown in Figure 4.9. There is a reasonable agreement between the section where DITF is not observed and the section where the horizontal stress difference is relatively small compared to the surrounding formation. Therefore we confirm that our stress analyses taking in account the viscoelastic properties of the gas shales gives reasonable results to the first order for predicting variation of stress magnitudes along the length of the well.

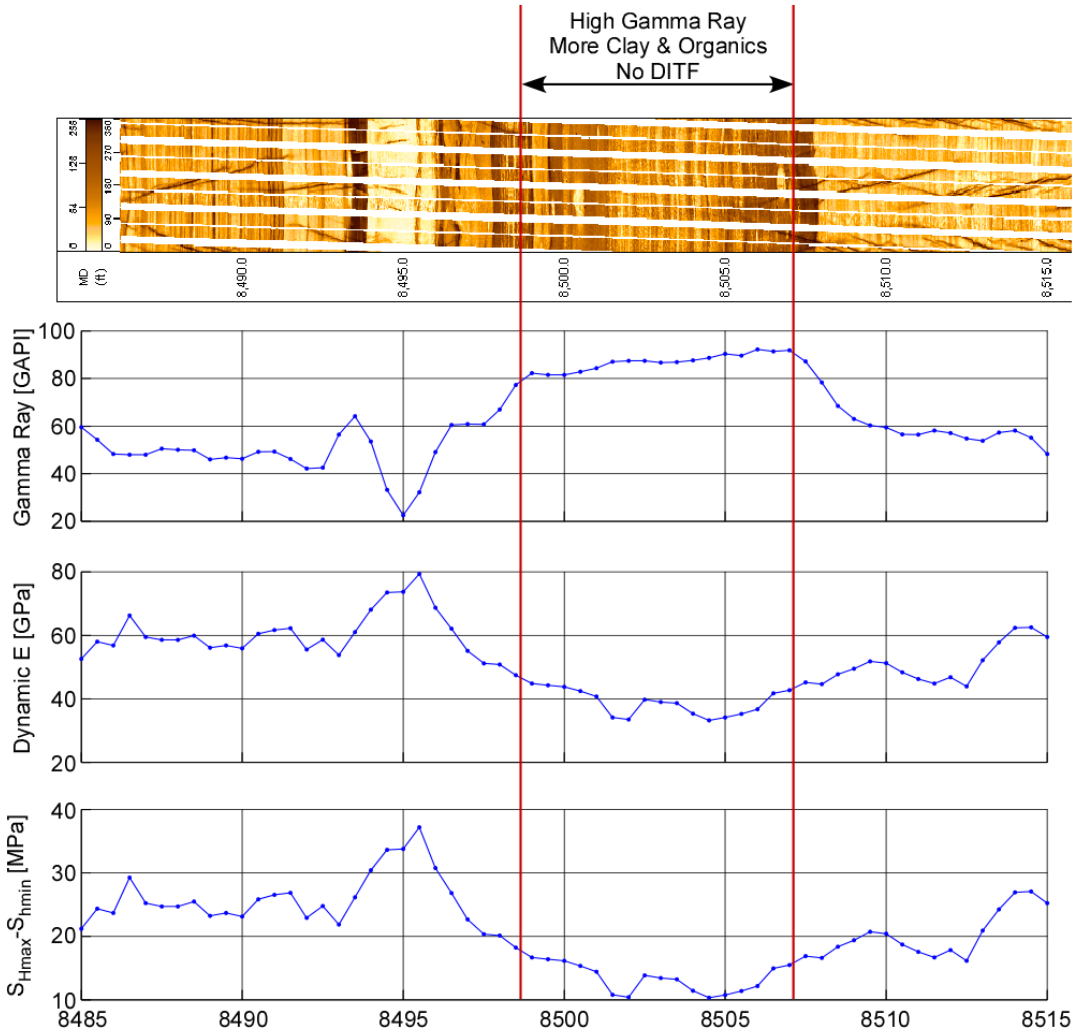

Figure 5.20: Horizontal stress difference profile calculated using the sonic log data.

5.7 Discussions

The stress analysis presented in the previous section yields reasonable first order agreement between the observed stress variation in the Barnett shale and the predicted stress variation. However, the power-law expression we used is merely a phenomenological description of the mechanical behavior that does not depend on the understanding of its physical mechanism. This also raises questions on the validity of extrapolating the power-law constitutive relation to geological time scale. In this

section, we review results from some complimentary experiments and other studies to discuss our approach and the effect of the simplifications we made on our stress analysis.

5.7.1 Some Physical Insights into the Creep Mechanism

5.7.1.1 Lateral and Volumetric Strain during Creep Deformation

As was described in section 5.3.3, we tailored our one-dimensional problem to address the stress relaxation behavior in shale gas reservoirs by taking the axial strain as the strain variable and the axial differential stress as the stress variable in our viscoelastic formulation. However under the triaxial stress boundary condition employed in our experiments, differential pressure under constant P_c, rock deformation is not one-dimensional. As differential load is applied parallel to the sample cylindrical axis, the rock shrinks in the direction parallel to the sample axis but also bulges out in the direction perpendicular to the sample axis. We refer to the latter as *lateral* deformation. Understanding the lateral deformation can be important in discussing the validity of our stress analysis since boundary conditions in the subsurface may sometimes be more of a constant strain boundary condition rather than a constant stress boundary condition. Thus lateral deformation is, to some extent, an artifact of the triaxial stress boundary condition employed in our experiments. If the boundary condition in the subsurface is such that it does not allow any lateral deformation, there will be additional stresses induced in the surrounding formation to keep the rock from deforming laterally. When this is the case, the rock deformation we characterize under lab triaxial stress boundary condition becomes an inaccurate representation of the actual deformation that takes place in the subsurface.

Figure 5.21 shows the axial, lateral, and volumetric strain data obtained from a 2 week long creep experiment using a Haynesville-1 vertical sample. The lateral strain data, the red data, shows that the sample first expands in the lateral direction as expected from the triaxial stress boundary condition, but in a relatively small magnitude compared to the axial strain, roughly about 2e-5. If we hypothetically

estimate how much additional pressure is needed to suppress this lateral deformation by using the modulus data in Figure 5.13 ($E_h \approx 50$ GPa), it will be on the order of a mega-pascal. Since the confining pressure is on the order of several tens of mega-pascal, the hypothetical induced-stress is fairly small relative to the pressure already applied to the rock. Such inference of the negligibly small lateral deformation was consistent in all of the creep experiments regardless of the sample type or the orientation. This is why we ignored the lateral deformation in our viscoelastic analysis since our stress analysis will still be accurate to the first order without taking into account the lateral deformation.

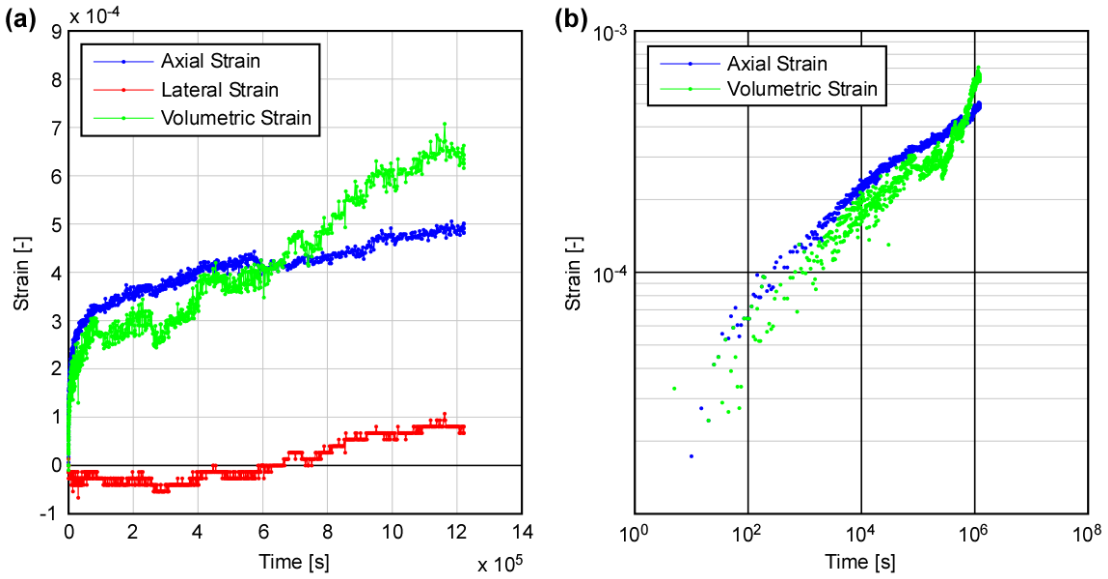

Figure 5.21: Strain data from a 2 week long creep experiment conducted with a Haynesville-1 vertical sample. (a) Axial, lateral, and volumetric strain data is plotted against time. (b) Axial and volumetric strain data is plotted against time in log-log space.

We also infer from the small magnitude of the lateral deformation that the volumetric strain is dominated by the axial strain. Therefore the mode of deformation observed in our creep experiments is compaction. This is also supported by the ultrasonic velocity measurements presented in Chapter 3. Ultrasonic velocity increased slightly during creep deformation, therefore suggesting the reduction of pore volume in the sample.

In the latter half of the 2 week long creep experiment, we observed a compactive lateral strain. The sample started to "cave-in" after about 4 days. This was also observed from the other 2 week long creep experiment conducted with a Haynesville-2 vertical sample. The micro-mechanical cause of such phenomenon cannot be discussed from the limited information we have so far. However, we acknowledge that this is a phenomenon that would enhance axial creep if the boundary condition were to ask for a constant lateral deformation condition. This further supports the conclusion that the mode of the sample deformation is compactive during creep.

5.7.1.2 Effect of Water and Possibility of Poroelastic Effects

To gain some insights into the physical mechanism controlling the creep behavior, we conducted an additional experiment using a Haynesville-1 vertical sample dried in an oven at 100 degrees Celsius for 3 months. Change in sample weight upon drying suggested that water volume equivalent to about 20 % of the pore volume was dried off by this procedure, which likely came from the clay-bound water molecules.

The creep behavior of the dried sample is compared with another Haynesville-1 vertical sample that was preserved under room-humidity condition in Figure 5.22. The confining pressure was 20 MPa for both samples and the exact same differential pressure history was applied to both samples. We see that the relation between time and strain for the oven-dried sample can also be expressed by a power-law at least for the 3 hour time period tested (Figure 5.22a). Also the oven-dried sample seems to exhibit less creep deformation as suggested by the smaller slope in the log(time)-log(strain) space. When the power-law constitutive parameters from these experiments are compared (Figure 5.22b), we find that the compliance constant, B, is not changed so much, but the main change occurs in the power-law exponent, n. Since B reflects the elastic property of the rock and n reflects the time-dependent behavior of the rock, we can interpret that the effect of completely drying off the clay-bound waters did not affect the elastic property of the rock, but affected the rate at which the time-dependent compaction occurs.

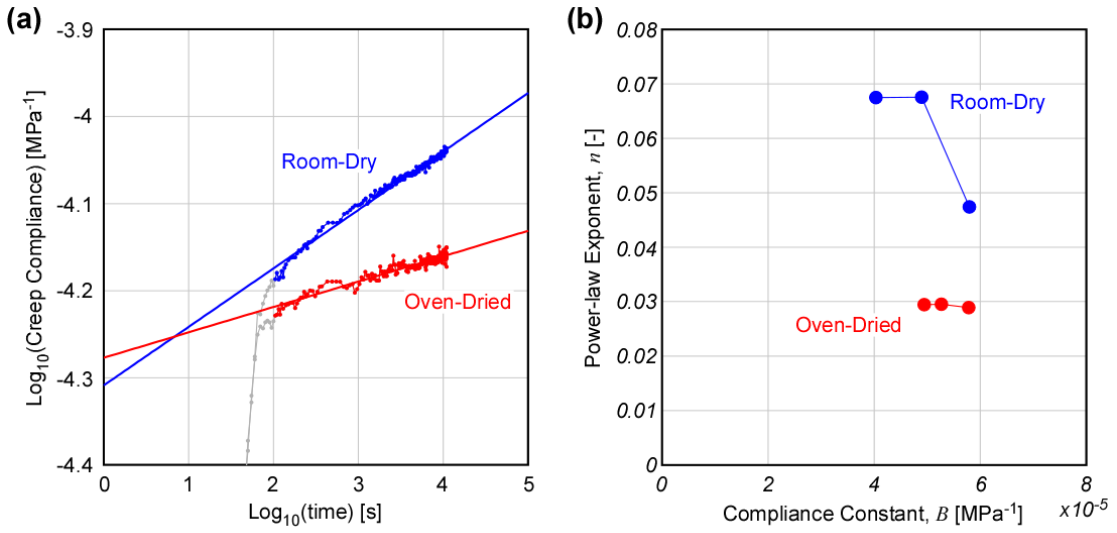

Figure 5.22: Comparison of creep behavior of a room-dried and an oven-dried Haynesville-1 vertical samples. The oven-dried sample was dried at 100 degrees Celsius for 3 months. (a) Comparison of creep data. (b) Comparison of power-law constitutive parameters.

The fact that the oven-dried samples also exhibited creep behavior suggests that the dry frame of the rock inherently exhibits time-dependent deformation behavior. But it is unclear what physical mechanism the additional time-dependent deformation in the room-dry sample accounts for. One possibility is that the additional deformation reflects poroelastic deformation due to the time-dependent diffusion of pore pressure in these low-permeability shales. However, we believe that poroelastic effects did not play a significant role in the time-dependent behavior for several reasons. First, the saturation of water in the pore volume, including clay-bound water, was at most 30-40% in the samples we tested. Since pore volume change upon application of the pressure steps was at most 0.2 % (Figure 5.5), at most tenth of the 2-8 % sample porosity (Figure 2.2), the pore pressure change could only have been a fraction of atmospheric pressure, up most about 0.01 MPa. Such small pore pressure change is 2-3 orders smaller than the applied pressure steps. Also, total sample deformation is enhanced by the presence of water in the room-dry sample, rather than suppressed by the additional stiffness from the pore fluid. If the presence of water caused poroelastic effects, the blue data in Figure 5.22a should plot lower than the red data, but appear to "catch up" to the blue data as the supposed pore pressure drains out of the sample. For

these reasons, we suggest that poroelastic effects were not the major cause of time-dependent behavior exhibited by the studied gas shale samples.

5.7.1.3 Suggestions for the Physical Mechanism of Creep

Compaction occurs as a result of grain rearrangement facilitated by the relative motion, or the sliding, of the grains. The fact that the time-dependent creep behavior was affected by the absence of water in the pore space suggests that the physical mechanism responsible for the grain sliding is a hydrolytically-assisted mechanism. This is a satisfactory observation since the presence of water is known to lower the frictional coefficient of most minerals, especially clay minerals (Moore and Lockner, 2004). Sub-critical crack growth is another mechanism that is enhanced by the presence of water, which is a mechanism responsible for the time-dependent deformation of silica-rich rocks (e.g. granite, sandstone) (Lockner et al., 1993; Chester et al., 2005). Both of these may be a plausible mechanism for the compactive creep deformation we observed since they can operate at room temperature conditions. However, creep of the gas shales was found to be independent of the confining pressure (Figure 5.7), thus making it difficult to believe that the creep deformation is facilitated by the frictional sliding between the grains. Thus it is more favorable to believe that the creep we observed is a compaction facilitated by sub-critical fracturing at the grain contacts.

However, very little is known about the sub-critical fracturing that takes place at low differential stress levels as in our experiments. We applied low stress levels to the rock in our experiment compared to previous studies on brittle creep behavior since the crust generally cannot support stresses higher than their frictional strengths. Many studies of creep deformation in the brittle regime (Lockner, 1993; Heap et al., 2009) apply enough stress to take their sample into tertiary creep, usually above 80% of the short-term rock strength. In these experiments, the creep strain rate dependence on differential pressure is found to be much higher than the linear dependence we found in our study. Heap et al. (2009) reports increase in strain rate by an order of magnitude upon 10% increase of the applied differential load in Darley Dale sandstones, a clay-

poor sandstone with about 13 % porosity. Thus we do not know if the observed linear dependence of creep strain, and creep strain rate, with differential pressure is consistent with the deformation mechanisms discussed in past studies.

It is extremely difficult to confirm the physical mechanism by direct observation of the deformation structure in our experiments. Studies of creep deformation in rocks (Lockner, 1993; Karner et al., 2003; Chester et al., 2005; Heap et al., 2009) usually identify the physical mechanism with the aid of direct observations of the deformation under the microscope. But this is not possible in our study since the creep strain is on the order of 10^{-4} which is not enough to create any observable change in the microstructure. The extremely fine grain size of the shales also makes it difficult to make clear observations on any individual structural features in the rock. A gas shale rock system is also extremely heterogeneous, composed of multiple minerals, which makes it difficult to single out a physical mechanism responsible for the creep. After all, we may be looking at a composite behavior of multiple mechanisms operating on different components of the rock.

We suggest that future experiments shall focus on observing creep deformation of gas shales at higher temperatures. Temperature affects the creep behavior of rocks and studying the temperature dependence of creep may provide conditional evidences to confirm the physical mechanism responsible for the creep behavior of gas shales at low pressure levels.

5.7.2 Power-law versus Other Common Viscoelastic Models

Viscoelastic behavior is oftentimes described by models composed of springs and dashpots (e.g. Kelvin model, Maxwell model, Burgers Model) where spring elements behave as a linear elastic component and dashpot elements behave as a viscous component. However we did not choose to use these models for several reasons.

One end-member behavior of these models is the Kelvin model (also referred as the Voigt model) which is composed of a spring and dashpot in parallel configuration (Figure 5.23a). Kelvin solids exhibit transient behavior such that the creep strain gradually approaches an asymptote value in an exponential manner. This model does not fit our laboratory data because: 1) our creep data was not found to be exponential, 2) creep continued even after 2 weeks (no asymptote), and 3) Kelvin solids do not exhibit any instantaneous strain, thus no elastic deformation, which cannot be true for rocks. Another end-member is a Maxwell model which is composed of a spring and dashpot in series (Figure 5.23b). A Maxwell solid first responds instantaneously to an input of stress then continues to deform at a constant strain rate. This model is also not suited to describe our laboratory data since 1) a Maxwell solid does not exhibit any transient behavior, and 2) it is inconceivable to believe that a rock continues to deform indefinitely at a constant strain rate as the observed mode of deformation of the creep behavior is compaction.

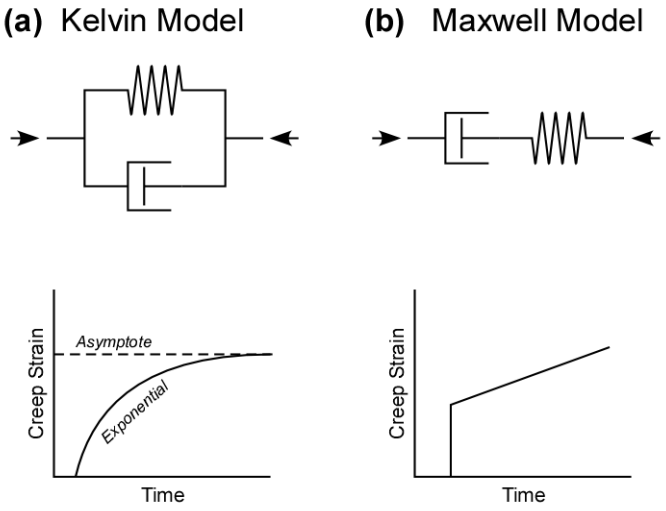

Figure 5.23: Schematic description of a Kelvin and Maxwell model and their creep behaviors.

The advantage of using springs and dashpots to describe a viscoelastic solid is that one can generalize the Kelvin and Maxwell models by combining many of them in a series or a parallel configuration. Although the end member behaviors (Kelvin and Maxwell) are usually somewhat unrealistic characterizations of the mechanical behavior of real materials, the generalization allows one to create a material with essentially any arbitrary viscoelastic behavior by introducing infinite numbers of Kelvin and/or Maxwell components. Thus, ultimately, our laboratory data can also be described by connecting as many Kelvin and Maxwell elements as we desire (i.e. an approach using a *retardation spectrum* or a *relaxation spectrum*; for details see Findley et al. (1976) and Lakes (2009)).

However, we do not choose to do this because such approach quickly makes the model overly complicated, and more importantly, looses uniqueness in the expression. It will be difficult to judge how many elements to introduce in the model since adding an element will always improve the fit of the model to the data. A power-law function of time produces all of the features observed in the lab: an instantaneous response, transient behavior, creep behavior that does not reach an asymptote, and continuously decaying strain rate. For these reasons, it is found from decade-long creep experiments of plastics and polymers (Findley et al., 1976) that a power-law formulation describes the long-term behavior better than other common models. Experiments with concretes were also observed to exhibit similar creep characteristics and the same power-law expression as Equation 5.9 was used to describe the creep compliance and relaxation modulus of asphalt concretes (Secor and Monismith, 1964; Lai and Fitzgerald, 1970). Although our material is not the same as those mentioned above, a power-law expression describes our laboratory data reasonably well. It was also favorable because it greatly simplified the stress analysis and allowed us to perform a first-order investigation of the importance of viscoelastic behavior.

5.7.3 Plastic Deformation during Cyclic Creep Deformation

In linear viscoelastic theory, time-dependent behavior is not dependent on the direction of deformation. That is, time-dependent behavior upon unloading of stress or

strain is obtained by simply switching the sign of the response to loading. We conducted an experiment with a cyclic loading history using a Haynesville-1 vertical sample to check if creep strain upon unloading of pressure obeys this simple relation. In this experiment, the differential pressure was held constant for an extended period of time between the unloading and reloading of pressure before going to the next pressure step. Figure 5.24 shows the creep strain observed under cyclic differential pressure steps between about 0-35 MPa at 30 MPa confining pressure. The strain data is colored in blue and red to differentiate between the deformations observed under changing-pressure and constant pressure, respectively.

We see from the data that creep in the opposite direction, we call this a rebound creep response, does occur upon unloading of the differential pressure. However, the rate of the rebound creep is not comparable to the creep rate upon first loading as suggested by linear viscoelastic behavior. The rebound creep seems to take place at a much slower rate. We also observe that there is a significant hysteresis in axial strain as indicated by the gap between where the strain started prior to the pressure step and where the strain is approaching by the rebound creep. These features suggest that the time-dependent deformational behavior of the studied shales has a significant plastic component and the behavior is not bi-directional. Therefore, the time-dependent behavior we observe in our experiments is best characterized as a mixture of viscoelastic and viscoplastic behavior.

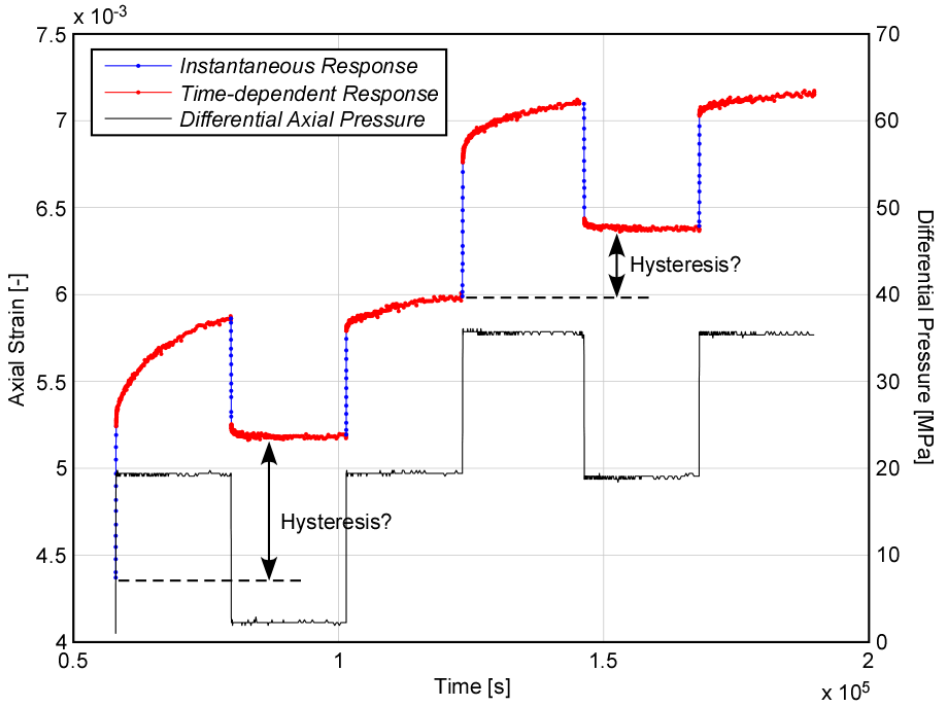

Figure 5.24: Creep data from an experiment with a cyclic loading history. Blue data points denotes data during the pressure step, and red data points denotes creep data under constant differential pressure.

If the time-dependent deformational property of the shale rocks is viscoplastic, this imposes a strong restriction on the use of viscoelastic theory to analyze the stress evolution in these reservoirs. If a reservoir had undergone any period of tectonic unloading, the stress evolution during that period cannot be analyzed by the viscoelastic behavior characterized in our experiments. In the stress analysis from the previous section, we chose the stress accumulation to occur under a monotonic loading condition by assuming a constant tectonic strain rate, so that the analysis would not suffer from the issues of visco-plastic behavior. However, the tectonic history of a basin may not always be of a monotonic nature as we simplified. Therefore if one attempts to perform a more complete stress analysis acknowledging the detail tectonic history of a region, the visco-plastic behavior and its rebound creep deformation needs to be examined carefully. This may be extremely challenging to investigate under lab time scale, thus may require the use of sophisticated numerical modeling based on sound understanding of the micro-mechanics of how visco-plastic deformation occurs.

5.7.4 Applicability of Results at In-situ Conditions

Although experiments were designed to capture in-situ rock behavior as much as possible, several conditions were either not reproduced in our experiments or not considered in our stress analyses. For instance, the temperature at which the samples were tested was much lower than in-situ conditions. Since ductile deformation of rocks are typically enhanced by temperature, the influence of time-dependent deformation may be more pronounced at in-situ conditions. However, proprietary test data show that change in creep behavior due to difference in temperature condition is smaller than the variability in creep behavior exhibited by samples with different compositions. We also acknowledge the significant uncertainty involved in the extrapolation of the laboratory-timescale constitutive relations to geological-timescales which does not guarantee the quantitative accuracy of the stress calculations. We also only considered the differential stress relaxation that occurs in within the horizontal plane. However, there may also be relaxation in the stress difference between the vertical and the horizontal principal stresses. The triaxial boundary conditions applied in our experiments did not permit us to evaluate these possibilities, but such effect may contribute to additional relaxation of horizontal stress differences depending on the faulting environment.

We note from these considerations that the quantitative results presented in this study may not necessary be accurate in their absolute values. However, our focus was on the contrast of viscoelastic behavior between rocks with different compositions and the associated variation in stress states within a reservoir. Therefore analyses based on our laboratory experiments are likely correct in the relative sense and the interpretations on the relation between viscoelastic properties and in-situ stress holds.

5.8 Conclusions

We performed laboratory creep experiments using rocks from several shale gas reservoirs to investigate its time-dependent deformational behavior. Conclusions obtained from the laboratory experiments are:

1. All shale gas reservoir rocks exhibited some degree of time-dependent creep deformation.
2. The strain response to the applied axial differential load was approximately linear, but was not dependent on the confining pressure.
3. The constitutive relation between strain and time is best described by a power-law function of time, $\varepsilon=Bt^n$, with the power-law exponent varying between 0-0.08.
4. Time-dependent deformational behavior characterized by the constitutive parameters, B and n, vary between reservoirs and within a reservoir.
5. Clay- and organic-rich samples tend to exhibit more time-dependent deformation characterized by higher power-law exponent values.
6. Viscoelastic behavior of gas shales is anisotropic such that loading of differential pressure perpendicular to the bedding yields higher constitutive parameters, B and n, than when the load is parallel to the bedding.
7. There may be a weak positive correlation between the elastic compliance of the rock and the power-law exponent value.

Although a complete description of the creep behavior asks for a viscoplastic description of the constitutive behavior, we focused on the creep behavior under monotonic loading condition and interpreted the behavior in the framework of viscoelastic theory. Using the power-law constitutive relation and the stress relaxation behavior inferred from the creep compliance data, we calculated the differential stress accumulation in these rocks that would result from tectonic loading at a constant strain rate. We conclude from the results that:

1. Differential stress accumulation is much lower than predicted by linear elasticity due to the viscoelastic stress relaxation behavior of the rocks.
2. Variation in viscoelastic behavior within a reservoir can create significant variations in the current state of stress within the reservoir.
3. Magnitudes of differential stress variation in the Barnett shale predicted from our laboratory data agrees with those inferred from observations of wellbore failures in the Barnett shale.

5.9 References

de Waal, J. A. and Smits, R. M. M., 1988, Prediction of reservoir compaction and surface Subsidence: Field application of a new model: SPE Formation Evaluation, 14214.

Dudley, J. W., Myers, M. T.. Shew, R. D., and Arasteh, M. M., 1998, Measuring compaction and compressibilities in unconsolidated reservoir materials by time-scaling creep: SPE Reservoir Evaluation & Engineering, 51324.

Chang, C., Moos, D., and Zoback, M. D., 1997, Anelasticity and dispersion in dry unconsolidated sand: International Journal of Rock Mechanics and Mining Sciences, **34**, Paper No. 048.

Chang, C., and Zoback, M. D., 2009, Viscous creep in room-dried unconsolidated Gulf of Mexico shale (I): Experimental Results; Journal of Petroleum Science and Engineering, **69**, 239-246.

Chester, F. M., Chester, J. S., Kronenberg, A. K., and Hajash, A., 2007, Subcritical creep compaction of quartz sand at diagenetic conditions: Effects of water and grain size, Journal of Geophysical Research, **112**, B06203, doi:10.1029/2006JB004317.

Curtis, J. B., 2002, Fractured shale-gas systems: AAPG Bulletin, **86(11)**, 1921-1938.

Findley, W. N., Lai, J. S., and Onaran, K., 1976, Creep and Relaxation of Nonlinear Viscoelastic Materials with an Introduction to Linear Viscoelasticity: Dover Publications.

Hagin, P. N., and Zoback, M. D., 2004a, Viscous deformation of unconsolidated sands-Part 1: Time-dependent deformation, frequency dispersion, and attenuation: Geophysics, **69**, 731-741.

Hagin, P. N., and Zoback, M. D., 2004b, Viscous deformation of unconsolidated sands-Part 2: Linear viscoelastic models: Geophysics, **69**, 742-751.

Hagin, P. N., and Zoback, M. D., 2007, Predicting and monitoring long-term compaction in unconsolidated reservoir sands using a dual power law model: Geophysics, 72, E165-E173.

Heap, M. J., Baud, P., Meredith, P. G., Bell, A. F., and Main, I. G., 2009, Time-dependent brittle creep in Darley Dale sandstone: Journal of Geophysical Research, **114**, B07203, doi:10.1029/2008JB006212.

Higgins, S., Goodwin, S, Donald, A., Bratton, T., and Tracy, G., 2008, Anisotropic stress models improve completion design in Baxter shale: SPE Annual Technical Conference and Exhibition, Denver, Co., September 21-24, 115736.

Karner, S. L., Chester, F. M., Kronenberg, A. K., and Chester, J. S., 2003, Subcritical compaction and yielding of granular quartz sand: Tectonophysics, **377**, 357-381.

Lai, J. S., and Fitzgerald, J. E., 1970, Thermorheological properties of asphalt mixtures: Highway Research Record, **313**, 18.

Lakes, R. S., 2009, Viscoelastic Materials, Cambridge University Press.

Lockner, D. A., 1993, Room temperature creep in saturated granite: Journal of Geophysical Research, **98**, 475-487.

Moore, D. E., and Lockner, D. A., 2004, Crystallographic controls on the frictional behavior of dry and water-saturated sheet structure minerals: Journal of Geophysical Research, **109**, B03401, doi:10.1029/2003JB002582.

Secor, K. E., and Monismith, C. L., 1964, Analysis and interrelation of stress-strain-time data for asphalt concrete: Transaction of the Society of Rheology, **8**, 19.

Sleep, N. H., and Zoback, M. D., 2007, Did earthquakes keep the early crust habitable?: Astrobiology, **7**, 1023-1032.

Suarez-Rivera, R., Green, S. J., McLennan, J., and Bai, M., 2006, Effect of layered heterogeneity on fracture initiation in tight gas shales: SPE Annual Technical Conference and Exhibition, San Antonio, Tx., September 24-27, 103327.

Zoback, M. D., 2007, Reservoir Geomechanics, Cambridge University Press.

Zoback, M. D., and Townend, J., 2001, Implications of hydrostatic pore pressures and high crustal strength for the deformation of intraplate lithosphere: Tectonophysics, **336**, 19-30.

Zoback, M. L., Zoback, M. D., Adams, J., Assumpcao, M., and Bell, S., 1989, Global patterns of tectonic stress: Nature, **341**, 291-298.

5.10 Appendix

5.10.1 Appendix A: Approximation of Laboratory Stress Input History as a Heaviside Step Function

In this section, we evaluate the validity of the approximation used in obtaining the creep compliance function, $J(t)$. Following customary approaches, we discarded the initial 10^2 seconds of the strain data in response to the pressure step, then divided the data by the magnitude of the pressure step to obtain an approximate form of $J(t)$. But as Equation 5.3 describes:

$$\varepsilon(t) = \int_0^t J(t-\tau)\frac{d\sigma(\tau)}{d\tau}d\tau \tag{5.3}$$

$J(t)$ can only be recovered strictly by deconvolving the observed strain data, $\varepsilon(t)$, with the pressure rate history, $\frac{d\sigma(t)}{dt}$.

We performed this deconvolution in order to recover the true creep compliance data. Figure 5A.1a shows an example of the creep and pressure data at the initial 350 seconds after the start of the pressure step. Since the pressure data (gray) show some fluctuation on the order of the measurement resolution, we started by approximating the pressure history as a bilinear trend (black lines) to smooth the data. This procedure was necessary to limit the unstable behavior that comes out after the deconvolution procedure that follows. Then the pressure rate history was calculated from the smoothed pressure data which simply results in a box car function (red data). Next the laboratory strain data (blue data) was numerically deconvolved with the smoothed pressure rate history in the time domain to obtain data that represents the creep compliance behavior. The recovered data after the deconvolution has a severe oscillatory signal super-imposed on the true creep compliance behavior (Figure 5A.1b, green data), so the moving average was taken with a window size of half the pressure ramp time (60/2=30 seconds) to finally recover the creep compliance data (black data). In theory, the same data processing can be done in the frequency domain to minimize

computational costs, but since the Fourier transform of the box car function is a sinc function, the division in the frequency domain lead to unstable results. Therefore, we performed the deconvolution in the time domain.

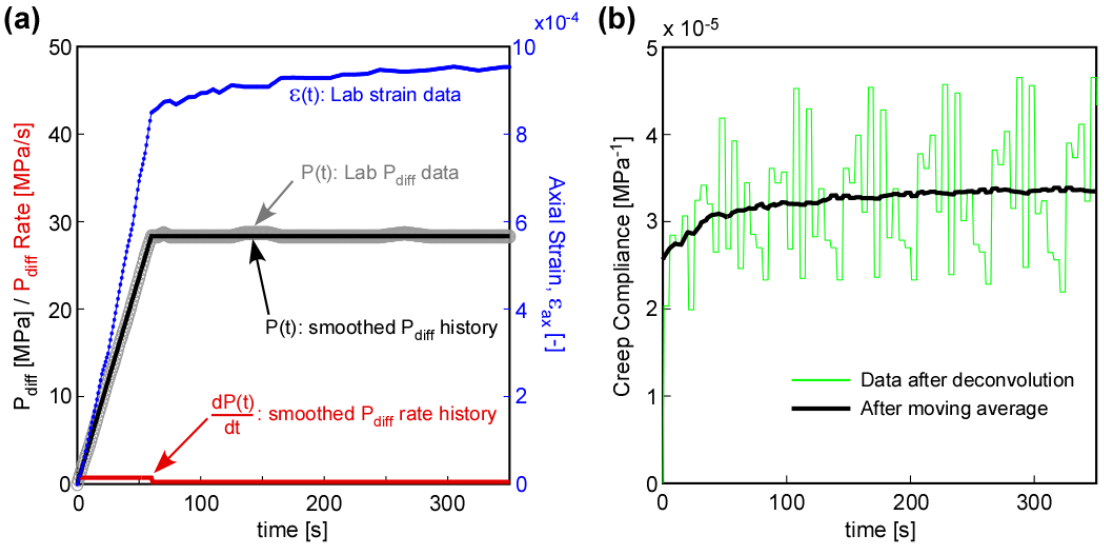

Figure 5A.1: (a) Strain and pressure data during the first 350 seconds after the application of a pressure step. (b) Data recovered after deconvolution of the strain data with the pressure rate history, and the moving average of the data.

Figure 5A.2 shows some examples of the comparison between the approximated creep compliance data (blue data) and the true creep compliance data recovered by deconvolution of the pressure rate history (red data). We see that they merge with each other after about 10^2 seconds and essentially overlap with each other after that. Hence we decided to discard the first 10^2 seconds of the data and use the rest of the data to obtain the constitutive parameters B and n. The 2 linear regressions using the approximate and true creep compliance data are very close to each other.

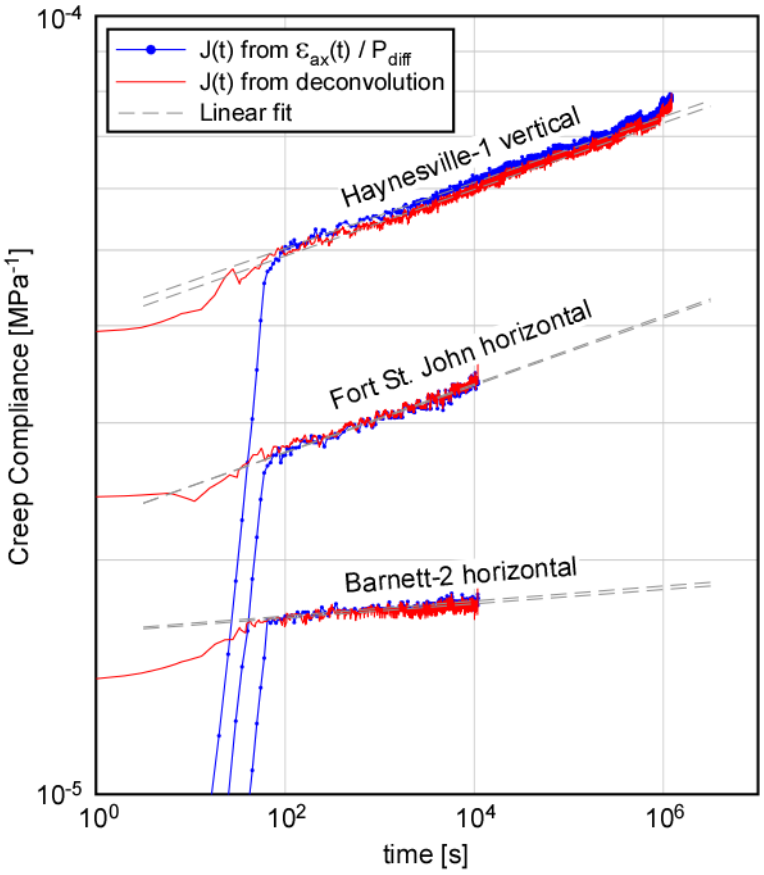

Figure 5A.2: Comparison between the approximated creep compliance data and the true creep compliance data. The gray dashed lines represent linear regression to both data.

The constitutive parameters recovered from the approximate and true creep compliance data is compared in Figure 5A.3. We confirm from the comparison that the values are essentially identical. Therefore the simple procedure of dividing the strain data with the magnitude of the pressure step, and then discarding the initial 10^2 seconds of the data is a reliable method to infer the creep compliance behavior of the samples.

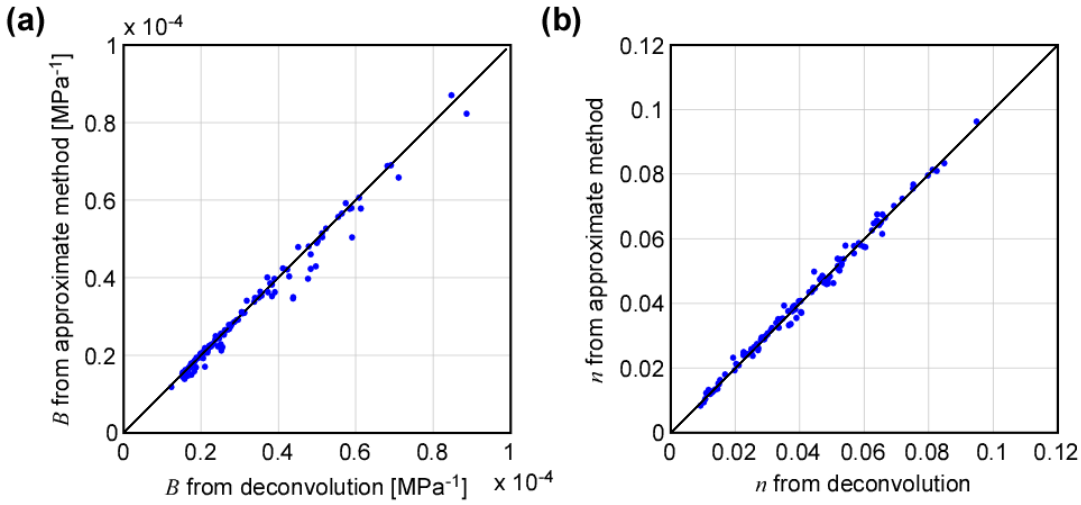

Figure 5A.3: Comparison of power-law constitutive parameters B and n recovered from the approximate and true creep compliance data.

5.10.2 Appendix B: Temperature Correction

Figuer 5A.4 shows the axial strain and temperature data collected in one of the long-term creep experiments. Temperature data (red data) was collected by a thermal couple that is floating inside the confining fluid in the pressure vessel. The temperature data typically showed fluctuations on the order of one degree during these weeks-long experiments, which was probably caused by the slight fluctuation in the room temperature. The strain data (blue data) collected by the LVDT sensors is clearly coupled with this temperature change, and the fluctuation is super-imposed on the creep strain data. Sometimes the temperature related signal is large enough to cause the strain data to show expansion which cannot occur as a result of the time-dependent creep deformation. Thus the data needs to be corrected to recover the true creep related signal.

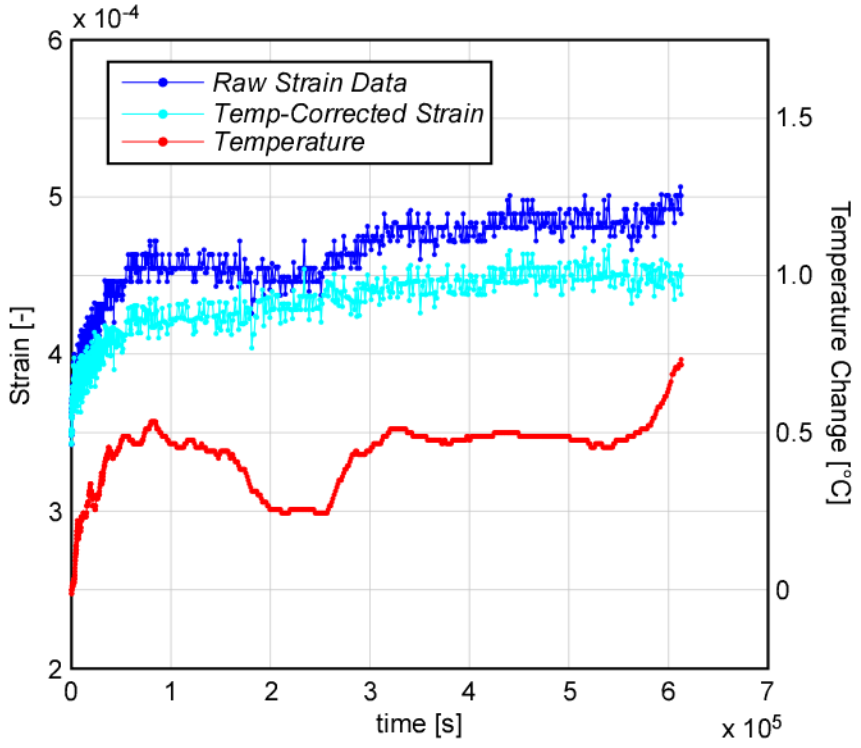

Figure 5A.4: Axial strain, temperature, and temperature-corrected axial strain data during a week long creep observation using a Haynesville-2 vertical sample.

The temperature related signal can be caused by 2 factors. First, the resistance of the metal coils used in the LVDT's can change with temperature which can change the electrical signal coming out of the sensors. Correction for such effect will be consistent between experiments, thus relatively easy to make. Another factor is the slight thermal expansion and contraction of the entire coreholder-LVDT-sample assembly that can cause the core-rods of the LVDT to either move forward or backwards depending on the contrast in thermal expansion coefficient between the individual components of the assembly (Figure 5A.5). Since the sample thermal expansion behavior can vary between experiments, depending on the kind of sample and how long they are, the correction may not be consistent between experiments.

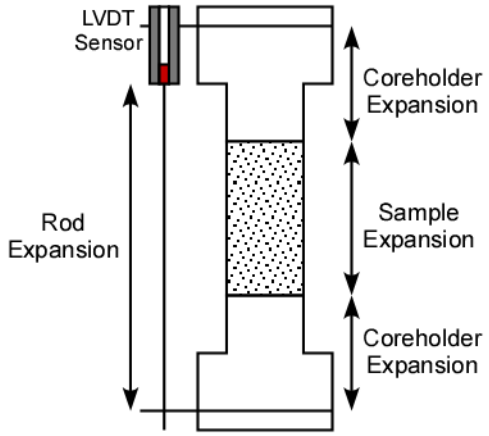

Figure 5A.5: Schematic diagram describing potential locations of thermal expansions or contraction caused by ambient temperature change.

At present, we do not know the relative contribution of the two causes of the temperature related signal. But since the samples used in the long-term experiments were of the same lengths (2") and had similar compositions (Haynesville-1 and Haynesville-2), we assume that the same temperature correction can be applied. After trial and error, we find that a correction of 3.5 microns/°C to the LVDT sensor reading takes out the temperature dependent fluctuation from the LVDT reading fairly well for all long-term creep data (cyan data).

5.10.3 Appendix C: Technical Issues for Stress Relaxation Experiments

Since we are ultimately interested in addressing the differential stress relaxation behavior of the shale gas reservoir rocks, it would be much logical to perform a stress relaxation test in the lab rather than creep experiments. Using data from creep experiments to infer the relaxation behavior requires an additional step of converting the creep compliance to a relaxation modulus by utilizing the Boltzmann superposition principle. However, performing a quality stress relaxation test with a strict constant strain boundary condition was not possible due to the technical difficulty in applying such boundary condition.

This is because the LVDT sensors we used to calculate the sample axial deformation did not only measure the sample deformation, but also the deformation of the core-holder. When pressure is applied to the sample, the steel core-holder also deforms simultaneously, thus the LVDT sensors attached to the core-holder (Figure 5A.6) reads the sum of the sample deformation and the core-holder deformation. Every laboratory axial strain data reported or used in this thesis is corrected for this artifact by subtracting the core-holder deformation (calibrated as a function of P_c and P_{diff}) when processing the data. Therefore the data reported in this thesis is not affected by this problem. However, this core-holder deformation prevented us from performing a quality stress relaxation test because the apparatus was only capable of controlling LVDT displacement reading rather than just the sample deformation.

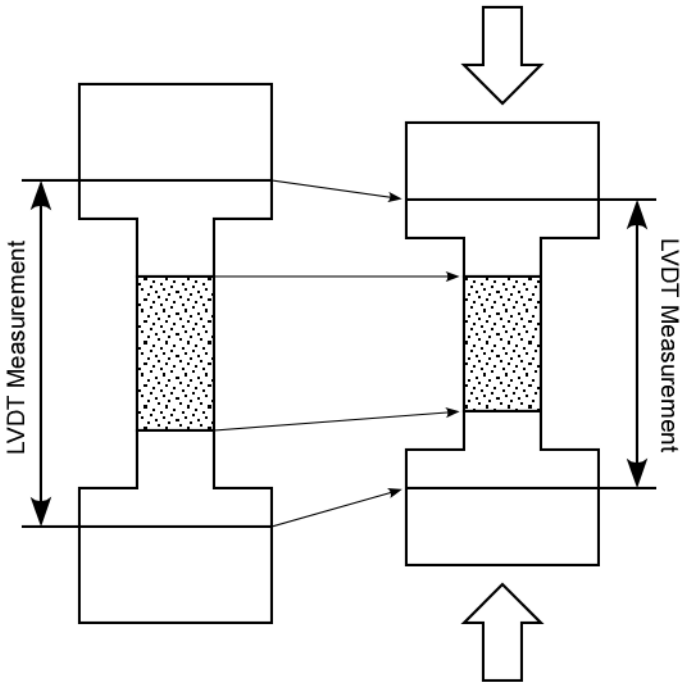

Figure 5A.6: Schematic diagram describing the relation between sample axial deformation and LVDT displacement measurement. The LVDT measures both the sample and core-holder deformation.

If we attempt to perform a stress relaxation experiment by holding the LVDT axial displacement reading constant, this produces a mixed creep and stress relaxation experiment (pseudo stress relaxation test). After a step of axial pressure is applied, the

viscoelastic response of the rock will decrease the axial pressure required to maintain the LVDT reading, which will cause the core-holder to expand elastically. Since the LVDT reading is kept constant, this expansion of the core-holder is absorbed by the shrinkage of the sample. The result is a slight creep deformation of the sample (Figure 5A.7).

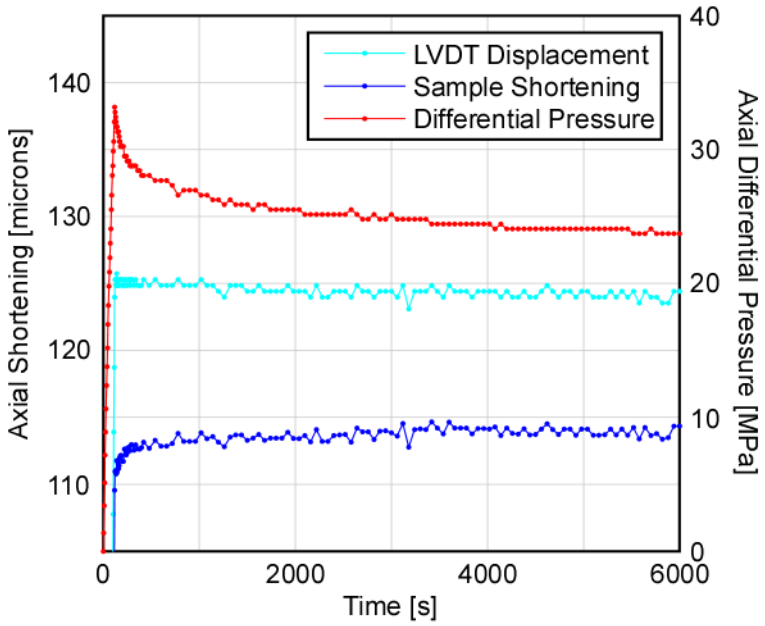

Figure 5A.7: An example of data from a pseudo stress relaxation experiment. The triaxial apparatus is controlling the axial differential pressure to maintain the LVDT displacement reading constant. Note the blue data that shows some creep behavior.

In principle, we can numerically de-convolve this slight creep response from the data to obtain the relaxation modulus of the sample using Equation 5.4. But this can not be done so well numerically, due to the noisy nature of the laboratory data. Smoothing of the input signal cannot be done as in the case shown in Figure 5A.1 where the intended pressure ramp was known exactly. This is why we focused on studying the creep behavior. A constant stress condition required in a creep experiment is much easier to achieve by simply using the internal load cell reading.

5.10.4 Appendix D: Verification of Linearity through Pseudo Stress Relaxation Experiments

Although pseudo stress relaxation experiments alone may not allow us to extract accurate information about the viscoelastic behavior of the samples, we can still use the data to verify linearity and Boltzmann superposition. We assumed that the stress relaxation modulus function, $E(t)$, is also described in a power-law formulation as in Equation 5.14, and forward modeled the pseudo stress relaxation data by convolving $E(t)$ with the axial strain rate data that exhibits slight creep behavior. The constitutive parameters were chosen according to what was found from the creep experiments.

Figure 5A.8 shows the result of the forward modeling (magenta data) for two pseudo stress relaxation experiments. We see that the experimental observation of differential pressure relaxation can be modeled very well using a power-law relaxation modulus. Also the optimum power-law constitutive parameters used in the forward modeling are very similar to those obtained from the creep experiments. The values all fall within the range of values suggested from Figure 5.11. These observations confirm that linearity and Boltzmann superposition holds at least in within the time scale considered in the laboratory, and the relaxation modulus of the samples can be described by a power-law function.

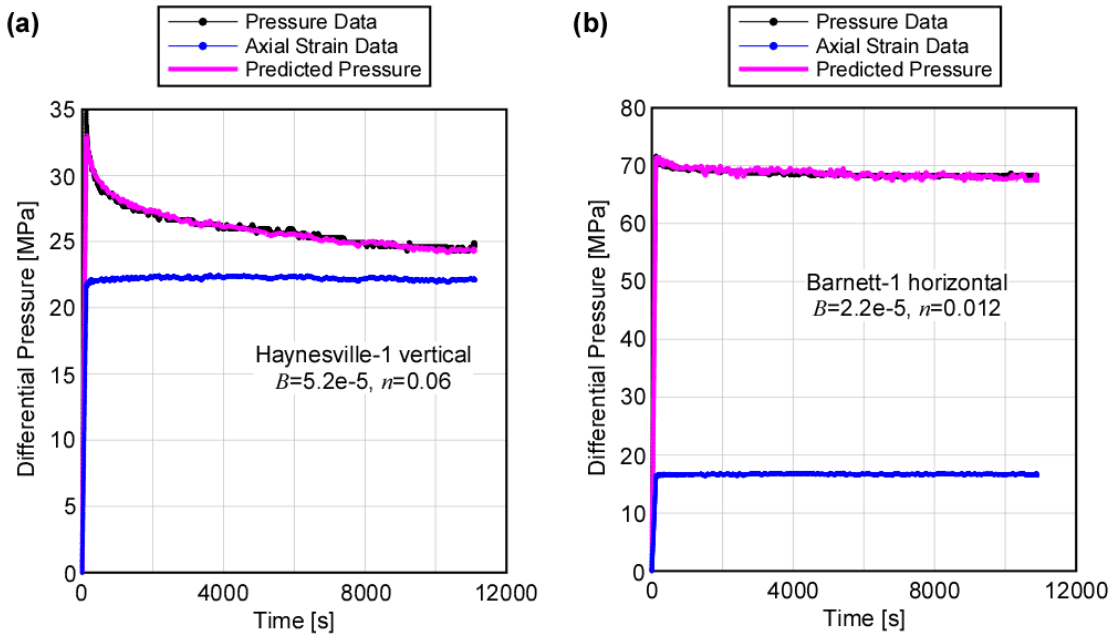

Figure 5A.8: Two examples of forward modeling of the pseudo stress relaxation data. The black blue data is the axial strain data, and the black data is the pressure data. The magenta data is the pressure data modeled using the strain data and a power-law stress relaxation function with the parameters shown in the figures. (a) Haynesville-1 vertical sample, (b) Barnett-1 horizontal sample.

Chapter 6

FRICTIONAL PROPERTIES OF SAPONITE-RICH GOUGE FROM A SERPENTINITE-BEARING FAULT ZONE ALONG THE GOKASHO-ARASHIMA TECTONIC LINE, CENTRAL JAPAN*

Abstract

We studied a serpentinite-bearing fault zone in Gokasho-Arashima Tectonic Line, Mie Prefecture, central Japan, characterizing its internal structures, mineral assemblage, permeability, and frictional properties. The fault core situated between the

* This paper was written with Toshihiko Shimamoto and Diane Moore, and has been previously published in Journal of Structural Geology

serpentinite breccia and the adjacent sedimentary rocks is characterized by a zone locally altered to saponite. The clayey gouge layer separates fault rocks of serpentinite origin containing talc and tremolite from fault rocks of sedimentary origin containing chlorite but no quartz. The minerals that formed within the fault are the products of metasomatic reaction between the serpentinite and the siliceous rocks. Permeability measurements show that the serpentinite breccia and fault gouge have permeability of 10^{-14}~10^{-17} m2 and 10^{-15}~10^{-18} m^2, respectively, at 5~120 MPa confining pressure. Frictional coefficient of the saponite-rich clayey fault gouge ranged between 0.20~0.35 under room dry condition, but was reduced to 0.06~0.12 when saturated with water. The velocity dependence of friction was strongly positive, mostly ranging between 0.005~0.006 in terms of a-b values. The governing friction law is not constrained yet, but we find that the saponite-rich gouge possesses an evolutional behavior in the opposite direction to that suggested by the rate and state friction law, in addition to its direct velocity dependence.

6.1 Introduction

Serpentinites frequently occur along major faults and plate boundaries and its rheological behavior is believed to play a major role in tectonics and seismicity. For instance, weak serpentinite shells are thought to accommodate the diapiric motion of mantle materials which exposes mantle peridotites along mountain belts (Hess, 1955). Guillot et al. (2000) suggested that serpentinized mantle wedges at subduction zones facilitate the exhumation of eclogitized oceanic crusts by acting as lubricants. Early measurements of serpentinite rock strengths (Raleigh and Paterson, 1965) observed embrittlement and significant reduction of strength at elevated temperatures due to enhanced pore pressure by dehydration, and suggested that serpentinites and other hydrated phases could extend brittle faulting to greater depths in subduction zones. Recent high-pressure high-temperature laboratory experiments (Hilairet et al., 2007) also showed that serpentinites would accommodate ductile deformation at upper mantle conditions, and its deformation could occur at strain rates comparable to post-seismic deformation and slow earthquakes.

The presence of serpentinites along certain subduction zones and the creeping section of the San Andreas fault have also stimulated the investigation of its relation to the seismicity/aseismicity of these plate boundaries. Discoveries of serpentinite seamounts in the Izu-Bonin and Marina forearcs (Fryer et al., 1990; Fujioka et al., 1995) and the seismic structure indicative of hydrated mantle wedges and serpentine diapirs in these trenchs (Takahashi et al., 1998; Kamimura et al., 2000) suggested that the serpentinites are responsible for the absence of large subduction earthquakes in this region (Hyndman and Peacock, 2003). Serpentinite is commonly found along faults of the San Andreas system in central and northern California that are characterized by creep (e.g., Allen, 1968; Hanna et al., 1972; Irwin and Barnes, 1975; Moore and Rymer, 2007). Laboratory experiments investigating the frictional properties of serpentine minerals (Reinen et al., 1994; Moore et al., 1996, 1997; Morrow et al., 2000) revealed that serpentine minerals are weaker than typical crustal materials.

Recently, attention has been directed to the mineral species produced by the metasomatic reaction between serpentinites juxtaposed against crustal rocks. Reactions are facilitated by silica-rich hydrothermal fluids, typically producing mineral assemblages containing talc, actinolite/tremolite, chlorite, and carbonates. (Phillips and Hess, 1936; Curtis and Brown, 1969; Koons, 1981; Sanford, 1982; Mori et al., 2007; Viti and Collettini, 2009; Soda and Takagi, 2010; Moore and Rymer, 2010). If fault slip occurs along margins of serpentinites, mechanical properties of these metasomatic products would ultimately control the mechanical behavior of serpentinite-bearing faults and diapirs. In fact, Lockner et al. (2011) argue that saponite, a Mg-rich smectite clay formed by reaction of serpentinite with quartzo-feldspathic rocks, rather than serpentine species can explain the low frictional strength of the San Andreas fault suggested by the lack of a heat-flow anomaly (Brune et al., 1969; Lachenbruch and Sass, 1980) and the orientation of maximum horizontal stress (Zoback et al., 1987), at least at 2.7 km depth in the central creeping section.

These studies therefore highlight the importance of understanding not only the serpentinite itself, but also the structure/composition of the entire fault zone to understand the mechanical significance of serpentinites in various tectonic settings. This study reports the internal structure of a serpentinite-bearing fault along the Gokasho-Arashima Tectonic Line, Mie prefecture, Japan and results from laboratory measurements on the fault zone permeability and the frictional/rheological properties of the fault gouge. We find that the fault core is composed of saponite-rich gouges which exhibit extremely low frictional coefficient and prominently velocity strengthening properties.

6.2 Geological Setting

The Gokasho-Arashima tectonic line (referred as G-A Line hereafter) is a major serpentinite-bearing fault structure that cuts through the Chichibu Belt of Shima Peninsula, longitudinally but slightly obliquely, in the NE-SW direction. The Chichibu Belt in this area lies between the Mikabu tectonic line and the Butsuzo tectonic line, which separate the Chichibu Belt from the Sambagawa Belt on the northern side and from the Shimanto Belt on the southern side, respectively, as commonly seen in southwest Japan (Figure 6.1a). The Chichibu Belt mainly consists of accretionary complexes and forearc basin deposits from the Jurassic to early Cretaceous period. Branching faults exist to the southeast of the main trace of the G-A Line, which dissects the Chichibu Belt into alternating units or lens-like blocks (Figure 6.1b). The geology of the area around the G-A Line has been studied in detail by Yamagiwa (1957), Saka et al. (1979, 1988) and Katoh et al. (1992). Due to the presence of granitic rocks, metamorphic rocks, and felsic tuff characteristic of the Kurosegawa Tectonic Zone (Ichikawa, 1956) on Shikoku Island, the G-A Line is interpreted to be a serpentine mélange that serves as the eastward extension of the Kurosegawa Tectonic Zone (Hamada, 1963; Saka et al., 1988; Yoshikura and Terashima, 1984). The precise tectonic history of the Kurosegawa Tectonic Zone is still under debate, but Kato and Saka (2003) suggested that the Kurosegawa Tectonic Zone was once a dextral strike-slip transform fault that was active between 120 and 100 Ma in response to the

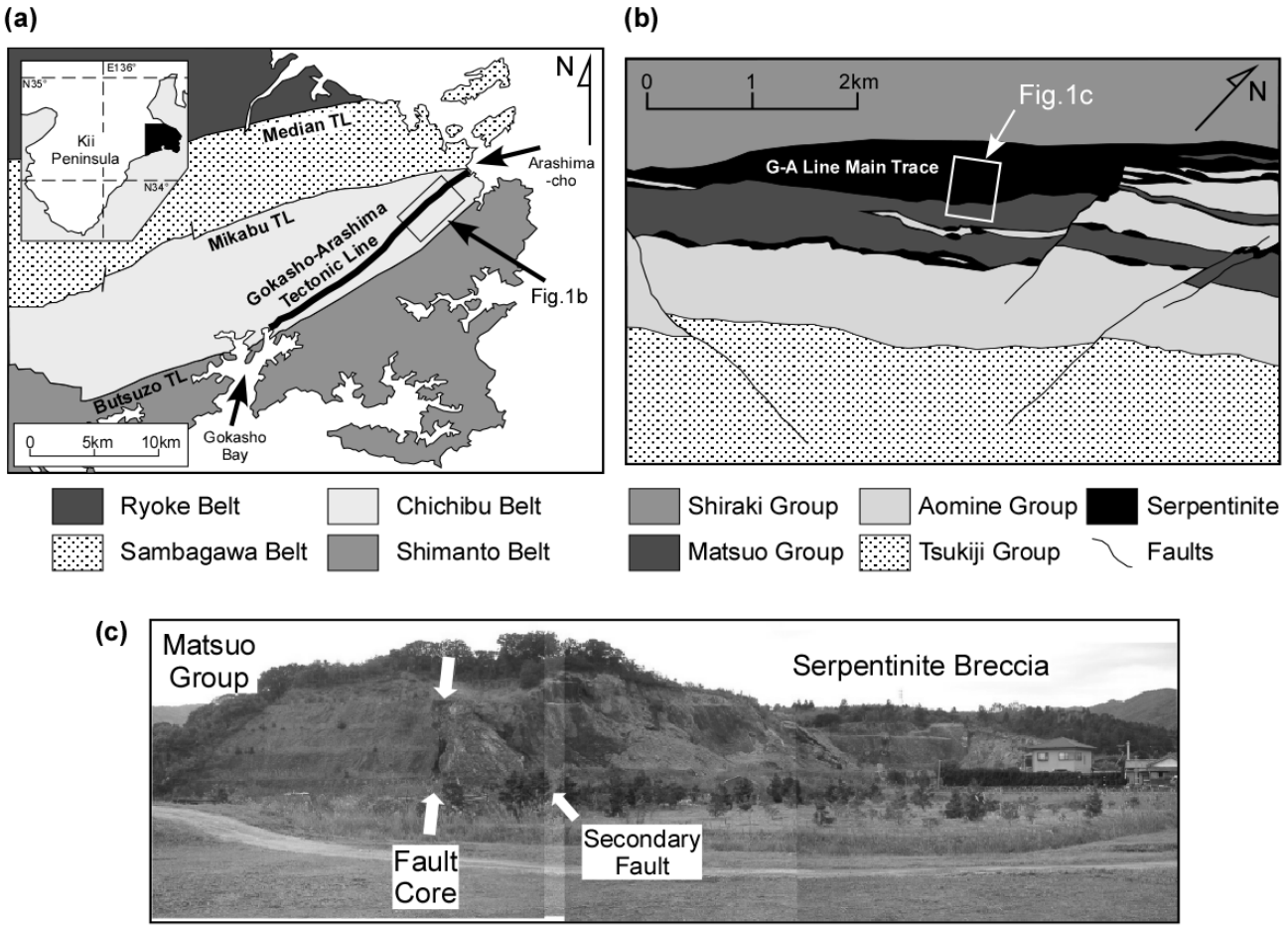

Figure 6.1: (a) Geological map of Shima Peninsula reproduced from Saka (1979), (b) Local geological map around the studied outcrop modified from Saka (1988), (c) Photograph of the studied outcrop near Matsuo station. The entire photograph shows the outcrop that spans about 250 m horizontally.

subduction of the oceanic ridge between the “Izanagi” plate and “Kula” plate. However, recent activity of the G-A Line is not known and the G-A Line is not identified as an active fault.

Serpentinite inclusions along the faults of G-A Line exhibit strongly foliated structure parallel to the fault surface whose orientation is nearly vertical (Figure 6.1c), except at the western end of the exposed G-A Line (Saka et al., 1988). The main trace of the G-A Line traverses the Shima peninsula from Gokasho Bay to Arashima-cho, and the width of the serpentinite body along it varies between 20 and 700 m. Serpentinites in the branching faults more commonly appear as lens-shaped inclusions with widths of at most a few meters. We focused our study on the fault boundary between the main trace serpentinite and the Matsuo group, a Cretaceous forearc basin deposit, where the widest serpentinite body was exposed (Figure 6.1c). A large outcrop from an abandoned quarry allowed us to observe the fault zone structure.

6.3 Fault Zone Structures and Mineralogy

6.3.1 Matsuo Outcrop

At the studied fault outcrop, the serpentinite body constituting the fault zone of the G-A Line is exposed for about 300 m to the north of the fault plane and the Matsuo sedimentary rocks are exposed for about 80 m to the south (Figure 6.1c). The main boundary fault is nearly vertical, consistent with the general trend of the G-A Line in this region (Yamagiwa, 1957; Saka et al., 1988), and a secondary branching fault dipping to the North is also exposed close to the boundary fault.

The entire serpentinite body is highly deformed and foliated to form a foliated fault breccia. Foliation is predominantly vertical close to the main fault (within 30 m), and is mainly composed of lens-shaped fragments less than 5 cm in size. However at regions farther away from the fault plane (> 30 m), clast size increases and foliation wraps around the clasts, causing the texture to appear more random in the central part of the serpentinite body. The appearance of the serpentinite can be quite variable

ranging from white/flaky to black/massive. Powder XRD analyses of the 7 serpentinite breccia samples showed that antigorite and lizardite are the main constituents with minor amounts of talc, brucite, and calcite in some samples. Xonotlite veins are probably also present in the serpentinites, since a large (~30 cm) platy crystal was found on a serpentinite block in the quarry.

The structure of the exposed Matsuo group was difficult to observe due to coloration from weathering and minor vegetation, but it appeared to be fractured and probably displaced by slip along these fractures, especially near the fault plane. Rock types ranged from siltstone to sandstone, and possibly conglomerate as reported by Saka et al. (1988).

6.3.2 Internal Structure of the Fault Core

The fault core region is easily identified from the eroded area of the outcrop along the lithological boundary (Figure 6.1c). The total thickness of the fault core is about 1 m, within which several distinct structural zones are identified (Figure 6.2). From the serpentinite side to the Matsuo group side, these zones are: (1) black/greenish-gray/gray foliated gouge, (2) clayey gouge and (3) black/dark-gray cataclasite.

The foliated gouge is the transition from the vast serpentinite breccia to the clayey fault gouge. Moving from the serpentinite breccia to the clayey gouge, the color changes from black to greenish-gray/gray, clast size decreases, and some clayey vein-like streaks appear. Microscopic observation reveals serpentine fragments within the clayey matrix (Figures 6.3a and 6.3b). XRD patterns indicate a decrease in serpentine content and an increase in tri-octahedral smectite clays approaching the clayey fault gouge (Figure 6.4). Actinolite/tremolite, talc, and calcite were also identified from the XRD patterns.

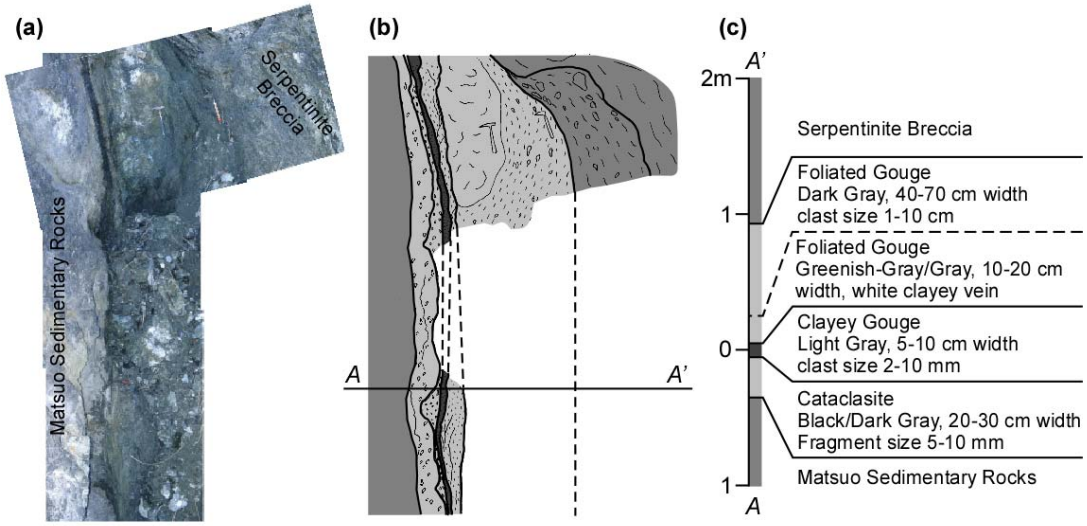

Figure 6.2: (a) Photograph of the exposed fault core, (b) Interpreted sketch of the fault core, (c) Descriptions of the structural zones.

The clayey gouge zone of 3-8 cm thickness is thought to be the zone experiencing the strongest deformation. Although foliation is present at thin-section scale, foliation at outcrop scale in this zone is nearly invisible, reflecting the finer grain sizes (Figures 6.3c and 6.3d). Microscopic observations combined with bulk powder XRD analyses show that this zone is predominantly composed of tri-octahedral smectites, by approximately 80% or more, with minor amounts of serpentine clasts originating from the host rock. Actinolite/tremolite, talc, and calcite were also identified from the XRD patterns, the same as in the foliated gouge samples (Figure 6.4).

Exposure of the black/dark-gray cataclasite is relatively poor and discontinuous, but this zone seems to represent fault rocks derived mainly from the Matsuo sedimentary rocks. This zone is generally cohesive, except at the contact with the clayey gouge, as these fault rocks were found outside of the eroded portion of the fault core. The cataclasite is 20-30 cm thick, and it is composed mostly of a dark cohesive matrix with some white fragments originating from the Matsuo group floating within the matrix. Thin sections commonly show the presence of aggregates of sandy grains representing fragments from the Matsuo group (Figures 6.3e and 6.3f). Bulk XRD patterns revealed the presence of tri-octahedral smectites, chlorite, plagioclase, and

calcite but no serpentine, or quartz (Figure 6.4). Trace amounts of talc, actinolite/tremolite, and mica were found in one sample which probably mixed from the other zones.

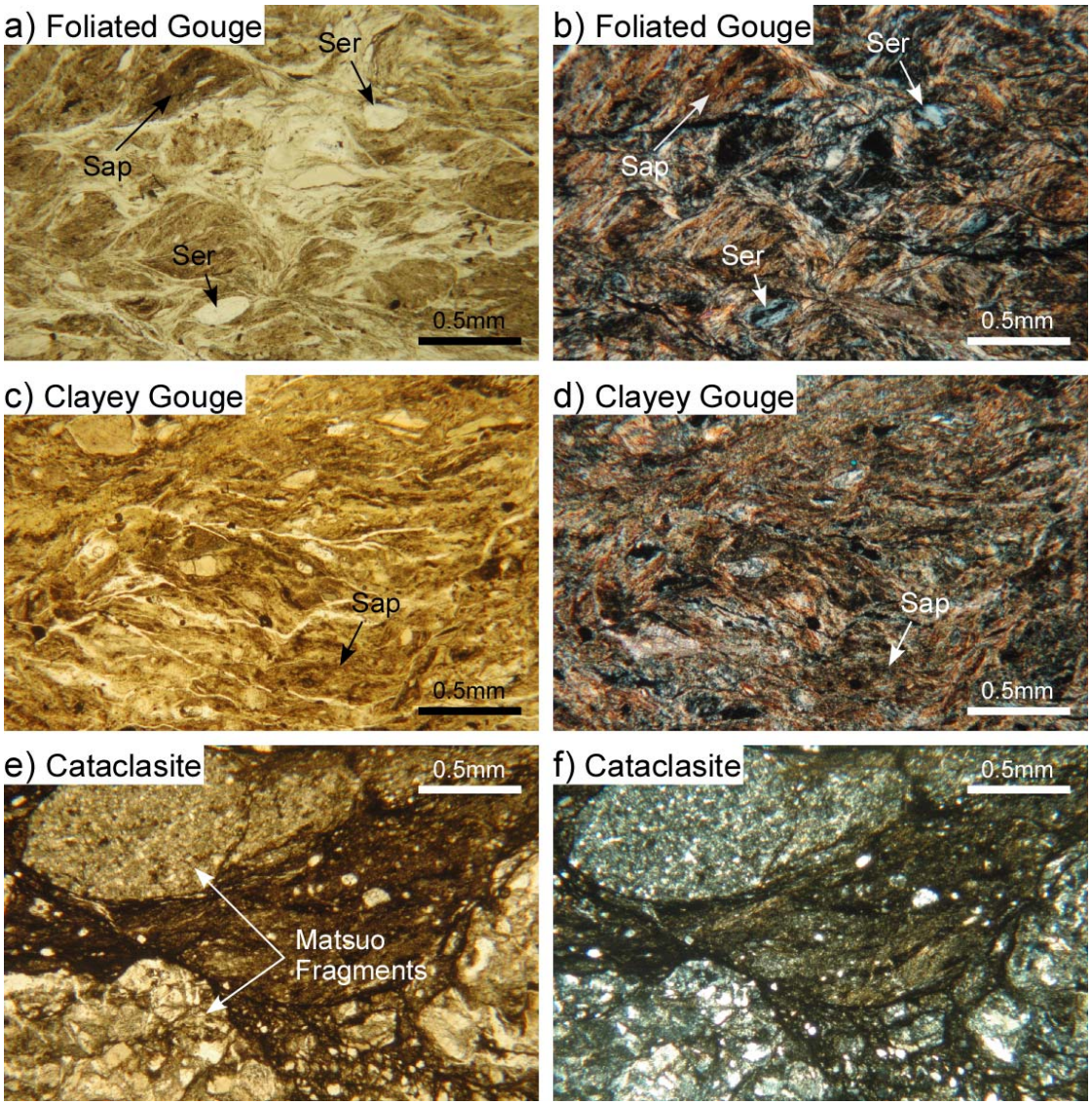

Figure 6.3: Photomicrographs of samples from the different core zones under polarized and cross-polarized light: (a,b) foliated gouge; (c,d) clayey gouge; (e,f) cataclasite. Ser: Serpentinite, Sap: Saponite.

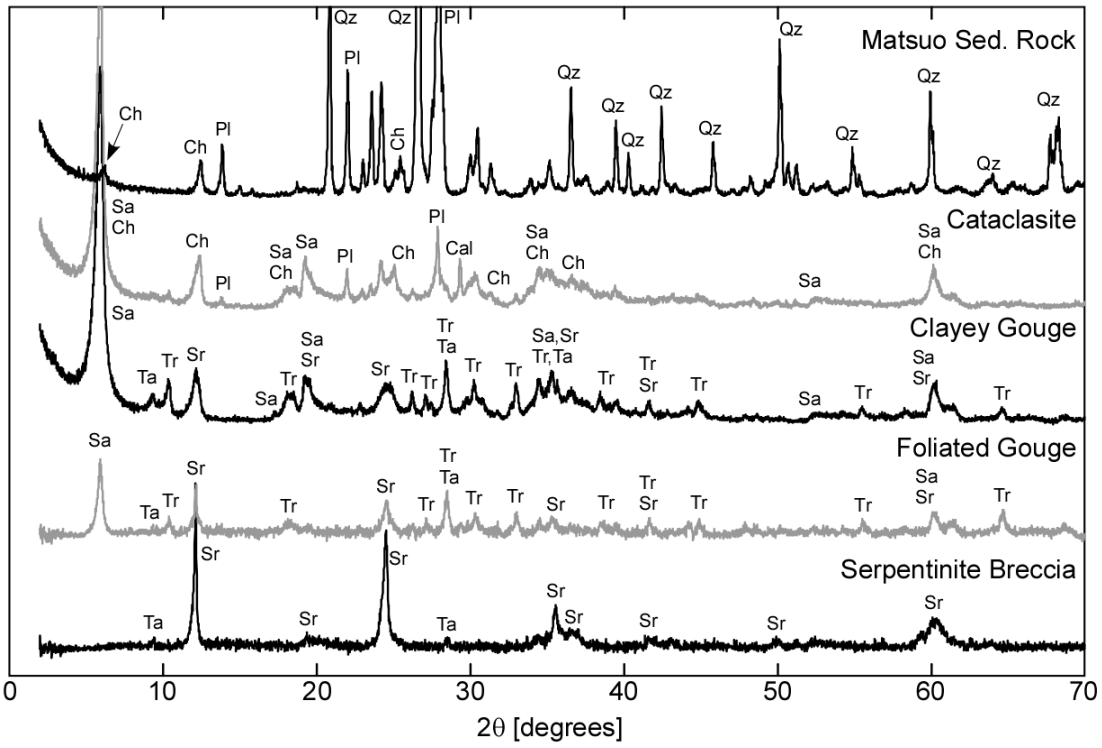

Figure 6.4: Bulk powder XRD patterns of the serpentinite breccia, foliated gouge, clayey gouge, cataclasite, and a sedimentary rock from Matsuo Group. Note that the bottom two data (e.g. serpentinite and foliated gouge) was obtained in a different X-ray equipment and the background is removed. Cal: Calcite, Ch: Chlorite, Pl: Plagioclase, Qz: Quartz, Sa: Saponite, Sr: Serpentinite, Ta: Talc, Tr: Tremolite.

6.3.3 Mineralogical Zoning

Additional SEM observations were conducted on several samples to aid the identification of smectite and amphibole minerals. An image of a sample from the clayey gouge zone is shown in Figure 6.5 where these minerals were co-located. Elemental spectra confirm that cations in these minerals are dominated by magnesium, therefore we identified the tri-octahedral smectite as saponite and the amphibole as tremolite. Interestingly, several bright appearing grains were identified as andradite garnet, which was not identified in the bulk XRD patterns of the clayey gouge.

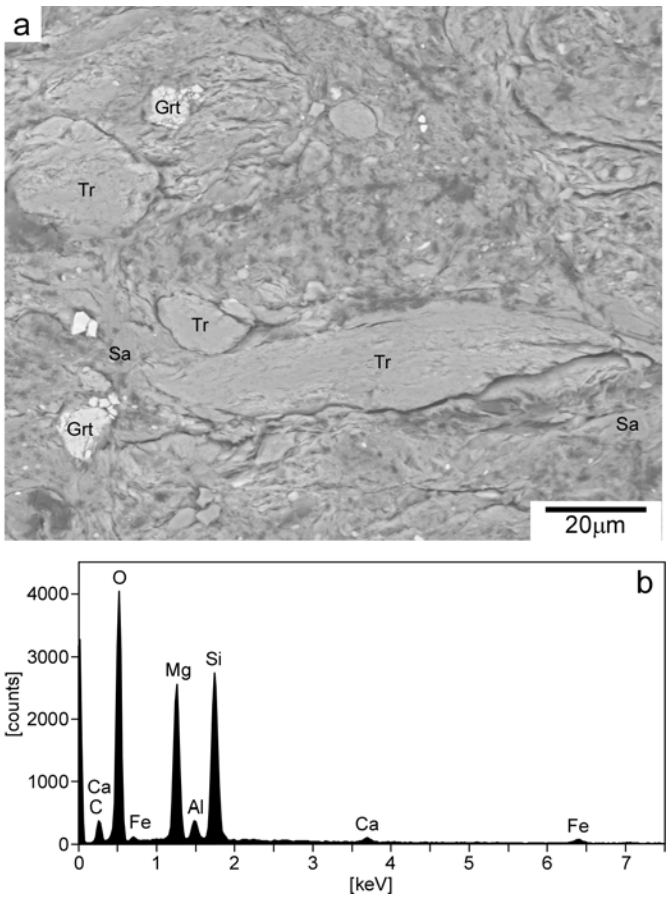

Figure 6.5: (a) A backscattered-electron SEM image of the clayey gouge showing a region containing saponite, tremolite and andradite garnet. Sap: Saponite, Tr: Tremolite, Grt: Andradite Garnet. (b) An EDS spectrum of the spot labeled saponite in (a).

Table 6.1 summarizes the mineralogical information for the different structural zones collected by all XRD measurements and SEM-EDS spectra. The mineralogical profile exhibits a clear zonation: (1) the concentration of saponite within the zones of the fault core, (2) the presence of talc, tremolite, and andradite garnet specifically in the foliated gouge and clayey gouge zone, (3) the absence of quartz in the Matsuo-origin cataclasite zone despite its abundance in the sedimentary host rock, and (4) the occurrence of chlorite only in the cataclasite and Matsuo sedimentary rocks.

Table 6.1: Minerals identified in each structural zone.

Mineral	Matsuo Sed. Rock	Cataclasite	Clayey Gouge	Foliated Gouge	Serpentinite
Serpentine			○	○	○
Calcite		○	○	○	○
Talc		T	○	○	○
Tremolite		T	○	○	
Saponite		○	○	○	
Chlorite	○	○			
Plagioclase	○	○			
Quartz	○				
Mica	○	T			
Others	Feldspar		Andradite Garnet	Andradite Garnet*2	Brucite, Xonotlite

*1 Open circles represent presence of the mineral, the "T" symbol represent presence in trace amounts
*2 Andradite Garnet is not confirmed, but expected in the foliated gouge

6.4 Transport Properties

Permeability measurements were conducted for some serpentinites, sedimentary rocks from the Matsuo group, and fault rocks from the fault core. Samples were prepared either by punching 2 cm diameter copper or stainless steel tubes into the incohesive outcrop surface, or by coring 2 cm diameter plugs from intact bulk rock samples. Samples were trimmed to a cylindrical shape, and then oven-dried before measurements. Permeability was measured in a triaxial vessel at 5-120 MPa isotropic confining pressure by applying a constant nitrogen pore pressure gradient and measuring the steady gas flow rate (see Tanikawa and Shimamoto, 2006 for details). Several pore pressure gradients were used in order to deduce the water permeability by correcting for the 'slip' effect (Klinkenberg, 1941). However, the estimated water permeability was lower than the gas permeability by at most a factor of 3, which is relatively insignificant compared to the variation between different samples, so we only report the gas permeability for the purpose of comparing data between samples. Direction of gas flow was parallel to the shear-induced foliation, thus the

measurements represent fault parallel permeabilities for the fault rocks and serpentinite breccia.

Figure 6.6 shows some representative results of the permeability measurements. Most Matsuo sedimentary rock samples were heavily weathered, so we report only two measurements for a fine-sandstone and very fine sandstone samples, which we believe represent the undamaged permeability. The permeability of the sandstone decreased from 10^{-15} to 10^{-17} m^2 as confining pressure was raised from 5 to 120 MPa, and it showed some hysteresis upon pressure cycling. Permeability of all fault core samples (breccia, clayey gouge, foliated gouge) followed a nearly identical trend.

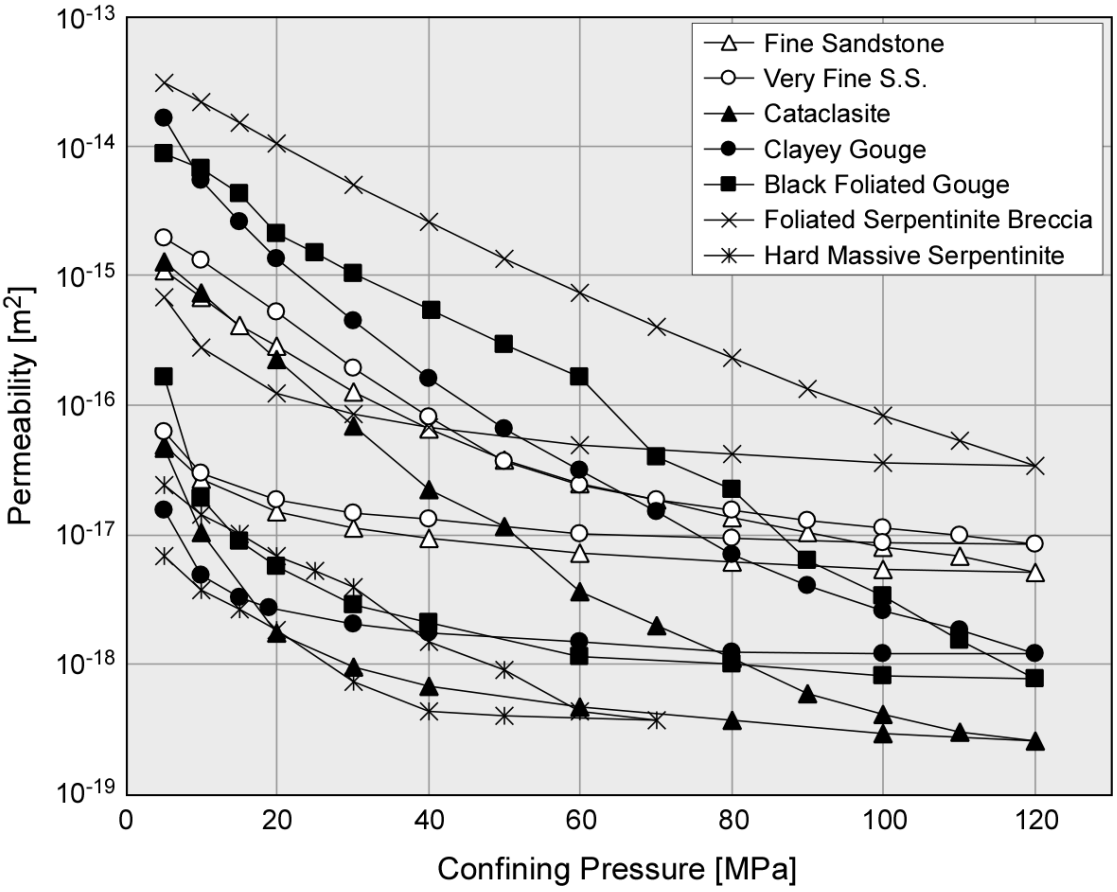

Figure 6.6: Representative results from the permeability measurements. Confining pressure was first increased from 5 MPa to 120 MPa and then decreased back down to 5 MPa, except for in the hard massive serpentinite clast measurement where permeability was too low to measure above 70 MPa in our apparatus.

Permeability decreased from about 10^{-14} to 10^{-18} m^2 upon pressurization and exhibited significant hysteresis, with permeability increasing by only one order of magnitude upon de-pressurization. Results of several serpentinite samples vary by up to 3 orders of magnitudes at a given pressure. This reflects the heterogeneous nature of the breccia texture at the scale of our 2-cm diameter sample. The sample cored from a black, hard serpentinite clast in the breccia exhibits the lowest permeability, 3×10^{-17} – 3×10^{-19} m^2, whereas the sample collected from the foliated serpentinite matrix shows much higher permeability, 3×10^{-14} – 3×10^{-17} m^2.

6.5 Frictional Properties

6.5.1 Experimental Method

The frictional properties of the saponitic clayey gouge were studied in a direct-shear frictional apparatus as described in Kawamoto and Shimamoto (1997) and Noda and Shimamoto (2009). The sliding frictional coefficient at several normal stresses (15-45 MPa) and load-point velocities ranging from 0.0014-140 μm/s were measured in both dry (room humidity) and wet conditions. Powder samples of the clayey gouge were prepared by disaggregating and gently crushing the natural sample with a mortar and pestle until it passed a sieve with 106 μm apertures. Two grams of powdered sample were sandwiched between 3 gabbro blocks which formed two rectangular fault surfaces, each one of dimensions 4 cm by 5 cm. This produced a fault of about 0.2 mm in thickness. A wet condition was achieved and maintained by allowing water to seep in from the bottom by capillary action during pre-compaction and by covering the fault plane by wet paper towels. Gouge was pre-compacted under 45 MPa fault normal stress for at least 4 hours for all experiments, so the pore pressure would equilibrate with atmospheric pressure. Thus all experiments were conducted at drained conditions. In this paper, displacement or velocity refers to the load-point displacement or load-point velocity, unless otherwise specified.

Results from all experiments are shown in Figure 6.7. As loading started at 14 μm/s, shear stress on the fault plane increased until the fault started to slip at displacement less than 1 mm. Shear stress after the initiation of slip was more or less constant up to about 5 mm displacement, but then shear stress either stayed constant or exhibited strain hardening. We believe that this strain hardening effect was caused by the combination of increase in effective shear strain rate due to gouge thinning and the velocity strengthening properties of this gouge, as discussed later. Although fault normal displacements of the loading column were not measured during the experiments, gouge extrusion observed from the edge of the fault planes was more severe in dry experiments conducted at high normal stress, perhaps consistent with the

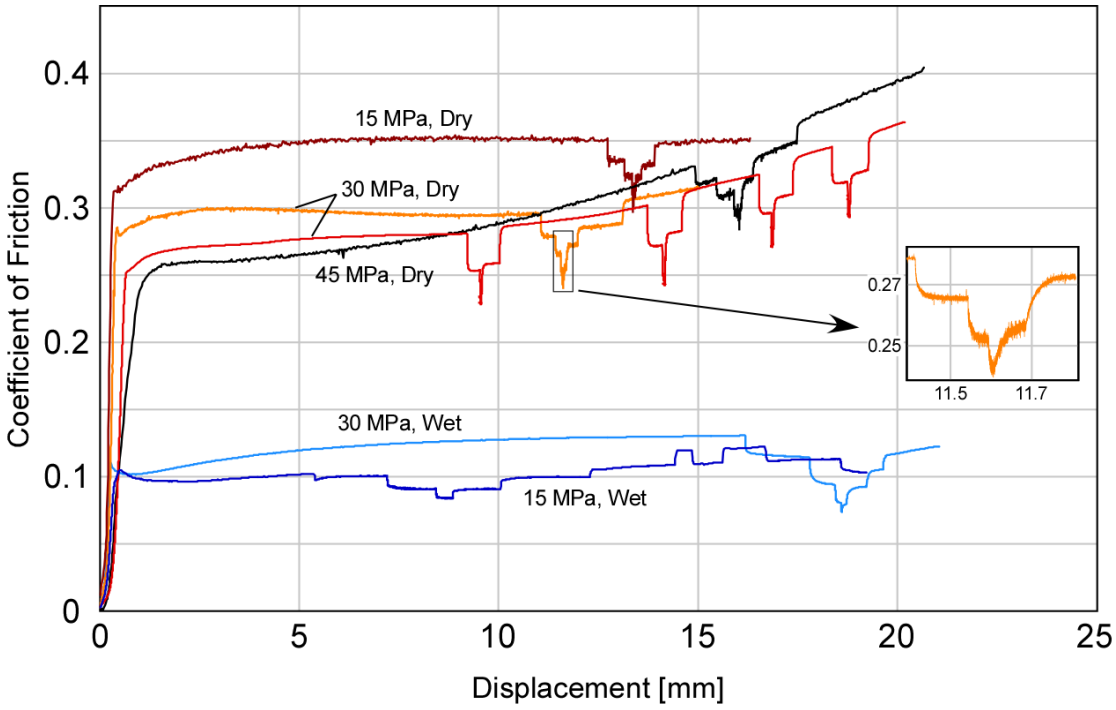

Figure 6.7: Friction data for the 6 experiments conducted. These are data prior to the de-trending process. The inset is an expanded view of the data collected at the lowest velocity (0.0014 μm/s) for one of the room-dry experiments tested at 30 MPa. The velocity history from the 15 MPa wet experiment is shown in Figure 6.10. In one of the 30 MPa room-dry experiment (the red data), velocity started from 14 μm/s, and then cycled 4 times between 14 μm/s and 0.0014 μm/s by applying velocity steps of factor 100. Velocities in all other experiments started from 14 μm/s stepped down 4 times by a factor of 10, down to 0.0014 μm/s, and then stepped up 4 times by a factor of 10, up to 14 μm/s.

greater strain hardening observed at high normal stresses (Figure 6.7). Therefore for the purpose of analyzing velocity dependence of friction, the data after 5 mm displacement are de-trended by subtracting the trend of a polynomial function that fits the data during 14 μm/s velocity.

Step changes in load-point velocity, by a factor of either 10 or 100, were introduced multiple times during each experiment to observe velocity-dependent changes in frictional coefficients. Ideally, the fault surface was slid for enough distance at each velocity to confirm the steady-state shear strength before going to the next velocity. However, although the majority of the change in shear strength was probably observed, enough fault slip may not have been achieved during the slower velocities (0.014-0.0014 μm/s) to confirm the steady-state shear strength (see inset of Figure 6.7).

6.5.2 Steady-state Friction

Frictional shear strengths at 5 mm displacement during sliding at 14 μm/s velocity ranged between 0.20-0.35 for dry experiments, and the frictional coefficients were lower at higher normal stresses (Figures 6.8a and 6.8b). In the wet experiments, the frictional coefficient was at extremely low values between 0.06–0.12, where in this case, the coefficient was slightly higher overall for the higher normal stress experiment (Figures 6.8a and 6.8b).

The steady-state values of the frictional strength after each step change in velocity were also measured from the de-trended data (Figure 6.8b). Frictional coefficient increases with increase in velocity, thus velocity strengthening, for all velocity step changes made in the experiments. The slopes of the lines fitted to the data sets in Figure 6.8 suggest that a-b values, which describe the velocity dependence of friction in the context of rate- and state-dependent friction theory (Dieterich, 1979; Ruina, 1983), lie between 0.005-0.006 for all experiments except for one wet experiment conducted at 15 MPa normal stress. This experiment showed a lower a-b value of 0.0032 and was conducted using gouge powders prepared from a different

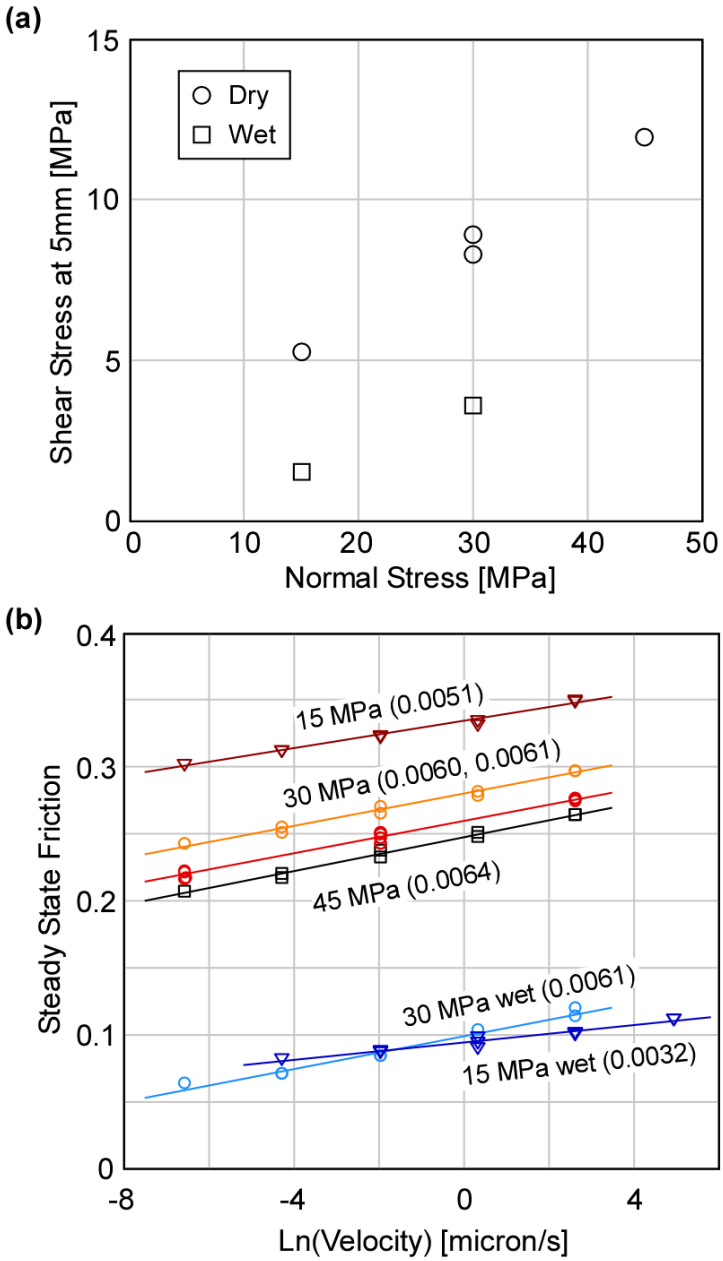

Figure 6.8: (a) Shear stress at 5 mm displacement vs. normal stress, (b) Steady-state friction at each velocity plotted against natural logarithm of the slip rate. Steady-state friction was obtained from the de-trended data. Each line is a linear fit to the data, with the slope corresponding to the a-b value in parentheses.

batch of the same clayey fault gouge. A slight variation in mineral composition may have affected the mechanical behavior, although all clayey gouge samples analyzed by powder XRD showed nearly identical mineralogy with some variation in calcite content.

6.5.3 Transient Friction between Steady States

As seen in Figure 6.7, some amount of displacement is required in order to obtain steady-state friction after a step change in velocity. We refer to this as the observed "transient" behavior of friction. Because a friction-testing apparatus does not have infinite stiffness, a finite amount of load-point displacement is always required for the loading column to shrink/expand to match the changing level of frictional strength caused by the introduction of velocity change. This is one cause of the observed transient behavior. On the other hand, rock shear strength is well-known to exhibit evolutional behavior between steady states. Such behavior is frequently described in a rate- and state-dependent law (Dieterich, 1979; Ruina, 1983) with the general form as described below,

$$\mu = \mu_0 + a\ln\left(\frac{V}{V_0}\right) + b\ln\left(\frac{\theta}{\theta_0}\right) \quad \text{where } \dot{\theta} = \dot{\theta}\left(\theta, V, d_c\right) \tag{6.1}$$

where a and b are constants, μ_0 and θ_0 are the steady-state frictional coefficient and state variable at reference velocity V_0, respectively. The second term in the equation describes the direct response of friction upon velocity change, and the third term describes the change in friction dependent on a state variable, θ, which evolves according to an evolution law described in differential form. Therefore the evolutional behavior of rock/gouge friction could also cause the observed transient behavior. Identifying whether the transient behavior observed in our experiments is caused solely by an experimental artifact due to finite stiffness, or also from the intrinsic evolutional behavior of the gouge material is important for the formulation of the frictional constitutive law and extrapolation of the laboratory results to fault stability analyses in a tectonic setting.

In order to evaluate the presence of any intrinsic evolutional frictional behavior of our samples, we calculated the load-point displacement, D_a, required to complete 95% of the friction change under a purely velocity-dependent friction law. Such a friction law is achieved by removing the third term from Equation 6.1. For a step

change in load-point velocity from V_0 to U, Noda and Shimamoto (2009) derived analytical expressions for the transient change in fault slip velocity, V.

$$V = \begin{cases} U/2\left(1+\tanh\left(t/\left(2a/kU\right)-1.099\right)\right) & \left(U=10V_0\right) \\ U/2\left(1+\coth\left(t/\left(2a/kU\right)+0.053\right)\right) & \left(U=0.1V_0\right) \end{cases} \tag{6.2}$$

where t is time, a is essentially the same as the a-b value since b=0 for the current case, k is the stiffness of the loading column. Combining Equation 6.2 with Equation 6.1 without the third term allows us to model the hypothetical transient behavior of friction under a purely velocity-dependent friction law (the bold lines in Figure 6.9), and determine the load-point displacement, D_a, at which 95% of the change in friction is complete. For a step change in load-point velocity by a factor of 10 and 0.1, D_a is approximately 4.30a/k and 2.11a/k, respectively. We obtained a values from the changes in steady-state friction from each velocity step in our experiment. For the stiffness, k, we referred to the calibration of the piston and loading-column stiffness presented in Noda and Shimamoto (2009). Uncertainty of the stiffness k was considered to be within 20% when calculating the possible ranges of D_a.

Figure 6.9 plots the relative changes in frictional coefficient observed after each velocity step against the load-point displacement from a dry experiment conducted at 30 MPa normal stress. Displacement is normalized by D_a, and change in friction is normalized by the final change in steady-state friction, $\Delta\mu_{ss}$. Unfortunately, some of the slower-velocity steps were terminated shortly after the load-point displacement exceeded D_a, but some important features are observed in Figure 6.9. If friction of the gouge is purely velocity dependent, it should follow the bold black curve which completes 95% of the friction change at D=D_a. However in most cases, the experimental data lie inside the region shown by the two bold dark curves, which means that the observed friction is changing more slowly against displacement than predicted by a purely velocity-dependent frictional behavior. More than 5% of the

friction change is occurring beyond D_a. Such a trend also seems to be more obvious for the velocity-up steps. Similar observations were derived from other experiments as

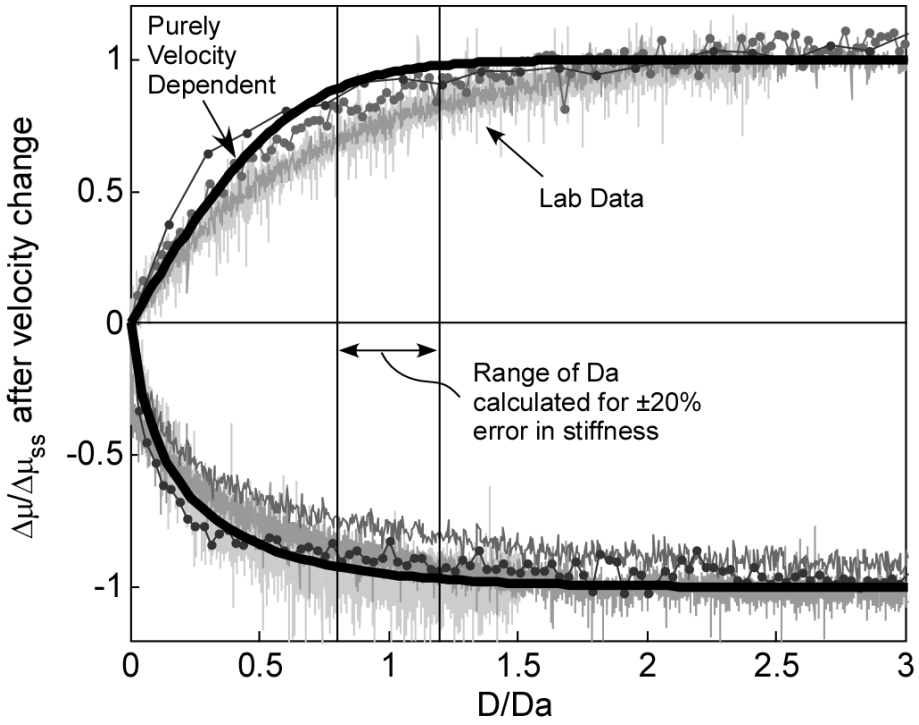

Figure 6.9: The change in friction after each velocity step plotted against displacement for the experiment conducted at 30 MPa normal stress in dry condition (orange data in Figure 6.7). Everything except for the two bold black curves is laboratory data. 4 velocity-down steps and 4 velocity-up steps were performed, all with velocity changes by a factor of 10. Data shown by filled circles are sparse since they represent data from higher velocities. The bold black curve indicates the predicted change in friction by a purely velocity-dependent friction law, which is given by assigning b=0 in Equation 6.1. Such curve is calculated by using the a-b values shown in Figure 6.8 (b), and by assigning a loading column stiffness taken from Noda and Shimamoto (2008). At D/Da=1, the bold black curve completes 95% of the transient change in friction. The two vertical lines indicate the range of uncertainty in Da for stiffness error ±20 %.

well. Therefore, we propose that the transient change in frictional coefficient was caused partly by the intrinsic evolution of the friction of the gouge material, rather than the deformation of the loading-column alone. It is also noted that the evolutional behavior occurs in the opposite sense as described by the third term in Equation 6.1 as will be discussed later.

Some unique but interesting transient frictional responses were also observed from the wet experiment conducted at 15 MPa normal stress, whose gouge powder sample was prepared from a different batch of clayey fault gouge sample (Figure 6.10).

The transient change in friction is a simple monotonic decay at lower velocities, as in the other experiments. However at higher velocities, friction exhibits a rather

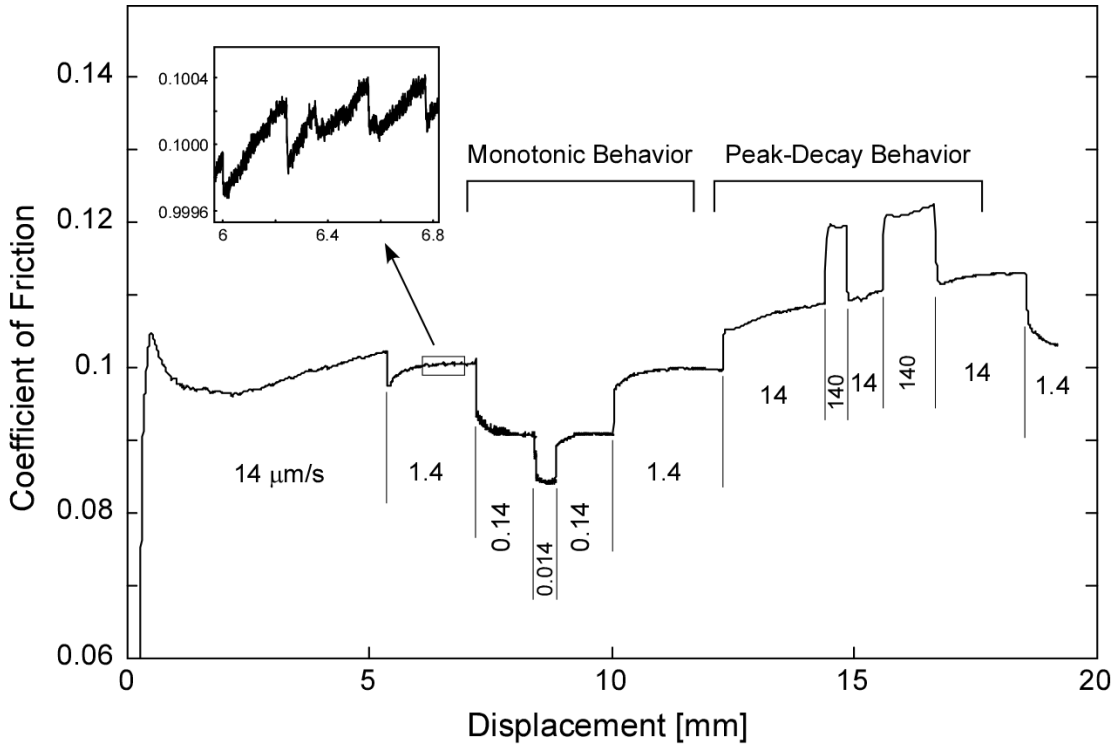

Figure 6.10: The friction data for experiment conducted at 15 MPa normal stress under wet condition. Load-point velocity is indicated below the data. Inset shows an expanded view of the stick-slip-like behavior observed during shear at 1.4 μm/s load-point velocity. Monotonic changes in friction upon a step change in velocity are seen at lower velocities. Peak-Decay behavior appears upon step changes in velocity at faster velocities.

complicated combination of peak, decay, and re-strengthening transient behavior (Figure 6.10). Such a transition in the transient response is not observed in the other experiments, but it evokes the possibility of a transition in the frictional behavior. A slightly unstable, stick-slip-like fluctuation in friction is observed during sliding at 1.4 and 14 μm/s (Figure 6.10 inset). The drop in frictional strength is not instantaneous as in typical stick-slip instability, but rather slow, taking place on the order of seconds.

6.6 Discussion

6.6.1 Metasomatism in the Fault Core Region

The textural and mineralogical zonations documented across the fault core (Figure 6.2, Table 6.1) indicate that the fault records at least two stages in its development, accompanying progressive exhumation. The first stage began when the serpentinite was faulted against the Matsuo Group sedimentary rocks along the G-A Tectonic Line. Contacts between serpentinite and felsic country rocks are known to produce metasomatic reaction zones under hydrothermal conditions (e.g., Phillips and Hess, 1936; Curtis and Brown, 1969; Koons, 1981; Sanford, 1982; Mori et al., 2007; Viti and Collettini, 2009; Soda and Takagi, 2010; Moore and Rymer, 2010). In such settings, hydrothermal fluids facilitate the migration of MgO from the serpentinite to the country rock and the migration of SiO2 from the country rock to the serpentinite. The amount and direction of transfer of other elements may vary somewhat, depending on the specific pressure, temperature, and compositional conditions associated with the developing reaction zone (e.g., Sanford, 1982). Here, fluid-assisted migration of elements across the G-A Tectonic Line led to the crystallization of talc and tremolite/actinolite in the foliated gouge on the serpentinite side and of chlorite in the cataclasite on the Matsuo Group side. Quartz was completely removed from the cataclasite by reaction, as has also been observed in other reaction zones (Phillips and Hess, 1936). The wide zone of relatively high-permeability serpentinite breccia may have facilitated reaction by providing a path for the supply of hydrothermal fluids. The talc-tremolite-chlorite-andradite garnet assemblage indicates crystallization at greenschist- to subgreenschist-facies conditions (Sanford, 1982; Soda and Takagi, 2010), corresponding to temperatures between approximately 250° and 400°C.

The clayey gouge zone formed subsequently at the contact between the cataclasite and foliated gouge, and it contains clasts derived from those zones (Figure 6.5a). The conversion of trioctahedral smectite to chlorite with increasing depth and temperature has been well documented in a variety of diagenetic and low-grade metamorphic environments (e.g., Inoue and Utada, 1991; Murakami et al., 1999;

Robinson et al., 2002). Conversely, growth of the Mg-rich saponitic smectite clays in the clayey gouge may reflect shearing-enhanced reactions along the fault plane at shallower depths and lower temperatures than those attained during formation of the chlorite-bearing assemblages. Moore and Lockner (2010) have duplicated such reactions in triaxial experiments in which serpentinite was sheared against granite at hydrothermal conditions.

Two active shear zones (CDZ, SDZ) that were identified based on casing deformation in the SAFOD borehole crossing the San Andreas fault near Parkfield, California were successfully cored in 2007 (Zoback et al., 2010). Both the CDZ and SDZ are foliated gouge zones that consist of porphyroclasts of sedimentary rock and serpentinite in a matrix of the Mg-rich smectite clays saponite ± corrensite (Moore and Rymer, 2010; Holdsworth et al., 2011). Textures of the CDZ and SDZ gouges are remarkably similar to those of the clayey fault gouge zone shown in Figure 6.5a. The SAFOD core was retrieved from ~2.7 km depth, where temperatures of ~112-114°C were recorded (Zoback et al., 2010). By correlation, the saponitic clays of the G-A Tectonic Line may also have formed at ≤3 km depth. Interestingly, some serpentinite porphyroclasts in the SAFOD gouges also contain talc, tremolite/actinolite, chlorite, and andradite garnet (Moore and Rymer, 2010), although the higher-temperature alteration minerals form a much smaller proportion of those gouges than is observed here.

6.6.2 Steady-state Friction of Clayey Gouge

Results of our friction experiments are in good agreement with past studies on clay friction. Although our experiments were conducted at room temperature, the low coefficient of friction of ~0.1 measured under wet condition is consistent with frictional coefficients of saponite-rich gouge, about 0.15, collected from the SAFOD borehole (Lockner et al., 2011; Carpenter et al., 2011). Difference in the coefficient of friction under dry and wet conditions is also in agreement with other studies (Morrow et al., 2000; Moore and Lockner, 2007; Ikari, 2007). Ikari et al. (2007) observed change in friction with water content, from oven-dried to hydrated samples, and

observed that friction decreases from about 0.4–0.5 to <0.1 for pure Ca-montmorillonite samples upon incremental hydration. If we consider that our "dry" samples were actually partially hydrated by atmospheric moisture, the observed decrease in friction from 0.2–0.35 to 0.06–0.12 upon saturation by water is in agreement with Ikari et al. (2007) although the types of smectite tested are different.

The observed change in frictional coefficient in response to changes in normal stress is also consistent with those observed in past studies conducted on montmorillonite gouges (Ikari et al., 2007; Moore and Lockner, 2007 and references therein). For our "dry" experiments friction decreases with normal stress, which is thought to be caused by the decrease in pore volume, thus resulting in an increased degree of saturation at higher normal stress, as proposed by Wang et al. (1980) and reviewed by Moore and Lockner (2007). On the other hand, friction increased slightly with normal stress in our "wet" fully-saturated experiments. Such increase in friction is also observed in well-drained, saturated montmorillonite friction experiments (Morrow et al., 1992; Moore and Lockner, 2007), and it is thought to be controlled by the interlayer water film thickness, which decreases upon increase in normal stress (Moore and Lockner, 2007).

Friction was consistently velocity strengthening throughout the velocity range tested in our experiments. Velocity dependence of montmorillonite is usually found to be velocity strengthening (Morrow et al., 1992; Moore and Lockner, 2007), although some studies (Saffer and Marone, 2003; Ikari et al., 2007) report changes in velocity dependence of montmorillonite friction with changes in normal stress or slip rate. We do not see a change in velocity dependence with slip rate, but did observe a difference in the a-b value between the two wet experiments conducted. Whether this was caused by the change in normal stress or the slight difference in mineral composition is not known from the two experiments, but shall be investigated in future experiments.

6.6.3 Transient Frictional Behavior of Clayey Gouge

The monotonic-decay of transient friction upon velocity change seen in our experiments has also been observed in other studies of phyllosilicate-mineral friction. Reinen et al. (1991) observed such behavior for antigorite and lizardite at low slip rates (< 0.03 μm/s), Moore et al. (1996) for chrysotile (0.1–10 μm/s), Moore and Lockner (2008) for talc (0.0032–3.2 μm/s), and Ikari et al. (2009) for various clay-rich samples at higher slip rates (1~300 μm/s; Ca-montmorillonite, illite, chlorite; Ikari et al., 2009). These observations raise a question on whether friction of clay minerals should also be described by the exact form of the rate- and state-friction law (Equation 6.1). In the rate- and state-friction law, the direct effect (second term) and evolution effect (third term) act in the opposite sense at different time-scales upon a velocity change when parameters a and b are taken as positive values, which is not observed in the monotonic-decay trend of these clay friction data.

One way to explain the transient friction is to neglect the evolution effect (b=0), similar to the approach of determining D_a in section 5.2, which could be viewed analogous to a flow constitutive law (Reinen et al., 1992) or viewed as the saturation of contact area at the fault surface (Ikari et al., 2009). However, Figure 6.9 and many results by Ikari et al. (2009) show that friction change takes place beyond the displacement required for loading column shrinkage/expansion. Ikari et al. (2009) expressed the remaining transient behavior using a negative state evolution effect by assigning negative values for b. While such an approach is useful for the phenomenological description of the frictional behavior in the framework of rate and state friction, the physical meaning is questionable since the state evolution effect is generally physically understood to be the manifestation of the time dependency of static friction (Dieterich, 1972, 1979). Given additionally that our data have unevenness in the total slip achieved at a given slip velocity, being much shorter for slower velocities, we refrain from fitting a rate and state friction law using negative b values to explain the experimental data, but we point out that an intrinsic friction evolution in the positive velocity-dependent direction is taking place in the studied

saponite-rich gouge, which would be opposite to the sense of the state evolution effect described by the rate and state friction law.

A possible formulation of such behavior perhaps is similar to that presented by Noda and Shimamoto (2010). Their rate- and state-dependent flow law accounts for the direct and evolution effect, which both act in the velocity-strengthening direction as seen in their halite friction experiments. Since their experiments were done within the fully plastic regime of halite, where flow stress is insensitive to normal stress, the same formulation may not apply directly to clay friction. However the transition to pressure-insensitive frictional strength of a montmorillonite at high pressures observed by Saffer and Marone (2003) and Ikari et al. (2007) encourages the investigation of such analogy, although such pressure-insensitivity may have been caused by pore fluid over-pressure during their experiments (Moore and Lockner, 2007).

Such ductile flow behavior is also observed to transition into, and out of, brittle frictional behavior in response to the change in shearing rate, temperature, or pressure. Reinen et al. (1992) described the transition from a flow-like law to brittle friction in serpentinites using a two-mechanism model where two independent flow and friction laws were connected in an iso-stress fashion. More recently, Shimamoto and Noda (2010) attempted to connect the rate- and state-dependent flow/friction laws using a hyperbolic tangent function to allow the smooth transition from flow- to friction-governed rheology. Interestingly, the predicted change in the transient behavior of friction illustrated in Noda and Shimamoto (2011, this issue) qualitatively matches quite well with the observed change in transient behavior from our experiments conducted at 15 MPa under wet condition (Figure 6.10). In our data, the transition from monotonic-decay to peak-decay behavior occurs between 1.4 and 14 μm/s. This is also the slip rate at which the slow stick-slip-like unstable behavior was observed, possibly analogous to the instability observed by Shimamoto (1989) and Noda and Shimamoto (2010) in halite shear zones in the semi-ductile regime, although the slow stick-slip observed in halite shear zones occurred in a velocity-weakening regime

rather than a velocity-strengthening regime. This invokes the possible presence of a brittle-ductile transition in the constitutive behavior of clay-rich fault gouges, thus motivating further investigation of the friction/flow constitutive properties of clayey fault gouges, as low-frequency type deformation has been identified at depths near the brittle-ductile transition along plate boundaries (Obara, 2002).

6.6.4 Applicability of Laboratory Results and its Implications

Extrapolation of the laboratory results presented here to subsurface settings requires careful consideration of the discrepancy between laboratory and natural conditions. Although water permeability was estimated to be roughly in the same order as the measured nitrogen gas permeability, some of our results may not directly represent in-situ permeability since samples were oven-dried prior to the measurements. The artifact of drying samples is probably most significant in samples with large amounts of swelling clay (i.e. clayey gouge, foliated gouge), in which creation of artificial porosity upon drying is expected due to the removal of interlayer and adsorbed water. Part of the drastic permeability reduction with confining pressure in these fault core samples should reflect the collapse of the additional pore volume that was created by drying these samples. Measured permeability of the Matsuo group also may not reflect the macroscopic permeability of the formation as our 2 cm diameter sample is not large enough to adequately sample the fractures present at outcrop scale. Some measurements were made on fractured samples, but to upscale such data to infer the macroscopic permeability requires statistical information of the fracture distribution which we do not have. However, the permeability of the serpentinite breccia is more reliable. The serpentinite was found to be nearly monomineralic, without swelling clays, and our measurements were able to capture the heterogeneous nature of the breccia texture. Since we expect that fluid flow would be dominated by the most permeable member, the estimated water permeability of the foliated serpentinite matrix of 10^{-14} – 10^{-17} m^2 at 5–120 MPa is expected to be close to the in-situ permeability of the serpentinite breccia in the subsurface. Large

serpentininte-bearing fault zones hosting a vast zone of permeable damage zone like the G-A Line shall be important conduits for fluid migration in the crust.

Room-dry friction experiments may give useful insight about the physical mechanism taking place during shearing and its control on friction, but "wet" experiments are more relevant to the in-situ frictional behavior of the clayey gouge since fault gouge is not dry in the subsurface. Water-saturated friction of the saponite-rich gouge is extremely low, ~ 0.1, and strongly velocity strengthening, which would favor a weak, stable sliding fault when it was active. The in-situ fault strength could be even lower if we acknowledge that the laboratory fault (~ 0.2 mm) was thinner than the clayey gouge (several cm) by two orders of magnitude. The lowest velocity tested in our experiments, 0.0014 μm/s (= 4.4 cm/yr), was comparable to tectonic fault slip rates, but the shear strain rate was probably higher by at least two orders of magnitude compared to what the clayey gouge experienced under similar tectonic fault slip rates. If we extrapolate the velocity-strengthening trend down to even lower slip rates to account for the difference in thickness, friction can be well below 0.05 at tectonic fault slip rates creating a nearly frictionless fault zone.

We have reported observations and laboratory results showing that the fault zone in the studied outcrop hosts a peculiar mineral assemblage characterized by the local presence of an extremely weak saponite-rich gouge that was created by hydrothermal metasomatic reactions. It is likely that the permeable nature of the fault zone played a key role in the evolution of the fault zone mineralogy, eventually weakening the shallow portion of the fault. Our study highlights the importance of chemical reactions along fault zones that could ultimately alter the mechanical property of the fault itself over the course of its geological history.

6.7 References

Allen, C.R., 1968. The tectonic environments of seismically active and inactive areas along the San Andreas fault system. In: Dickinson, W.R., Grantz, A. (Eds.), Proceedings of Conference on Geologic Problems of San Andreas Fault System. Stanford University Publications in the Geological Sciences 11, 70–80.

Brune, J.N., Henyey, T.L., Roy, R.F., 1969. Heat flow, stress and rate of slip along the San Andreas fault, California. Journal of Geophysical Research 74, 3821–3827.

Carpenter, B.M., Marone, C., Saffer, D.M., 2011. Weakness of the San Andreas Fault revealed by samples of the active fault zone, Nature Geoscience 4, 251–254, doi:10.1038/ngeo1089.

Curtis, C.D., Brown, P.E., 1969. The metasomatic development of zoned ultrabasic bodies in Unst, Shetland. Contributions to Mineralogy and Petrology 24, 275–292.

Dieterich, J.H., 1972. Time-dependent friction in rocks. Journal of Geophysical Research 77(20), doi:10.1029/JB077i020p03690.

Dieterich, J.H., 1979. Modeling of rock friction: 1. Experimental results and constitutive equations. Journal of Geophysical Research 84(B5), 2161–2168, doi:10.1029/JB084iB05p02161.

Fryer, P., Pearce, J.A., Stokking, L.B., et al., 1990. Proceedings of the ODP, Initial Reports, 125, College Station, Texas (Ocean Drilling Program) 69-80, doi:10.2973/odp.proc.ir.125.1990.

Fujioka, K., Tanaka, T., Aoike K., 1995. Serpentine seamount in Izu-Bonin and Mariana Forearcs - Observation by a submersible and its relation to onland serpentinite belt-. Journal of Geography 104(3), 473–494. (in Japanese)

Guillot, S., Hattori, K., de Sigoyer, J., 2000. Mantle wedge serpentinization and exhumation of eclogites: insights from eastern Ladakh, northwest Himalaya. Geology 28, 199–202.

Hamada, T., 1963. On the Gokasho-Arashima Tectonic Line. Journal of the Geological Society of Japan 69, 208–209. (in Japanese)

Hanna, W.F., Brown, R.D., Jr., Ross, D.C., Griscom, A., 1972. Aeromagnetic reconnaissance and generalized geologic map of the San Andreas fault between San Francisco and San Bernardino, California. U. S. Geological Survey Geophysical Investigations Map GP-815.

Hess, H.H., 1955. Serpentines, orogeny and epeirogeny. Geological Society of America Special Paper 62, 391–408.

Hilairet, N., Reynard, B., Wang, Y., Daniel, I., Merkel, S., Nishiyama, N., Petitgirard, S., 2007. High-pressure creep of serpentine, interseismic deformation, and initiation of subduction. Science 318, 1910–1913.

Holdsworth, R.E., Van Diggelen, E.W.E., Spiers, C.J., De Bresser, J.H.P., Walker, R.J., Bowen L.A., 2011. Fault rocks from the SAFOD core samples: Implications for weakening at shallow depths along the San Andreas Fault, California. Journal of Structural Geology 33, 132–144, doi:10.1016/j.jsg.2010.11.010.

Hyndman, R.D., Peacock, S.M., 2003. Serpentinization of the forearc mantle. Earth and Planetary Science Letters 212, 417–432.

Ichikawa, K., Ishii, K., Nakagawa, C., Suyari, K., Yamashita, N., 1956. Die Kurosegawa Zone. Journal of the Geological Society of Japan 62, 82–103. (in Japanese with German abst.)

Ikari, M.J., Saffer, D.M., Marone, C., 2007. Effect of hydration state on the frictional properties of montmorillonite-based fault gouge. Journal of Geophysical Research 112, B06423, doi:10.1029/2006JB004748.

Ikari, M.J., Saffer, D.M., Marone, C., 2009. Frictional and hydrologic properties of clay-rich fault gouge. Journal of Geophysical Research 114, B05409, doi:10.1029/2008JB006089.

Inoue, A., Utada, M., 1991. Smectite-to-chlorite transformation in thermally metamorphosed volcanoclastic rocks in the Kamikita area, northern Honshu, Japan. American Mineralogist 76, 628–640.

Irwin, W.P., Barnes, I., 1975. Effect of geologic structure and metamorphic fluids on seismic behavior of the San Andreas fault system in central and northern California. Geology 3, 713–716.

Kamimura, A., Kasahara, J., Hino, R., Shinohara, M., Shiobara, H., Kanazawa, T., 2000. The significance of water on plate subduction and the seismic velocity structure across the serpentine diapir in the Izu-Bonin Trench. Journal of Geography 109(4), 506–516. (in Japanese)

Kato, K., Saka, Y., 2003. Kurosegawa Terrane as a transform fault zone in southwest Japan. Gondwana Research 6(4), 669–686.

Katoh, K., Saka, J., Iwasaki, J., Tsuchiyama, S. 1992. The Kurosegawa Tectonic Terrane in the western Shima Peninsula, southwest Japan. Journal of the Geological Society of Japan 98(12), 1149–1152. (in Japanese with English abstract)

Kawamoto, E., Shimamoto, T., 1997. Mechanical behavior of halite and calcite shear zones from brittle to fully-plastic deformation and a revised fault model. Proceedings of the 30th International Geological Congress 14, 89–105.

Klinkenberg, L.J., 1941. The permeability of porous media to liquids and gases. Drilling and Productions Practices, American Petroleum Institute, 200–213.

Koons, P.O., 1981. A study of natural and experimental metasomatic assemblages in an ultramafic-quartzofeldspathic metasomatic system from the Haast Schist, South Island, New Zealand. Contributions to Mineralogy and Petrology 78, 189–195.

Lachenbruch, A.H., Sass, J.H., 1980. Heat flow and energetics of the San Andreas fault zone. Journal of Geophysical Research 85, 6185–6223.

Lockner, D.A., Morrow, C., Moore, D., Hickman, S., 2011, Low strength of deep San Andreas Fault gouge from SAFOD core. Nature 472, 82–85, doi:10.1038/nature09927.

Moore, D.E., Lockner, D.A., 2007. Friction of the smectite clay montmorillonite: A review and interpretation of data. In: Dixon, T.H., Moore, J.C. (Eds.), The Seismogenic Zone of Subduction Thrust Faults. Columbia University Press, New York, 317–345.

Moore, D.E., Lockner, D.A., 2008. Talc friction in the temperature range 25-400°C: Relevance for fault-zone weakening. Tectonophysics 449, 120–132.

Moore, D.E., Lockner, D.A., 2010. Metamorphic petrology meets rock mechanics: Solution-transfer creep and reaction weakening of serpentinite sheared against crustal rocks. Abstract MR13B-01 presented at 2010 Fall Meeting, AGU, San Francisco, Calif., 13-17 Dec.

Moore, D.E., Lockner, D.A., Ma, S., Summers, R., Byerlee, J.D., 1997. Strengths of serpentinite gouges at elevated temperatures. Journal of Geophysical Research 102, 14,787–14,801.

Moore, D.E., Lockner, D.A., Summers, R., Ma, S., Byerlee, J.D., 1996. Strength of chrysotile–serpentinite gouge under hydrothermal conditions: Can it explain a weak San Andreas fault? Geology 24, 1041–1044.

Moore, D.E., Rymer, M.J., 2007. Talc, serpentinite, and the creeping section of the San Andreas fault. Nature 448, 795–797.

Moore, D.E., Rymer, M.J., 2010. Metasomatic origin of fault gouge comprising the two actively creeping strands at SAFOD. Abstract T41A-2105 presented at 2010 Fall Meeting, AGU, San Francisco, Calif., 13-17 Dec.

Morrow, C., Moore, D., Lockner, D., 2000. The effect of mineral bond strength and adsorbed water on fault gouge frictional strength. Geophysical Research Letters 27(6), 815–818.

Morrow, C., Radney, B., Byerlee, J., 1992. Frictional strength and the effective pressure law of montmorillonite and illite clays. In: Evans, B., Wong, T.F. (Eds.), Fault Mechanics and Transport Properties of Rocks. Elsevier, New York, 69–88.

Mori, Y., Nishiyama, T., Yanagi, T., 2007. Chemical mass balance in a reaction zone between serpentinite and metapelites in the Nishisonogi metamorphic rocks, Kyushu, Japan: Implications for devolatilization. Island Arc 16, 28–39.

Murakami, T., Sato, T., Inoue, A., 1999. HRTEM evidence for the process and mechanism of saponite-to-chlorite conversion through corrensite. American Mineralogist 84, 1080–1087.

Noda, H., Shimamoto, T., 2009. Constitutive properties of clayey fault gouge from the Hanaore fault zone, southwest Japan. Journal of Geophysical Research 114, B04409, doi:10.1029/2008JB005683.

Noda, H., Shimamoto, T., 2010. A rate- and state-dependent ductile flow law of polycrystalline halite under large shear strain and implications for transition to brittle deformation. Geophysical Research Letters 37, L09310, doi:10.1029/2010GL042512.

Noda, H., Shimamoto, T., 2011. Transient behavior and stability analyses of halite shear zones with an empirical rate-and-state friction to flow law. Journal of Structural Geology (this issue)

Obara, K., 2002. Nonvolcanic deep tremor associated with subduction in southwest Japan. Science 296, 1679–1681.

Phillips, A.H., Hess, H.H., 1936. Metamorphic differentiation at contacts between serpentinite and siliceous country rocks. American Mineralogist 21(6), 333–362.

Raleigh, C.B., Paterson, M.S., 1965. Experimental deformation of serpentinite and its tectonic implications. Journal of Geophysical Research 70(16), 3965–3985.

Reinen, L.A., Weeks, J.D., Tullis, T.E., 1991. The frictional behavior of serpentinite: Implications for aseismic creep on shallow crustal faults. Geophysical Research Letters 18(10), 1921–1924, doi:10.1029/91GL02367

Reinen, L. A., Tullis, T. E., Weeks, J. D., 1992. Two-mechanism model for frictional sliding of serpentinite, Geophysical Research Letters 19(15), 1535–1538, doi:10.1029/92GL01388.

Reinen, L A., Weeks, J.D., Tullis, T E. 1994. The frictional behavior of lizardite and antigorite serpentinites: Experiments, constitutive models, and implications for natural faults. Pure and Applied Geophysics 143(1-3), 317–358.

Robinson, D., Schmidt, S.Th., Santana de Zamora, A., 2002. Reaction pathways and reaction progress for the smectite-to-chlorite transformation: Evidence from hydrothermally altered metabasites. Journal of Metamorphic Geology 20, 167–174.

Ruina, A.L., 1983. Slip instability and state variable friction laws, Journal of Geophysical Research 88, 10,359–10,370, doi:10.1029/JB088iB12p10359.

Saffer, D.M., Marone, C., 2003. Comparison of smectite- and illite-rich gouge frictional properties: Application to the updip limit of the seismogenic zone along subduction megathrusts. Earth and Planetary Science Letters 215, 219–235.

Saka, Y., Tsukamoto, K., Ohya, Y., Umino, R., 1979. Stratigraphy of the Upper Mesozoic beds in the western Shima Peninsula, Southwest Japan, Journal of the Geological Society of Japan 85(2), 81–96. (in Japanese with English abstract)

Saka, Y., Tezuka, S., Okada, Y., Ichikawa, M., Takagi, H., 1988. Gokasho-Arashima Tectonic Line, as a serpentinite mélange zone, in the Shima Peninsula, Southwest Japan. Journal of the Geological Society of Japan 94(1), 19–34. (in Japanese with English abstract)

Sanford, R., 1982. Growth of ultramafic reaction zones in greenschist to amphibolite facies metamorphism. American Journal of Science 282, 543–616.

Shimamoto, T., 1989. Mechanical behaviours of simulated halite shear zones: implications for the seismicity along subducting plate-boundaries. In: Karato, S., Toriumi, M. (Eds.), Rheology of Solids and of Earth, Oxford University Press, USA, 351–373.

Shimamoto, T., Noda, H., 2010. A new brittle to plastic constitutive law and its implications for subduction-zone seismicity. Abstract T24A-01 presented at 2010 Fall Meeting, AGU, San Francisco, Calif., 13-17 Dec.

Soda, Y., Takagi, H., 2010. Sequential deformation from serpentinite mylonite to metasomatic rocks along the Sashu Fault, SW Japan. Journal of Structural Geology 32, 792–802.

Takahashi, N., Suyehiro, K., Shinohara, M., 1998. Implications from the seismic crustal structure of the northern Izu-Bonin arc. The Island Arc 7, 383–394.

Tanikawa, W., Shimamoto, T., 2006. Klinkenberg effect for gas permeability and its comparison to water permeability for porous sedimentary rocks. Hydrology and Earth System Sciences Discussions 3, 1315–1338.

Viti, C., Collettini, C., 2009. Growth and deformation mechanisms of talc along a natural fault: a micro/nanostructural investigation. Contributions to Mineralogy and Petrology 158, 529–542, doi:10.1007/s00410-009-0395-4.

Wang, C.Y., Mao, N.H., Wu, F.T., 1980. Mechanical properties of clays at high pressure. Journal of Geophysical Research 85, 1462–1468.

Yamagiwa, N., 1957. Stratigraphy and Geological Structure of the Eastern Area of Shima Peninsula. Journal of the Geological Society of Japan 63, 263–272.

Yoshikura, S., Terashima, T., 1984. Geological significance of the amphibolite from the Gokasho-Arashima Tectonic Line in the middle part of the Shima Peninsula. Journal of Mineralogy, Petrology, and Economic Geology 79, 311–317. (In Japanese with English abstract)

Zoback, M.D., Zoback, M.L., Mount, V.S., Suppe, J., Eaton, J.P., Healy, J.H., Oppenheimer, D., Reasenberg, P., Jones, L., Raleigh, C.B., Wong, I.G., Scotti, O., Wentworth, C., 1987. New evidence for the state of stress on the San Andreas fault system. Science 238, 1105–1111.

Zoback, M., Hickman, S., Ellsworth, W., 2010. Scientific drilling into the San Andreas Fault zone. EOS, Transactions, American Geophysical Union 91, 197–199.